Rare-Earth-Based Nanoparticles: From Microwave-Assisted Synthesis to Potential Applications

Nan Liu

A thesis submitted in partial fulfillment of the requirements for the

Doctorate in Philosophy Degree in Chemistry

Department of Chemistry and Biomolecular Sciences

Faculty of Science

University of Ottawa

Abstract

Lanthanide (Ln^{3+})-based nanoparticles (NPs) are promising candidates for various applications, *e.g.*, bioimaging, therapy, catalysis, and energy conversion, due to their unique optical and magnetic properties. Ln^{3+}-based NPs are capable of emitting UV and visible light (upconversion, UC) as well as near-infrared (NIR) light (downshifting) when excited with NIR light (*e.g.*, 980 nm). Microwave (MW)-assisted synthesis of sodium rare-earth (RE = Y + Gd) tetrafluoride, $NaREF_4$, NPs has attracted increasing attention due to its significantly shorter reaction time and high reproducibility compared to the conventional thermal decomposition or solvothermal methods.

$NaREF_4$ can crystallize in two crystalline phases, namely the cubic (α) and the hexagonal (β) crystal structure. The high-symmetry α-phase is more efficient for the magnetic properties, while the lower-symmetry β-phase is more suitable for the optical properties. The present thesis aims to (i) explore the MW-assisted approach towards the synthesis of the whole family of $NaREF_4$ NPs, and evaluate their crystalline phase accessibility (Chapter 4), to (ii) control the architecture of core/multi-shell $NaREF_4$ NPs seeking multimodal functionalities (Chapter 5), and subsequently to (iii) expand the synthesis approach to other fluoride materials beyond $NaREF_4$ NPs, *i.e.*, $NaMnF_3$ (Chapter 6).

More precisely, a series of sub-10 nm $NaREF_4$ NPs (RE = Y, Pr, Nd, Sm, Eu, Gd, Tb, Dy, Ho, Er, Yb, Lu) were prepared using a MW-assisted approach. The accessibility of these $NaREF_4$ NPs in α- and β-phase as a function of the RE ion choice was investigated. The results showed that using the MW-assisted approach, α-$NaREF_4$ NPs could be obtained for the whole RE family, while the β-$NaREF_4$ NPs were only accessible for the lighter RE ions (Pr to Dy). An adapted ligand removal procedure using a HCl solution of pH 1.5 was developed to render these NPs water dispersible, and the chemical stability of the obtained NPs under the acidic conditions was investigated. Interestingly, upon acidic treatment, some of the α/β-$NaREF_4$ NPs underwent a phase transformation from $NaREF_4$ to REF_3, pointing towards challenges with respect to chemical stability. Indeed, a correlation between the thermodynamic stability of the α/β-$NaREF_4$ and the

hexagonal/orthorhombic REF_3 phases – as a function of RE ion choice – and the chemical stability of the NPs was found (Chapter 4).

The design of core/shell/shell (CSS) architectures allows engineering different Ln^{3+} ions in separate layers in one NP, optimizing their optical properties and generating new functionalities. Having gained new knowledge from the synthesis of $NaREF_4$ core NPs, further optimization of the MW-assisted synthesis approach to control the architecture of CSS NPs was conducted. For example, opto-magnetic CSS NPs were explored as potential multimodal imaging probes. Therefore, β-$NaGdF_4$:Yb^{3+},Er^{3+}/$NaGdF_4$/$NaDyF_4$ CSS NPs were synthesized (Chapter 5). Careful tuning of the MW reaction conditions allowed for tuning of the inner shell thickness from *ca.* 3 to 6 nm. Such control is crucial to physically separate the luminescent Er^{3+}/Yb^{3+} ion pair in the core from the magnetic Dy^{3+} ions (emission quencher) in the outer shell, ultimately preventing UC loss. The mechanism of UC loss was investigated in detail by evaluating the Er^{3+} UC intensities and the excited state lifetimes of Yb^{3+} and Er^{3+} as a function of the inner shell thickness. The results demonstrated that a 4 nm thick $NaGdF_4$ inner shell did not only restore but enhanced the UC emission of Er^{3+}. In addition, the effect of the outer $NaDyF_4$ shell thickness on the particles' magnetic and X-ray computed tomography (CT) performance was investigated. Careful shell thickness tuning unveiled that the CSS NPs with the thickest outer shell thickness (4 nm) possessed superior magnetic resonance imaging (MRI) T_2 and CT contrast effects than that of other MRI and CT contrast agents (Chapter 5).

Inspired by the promising CSS architecture, β-$NaGdF_4$:Yb^{3+},Er^{3+}/$NaGdF_4$:Tm^{3+}/$NaGdF_4$ CSS NPs were synthesized to investigate their thermometric properties (Chapter 7). This is the latest work in progress, exploring future research directions.

The versatility of the developed MW-assisted approach was further explored to synthesize $NaMnF_3$ particles. $NaMnF_3$ particles have been reported as alternative candidates for MRI T_1 contrast agents. A stringent adjustment of the reaction conditions was conducted, including the Na^+-to-Mn^{2+} metal ion ratio, nucleation and growth temperatures, as well as reaction time. Interestingly, this MW-assisted method enabled the production of $NaMnF_3$ particles with specific morphologies (nanorods and ribbons) beyond well-established plates by varying the Na^+-to-Mn^{2+}

metal ion ratio. Moreover, the obtained $NaMnF_3$ particles exhibited promising contrast effect as MRI T_1 contrast agents (Chapter 6).

Overall, the MW-assisted approach led to promising achievements for the synthesis of $NaREF_4$ NPs and could be extended to other types of fluoride materials, *i.e.*, $NaMnF_3$. The concept of fabricating multilayer NPs by use of MW-assisted routes that offered control over shell thicknesses provided insights for the future architecture design of Ln^{3+}-based materials for their *e.g.,* biomedical applications and beyond. Further extension of these studies is expected to provide knowledge valuable for the future design of fluoride-related materials for their diverse applications.

Acknowledgments

First and foremost, I would like to express my most sincere gratitude to my supervisor, Prof. Eva Hemmer, for her guidance, support and encouragement. I learnt a lot from her self-motivated and optimistic attitude to life, and energetic research style. I also thank Eva for patiently teaching me on academic writing in a way that make my writings easily understandable by general audience. Dear Eva, I really appreciate your endless patience and help during the seven years study in your group!

I would like to thank all collaborators for their grateful supports and inspiring discussions to my work presented in this thesis. I would like to thank Prof. Adam Shuhendler for his contribution to the cell toxicity experiments and all the valuable suggestions during my study. I want to thank Prof. Tom Al for sharing the CT instrument with us and Dr. Samuel Morfin for performing measurements with me. I also thank Prof. Nicolas Bordenave for providing the NMR relaxometry.

I also thank all the technical staffs in the Department of Chemistry and Biomolecular Sciences. I want to thank Dr. Yun Liu for her training and help with TEM/SEM/TGA measurements. I thank Dr. Jeffrey Ovens for his training and help with XRD measurements. I also want to thank Wendy Pell for her help with FTIR/DLS measurements.

I would also like to thank all the members, both former and present, of the Hemmer group, for supporting each other. In particular, I thank Dr. Emille M. Rodrigues for her optical training. I thank Dr. Christian Homann for his always patient guidance.

I also want to thank my parents and sisters for their support and endless love. Last but not least, I want to thank myself for not giving up!

Table of Contents

Abstract ii
Acknowledgments v
Table of Contents vi
List of Publications x
List of Tables xiii
List of Figures xv
List of Abbreviations xxxiv
List of Symbols xxxvi
Statement of Contribution xxxviii
Chapter 1. Introduction 1
1.1 Optical Properties of the Lanthanides 2
1.1.1 Upconversion Mechanism 3
1.1.2 Doping Concentration 5
1.1.3 Host Lattice Choice 5
1.1.4 Luminescence Enhancement – Core/Shell Concept 7
1.1.5 Temperature-Dependent Photoluminescent – Temperature Sensing 9
1.2 Magnetic Properties of the Lanthanides 12
1.3 Potential Bioimaging Applications 13
1.3.1 Optical Imaging Probes 14
1.3.2 MRI Contrast Agents 16
1.3.2.1 Gd^{3+}-Based Nanoparticles Based T_1 Contrast Agents 18
1.3.2.2 Mn^{2+}-Based T_1 Contrast Agents 21
1.3.2.3 Ln-Based T_2 Contrast Agents 22
1.3.3 CT Contrast Agents 23
1.3.3.1 Basic Principles of CT Imaging 23
1.3.3.2 Ln^{3+}-Based NPs as CT Contrast Agents 25
1.3.4 Ln^{3+}-Based NPs for Multimodal Bioimaging 27
1.4 Synthesis of $NaREF_4$ Nanoparticles 30
1.4.1 Particle Formation: Growth Mechanism 30

1.4.2 Microwave-Assisted Synthesis of $NaREF_4$ Particles 31
1.4.2.1 Microwave-Assisted Synthesis of $NaYF_4$ 33
1.4.2.2 Crystalline Phase Control of $NaREF_4$ 36
1.4.2.3 Effect of Precursor Chemistry on Particle Size 38
1.4.2.4 $NaREF_4$ Core/Multi-Shell NPs 39
1.5 Surface Modification of Ln^{3+}-based NPs 40
1.5.1 Ligand Removal 41
1.5.2 Ligand Exchange 41
Chapter 2. Objectives 43
Chapter 3. Experimental Details and Characterization Techniques 44
3.1 Chemicals 44
3.2 Microwave-Assisted Synthesis of $NaREF_4$ NPs 45
3.2.1 Synthesis of Rare Earth Trifluoroacetate Precursor 45
3.2.2 Synthesis of α/β-$NaREF_4$ Core NPs 45
3.2.3 Synthesis of β-$NaGdF_4$:Yb^{3+},Er^{3+}/$NaREF_4$ (RE = Gd, Dy) Core/Shell NPs 48
3.2.4 Synthesis of β-$NaREF_4$:Yb^{3+},Er^{3+}/$NaGdF_4$/$NaDyF_4$ Core/Shell/Shell NPs 49
3.3 Microwave-Assisted Synthesis of $MMnF_3$ (M = Na and K) Particles 51
3.3.1 Microwave-Assisted Synthesis of $NaMnF_3$ Particles 51
3.3.2 Microwave-Assisted Synthesis of $KMnF_3$ Particles 52
3.4 Surface Modifications of the Particles Towards Water Dispersibility 52
3.4.1 Ligand-Free NPs 52
3.4.2 Surface Modification with Citrate Groups 53
3.4.3 Surface Modification with Poly(acrylic acid) 53
3.5 Characterizations Techniques 53
3.5.1 Powder X-Ray Diffraction (XRD) 53
3.5.2 Transmission Electron Microscopy (TEM) 54
3.5.3 Selected Area Electron Diffraction (SAED) Measurements 54
3.5.4 Scanning Electron Microscopy (SEM) 55
3.5.5 Energy Dispersive X-ray (EDX) Measurements 55
3.5.6 Fourier Transform Infrared (FTIR) Spectroscopy 56
3.5.7 Thermogravimetric Analyses (TGA) 56
3.5.8 Dynamic Light Scattering (DLS) 56
3.5.9 Inductively Coupled Plasma Optical Emission Spectroscopy (ICP-OES) 56

3.5.10 Time-Domain Nuclear Magnetic Resonance (NMR) Relaxivity Measurements 57
3.5.11 Magnetic Resonance Imaging (MRI) Relaxivity Measurements 57
3.5.12 Photoluminescence Spectroscopy 58
3.5.13 X-Ray Absorption Spectroscopy 59
3.5.14 Radiograph Imaging 59
3.5.15 Computed Tomography Imaging 59
3.6 Cytotoxicity of Ln-NPs 60
Chapter 4. Water Dispersible Ligand-Free Rare Earth Fluoride Nanoparticles: Water Transfer *versus* $NaREF_4$-to-REF_3 Phase Transformation 61
4.1 Introduction 62
4.2 Results and Discussion 64
4.2.1 Formation of GdF_3 as a Function of the Crystalline Phase of the OA-Capped $NaGdF_4$ NPs 64
4.2.2 Assessment of pH for Successful Ligand Removal 66
4.2.3 Formation of GdF_3 from OA-Capped α-$NaGdF_4$ 69
4.2.4 RE^{3+} Ion Dependence of the Chemical Stability and Phase Transformation of $NaREF_4$ NPs 74
4.2.5 Ln^{3+} Dopant Influence on the Formation of REF_3 From OA-Capped Ln^{3+}-Doped α/β-$NaGdF_4$ (Ln = Nd, Eu, Tb, Er/Yb) 84
4.2.6 Optical Properties 89
4.3 Conclusions 95
Chapter 5. Core-Multi-Shell Design: Unlocking Multimodal Capabilities in Lanthanide-based Nanoparticles as Upconverting, T_2-Weighted MRI and CT Probes 97
5.1 Introduction 98
5.2 Results and Discussion 98
5.2.1 Synthesis and Structural Characterization of Dy-CSS NPs 98
5.2.2 Optical Properties of Dy-CSS NPs 101
5.2.3 Rendering the NPs Water-Dispersible: Citrate-Capping 111
5.2.4 Citrate-Capped Dy-CSS NPs for MR Imaging 116
5.2.5 Citrate-Capped Dy-CSS NPs for CT Imaging 120
5.3 Conclusions 124
Chapter 6. Microwave-Assisted Synthesis of $NaMnF_3$ Particles with Tuneable Morphologies 126
6.1 Introduction 127
6.2 Results and Discussion 128
6.2.1 Synthesis of $NaMnF_3$ Particles 128

6.2.2 Poly(acrylic acid)-Capped $MMnF_3$ Particles for T_1 Relaxivity 138
6.3 Conclusions 141
Chapter 7. Summary and Outlook 142
7.1 Summary 142
7.2 Outlook 144
7.2.1 Expanding Material Choice 144
7.2.2 Understanding Core/Shell Cation Intermixing 144
7.2.3 Er^{3+}/Tm^{3+}-Based core/shell/shell NPs as NIR-III Nanothermometers 145
7.2.4 Challenges of Ln^{3+}-Based Nanothermometry 149
7.2.5 Challenge of Enhancing the Quantum Yield of Upconverting Nanoparticles 149
7.2.6 Challenges Related to Nanomaterials for Biomedical Applications 149
References 151

List of Publications

First Author Papers:

1. **Nan Liu**, Christian Homann, Samuel Morfin, Meghana Kesanakurti, Nicholas D. Calvert, Adam J. Shuhendler, Tom Al, and Eva Hemmer, *Core-Multi-Shell Design: Unlocking Multimodal Capabilities in Lanthanide-based Nanoparticles as Upconverting, T_2-Weighted MRI and CT Probes*, *Nanoscale* **2023**, 15, 19546-19556.
2. **Nan Liu**, Jessica Holmes, Nicolas Bordenave, and Eva Hemmer, *Microwave-Assisted Synthesis of $NaMnF_3$ Particles with Tuneable Morphologies*, *Chemical Communications* **2021**, 57, 11799-11802.
3. **Nan Liu**, Nicholas Gobeil, Parrish Evers, Isabel Gessner, Emille M. Rodrigues, and Eva Hemmer, *Water Dispersible Ligand-Free Rare Earth Fluoride Nanoparticles: Water Transfer versus $NaREF_4$-to-REF_3 Phase Transformation*, *Dalton Transactions* **2020**, 49, 16204-16216.

Co-Authored Papers:

4. Abigale Puccini, **Nan Liu** and Eva Hemmer, *Praseodymium-Doped Nanoparticles: Candidates for Near-Infrared-II Double- and Dingle-Band Nanothermometry*, *ACS Materials Letter* **2024**, 6, 1327-1337. **(Contributions: temperature-dependent and low-temperature photoluminescence measurements for powder samples as well as the FTIR and DLS measurements).**
5. Abigale Puccini, **Nan Liu** and Eva Hemmer, *Lanthanide-Based Nanomaterials for Temperature Sensing in the Near-Infrared Spectral Region: Illuminating Progress and Challenges (mini-review)*, *Nanoscale* **2024**, 16, 10975-10993. **(Contributions: original draft writing for the sections of NIR-II/III nanothermometry, future directions and fundamental aspects).**
6. Christian Homann, **Nan Liu**, Helliomar Barbosa and Eva Hemmer, *Impact of Synthesis Routes on the Optical Performance of Upconverting and Near-Infrared Emitting Lanthanide-Doped*

Nanoparticles, ***Handbook on the Physics and Chemistry of Rare Earths***, Elsevier, **2024**, ISSN 0168-1273. (**Contributions: original draft writing for the section on microwave-assisted synthesis**).

7. Hudson A. Bicalho, Christopher Copeman, Helliomar P. Barbosa, P. Rafael Donnarumma, Zoey Davis, Victor Quezada-Novoa, Jose de J. Velazquez-Garcia, **Nan Liu**, Eva Hemmer and Ashlee J. Howarth, *Synthesis, characterization and photophysical properties of a new family of rare-earth cluster-based metal-organic frameworks*, *Chemistry - A European Journal* **2024**, e202402363. (**Contributions: low-temperature photo-luminescence measurements**).
8. Emille M. Rodrigues, Nicholas D. Calvert, Justin C. Corriveau, **Nan Liu**, Adam J. Shuhendler and Eva Hemmer, *Phytoglycogen Encapsulation of Lanthanide-Based Nanoparticles as Optical Imaging Platform with Therapeutic Potential*, *Small* **2022**, 18, 2107130. (**Contributions: synthesis of Nd-based core/shell nanoparticles**).
9. Riccardo Marin, Natalie C. Millan, Laura Kelly, **Nan Liu**, Emille M. Rodrigues, Muralee Murugesu and Eva Hemmer, *Luminescence Thermometry Using Sprayed Films of Metal Complexes*, *Journal of Materials Chemistry C* **2022**, 10, 1767-1775. (**Contributions: photo-luminescence stability measurements**).
10. lias Halimi, Emille Martinazzo Rodrigues, Steven L. Maurizio, Tina Sun, Manjot Grewal, Emma M. Boase, **Nan Liu**, Riccardo Marin and Eva Hemmer, Pick your precursor! *Tailoring Size and Crystal Phase of Microwave-Synthesized sub-10 nm Upconverting Nanoparticles*, *Journal of Materials Chemistry C* **2019**, 7, 15364-15374. (**Contributions: synthesis of cubic core/shell nanoparticles**).

Conference Contributions:

1. **Liu N.** and Hemmer E., Core-Multi-Shell Design: Unlocking multimodal capabilities in lanthanide-based nanoparticles as upconverting, T_2-weighted MRI and CT probes, 4th Conference on Properties, Design, and Applications of Upconversion Nanomaterials (**UPCON 2024**), Montreal, Canada, April **2024** (oral presentation).

2. **Liu N.** and Hemmer E., Microwave-assisted synthesis of lanthanide-based nanoparticles: tailoring size, architecture, and crystalline phase, Canadian Chemistry Conference and Exhibition (**CSC 2023**), Vancouver, Canada, June **2023** (oral presentation).
3. **Liu N.** and Hemmer E., Opto-magnetic nanomaterials: from synthesis design to biomedical applications, **MRS** Spring Meeting & Exhibit, online meeting, May **2022** (oral presentation).
4. **Liu N.**, Marin R., Mazouzi Y., Cron G. O., Shuhendler A., and Hemmer E., Effect of crystallinity on the T_1-shortening behaviour of $NaGdF_4$ nanoparticles as MRI contrast agents, 45^{th} International Conference & Exposition on Advanced Ceramics & Composite (**ICACC 2021**), online meeting, August **2021** (oral presentation).
5. **Liu N.**, Gobeil N., Evers P., Gessner I., Rodrigues E. M., and Eva Hemmer, Water dispersible ligand-free rare earth fluoride nanoparticles: water transfer versus $NaREF_4$-to-REF_3 phase transformation, The 6.5^{th} Crystal Engineering and Emerging Materials Workshop of Ontario and Quebec (**CEMWOQ 6.5**), online meeting, May **2020** (oral presentation).
6. **Liu N.**, Marin R., Mazouzi Y., Cron G. O., Shuhendler A., and Hemmer E., Cubic *versus* hexagonal-Effect of crystallinity on the T_1-shortening behaviour of $NaGdF_4$ nanoparticles as MRI contrast agents, Ottawa-Carleton Chemistry Institute Day (**OCCI Day 2019**), Ottawa, Canada, May **2019** (oral presentation).

List of Tables

Table 1.1. Pros and cons of imaging modalities described in this thesis. 27

Table 3.1. Overview of the experimental conditions used in the microwave-assisted synthesis of OA-capped α/β-$NaREF_4$ NPs as well as the representative average NP size (± standard deviation). 47

Table 4.1. Overview of the experimental conditions used for the evaluation of the pH dependence of the ligand removal for α-$NaGdF_4$ NPs and size of the resulting GdF_3 NPs. 71

Table 4.2. Comparison between the values of the interplanar distances (d) calculated from Scherrer equation using the main reflections in the recorded XRD patterns shown in Figure 4.12, those obtained from the first and second rings of the SAED patterns shown in Figure 4.14, and the standard values from the PDF cards for the Ho- and Lu-based samples. 80

Table 4.3. Overview of all obtained lifetime values. 92

Table 4.4. Overview of NP concentrations, excitation wavelength (λ_{EX}), and power of the excitation source used for steady state and time-resolved spectroscopy of OA-capped and LF-Ln^{3+}-doped $NaGdF_4$ and GdF_3 NPs. 93

Table 5.1. Overview of the compositions and dimensions of the core, CS, and CSS NPs used in this study. Green shaded samples were used to study the effect of inner shell thickness on UC. Blue shaded samples were used to study the effect of outer shell thickness on MRI and CT performance. Sample ^{4nm}Dy-CSS^{3nm} was used in both studies, the first and second superscript indicate the thickness of the inner and outer shell. 100

Table 5.2. Lifetime values extracted from the decay curves of the Yb^{3+} emission under 980 nm. 105

Table 5.3. Relaxivity values r_2 and r_1 of Cit-Dy-CSS NPs at 7 T. Relaxivity values and the associated errors were obtained from the linear fitting procedure of the data sets reported in Figure 5.18, Figure 5.19, and Figure 5.21. 118

Table 5.4. Comparison of MRI T_2 relaxivity values of clinically used iron oxide NPs, Dy-based chelates, and Dy-based NPs. The table also shows examples for multimodal CAs for additional optical and CT imaging. 121

Table 5.5. CT capabilities of Cit-Dy-CSS NPs and Iohexol solution measured at 110 kV. 124

List of Figures

Figure 1.1. Ionic radius and valence configuration of RE^{3+} ions. From La^{3+} to Lu^{3+}, the number of electrons on the 4f orbitals increases with increasing atomic number. The electron configurations of La^{3+}, Gd^{3+}, and Lu^{3+} show empty, half-filled, and completely filled 4f orbitals, respectively. Figure taken from [11] with permission. 1

Figure 1.2. Schematic representation of energy transfer processes leading to Ln^{3+}-based upconversion. (A) Excited state absorption (ESA) and (B) energy transfer upconversion (ETU). The arrows indicate the direction of energy flow between different energy states. (C) ETU energy transfer process for the upconversion process commonly found for the Yb^{3+}/Er^{3+} ion pair under excitation at 980 nm. Non-radiative transfers are indicated by dotted curved arrows, and non-radiative multiphoton relaxations are indicated by wavy arrows. (D) Cross relaxation (CR) process. Figure (A) and (B) redrawn from [20], (C) redrawn from [19], (D) redrawn from [21] with permission. 4

Figure 1.3. Crystalline structure of (A) the cubic and (B) hexagonal phases of $NaREF_4$ particles. Figure adopted from [30] with permission. 7

Figure 1.4. Schematic representation of core/shell (CS) and core/multi-shell architectures. (B) UC intensity enhancement of β-$NaGdF_4$:Yb^{3+},Er^{3+}/$NaGdF_4$ CS NPs compared to the corresponding core NPs. 8

Figure 1.5. Typical thermal resolution vs. spatial resolution for various thermometry techniques, seeking sub-micrometric resolution. Orange dots indicate techniques based on luminescent nanoparticles. In this case, the spatial resolution is given by the experimental set-up (usually a

microscope) and thus it is diffraction-limited. As a consequence, the precise spatial resolution will depend on the wavelength of the light applied, so it will be smaller for UV probes and larger for near-IR probes. Figure taken from [47] with permission. 10

Figure 1.6. (A) Double-band and (B) single-band based luminescence nanothermometry. 11

Figure 1.7. (A-D) Bright field and UC luminescence images showing the uptake of $NaYF_4$:Yb^{3+},Er^{3+} NPs by rat bone marrow derived mesenchymal stem cells (A,B) and skeletal myoblasts (C,D). The cells were maintained in their respective culture mediums and incubated with 50 µg/mL NPs for 24 h. Figures taken from [64] with permission. 14

Figure 1.8. Tissue transmission of NIR-III light is superior to that of visible light. (A) NIR-III light (1525 nm) emitted from Er-doped NPs was significantly more effective at transmitting through blood and pigmented tumour tissue than visible light at 550 nm. Bar graph data in (a) are expressed as mean values ± standard error; n = 3 ($P < 0.01$). (B) Transmission spectra of visible (white region), NIR-I (grey region) and NIR-II/III (blue region) light reveal that longer NIR light exhibited lower absorbance and improved transmission through strong tissue absorbers such as blood and pigmented tumor tissue. (C) The NIR-III emissions from NPs patterned into the shape of an 'R' and irradiated with 980 nm light ('low': 0.14 W cm^{-2}; 'high': 0.5 W cm^{-2}) were more clearly visualized through a mouse body and at lower power densities than visible emissions due to reduced scattering and absorbance. Figures taken from [72] with permission. 16

Figure 1.9. Principle of magnetic resonance imaging. Spins align parallel or antiparallel to the magnetic field and process under Larmor frequency (ω_0). After induction of RF pulse, magnetization of spins changes. Excited spins take relaxation process of T_1 relaxation and T_2 relaxation. Figure adapted from [77] with permission. 17

Figure 1.10. Factors including particle size (A, B), crystalline phase (C) and surface modification (D) influence the MRI T_1 relaxivity. Figure (A) taken from [84], figure (B) redrawn from [93], figure (C) taken from [88] with permission. 19

Figure 1.11. Parameters of (A) particle size and (B) surface influencing MRI T_2 relaxivity. Figure A taken from [110], figure B taken from [108] with permission. 22

Figure 1.12. Schematic of a CT system. Multiple X-ray projections are acquired over a 360° rotation around the subject. These individual x-ray projections are then reconstructed to produce 2D cross-sectional images and 3D volumes. Figure taken from [112] with permission. 24

Figure 1.13. In vivo CT coronal view images of a rat after intravenous injection of 1 mL of Yb-NPs (70 mg Yb/mL) solution at timed intervals. (A) Heart and liver, (B) spleen and kidney. (C, D) Corresponding 3D renderings of in vivo CT images. Figures taken from [131] with permission. .. 26

Figure 1.14. Proposed energy transfer processes for the quenching of UC emission caused by Dy^{3+} ions. Vertical and wavy arrows represent non-radiative transitions, curved arrows represent non-radiative energy transfer, green and red arrows represent green and red emissions. Figure taken from [139] with permission. 29

Figure 1.15. $NaYbF_4:Tm^{3+}/CaF_2/NaDyF_4$ CSS NPs used as multimodal UC/T_2-weighted MRI/CT imaging probes for lymphatic imaging. Figure taken from [132] with permission. 29

Figure 1.16. LaMer diagram: visualization of the three, timely separated growth and nucleation stages during a particle synthesis (I, II and III). C_s represents the saturation concentration of monomers in the reaction solution. C_{min} and C_{max} indicate the bottom limit (minimum) and the top limit (maximum) concentrations, respectively, that determine the range of supersaturation of the monomers. Figure taken from [147] with permission. 30

Figure 1. 17. Two main heating mechanisms under microwave irradiation: (A) dipolar polarization; (B) ionic conduction mechanism. Figure taken from [159] with permission. 32

Figure 1.18. (A) TEM images of α-$NaYF_4$:Yb^{3+},Er^{3+} NPs prepared using a MW-assisted thermal decomposition approach with different RE-TFA precursor concentrations.[162, 166] Scale bars: 100 nm. (B) SEM images of β-$NaYF_4$:Er^{3+},Yb^{3+} microparticles synthesized with a MW-assisted hydrothermal method with or without EDTA as an additive.[164, 167] Figures adapted from [162, 164, 166, 167], with permission. 34

Figure 1.19. Crystalline phase control and phase formation mechanism of $NaREF_4$ NPs by MW-assisted synthesis. (A) Effect of the Na^+-to-RE^{3+} ion ratio and precursor concentration on phase formation. (1) XRD patterns revealed the obtained $NaGdF_4$ NPs were in α- or β-phase when the Na^+-to-Gd^{3+} ratio was 1:1 or 2:1 respectively, (precursor concentration: 0.125 mol/L). (2) NPs exhibiting a phase mixture were obtained for improper precursor concentration and Na^+-to-RE^{3+} ratio. (3) Pure β-phased NPs obtained when the Na^+-to-Gd^{3+} ratio was 3:1 at 0.625 mol/L precursor concentration. XRD patterns (B) and TEM images (C) of $NaRF_4$ NPs synthesized at different reaction time (C-1) and reaction temperature (C-2). XRD references: α-$NaGdF_4$ (PDF#: 00-027-0697, light grey lines), β-$NaGdF_4$ (PDF#: 01-080-8787, black lines). 37

Figure 1.20. Strategies to $NaRF_4$ core/shell NPs by MW-assisted synthesis. (A) TEM images of core (1), CS (2), CSS NPs (3), and their corresponding size distributions (4) when OAm was used as co-solvent in the reaction mixture. (B) Effect of reaction time. Photographs of $NaREF_4$ CS NPs dispersed in toluene under excitation with a 980 nm 50 mW laser pointer. Brighter green upconversion emission was observed with thicker undoped shell (4.1 nm) yielding from 30 min

shell growth compared to 10 min (2.5 nm shell thickness). Figure (A) adapted from [38], figure (B) adapted from [158] with permission. 39

Figure 1.21. Typical surface modification strategies used for making hydrophilic Ln^{3+}-doped NPs with pendant functional groups. Figure taken from [175] with permission. 40

Figure 3.1. Schematic representation of the synthesis of $NaREF_4$ (A) core and (B) core/shell NPs. This figure was made in BioRender (www.biorender.com). 46

Figure 3.2. Schematic representation of MW-assisted shell thickness control in CS NPs. The nominal ratio between $NaGdF_4$:Yb^{3+},Er^{3+} core NPs, and the amount of shell precursors was used to illustrate the shell thickness control. 49

Figure 3.3. (A) TEM image of "flower-like" CS NPs and (B) their corresponding size distribution. 49

Figure 3.4. Schematic representation of MW-assisted shell thickness control in core/shell/shell NPs. 50

Figure 4.1. Formation of hexagonal GdF_3 upon treatment of $NaGdF_4$ NPs at pH 1.5 (20 h) as a function of their crystalline phase: (A-1) XRD patterns of β-$NaGdF_4$ NPs before (OA-capped) and after treatment at pH 1.5 (ligand-free, LF). (B-1) XRD patterns of OA-capped α-$NaGdF_4$ NPs and resulting LF-hexagonal GdF_3 particles. References: α-$NaGdF_4$, PDF card [00-027-0697] (black line, B); β-$NaGdF_4$, PDF card [01-080-8787] (black line, A); hexagonal EuF_3, PDF card [00-032-0373] (light grey line, A and B; this card was used as no reference for hexagonal GdF_3 is available). (A-2) and (B-2): TEM images of OA-capped β- and α-$NaGdF_4$ NPs obtained by MW-assisted synthesis approach. (A-3) and (B-3): TEM images of LF-NPs obtained upon stirring of the respective OA-NPs shown in (A/B-2) at pH 1.5 for 20 h. The inset shown in (B-3) is the higher magnification image,

note the different scale bars for (B-3). (A-4/5) and (B-4/5): Average particle sizes and size distributions of OA-capped β- and α-$NaGdF_4$ NPs as well as their respective LF-NPs. 64

Figure 4.2. Effect of (A) the $NaREF_4$ crystalline phase on the pH necessary for ligand removal, (B) surface chemistry on ligand removal, and (C) particle size on phase transformation upon ligand removal. (A-1/2) TEM images of β-$NaGdF_4$ NPs synthesized using oleic acid and OAm before and after ligand removal at pH 3 (20 h) reveal the poor quality of LF-NPs obtained under these conditions. XRD patterns of both samples are shown in (A-3). Reflections at 39° due to NaF (a possible by-product of NP synthesis)[158] were removed for clarity. Size and size distribution of (A-1) are given in Figure 4.1 (A-4). (B-1/2) TEM images of β-$NaGdF_4$:Er^{3+},Yb^{3+}/$NaGdF_4$ CS NPs (only OA was used during shell growth) before and after ligand removal at pH 3 (20 h) demonstrate the successful transfer of the NPs into the aqueous phase. XRD patterns of both samples are shown in (B-3). Size and size distribution are given in (B-4/5). (C-1/2) TEM images of larger α-$NaGdF_4$:Er^{3+},Yb^{3+}/$NaGdF_4$ CS NPs before and after ligand removal at pH 1.5 (4 h) indicate phase transformation into hexagonal GdF_3 (see C-3 for XRD patterns) despite the larger particle size (no OAm was used for shell growth). (C-4) Size and size distribution of (C-1). (D) Representative FTIR spectra recorded of $NaGdF_4$ NPs grown in the presence (NPs-OA/OAm) and absence (NPs-OA) of OAm, respectively. Spectra obtained of pure oleic acid and OAm used in the synthesis are also shown. References: β-$NaGdF_4$, PDF card [01-080-8787] (black line in A/B-3); α-$NaGdF_4$, PDF card [00-027-0697] (black line in C-3); hexagonal EuF_3, PDF card [00-032-0373] (light grey line in C-3). 67

Figure 4.3. The effect of pH on ligand removal and phase transformation of OA-capped α-$NaGdF_4$ NPs. TEM images (higher magnification images are shown as insets) of LF particles obtained upon

treatment of OA-capped α-$NaGdF_4$ NPs at (A) pH 2.5, (B) pH 2, (C) pH 1.5, and (D) pH 1. Treatment at pH 3 did not yield any particle transfer from the organic into the aqueous phase. 70

Figure 4.4. Average sizes and size distributions of particles obtained upon treatment of α-$NaGdF_4$ NPs for 20 h at (A) pH 1.5, (B) pH 2.0, and (C) pH 2.5, respectively. (C) In addition to the diameter, the average thickness of the plate-like structures is given as determined from plates that self-arranged perpendicular to the TEM grid. Similar dimensions were observed for the other GdF_3 structures. 71

Figure 4.5. XRD patterns of particles obtained upon treatment of α-$NaGdF_4$ NPs for 20 h at pH 1, 1.5, 2, and 2.5, respectively. Reference**:** hexagonal EuF_3, PDF card [00-032-0373]. 72

Figure 4.6. (1) TEM images and (2) size distributions of hexagonal GdF_3 particles obtained by stirring of α-$NaGdF_4$ NPs at pH 1.5 for (A) 1 h, (B) 4 h, (C) 8 h, and (D) 20 h, respectively. Scale bars: 1 μm. 73

Figure 4.7. XRD patterns revealing hexagonal GdF_3 as the sole crystalline phase upon treatment of α-$NaGdF_4$ NPs at pH 1.5 for 1, 4, 8, and 20 h, respectively. Reference**:** hexagonal EuF_3, PDF card [00-032-0373]. 73

Figure 4.8. XRD patterns of α-$NaREF_4$ NPs obtained by microwave-assisted thermal decomposition. RE refers to the rare earth ions studied as labelled for each pattern. References: α-$NaYF_4$, PDF card [00-006-0342]; α-$NaPrF_4$, PDF card [00-022-1393]; α-$NaNdF_4$, PDF card [00-028-1114]; α-$NaSmF_4$, PDF card [00-027-0778]; α-$NaGdF_4$, PDF card [00-027-0697] (this card was also used for RE = Eu, Tb, Dy); α-$NaHoF_4$, PDF card [01-077-2040]; α-$NaErF_4$, PDF card [01-077-2041]; α-$NaYbF_4$, PDF card [01-077-2043] (this card was also used for RE = Lu). 75

Figure 4.9. TEM images of (1) OA-capped α-$NaREF_4$ NPs as well as (2) LF particles obtained after treatment of the NPs shown in (1) at pH 1.5 for 4 h. RE refers to the rare earth ions studied as labelled in each image, A to L. 76

Figure 4.10. Average sizes and size distributions of the OA-capped α-$NaREF_4$ NPs used for ligand removal (pH 1.5, 4 h). 76

Figure 4.11. Average sizes and size distributions of the LF-NPs shown in Figure 4.9 (A2 to L2) obtained by treatment of the OA-capped α-$NaREF_4$ NPs at pH 1.5 for 4 h. The insets in B to E provide an estimated value for the thickness of the obtained plates. Dimensions given in G correspond to the length, width and thickness of the TbF_3 bundle-like structures. The inset in I shows the length and width of the nanorods ascribed to HoF_3 as minor, secondary phase. 77

Figure 4.12. XRD patterns of LF-NPs obtained from α-$NaREF_4$ NPs upon stirring at pH 1.5 for 4 h. References: black lines – α-$NaYF_4$, PDF [00-006-0342]; α-$NaGdF_4$, PDF card [00-027-0697], used for α-$NaDyF_4$; α-$NaHoF_4$, PDF card [01-077-2040]; α-$NaErF_4$, PDF card [01-077-2041]; α-$NaYbF_4$, PDF card [01-077-2043] (this card was also used for α-$NaLuF_4$); grey lines – hexagonal PrF_3, PDF card [00-046-1167]; hexagonal NdF_3, PDF card [00-009-0416]; hexagonal SmF_3, PDF card [00-012-0792]; hexagonal EuF_3, PDF card [00-032-0373] (this card was also used for hexagonal GdF_3); orthorhombic TbF_3, PDF card [00-037-1487]; orthorhombic HoF_3, PDF card [00-023-0284]; orthorhombic LuF_3, PDF car [00-032-0612]. 78

Figure 4.13. TEM image of LF-NPs and ribbon-like structures obtained upon stirring OA-capped α-$NaLuF_4$ NPs at pH 1.5 for 4 and 20 h, respectively. 78

Figure 4.14. (A) TEM images showing the highlighted areas from which the SAED patterns shown in (B) were obtained. (1) LF-HoF_3 structures of rod-like morphology, (2) LF-$NaHoF_4$ NPs, (3) LF-LuF_3 band-like structures; (4) LF-$NaLuF_4$ NPs. 79

Figure 4.15. XRD patterns of β-$NaREF_4$ NPs obtained by MW-assisted approach. RE refers to the rare earth ions studied as labelled for each pattern. References: β-$NaPrF_4$, PDF card [01-082-4240]; β-$NaNdF_4$, PDF card [00-027-0756]; β-$NaSmF_4$, PDF card [00-027-0779]; β-$NaEuF_4$, PDF card [00-028-1085]; β-$NaGdF_4$, PDF card [01-080-8787]; β-$NaTbF_4$, PDF card [00-027-0809]; β-$NaDyF_4$, PDF card [00-027-0687]. 82

Figure 4.16. (A-G) TEM images of (1) OA-capped β-$NaREF_4$ NPs and (2) their respective LF particles obtained by stirring at pH 1.5 for 20 h. RE = (A) Pr, (B) Nd, (C) Sm, (D) Eu, (E) Gd, (F) Tb, and (G) Dy. Scale bars: 50 nm (unless noted otherwise). (H) XRD patterns of LF β-$NaREF_4$ (RE = Eu, Gd, Tb, Dy) and hexagonal REF_3 (RE = Pr, Nd, Sm) NPs, respectively. References: grey lines – hexagonal PrF_3, PDF card [00-046-1167]; hexagonal NdF_3, PDF card [00-009-0416]; hexagonal SmF_3, PDF card [00-012-0792] ; black lines – β-$NaEuF_4$, PDF card [00-028-1085]; β-$NaGdF_4$, PDF card [01-080-8787]; β-$NaTbF_4$, PDF card [00-027-0809]; β-$NaDyF_4$, PDF card [00-027-0687]. 83

Figure 4.17. Average particle sizes and size distributions of (1) OA-capped β-$NaREF_4$ NPs and (2) their respective LF counterparts obtained by stirring at pH 1.5 for 20 h. RE = (A) Pr, (B) Nd, (C) Sm, (D) Eu, (E) Gd, (F) Tb, and (G) Dy. 84

Figure 4.18. (A-1) XRD patterns of OA-capped α-$NaGdF_4$ NPs doped with 10% Nd^{3+}, 10% Eu^{3+}, 10% Tb^{3+}, and 2%/20% Er^{3+}/Yb^{3+}, respectively. (A-2) XRD patterns of hexagonal LF-GdF_3 doped with 10% Nd^{3+}, Eu^{3+}, and Tb^{3+}, respectively, as well as GdF_3 doped with 2%/20% Er^{3+}/Yb^{3+} exhibiting an orthorhombic crystalline phase (the sharp reflections at 25.5° and 29.1° [marked by *] point

toward the presence of hexagonal GdF_3 as secondary phase). References: α-$NaGdF_4$, PDF card [00-027-0697] (black lines in A-1); hexagonal EuF_3 (for GdF_3), PDF card [00-032-0373] (black lines in A-2); orthorhombic GdF_3, PDF card [00-049-1804] (light grey lines). (B-E) TEM images and their corresponding size distributions of (1-2) OA-capped α-$NaGdF_4$ and (3-4) LF-GdF_3 particles doped with (B) 10% Nd^{3+}, (C) 10% Eu^{3+}, (D) 10% Tb^{3+}, and (E) 2%/20% Er^{3+}/Yb^{3+}, respectively. 86

Figure 4.19. XRD patterns of (A-1) OA-capped and (A-2) LF-β-$NaGdF_4$ NPs doped with 10% Nd^{3+} and 2%/20% Er^{3+}/Yb^{3+}, respectively. References: β-$NaGdF_4$, PDF card [01-080-8787]. (B-C) TEM images of (1) OA-capped and (2) LF-β-$NaGdF_4$ NPs doped with (B) 10% Nd^{3+}, and (C) 2%/20% Er^{3+}/Yb^{3+}, respectively. All LF-NPs were obtained by stirring at pH 1.5 for 20 h. The respective average sizes and size distributions are shown in (D) and (E). 87

Figure 4.20. SEM images of LF- (A) hexagonal GdF_3 doped with 10% Tb^{3+} and (B) orthorhombic GdF_3 co-doped with 2% Er^{3+} and 20% Yb^{3+}. Both samples were obtained upon stirring of the respective Ln^{+}-doped α-$NaGdF_4$ NPs at pH 1.5 for 20 h. 87

Figure 4.21. Representation of the relative stability of the $NaREF_4$ and REF_3 crystalline phases depending on the RE ion. 88

Figure 4.22. (A/B-1) Excitation and emission spectra of OA-capped α-$NaGdF_4$ NPs doped with (A-1) 10% of Eu^{3+} and (B-1) 10% of Tb^{3+}. (A/B-2) Excitation and emission spectra of hexagonal LF-GdF_3 NPs doped with (A-2) 10% of Eu^{3+} and (B-2) 10% of Tb^{3+}. (C-1/2) NIR emission spectra obtained under 808 nm laser excitation of (1) OA-capped α-$NaGdF_4$ and (2) LF-GdF_3 NPs doped with 10% of Nd^{3+}. (D-1/2) Upconversion emission spectra obtained under 980 nm laser excitation of (1) OA-capped α-$NaGdF_4$ and (2) LF-GdF_3 NPs co-doped with 2% Er^{3+} and 20% Yb^{3+}. Excitation

wavelengths, λ_{EX}, and monitored emission wavelengths, λ_{EM}, are indicated in the respective figures (A) to (D). 90

Figure 4.23. Energy level schemes for (A) the Eu^{3+}/Gd^{3+}, (B) the Tb^{3+}/Gd^{3+}, (C) Nd^{3+}, and (D) Er^{3+}/Yb^{3+} showing the respective f-f transitions. 91

Figure 4.24. Fluorescence decay curves and respective lifetime values for the indicated transitions of samples doped with (A) Eu^{3+} (10%), (B) Tb^{3+} (10%)..... 91

Figure 4.25. NIR emission spectra for (A-1) OA-capped and (A-2) ligand-free Nd^{3+}-doped β-$NaGdF_4$ as well as upconversion emission spectra for (B-1) OA-capped and (B-2) ligand-free Er^{3+}/Yb^{3+}-doped β-$NaGdF_4$. 94

Figure 4.26. Fluorescence decay curves and respective lifetime values for the indicated transitions of (A) OA-capped α-$NaGdF_4$ doped with Er^{3+}/Yb^{3+}, (B) and (C) OA-capped and LF-β-$NaGdF_4$ doped with Er^{3+}/Yb^{3+}, and (D) α- and β-$NaGdF_4$ doped with Nd^{3+} (10%). IRF: instrument response function of the InGaAs detector. 94

Figure 5.1. (A) Schematic illustration of the CSS Dy-NP architecture proposed as multimodal optical/T_2/CT probe. (B-D) TEM images and sizes of OA-capped (1) core β-$NaGdF_4$:Yb^{3+},Er^{3+}, (2) β-$NaGdF_4$:Yb^{3+},Er^{3+}/$NaGdF_4$ CS, and (3) β-$NaGdF_4$:Yb^{3+},Er^{3+}/$NaGdF_4$/$NaDyF_4$ CSS NPs. The $NaGdF_4$ inner shell thickness and $NaDyF_4$ outer shell thickness are indicated in brackets. Core sizes and outer shell thicknesses were kept comparable, while the thickness of the inner shell increased from B to D. The 50 nm scale bar applies to all TEM images. 99

Figure 5.2. XRD patterns of OA-capped CSS β-$NaGdF_4$:Yb,Er/$NaGdF_4$/$NaDyF_4$ (Dy-CSS) with different inner shell thicknesses of 3.0 nm (^{3nm}Dy-CSS^{3nm}), 3.9 nm (^{4nm}Dy-CSS^{3nm}), and 5.7 nm (^{6nm}Dy-CSS^{3nm}), respectively. Reference: β-$NaGdF_4$, PDF card [01-080-8787]. 101

Figure 5.3. Size distributions of (A) ^{3nm}Dy-CSS^{3nm}, (B) ^{4nm}Dy-CSS^{3nm}, as well as (C) ^{6nm}Dy-CSS^{3nm} NPs and their corresponding CS (^{3nm}CS, ^{4nm}CS, ^{6nm}CS) and core NPs, demonstrating the varying thickness of the inner shell, while keeping core size and outer shell thickness constant. 101

Figure 5.4. (A) UC spectra of OA-capped ^{3nm}Dy-CSS^{3nm} (1), ^{4nm}Dy-CSS^{3nm} (2), and ^{6nm}Dy-CSS^{3nm} (3) NPs (blue) as well as their corresponding core (green) and CS (pink) NPs. All spectra were obtained under 980 nm laser excitation. Power density = 6.0 W/cm^2, [NP] = 5 mg/mL in toluene. (B) Partial energy level diagram for Er^{3+}/Yb^{3+} and Dy^{3+}, schematically showing how the addition of an inner shell physically separates Er^{3+}/Yb^{3+} from Dy^{3+} ions, thus, preventing Dy^{3+}-induced loss of the UC. Solid lines are radiative transitions, dotted lines indicate energy transfer, and wavy lines are non-radiative transitions. (C) Luminescence decay curves of the Yb^{3+} emission under 980 nm excitation obtained from core, CS, and CSS NPs. 102

Figure 5.5. (A) XRD patterns of OA-capped α-$NaDyF_4$:Yb,Er core and β-$NaGdF_4$:Yb,Er/$NaDyF_4$ (Dy-CS) core-shell NPs. References: red line – α-$NaDyF_4$, PDF card [00-027-0697]; black line – β-$NaGdF_4$, PDF card [01-080-8787]. (B and C) (1) TEM images and (2) their corresponding size distributions of OA-capped (B) α-$NaDyF_4$:Yb,Er and (C) β-$NaGdF_4$:Yb,Er/$NaDyF_4$ NPs. Scale bars: 50 nm. Note that β-$NaDyF_4$:Yb,Er is not accessible *via* our MW-assisted synthesis.[252] Therefore, α-$NaDyF_4$:Yb,Er was used as a similar-sized reference core sample. 103

Figure 5.6. UC spectra of OA-capped α-$NaDyF_4$:Yb,Er, β-$NaGdF_4$:Yb,Er, and β-$NaGdF_4$:Yb,Er/$NaDyF_4$ CS NPs. All spectra were obtained under 980 nm laser excitation. Power density = 6.0 W/cm^2, [NP] = 5 mg/mL in toluene. 104

Figure 5.7. Integrated $^4S_{3/2} \rightarrow {}^4I_{15/2}$ and $^4F_{9/2} \rightarrow {}^4I_{15/2}$ Er^{3+} emission intensities versus 980 nm excitation power for OA-capped (A) β-$NaGdF_4$:Yb,Er (core), (B) Dy-CS, (C) ^{4nm}CS, (D) ^{4nm}Dy-CSS^{3nm}, (E) ^{6nm}CS, and (F) ^{6nm}Dy-CSS^{3nm} NPs. 106

Figure 5.8. Luminescence decay curves of the (A) $^4S_{3/2} \rightarrow {}^4I_{15/2}$ (540 nm) and (B) $^4F_{9/2} \rightarrow {}^4I_{15/2}$ (650 nm) Er^{3+} transitions for (1) Dy-CS, (2) ^{4nm}Dy-CSS^{3nm}, and (3) ^{6nm}Dy-CSS^{3nm} NPs and their corresponding core and CS NPs in toluene. λ_{ex} = 980 nm. 107

Figure 5.9. Partial energy level diagrams for UC pair Yb^{3+}/Er^{3+} and Dy^{3+} as well as mechanisms resulting in the observed architecture-dependent green and red UC emission intensities of (A) core, (B) Dy-CS, (C) CS, and (D) Dy-CSS NPs. The following dominating mechanisms are proposed based on UC emission intensities as well as Yb^{3+} and Er^{3+} excited state lifetimes: (A) Loss of UC emission due to surface quenching. (B) Loss of UC emission due to Dy^{3+}-mediated energy migration to the NP surface. (C) Enhancement of UC emission due to prevention of surface quenching. (D) Restoration and enhancement of UC emission due to prevention of Dy^{3+}-mediated energy migration and protection of the Er^{3+} excited states from surface quenching. 109

Figure 5.10. Dy-CSS NPs with tuned outer shell thickness: (1-3) TEM images and (4) their corresponding size distributions of OA-capped (A) ^{4nm}Dy-CSS^{1nm}, (B) ^{4nm}Dy-CSS^{3nm} and (C) ^{4nm}Dy-CSS^{4nm} NPs. The core diameter and the thickness of the inner shell were kept constant. The 50 nm scale bar applies to all TEM images. 110

Figure 5.11. XRD patterns of OA-capped ^{4nm}Dy-CSS^{1nm}, ^{4nm}Dy-CSS^{3nm} and ^{4nm}Dy-CSS^{4nm} NPs with tunable outer shell thickness. Reference: β-$NaGdF_4$, PDF card [01-080-8787]. 110

Figure 5.12. UC spectra of OA-capped (A) ^{4nm}Dy-CSS^{1nm}, (B) ^{4nm}Dy-CSS^{3nm} and (C) ^{4nm}Dy-CSS^{4nm} NPs (blue) as well as their corresponding core (green) and CS (pink) NPs. All spectra were

obtained under 980 nm laser excitation. Power density = 6.0 W/cm^2, [NP] = 5 mg/mL in toluene. 111

Figure 5.13. (A) TEM images of Cit-^{4nm}Dy-CSS^{1nm} (1), Cit-^{4nm}Dy-CSS^{3nm} (2), Cit-^{4nm}Dy-CSS^{4nm} (3) and Cit-^{6nm}Dy-CSS^{3nm}. The 50 nm scale bar applies to all TEM images. (B) FTIR spectra of citrate- and OA-capped ^{4nm}Dy-CSS^{3nm} NPs as well as citrate used as a reference. (C) XRD pattern of Cit-^{4nm}Dy-CSS^{3nm} NPs. Reference: β-$NaGdF_4$, PDF card [01-080-8787]. (D) DLS curve of Cit-^{4nm}Dy-CSS^{3nm} NPs dispersed in water. DLS data revealed a hydrodynamic diameter of 23.4 nm (polydispersity index, PDI: 0.27). 112

Figure 5.14. Cell viability of A549 cells incubated with Cit-^{4nm}Dy-CSS^{3nm} NPs at different concentrations (0, 50, 250, and 500 μg/mL) for 24 h at 37 °C. 113

Figure 5.15. Upconversion (A) and downshifting (B) luminescence spectra of Cit-^{4nm}Dy-CSS^{3nm} NPs (5 mg/mL in water for UC emission, 10 mg/mL in water for NIR emission) obtained under 980 nm laser excitation. Power densities used to trigger UC and NIR emission were 6.0 W/cm^2 and 33.3 W/cm^2, respectively. 114

Figure 5.16. Overall UC emission intensity of Cit-^{4nm}Dy-CSS^{3nm} NPs as a function of incubation time in H_2O and PBS at (A) room temperature and (B) 37 °C. 114

Figure 5.17. (A) Temperature-dependent emission spectra of Cit-^{4nm}Dy-CSS^{3nm} NPs dispersed in water. (B) Luminescence intensity ratio (LIR) between the two green emission bands stemming from the $^2H_{11/2}$ and $^4S_{3/2}$ excited levels plotted against temperature. (C) Natural logarithm of LIR plotted as a function of the inverse absolute temperature (Boltzmann's plot). (D) Relative thermal sensitivity, S_r, plotted as a function of the temperature. 115

Figure 5.18. (A) T_2-weighted MR images of Cit-Dy-CSS NPs with varying $NaDyF_4$ outer shell thickness (Cit-^{4nm}Dy-CSS^{1nm}, Cit-^{4nm}Dy-CSS^{3nm} and Cit-^{4nm}Dy-CSS^{4nm}) as a function of the Dy^{3+} concentration. (B) Relaxation rate R_2 (= $1/T_2$) of water protons plotted against the molar concentration of Dy^{3+} at 7 T. Solid lines are linear fits**.** 116

Figure 5.19. Relaxation rate R_1 (= $1/T_1$) of water protons plotted against the molar concentration of Dy^{3+} for Cit-^{4nm}Dy-CSS^{1nm}, Cit-^{4nm}Dy-CSS^{3nm} and Cit-^{4nm}Dy-CSS^{4nm} NPs at 7 T. The solid lines are linear fits. 117

Figure 5.20. Dy^{3+}-to-Gd^{3+} ion ratio in the Dy-CSS NPs obtained from ICP measurements. 119

Figure 5.21. (A) T_2-weighted MR images of Cit-Dy-CSS NPs with varying $NaGdF_4$ inner shell thickness (Cit-^{4nm}Dy-CSS^{3nm} and Cit-^{6nm}Dy-CSS^{3nm}) as a function of the Dy^{3+} concentration. (B) Relaxation rate R_2 (= $1/T_2$) and (C) R_1 (=$1/T_1$) of water protons plotted against the molar concentration of Dy^{3+} for Cit-^{6nm}Dy-CSS^{3nm} and Cit-^{4nm}Dy-CSS^{3nm} at 7 T. Solid lines are linear fits. 119

Figure 5.22. X-ray absorption spectra for water, Iohexol, and Cit-^{4nm}Dy-CSS^{3nm} NPs using a tungsten X-ray tube operating at 150 kV. Peaks marked with stars belong to the X-ray source, tungsten. 122

Figure 5.23. CT values of (A) Iohexol, (B) Cit-^{4nm}Dy-CSS^{3nm} NPs, (C) Cit-^{6nm}Dy-CSS^{3nm} NPs, and (D) their corresponding normalized values as a function of X-ray source peak voltage. 122

Figure 5.24. (A) CT images of Cit-Dy-CSS (Cit-^{4nm}Dy-CSS^{1nm}, Cit-^{4nm}Dy-CSS^{3nm}, and Cit-^{4nm}Dy-CSS^{4nm}) NPs and clinically used CT CA Iohexol at different concentrations. (B) CT values for different concentrations of Cit-Dy-CSS NPs dispersed in water and Iohexol solutions. Solid lines are linear fits. 123

Figure 6.1. XRD patterns of orthorhombic $NaMnF_3$ particles obtained by a MW-assisted thermal decomposition approach using different Na^+-to-Mn^{2+} ratios: 1:1, 1.5:1, 2:1, and 3:1. T_a = 300 °C, T_b = 240 °C; t = 10 min. References: black line – orthorhombic $NaMnF_3$, PDF card [01-072-0291]; red line – NaF, PDF card [00-001-1184]..... 129

Figure 6.2. EDX spectra (1) and the corresponding SEM images (2) of the particles obtained using different Na^+-to-Mn^{2+} ratios: (A) 1:1, (B) 1.5:1, (C) 2:1, and (D) 3:1. Reaction temperature: T_a = 300 °C, T_b = 240 °C; reaction time = 10 min. Scale bars: 1 μm. 130

Figure 6.3. (1) TEM and (2) SEM images of $NaMnF_3$ particles synthesized using different Na^+-to-Mn^{2+} ratios: (A) 1:1, (B) 1.5:1, (C) 2:1 and (D) 3:1. Reaction temperature: T_a = 300 °C, T_b = 240 °C, reaction time = 10 min. Scale bars: 1 μm. 131

Figure 6.4. Size distributions of $NaMnF_3$ particles synthesized using different Na^+-to-Mn^{2+} ratios: (A) 1:1, (B) 1.5:1, (C) 2:1, and (D) 3:1. The insets in (A) and (B) provide the width distributions for the rods and ribbons obtained; insets in (C) and (D) provide the thickness distributions for the plates obtained. Reaction temperature: T_a = 300 °C, T_b = 240 °C; reaction time = 10 min..... 131

Figure 6.5. SEM images of the particles obtained using a 2:1 Na^+-to-Mn^{2+} ratio providing evidence for the proposed assembly of $NaMnF_3$ plates around NaF spheres – (A) partial and (B) full coverage of the spheres. The scale bar given in (B-2) applies to all four images. Upon further increase of the metal ion ratio to 3:1, SEM and TEM images showed an increasing number of these box-like assemblies. 132

Figure 6.6. (A) XRD patterns of $NaMnF_3$ particles obtained by a microwave-assisted thermal decomposition using a 2:1 Na^+-to-Mn^{2+} ratio and a nucleation temperature T_a of 260 °C, 270 °C,

280 °C, 290 °C, and 300 °C, respectively (growth temperature T_b = 240 °C; reaction time = 10 min). References: black line – orthorhombic $NaMnF_3$, PDF card [01-072-0291]; red line – NaF, PDF card [00-001-1184]. (B-D) Transmission electron microscopy (TEM) images of particles obtained at T_a of (B) 280 °C, (C) 290 °C, and (D) 300 °C. Scale bars: 500 nm. 134

Figure 6.7. (A) XRD patterns of $NaMnF_3$ obtained by a microwave-assisted thermal decomposition using a 2:1 Na^+-to-Mn^{2+} ratio and a particle growth temperature T_b of 240 °C, 250 °C, and 280 °C, respectively (nucleation temperature T_a = 300 °C; reaction time = 10 min). Reference: black line – orthorhombic $NaMnF_3$, PDF card [01-072-0291]; red line – NaF, PDF card [00-001-1184]. (B-D) TEM images of materials obtained at (B) 240 °C, (C) 250 °C, and (D) 280 °C. Scale bars: 500 nm. 135

Figure 6.8. (A and C): XRD patterns of $NaMnF_3$ particles synthesized at different reaction times: 1 min, 5 min, 10 min, and 20 min, using Na^+-to-Mn^{2+} ratios of (A) 1:1 and (C) 2:1, respectively. Reaction temperature: T_a = 300 °C, T_b = 240 °C. References: black line – orthorhombic $NaMnF_3$, PDF card [01-072-0291]; blue line – $NaMn_3F_7$, PDF card [00-027-0745]; red line – NaF, PDF card [00-001-1184]. (B and D): TEM images of the corresponding $NaMnF_3$ particles obtained using Na^+-to-Mn^{2+} ratios of (B) 1:1 and (D) 2:1 and reaction times of (1) 1 min, (2) 5 min, (3) 10 min, and (4) 20 min. Scale bars: 500 nm. 135

Figure 6.9. (A) XRD patterns of cubic-phase $KMnF_3$ particles synthesized by a microwave-assisted approach using K^+-to-Mn^{2+} ratios of 1:1 and 2:1. Reference: black line – cubic $KMnF_3$, PDF card [00-017-0116]. (B) and (C) show the corresponding TEM images of $KMnF_3$ particles obtained at K^+-to-Mn^{2+} ratios of (B) 1:1 and (C) 2:1. Reaction temperature: T_a = 300 °C, T_b = 240 °C; reaction time = 10 min. Scale bars: 500 nm. 137

Figure 6.10. FTIR spectra of PAA-capped $MMnF_3$ (M = Na, K) particles and PAA used as reference. 138

Figure 6.11. TGA profiles of PAA-capped $MMnF_3$ (M = Na, K) particles showing mass loss ascribed to PAA surface groups at temperatures up to ca. 500 °C. Comparable amounts of PAA were found for $NaMnF_3$ needles and plates obtained at Na^+-to-Mn^{2+} ratios of 1:1 and 3:1, exhibiting a mass loss of 2.4 % and 2.0 %, respectively. A larger amount of PAA (4.7 %) was observed for $KMnF_3$ particles, which may be explained by the particles' smaller size, thus, larger surface area. 139

Figure 6.12. (A-1) and (A-2): XRD patterns of oleate (OA)-capped $NaMnF_3$ particles (black lines) obtained by the microwave-assisted approach using Na^+-to-Mn^{2+} ratios of (A-1) 1:1 and (A-2) 3:1 and their respective PAA-capped samples (red lines). (A-3): XRD patterns of OA-$KMnF_3$ synthesized using a 1:1 K^+-to-Mn^{2+} ratio (black line) and the corresponding PAA-capped particles (red line). Reference: black line – orthorhombic $NaMnF_3$, PDF card [01-072-0291]; blue line – cubic $KMnF_3$, PDF card [00-017-0116]. Reaction temperature: T_a = 300 °C, T_b = 240 °C; reaction time: 10 min. (B-1) to (B-3) show the corresponding TEM images of the PAA-capped samples. Scale bars: 500 nm. 139

Figure 6.13. Relaxation rate R_1 (A) and R_2 (B) of water protons plotted against the molar concentration of Mn^{2+} for PAA-capped $NaMnF_3$ synthesized using 1:1 (red data points) and 3:1 (blue data points) Na^+-to-Mn^{2+} ratios under 0.47 T. Solid lines are linear fits. 140

Figure 6.14. Relaxation rates R_1 (A) and R_2 (B) of water protons plotted against the molar concentration of Mn^{2+} for PAA-capped $KMnF_3$ particles (synthesized using a 1:1 K^+-to-Mn^{2+} ratio) under 0.47 T. Solid lines are linear fits. 141

Figure 7.1. (A) XRD pattern of Er^{3+}/Tm^{3+}-based CSS NPs. Reference: β-$NaGdF_4$, PDF card [01-080-8787]. (B) TEM images of (1) core, (2) CS and (3) CSS NPs as well as (4) their corresponding size distributions. 146

Figure 7.2. (A) NIR emission spectrum of $^{Er/Tm}$CSS NPs under 980 nm excitation and (B) the corresponding energy diagram. 148

Figure 7.3. (A) Temperature-dependent emission spectra recorded on $^{Er/Tm}$CSS NPs under 980 nm excitation. Laser power density: 33 W/cm^2, shaded orange and green areas were used to calculate LIR. (B) Temperature-dependent LIR values and (C) relative thermal sensitivities of the $^{Er/Tm}$CSS NPs. 148

List of Abbreviations

CT	computed tomography
CS	core/shell
CSS	core/shell/shell
CA	contrast agent
Cit	citrate
DLS	dynamic light scattering
ETU	energy transfer upconversion
EDX	energy dispersive X-ray
FTIR	Fourier transform infrared spectroscopy
FDA	The United States food and drug administration
Gd-DTPA	gadolinium-diethylene-etriaminepentacetate
Gd-DOTA	gadolinium-1,4,7,10-tetraazacyclododecane-1,4,7,10-tetraacetic acid
Gd-TFA	gadolinium trifluoroacetate
HU	Hounsfield units
FWHM	full width at half maximum
ICP-OES	inductively coupled plasma optical emission spectroscopy
Ln	lanthanide
Ln^{3+}	trivalent lanthanide ion
LIR	luminescence intensity ratio
Ln-TFA	lanthanide trifluoroacetate
MRI	magnetic resonance imaging
MW	microwave
Mn-$(TFA)_2$	manganese trifluoroacetate
LF	ligand free
NMR	nuclear magnetic resonance
NP	nanoparticle
Na-TFA	sodium trifluoroacetate
NIR	near-infrared

OA	oleate
OAm	oleylamine
ODE	1-octadecene
PEG	polyethylene glycol
PAA	poly(acrylic acid)
PBS	phosphate-buffered saline
PDI	polydispersity index
PL	photoluminescence
QY	quantum yield
RF	radio frequency
RE	rare earth
RE-TFA	rare earth trifluoroacetate
S/V	surface-to-volume
SEM	scanning electron microscopy
SAED	selected area electron diffraction
TFA	trifluoroacetic acid
TEM	transmission electron microscopy
TGA	thermogravimetric analyses
UC	upconversion
UCNP	upconverting nanoparticle
XRD	X-ray diffraction

List of Symbols

α-, β-$NaREF_4$	cubic and hexagonal crystalline phase $NaREF_4$
λ (λ_{EX}, λ_{EM})	wavelength (excitation or emission, respectively)
λ	wavelength of the diffracted electrons
μ_{eff}	effective magnetic moment
μ	linear X-ray attenuation coefficient of a material
τ	lifetime
τ_R	rotational correlation time
θ	Bragg angle
ω_0	Larmor frequency
δT	thermal resolution
B	constant in Boltzmann equation
C_s	saturation concentration
C_{min}	minimum concentration for nucleation
C_{max}	absolute maximum concentration
d	interplanar distance
ΔE	energy gap between the emitting levels
I	X-ray output intensity
I_0	X-ray incident intensity
k	dimensionless shape factor
k_B	the Boltzmann factor
M_z	magnetization
pH	power of hydrogen
R	repeatability
R_{Au}	radius of the SAED ring of the Au standard
R_1	T_1 relaxation rate
R_2	T_2 relaxation rate
r_1	T_1 relaxivity
r_2	T_2 relaxivity

S_r	relative thermal sensitivity
T	Temperature (also Tesla, unit of magnetic field)
T_1	longitudinal relaxation time of water protons
T_2	transverse relaxation time of water protons
X	thickness of the object
Z	atomic number

Statement of Contribution

Some analytical techniques required in this thesis were performed by other technicians and colleagues at the University of Ottawa. TGA, EDX, SEM, and SAED measurements were performed by Dr. Yun Liu, manager of the Materials Characterization Core Facility. MRI measurements were performed by Prof. Gerd Melkus, assistant professor at the Department of Radiology. X-ray absorption and CT measurements were performed with Dr. Samuel Morfin, a post-doctoral fellow in Prof. Al's group under the guidance of Prof. Tom Al. Cell toxicity experiments were done by colleagues in Prof. Shuhendler's group, Meghana Kesanakurti and Dr. Nicholas D. Calvert, under the guidelines of Prof. Adam J. Shuhendler. Relaxivity measurements were done by myself under the guidance of Prof. Nicolas Bordenave. All other measurements, including PL, XRD, TEM, FTIR, DLS, and zeta potential, were performed by myself. This thesis was written by myself, under the guidance of Prof. Eva Hemmer.

Chapter 1. Introduction

The rare-earth (RE) elements refer to a group of 17 elements, including scandium (Sc), yttrium (Y), and 15 lanthanides (Ln) (from lanthanum to lutetium), which have numerous similar physical and chemical properties.[1] The history of RE elements dates back to 1751, when the first RE mineral was discovered in Sweden.[2] More than two centuries after the first achievements in RE chemistry, these elements have been developed for various applications, such as electronics (*e.g.*, fiber optics and lasers), magnetics (*e.g.*, computer hard drives), lighting/displays (*e.g.*, LED lighting and colour television), catalysts, phosphors, magnetic resonance imaging contrast agents (*e.g.*, Gd-chelates) and anti-counterfeiting.[3-7] Beyond their current practical uses, these elements are also being explored for potential applications in areas such as nanoparticle-based bioimaging, therapy, photocatalysis, photovoltaics, and thermal sensing.[8-10]

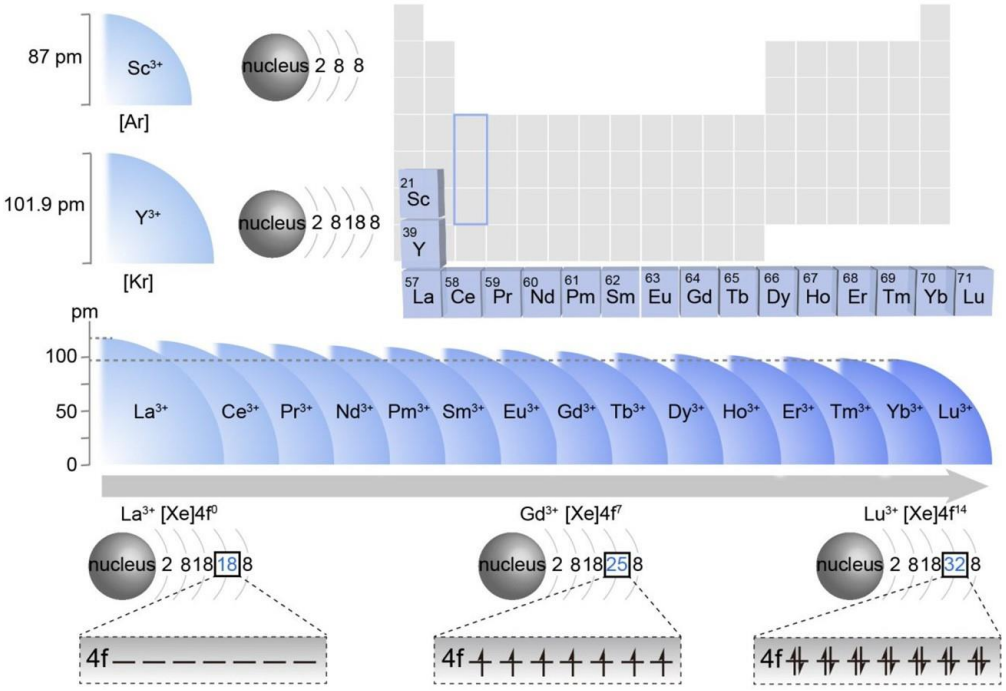

Figure 1.1. Ionic radius and valence configuration of RE^{3+} ions. From La^{3+} to Lu^{3+}, the number of electrons on the 4f orbitals increases with increasing atomic number. The electron configurations of La^{3+}, Gd^{3+}, and Lu^{3+} show empty, half-filled, and completely filled 4f orbitals, respectively. Figure taken from [11] with permission.

All the RE elements have similar ground state electronic configurations. For Sc and Y, the ground state configurations are $[Ar]3d^14s^2$ and $[Kr]4d^15s^2$, respectively (Figure 1.1). For the 15 Ln elements, La, Ce, Gd, and Lu share the $[Xe]4f^{n-1}5d^16s^2$ configurations, while other lanthanides share $[Xe]4f^n6s^2$ configurations. As a result, trivalent RE ions (RE^{3+}), are the most common and stable oxidation state.[12] Trivalent Ln ions (Ln^{3+}) have similar configuration $[Xe]4f^{n-1}$, which results in a systematic decrease in the ionic radius across the Ln series, a phenomenon known as Ln contraction.[13] Therefore, the ionic radii fall into a small range across the Ln series. Consequently, this allows to incorporate different Ln^{3+} ions simultaneously into a substrate with controlled concentrations and compositions (known as doping), which is crucial for the development of Ln^{3+}-doped materials with diverse properties. The electron configurations of Ln^{3+} ions endow them with particularly interesting optical and magnetic properties, which will be introduced in more detail in the following sections. In this thesis, "Ln^{3+}" will be used to discuss the optical and magnetic properties, and potential applications, while "RE^{3+}" will only refer to the discussion for the host materials.

1.1 Optical Properties of the Lanthanides

Ln^{3+} ions possess attractive optical properties because of their well-shielded 4f electrons. Due to this shielding effect provided by the 5s and 5p shells, the optical properties of Ln^{3+} ions originating from 4f → 4f transitions are less influenced by the surrounding environment and exhibit similar spectral features to those of free ions.[11] Of note, the 4f → 4f transitions can be affected by temperatures. This thermal dependence of spectral features from Ln^{3+} ions opens the field of luminescence temperature sensing (more details are described in Chapter 1.1.5).[10] Strictly speaking, the 4f → 4f electric diploe transitions are principally forbidden by the parity (Laporte) rule,[14] which states that the two energy levels involved in a transition must have opposite parity. Fortunately, this rule can be partially lifted by doping the Ln^{3+} ions into an asymmetric crystal field, *e.g.*, by choosing an inorganic host lattice or coordination complex with organic ligands that would not allow the lanthanide ion to occupy a site with spherical symmetry.[15] The unique electronic configuration of Ln^{3+} contributes to the characteristic optical properties of Ln^{3+}-based

materials including excellent photostability, large Stokes/anti-Stokes shifts, long luminescence lifetimes, and sharp-band emissions.[16]

Based on the transition pathways involved, the luminescence of Ln^{3+} can be classified into downshifting, downconversion, and upconversion.[17] In both downshifting and downconversion processes (Stokes shift process), the emitted light has a longer wavelength (lower-energy) than the excitation light. The downshifting process involves one emitting photon after absorbing one photon, while in the case of downconversion, an incident high-energy photon is converted into two or more lower-energy photons.[18] In contrast, upconversion (UC) is a nonlinear optical process in which the sequential absorption of two or more lower-energy photons (typically NIR light) leads to the emission of light at shorter wavelength (anti-Stokes shift).[17] One key requirement for UC is the presence of a metastable absorbing state, located between the ground and emitting states, that acts as a population reservoir. The UC mechanism will be described in more detail in the following.

1.1.1 Upconversion Mechanism

Two common mechanisms for UC processes are excited state absorption (ESA) and energy transfer upconversion (ETU).[19] UC in a single ion type system typically occurs *via* the ESA mechanism. As shown in Figure 1.2 A, ESA involves the sequential absorption of two or more photons, promoting an ion from the ground state to an excited state where UC occurs.[19] ETU is widely recognized as the most common mechanism for UC emission in nanoscale materials.[20] As illustrated in Figure 1.2 B, an ion I, also known as the sensitizer (usually with a high absorption cross-section), is first excited from the ground state (G) to its excited state (E1) by absorbing a photon. Then the ion I transfers the harvested energy to the excited state of ion II, known as the activator (usually an emitting ion), exciting the activator to its higher excited state E2 with the involvement of at least one additional photon. Following this energy transfer, UC emission can be obtained from the excited levels of the chosen activator ion.[20] A sensitizer is usually used together with an activator to enhance the photon absorption.

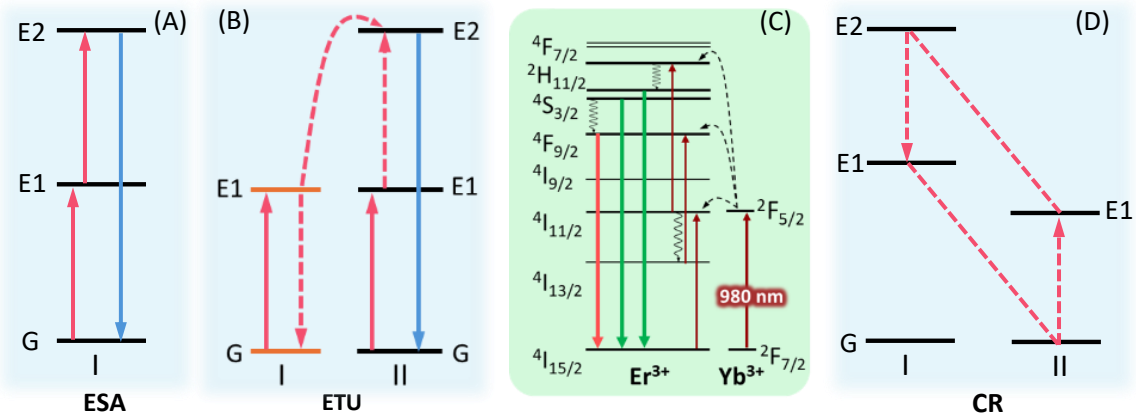

Figure 1.2. Schematic representation of energy transfer processes leading to Ln^{3+}-based upconversion. (A) Excited state absorption (ESA) and (B) energy transfer upconversion (ETU). The arrows indicate the direction of energy flow between different energy states. (C) ETU energy transfer process for the upconversion process commonly found for the Yb^{3+}/Er^{3+} ion pair under excitation at 980 nm. Non-radiative transfers are indicated by dotted curved arrows, and non-radiative multiphoton relaxations are indicated by wavy arrows. (D) Cross relaxation (CR) process. Figure (A) and (B) redrawn from [20], (C) redrawn from [19], (D) redrawn from [21] with permission.

For instance, Yb^{3+} ions are commonly used as a sensitizer for the activators, *e.g.*, Er^{3+} and Tm^{3+}, due to its relatively high absorption cross-section at 980 nm.[22] For example, in the UC process of the Yb^{3+}/Er^{3+} pair (Figure 1.2 C), the Yb^{3+} ion absorbs the photon energy from 980 nm light and is populated to its excited state $^2F_{5/2}$. Following the non-radiative energy transfer from the Yb^{3+} ion to the Er^{3+} ion, the Er^{3+} ion is promoted to its excited state, $^4I_{11/2}$. Subsequently, the sequential energy transfer processes promote the Er^{3+} ion to its higher excited states, *e.g.*, $^4F_{9/2}$ and $^4F_{7/2}$, before it returns to the ground state by emitting light in the red, green, and blue spectral range.[19]

The UC efficiency is influenced by the dopant ion concentration, the choice of host lattice, as well as the architectural design (*i.e.*, core/shell concept). These influencing parameters are described in more detail in the following paragraphs.

In addition to the UC process, Ln^{3+}-based materials can also be excited by UV or NIR light to emit in the visible-to-NIR regions (downshifting process), *i.e.*, UV-visible and NIR-NIR processes. The NIR-NIR process is particularly interesting for tissue imaging applications by matching the NIR transparency windows,[23] and will be discussed in Chapter 1.3.1.

1.1.2 Doping Concentration

Since 4f → 4f electronic transitions are Laporte-forbidden, inefficient absorption of the exciting light can be a serious problem. In principle, the absorption can be improved by increasing the concentration of the Ln^{3+} dopant in the material. However, one has to be aware that a higher concentration of Ln^{3+} dopants can introduce so-called cross-relaxation (CR) and energy-migration processes, inducing quenching of the UC emission.[21] As shown in Figure 1.2 D, CR is an energy transfer process, resulting from ion−ion interaction in which ion I transfers part of its excited energy to ion II through a process that can be summarized as E2 (ion I) + G (ion II) → E1 (ion I) + E1 (ion II). Ion I and ion II can be either the same or different, and ion II can also be in its excited state in some cases.[21] CR is one reason for the well-known "concentration quenching mechanism" of UC emission.[24] Hence, in most upconverting nanoparticles (UCNPs), the concentration of Er^{3+} does not exceed 3%, while the concentration of Tm^{3+} is usually around 0.5%.[19] One way to circumvent this concentration quenching effect caused by a high concentration of activators was reported by Zhao *et al.*, namely the use of a high laser irradiance density ($\sim 10^6$ W/cm^2).[25] The authors stated that the use of high excitation density could effectively reduce the probability of CR by decreasing the population density at the ground state. However, this uncovered UC enhancement strategy was limited to applications that permit a high irradiance density. Although CR process causes emission quenching, it can be intentionally used to tune the color output in a UCNP by populating an emitting level that corresponds to a desired emission wavelength.[26]

1.1.3 Host Lattice Choice

This section was taken from the published work: Handbook on the Physics and Chemistry of Rare Earths, Elsevier, 2024, ISSN 0168-1273. Christian Homann, Nan Liu, Helliomar Barbosa and Eva Hemmer.

A significant challenge in the design of efficient Ln^{3+}-doped NPs involves the meticulous selection of appropriate host materials. Doping the Ln^{3+} ions into a suitable inorganic host lattice (an asymmetric crystal field) partially allow the forbidden 4f → 4f electronic transitions, enabling

bright luminescence of Ln^{3+} ions.[27] Therefore, lowering the symmetry around the Ln^{3+} ions by tailoring the crystal structure enhances luminescence emission intensity.[21] A suitable host lattice must be capable of incorporating Ln^{3+} ions by substituting host ions of comparable size and charge. Moreover, good chemical stability is required to ensure the physical integrity of the NPs. Moreover, the best suited host materials have a low lattice phonon energy, minimizing non-radiative processes, while maximizing the radiative emission processes.[28]

To date, a myriad of host materials has been investigated including fluorides, chlorides, bromides, oxides, vanadates, tungstates, phosphates, oxysulphides, and oxychlorides.[29] Among these host materials, chlorides and bromides exhibit very low phonon energies (~300 cm^{-1}), which are ideal for higher efficiencies of the UC process; however, they are chemically unstable. In contrast to these halides, oxides exhibit excellent chemical and thermal stability but at the drawback of higher phonon energies (>500 cm^{-1}). Fluoride hosts offer an acceptable compromise. They possess low phonon energies (~350 cm^{-1}), good thermal and chemical stability, as well as accessible synthesis routes.

Hence, fluoride-based inorganic materials have emerged as the most popular host materials and received extensive investigation.[22] Sodium rare-earth tetra fluorides ($NaREF_4$), and especially $NaYF_4$ and $NaGdF_4$, have emerged as highly favored host materials due to their exceptional properties. They exhibit low phonon energy, suitable dopant sites (favourable in terms of symmetry aspects), dopant compatibility (*i.e.*, dopant ion substituting host ions), and good chemical and thermal stability. $NaREF_4$ can crystallize in two crystalline phases, namely the cubic (α) and the hexagonal (β) crystal structure.[19] As shown in Figure 1.3 A, the α-phase contains one type of cation site, which is randomly occupied by Na^+ and RE^{3+} ions (blue spheres). The crystallographic symmetry of both Na^+ and RE^{3+} are determined to be O_h.[30] In contrast, the crystalline structure of β-phase $NaREF_4$ consists of two types of relatively low-symmetry cation sites (blue and purple spheres), which are selectively occupied by Na^+ and RE^{3+} ions at C_{3h} site (Figure 1.3 B).[31] According to the Judd-Ofelt theory, which describes the electric-dipole transitions between the energy levels of the $4f^n$ configurations of the Ln^{3+} ions, the UC emission is heavily affected by the site symmetry of the Ln^{3+} dopant ions.

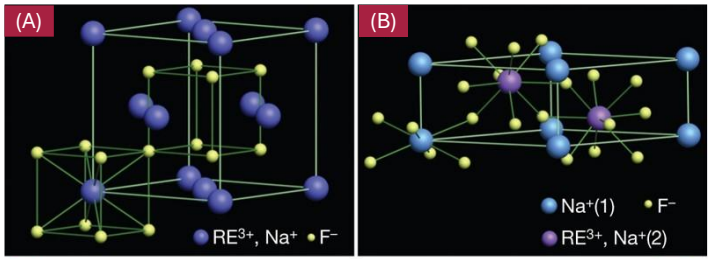

Figure 1.3. Crystalline structure of (A) the cubic and (B) hexagonal phases of $NaREF_4$ particles. Figure adopted from [31] with permission.

Overall, β-phase is more efficient for the UC process due to its lower symmetry, lower phonon energy as well as multiple cation dopant sites, and has been explored for most optical applications.[32, 33] Yet, in 2022, Quintanilla *et al.* reported that in the case of α-$NaGdF_4$, the quantum yield (QY) could increase and even surpass that of the β-phase when a decrease in NP size below 20 nm induced larger distortions of the doping ions in the crystal phase.[34]

1.1.4 Luminescence Enhancement – Core/Shell Concept

This section was taken from the published work: Handbook on the Physics and Chemistry of Rare Earths, Elsevier, 2024, ISSN 0168-1273. Christian Homann, Nan Liu, Helliomar Barbosa and Eva Hemmer.

While the nanoscale size endows numerous excellent properties to Ln^{3+}-based NPs, it also results in a larger relative surface area (*i.e.*, surface-to-volume ratio) than in the case of larger particles and bulk material. This results in more surface defects and thus, a higher risk of surface luminescence quenching.[35] The higher surface area makes NPs also more prone for solvent induced quenching effects, which are very pronounced on solvents that contain high-energy vibrations bands, *e.g.*, C–H (2900 – 3000 cm^{-1}) and O–H (3200 – 3700 cm^{-1}).[36] The emissions from these NPs are quenched by vibrational coupling with nearby high-energy vibrations of solvents and capping molecules.

The growth of a protecting shell around the Ln^{3+}-doped NP, resulting in a core/shell (CS) architecture, is an efficient strategy to prevent such devastating surface quenching effects.

Herein, the shell layer – typically, but not necessarily, made of the same host material as the core, while lacking the dopant – provides an effective passivation of the Ln^{3+} emitter from lattice defects located at the surface of the NPs and from potentially quenching surrounding environment as depicted in Figure 1.4 A. As a result, significant luminescent enhancement has been reported.[37]

In general, the direct comparison of core and CS emissions typically follows a similar pattern of a manifold fluorescence intensity increase (Figure 1.4 B), but it is also often being used as an indicator for the quality of the shell shielding ability. After the introduction of the CS concept by Boyer in 2007, Vetrone *et al.* proposed in 2009 the concept of the active shell. Rather than growing an inert shell, sensitizers Yb^{3+} or Nd^{3+} are doped into the shell to foster excitation and thus, boost emission intensity.[37, 38] Following the first simple CS architecture, core/multi-shell Ln^{3+}-based NPs started to emerge and are still very popular when seeking optimized emission intensities as well as optical properties. Herein, by controlling the shell composition and thickness, different Ln^{3+} emitters can be engineered in separate layers in one NP, making color tuning and more generally optical property control possible.[39] The potential applications of these CS NPs used as optical imaging probes will be described in Chapter 1.3.1. In addition, the design of CS architectures can also generate new functionalities in Ln^{3+}-based NPs used as *e.g.*, multimodal imaging probes,[40] which will be discussed in Chapter 1.3.4.

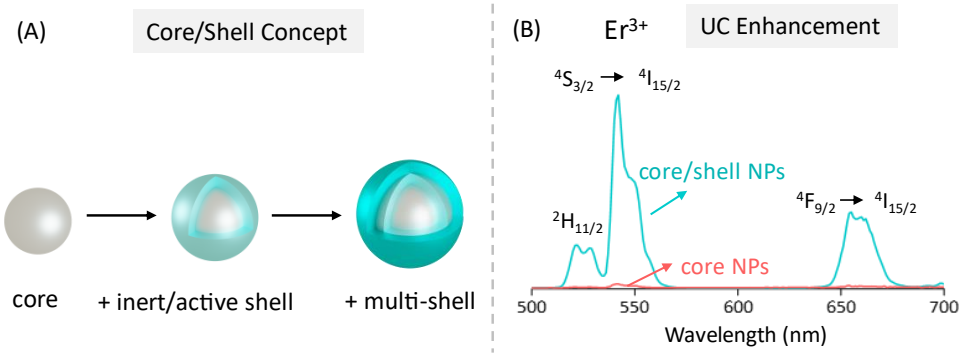

Figure 1.4. Schematic representation of core/shell (CS) and core/multi-shell architectures. (B) UC intensity enhancement of β-$NaGdF_4$:Yb^{3+},Er^{3+}/$NaGdF_4$ CS NPs compared to the corresponding core NPs.

While the CS concept has been successfully applied over the past years, more recently, concerns and open questions have come up regarding the actual CS structure. While it was always assumed to have a relatively "hard" border between the core and the shell, with distinct separation of ions into core *versus* shell, yet, recent reports have shown that this is unlikely in the synthesized CS NPs, and the occurrence of element intermixing in the entire NP was more likely.[41] One of the first studies on this topic was performed by Haase and coworkers, investigating the Eu^{3+} ion distribution in β-$NaEuF_4$/ $NaGdF_4$ CS NPs.[42] The authors found that the concentration of leaked Eu^{3+} ions on the particle surface was estimated to be 0.7% and 5.6%, depending on the choice of the shell precursors. While the CS architecture is suitable for property tuning and emission enhancement, better understanding of element intermixing is still needed to know how it affects the properties of Ln^{3+}-doped NPs and how it might be prevented.

1.1.5 Temperature-Dependent Photoluminescent – Temperature Sensing

This section was taken from the published work: Nanoscale, 2024, 16, 10975-10993. Abigale Puccini, Nan Liu, and Eva Hemmer.

As a last fundamental aspect of lanthanide luminescence, its temperature dependence shall be mentioned, which opens opportunities for contactless optical thermal sensing.[10] Detection of temperature with high thermal and spatial resolution is necessary for a wide range of industrial and research applications, including microelectronics, nanofluidics, and biomedicine.[10, 43-45] Conventional contact thermometers, which are considered an invasive thermal sensing technique, are not suitable when temperature is measured at scales below 10 µm.[46] To overcome this limitation, remote, minimally invasive luminescence nanothermometers have been developed to allow for local temperature sensing at the nanoscale (Figure 1.5).[47, 48] Luminescence nanothermometry refers to a spectroscopic technique in which temperature-dependent changes in the spectral features of an optical nanoprobe, *e.g.*, emission intensity, lifetime, spectral shape, or peak position, can be used to provide a remote thermal readout.[47, 49, 50] Using luminescence nanothermometry, temperature can be sensed in applications where conventional contact thermometers are ineffective, such as in harsh environmental conditions, in fast moving objects,

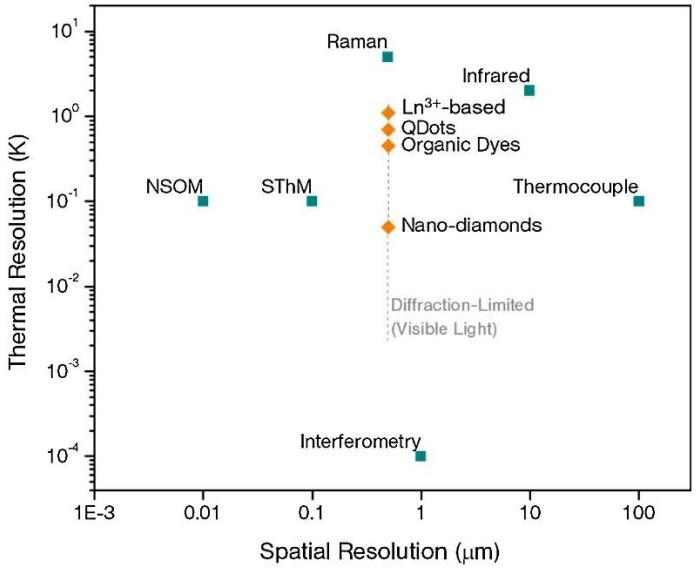

Figure 1.5. Typical thermal resolution *vs*. spatial resolution for various thermometry techniques, seeking sub-micrometric resolution. Orange dots indicate techniques based on luminescent nanoparticles. In this case, the spatial resolution is given by the experimental set-up (usually a microscope) and thus it is diffraction-limited. As a consequence, the precise spatial resolution will depend on the wavelength of the light applied, so it will be smaller for UV probes and larger for near-IR probes. Figure taken from [48] with permission.

and in the presence of strong electromagnetic fields.[51] It has also proven to be promising for remote *in vitro* or even *in vivo* thermal sensing.[45] The possibility for remote and minimally invasive temperature sensing has resulted in growing exploration of different materials and molecules capable of acting as luminescence thermometers at the nanoscale in recent years.

Due to their unique optical properties, Ln^{3+}-based NPs have been explored as candidates for luminescence nanothermometry in recent years. Since luminescence nanothermometry was not the major focus of this thesis, only the fundamental aspects are introduced in the following paragraphs.

Figures of Merit. The basic parameters used to describe the thermometric performance are briefly introduced in the following. Ratiometric approaches are widely applied as they are less affected by emitter concentration when compared to thermal sensing based on absolute emission intensity.[52] Herein, the thermometric parameter is the luminescence intensity ratio, LIR, commonly used to quantify a nanothermometer's thermometric performance. The LIR can be

quantified as the ratio between the integrated intensities of two emission bands that originate from two different and distant energy levels (double-band approach) or two Stark sublevels (single-band approach) (Figure 1.6 A/B).

Relative thermal sensitivity, S_r. A key figure of merit is the relative thermal sensitivity (S_r), which correlates the change in LIR with change in temperature. This quantitative parameter is used to assess and compare the performance of different thermometers. It is defined as:

$$S_r = \frac{1}{LIR}\frac{\partial LIR}{\partial T} \qquad \textbf{(Eq. 1.1)}$$

For Ln-NP-based double-band nanothermometers, S_r values greater than 1 % K^{-1} are currently considered as indicative of a sensitive nanothermometer. While the S_r values of single-band nanothermometers are intrinsically lower than those of double-band nanothermometers (typically < 1 % K^{-1}).[50, 53]

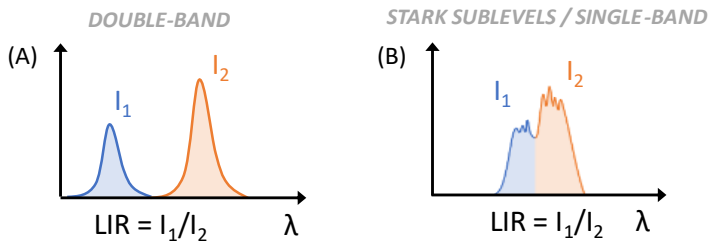

Figure 1.6. (A) Double-band and (B) single-band based luminescence nanothermometry.

Thermal resolution or temperature uncertainty, δT. Besides S_r, thermal resolution (also calls temperature uncertainty), δT, representing the smallest temperature change that can be resolved in a given measurement, is another important figure of merit. Depending on the experimental detection setup used, the acquisition conditions applied, and the signal-to-noise ratio in the experiment, δT might change. While there is still no full consensus within the nanothermometry community on how to standardize the determination of δT, it is often calculated by:

$$\delta T = \frac{1}{S_r}\frac{\delta LIR}{LIR} \qquad \textbf{(Eq. 1.2)}$$

Herein, δLIR/LIR is the relative uncertainty over the thermometric parameter. For LIR-based thermometry, δLIR/LIR is obtained as:

$$\frac{\delta LIR}{LIR} = \sqrt{\left(\frac{\delta I_1}{I_1}\right)^2 + \left(\frac{\delta I_2}{I_2}\right)^2} \quad \textbf{(Eq. 1.3)}$$

Where δI/I was estimated using the signal-to-noise ratio values, namely, dividing the standard deviation of the baseline by the maximum intensity value.

In general, the value of δT of a nanothermometer should be smaller than 1 K to achieve the sensitivity requirement.[46] However, methods to obtain δT are diverse and thus must be considered with care when using them to compare different nanothermometer systems.

Repeatability, R. The repeatability, R, describes the thermometer's ability to provide repeatedly the same result, under the same circumstances. This value generally should be higher than 90 % for good repeatability.

$$R = 1 - \frac{max(|LIR_i - LIR_{mean}|)}{LIR_{mean}} \quad \textbf{(Eq. 1.4)}$$

Where LIR_i is the luminescence intensity ratio at a given temperature measured for the i-th round of measurement, and LIR_{mean} is the average obtained from three independent measurements.

These concepts of the luminescence nanothermometry were used for the discussion in Chapter 5, but also in depth in work published by A. Puccini, N. Liu *et al.* on Pr^{3+}/Ho^{3+}-based NPs. The interested reader is referred to reference: *ACS Materials Lett. 2024, 6, 1327-1337*.

1.2 Magnetic Properties of the Lanthanides

In addition to their optical properties, Ln^{3+} ions are well known for their magnetic properties. With the exception of La^{3+} and Lu^{3+}, most Ln^{3+} ions exhibit paramagnetic properties in the ground state due to the presence of unpaired electrons in their 4f orbitals.[54] The magnetic moment, magnetic susceptibility, and electronic relaxation time of Ln^{3+} ions determined by their 4f electron configurations differ dramatically through the series.[55] For instance, Gd^{3+} has an

isotropic electronic ground state ($^8S_{7/2}$). Its half-filled f-orbital with 7 electrons has no net orbital momentum, resulting in a near zero spin–orbit interaction. Consequently, its electronic relaxation time is relatively long. In contrast, the asymmetric electron ground states of Dy^{3+} ($^6H_{15/2}$) and Ho^{3+} ($^5I_8$) endow them with shorter electronic relaxation time but larger magnetic moments and magnetic susceptibilities.[55] Due to their magnetic properties, some Ln^{3+} ions (*e.g.*, Gd^{3+}, Dy^{3+}, and Ho^{3+}) have been investigated, for instance, as contrast agents (CAs) in magnetic resonance imaging (MRI) to afford shortened relaxation time of protons and enhanced image contrast.[56] An introduction to MRI technology will be given in Chapter 1.3.2.

1.3 Potential Bioimaging Applications

Bioimaging is a technique used to visualize the structure of organisms, elucidate various biological functions, and monitor biological processes in real-time without physical interference.[57] It encompasses imaging at various scales, including *in vivo*, *in vitro*, and cellular, for research and clinical purposes.[9] Among the various imaging techniques currently available to healthcare providers and researchers, optical imaging allows for the investigation of real-time monitoring of biological phenomena with high spatial imaging resolution (*e.g.*, up to 100 nm) and sensitivity (in µM range),[58, 59] while MRI and X-ray computed tomography (CT) imaging come with the advantage to provide physiological and anatomical information with unlimited penetration depth.[60] Ln^{3+}-based materials are promising candidates for imaging probes (*e.g.*, optical, MRI and CT) due to their optical, magnetic, and X-ray attenuation properties, which will be described in the following sections.

Contrast agents (or imaging probes) are substances used to enhance the visibility of specific structures, tissues, or processes in imaging techniques. The requirements for an effective bioimaging contrast agent include safety, high contrast enhancement, biocompatibility, stability, proper clearance rate, proper formulation, and non-interference with biological functions.[61]

1.3.1 Optical Imaging Probes

As previously introduced, Ln^{3+}-based materials exhibit unique optical properties due to their capability to emit UV and visible light as well as NIR light when excited with NIR light (*e.g.*, 980 or 808 nm). This makes Ln^{3+}-based materials promising candidates as optical probes.[62] Compared to conventional optical probes (*e.g.*, quantum dots and organic dyes), which require excitation with UV-visible light, the use of NIR light provides several advantages, such as deeper penetration depth, weak autofluorescence, minimal photobleaching, and low phototoxicity.[63]

Upconversion luminescence imaging. Since the early 2000s, Ln^{3+}-doped nanomaterials have been investigated as luminescent probes for tissue and cell imaging.[64] One of the earliest demonstrations of Ln^{3+}-NPs as imaging probes was reported in 2008 by Jalil *et al.*.[65] They investigated the cellular imaging capacity of silica-coated $NaYF_4$:Yb^{3+},Er^{3+} NPs. The NPs were incubated with rat bone marrow-derived mesenchymal stem cells and skeletal myoblasts. When the NP-labeled cells were exposed to 980 nm NIR light, intense UC emissions with a high signal-to-noise ratio were observed (Figure 1.7). Moreover, the authors found that the NPs were mainly located at the cytoplasmic and the perinuclear regions, indicating the intracellular uptake of NPs.

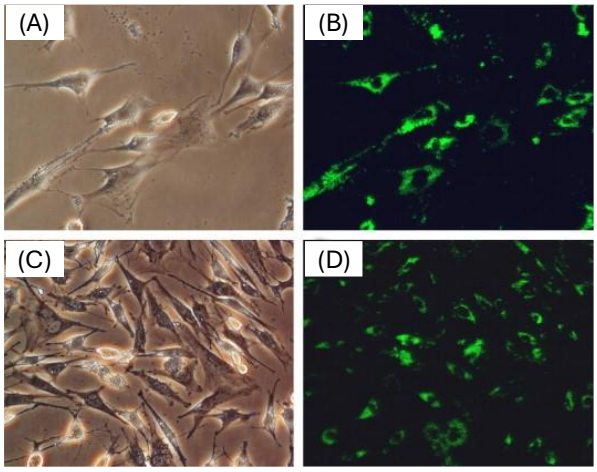

Figure 1.7. (A-D) Bright field and UC luminescence images showing the uptake of $NaYF_4$:Yb^{3+},Er^{3+} NPs by rat bone marrow derived mesenchymal stem cells (A,B) and skeletal myoblasts (C,D). The cells were maintained in their respective culture mediums and incubated with 50 µg/mL NPs for 24 h. Figures taken from [65] with permission.

Encouraged by the promising cellular imaging results, researchers have conducted *in vivo* imaging experiments using Ln^{3+}-NPs. To date, Ln^{3+}-NPs have been investigated in a variety of biological models for *in vivo* imaging studies, including bacteria,[66] Caenorhabditis elegans (C. elegans),[64] mice[9, 67], rabbits,[68] and even plants,[69] while most *in vivo* imaging studies were performed with mice.[9] For instance, Zhang and co-workers reported the first demonstration of the use of Ln^{3+}-NPs for mouse imaging.[67] The authors compared the penetration depth of excitation light (980 nm light) used for Ln^{3+}-NPs and quantum dots (UV light). Ln^{3+}-NPs injected subcutaneously into the groin and upper leg of Wistar rats, showed visible emissions from a depth of up to 10 mm upon 980 nm excitation. In contrast, no emissions were observed from the quantum dots under UV excitation. This study highlighted the promise of Ln^{3+}-NPs for *in vivo* imaging. Notably, other types of NIR-emitting materials including NIR-excitable quantum dots (*e.g.*, Ag_2S_3), carbon-based NPs, and novel molecules (*e.g.*, thiadiazole-based molecules), also show promise as optical imaging probes.[70]

NIR luminescence imaging. Despite considerable progress, UC luminescence imaging faces inherent limitations in resolution due to the large absorption and scattering effects of tissues on emitted visible light.[23] To address these concerns, luminescence imaging in the NIR wavelength range (optical transparency windows, 750 − 1870 nm), has gained significant attention in bioimaging in recent years.[71] NIR light offers deeper tissue penetration and lower scattering compared to UV/vis light.[72] The NIR transparency windows are typically divided into three sub-regions, NIR-I (700 – 950 nm), NIR-II (1000 – 1350 nm), and NIR-III (1550 – 1870 nm).[72] In 2013, Naczynski *et al.* were the first to achieve *in vivo* tumor and vascular imaging with high spatial resolution using NIR-emitting $NaYF_4$:Yb^{3+},Ln^{3+} (Ln = Er, Ho, Tm or Pr)/$NaYF_4$ CS nanoprobes.[73] By comparing the tissue transmission, the authors observed that NIR-III light (1525 nm emission of Er^{3+}) was significantly more efficient at transmitting through blood and pigmented tumour tissue than visible light at 550 nm (Figure 1.8). Since then, various efforts have been made to develop Ln^{3+}-nanoprobes for NIR imaging with continuously enhanced functionality and versatility.[8, 9, 63, 74] One of the very recent studies published by Chen *et al.* reported a series of Ln^{3+}-NPs (Ln = Er and Tm) emitting in the 1500 – 1900 nm spectral range as *in vivo* multiplexed imaging probes.[75]

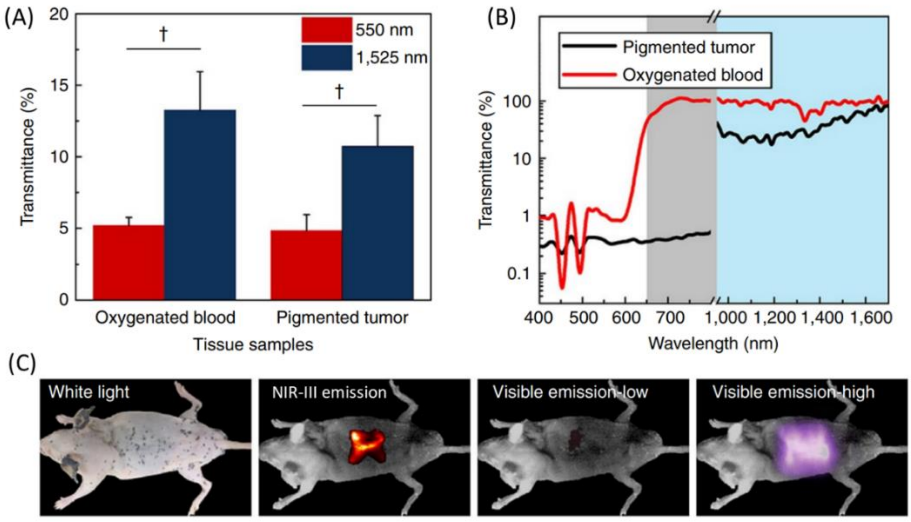

Figure 1.8. Tissue transmission of NIR-III light is superior to that of visible light. (A) NIR-III light (1525 nm) emitted from Er-doped NPs was significantly more effective at transmitting through blood and pigmented tumour tissue than visible light at 550 nm. Bar graph data in (a) are expressed as mean values ± standard error; n = 3 ($P < 0.01$). (B) Transmission spectra of visible (white region), NIR-I (grey region) and NIR-II/III (blue region) light reveal that longer NIR light exhibited lower absorbance and improved transmission through strong tissue absorbers such as blood and pigmented tumor tissue. (C) The NIR-III emissions from NPs patterned into the shape of an 'R' and irradiated with 980 nm light ('low': 0.14 W cm^{-2}; 'high': 0.5 W cm^{-2}) were more clearly visualized through a mouse body and at lower power densities than visible emissions due to reduced scattering and absorbance. Figures taken from [73] with permission.

The multiplexed imaging was obtained by combining two types of Ln^{3+}-based CSS NPs, namely β-$NaYbF_4$:Er(2%)/$NaYbF_4$/$NaYF_4$ with an emission at 1532 nm and β-$NaYbF_4$:Tm(5%)/$NaYbF_4$/$NaYF_4$ with an emission at 1852 nm. The results exhibited that by using NIR-III probes, high resolution static and dynamic multiplexed imaging on blood vessels, intestines, tumor lymph tubes and nodes was successfully achieved.

1.3.2 MRI Contrast Agents

MRI is a non-invasive technique that offers high soft tissue contrast and high spatial resolution, and is hence widely used in clinical diagnostic practice.[76] The fundamental principle of MRI is based on nuclear magnetic resonance (NMR) and the relaxation of proton spins in a magnetic field.[77] When the nuclei of protons are exposed to a strong magnetic field, their spins align either

parallel or antiparallel to the magnetic field. During their alignment, the spins undergo a precession at a specific frequency, known as the Larmor frequency (ω_0, Figure 1.9). When a resonance frequency in the radio-frequency (RF) range is applied to the nuclei, the protons absorb the energy and are excited to the antiparallel state. After the disappearance of the RF pulse, the excited nuclei return to their initial, lower-energy state through a process called relaxation. There are two different relaxation pathways: one is called longitudinal or T_1 relaxation, involving the decreased net magnetization (M_z) by recovering to the initial state. The other one is called transverse or T_2 relaxation, involving the induced magnetization on the perpendicular plane (M_{xy}) disappearing by the dephasing of the spins.[78]

When the characteristic relaxivity of protons within different domains is not sufficient to generate an informative image, the use of CAs can significantly enhance the anatomic or pathologic details under investigation.[60] Today, almost 50% of MR images use some form of contrast agents in clinic applications, and there is a dozen US Food and Drug Administration (FDA) approved CAs (*e.g*, Gd^{3+}-chelates).[79]

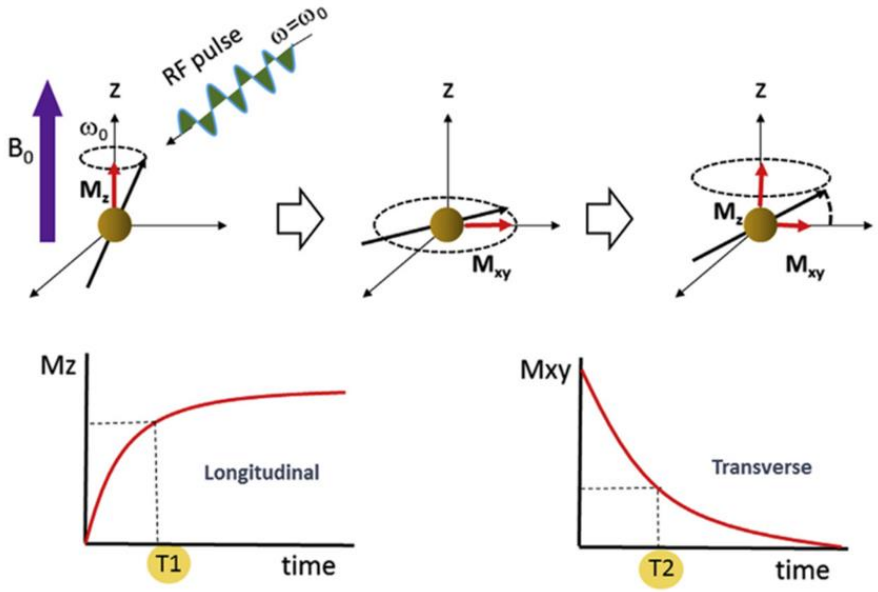

Figure 1.9. Principle of magnetic resonance imaging. Spins align parallel or antiparallel to the magnetic field and process under Larmor frequency (ω_0). After induction of RF pulse, magnetization of spins changes. Excited spins take relaxation process of T_1 relaxation and T_2 relaxation. Figure adapted from [78] with permission.

The contrast enhancement of MRI arises from the interaction between the CA and the surrounding water protons. The use of CAs can shorten the longitudinal (T_1) or transverse (T_2) relaxation time of nearby water molecules. Usually, T_1 CAs are applied to increase the signal intensity, resulting in a positive contrast enhancement (brightening image) in T_1-weighted MRI, while T_2 CAs decrease the signal intensity, providing a negative contrast enhancement (darkening image) in T_2-weighted MRI.[80] Both effects are described in more detail in the following paragraphs.

1.3.2.1 Gd^{3+}-Based Nanoparticles Based T_1 Contrast Agents

Gd^{3+} ions have the highest number of unpaired electrons (7) in their 4f electronic configuration and nearly no net orbital momentum, resulting in a negligible spin-orbit coupling. As a result, Gd^{3+} ions have a relatively long electronic relaxation time and have been widely used in MRI as T_1 CAs.[81] Clinically used T_1 CAs are Gd^{3+}-chelates, for instance, gadolinium-diethylene-etriaminepentacetate (Gd-DTPA) and gadolinium-1,4,7,10-tetraazacyclododecane-1,4,7,10-tetraacetic acid (Gd-DOTA).[80] However, despite their frequent real-life application, there are still ongoing limitations for Gd^{3+}-chelates that are currently addressed by researchers. For instance, because of their low molecular weight, Gd^{3+}-chelates lack specificity and show limitations for long-term tracking.[82] In addition, there is also the possible occurrence of nephrogenic systemic fibrosis associated with exposure of these CAs to patients suffering from poor kidney function.[83, 84]

To address these drawbacks, in recent years, Gd^{3+}-based NPs have attracted growing attention. These NPs have longer blood circulation time and a large density of Gd^{3+} ions on their surface, which dramatically increases the concentration of the contrast-providing species in the region of interest.[85] In addition, embedding Gd^{3+} ions into a matrix, such as inorganic NPs, where they are firmly held, can reduce their leakage from the probe, lowering levels of free Gd^{3+} ions and hence contributing to lower toxicity.[86] The recently developed Gd^{3+}-based NPs, including gadolinium oxide (Gd_2O_3),[87] sodium gadolinium fluoride ($NaGdF_4$)[85, 88, 89] and gadolinium fluoride (GdF_3)[90] have been extensively explored as alternative T_1 contrast agents because of their controllable

particle size and morphology. Factors, such as particle size, crystalline phase, and surface modification, influencing T_1 relaxivity (also called r_1, used as figure of merit to compare the contrast performance of different CAs), are described in more detail in the following.

Size effect. Johnson *et al.* synthesized size-tunable ultra-small $NaGdF_4$ NPs with four different sizes (2.5 to 8 nm) and found that the r_1 value increased with decreasing size from 3.0 mM^{-1} s^{-1} for 8.0 nm NPs to 7.2 mM^{-1} s^{-1} for the smallest 2.5 nm NPs (Figure 1.10 A).[85] For NPs with comparable surface chemistry and similar shapes, the surface-to-volume (S/V) ratio was strongly dependent on particle size, smaller sizes bringing higher S/V ratios. A higher S/V ratio allowed more surface Gd^{3+} ions to interact with water molecules and thus, resulting in a larger r_1 value. A similar size effect was also observed by Bridot *et al.* for ultra-small Gd_2O_3 NPs.[91] They found that the r_1 values increased when NP size decreased from 4.6 nm to 2.2 nm. However, this size effect is only valid in a certain size range.

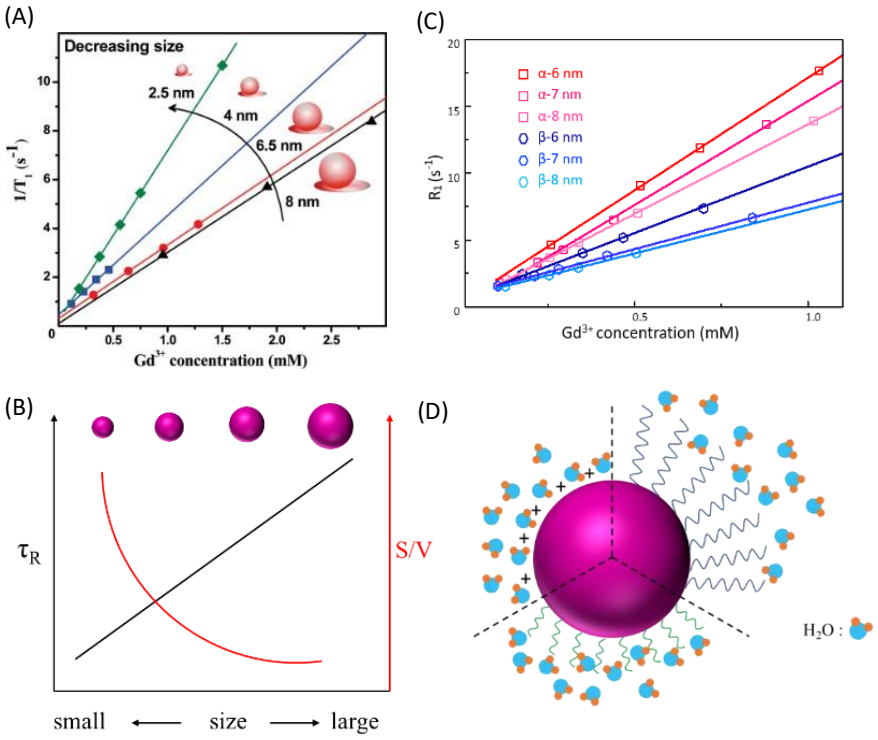

Figure 1.10. Factors including particle size (A, B), crystalline phase (C) and surface modification (D) influence the MRI T_1 relaxivity. Figure (A) taken from [85], figure (B) redrawn from [94], figure (C) taken from [89] with permission.

For example, Hou *et al.* prepared $NaGdF_4$ NPs with three sizes (5, 15, and 20 nm) and found that both 5 nm and 20 nm-sized NPs exhibited higher r_1 values than the 15 nm-sized NPs.[92] This was because there were two parameters affecting the r_1 value, *i.e.*, S/V ratio and rotational correlation time (τ_R). τ_R indicates the tumbling rate of the NPs, and a slower tumbling rate (large τ_R) is generally in favor of higher r_1.[93] With the increasing NP size, the S/V ratio decreased but τ_R value increased. Hence, for 20 nm-sized NPs, the contribution of τ_R was dominant to obtain a higher r_1 value.[92] And in case of 5 nm-sized NPs, the S/V ratio was dominated. Combining the negative correlation between S/V and τ_R, a nonmonotonic behavior accompanied by size change was the result (Figure 1.10 B).

Crystalline phase effect. Apart from the size effect, the crystalline phase also has an influence on T_1 relaxivity. We investigated the effect of host crystallinity on T_1 relaxivity by synthesizing $NaGdF_4$ NPs in α- and β-phase with comparable sizes (6 – 8 nm) (Figure 1.10 C).[89] The synthesized oleate-capped NPs were transferred to water using trisodium citrate by a ligand-exchange method. With comparable size, morphology and surface coating, the r_1 values of α-phase $NaGdF_4$ NPs were found to be twice as high as that of their β-analogues. Upon thorough physicochemical characterization of the NPs, the larger r_1 featured by citrate-coated α-$NaGdF_4$ NPs was ascribed to the reduced amount of citrate groups as a function of the crystalline phase and therewith correlated larger hydrodynamic diameter. The elevated r_1 values observed for α-NPs were further in good agreement with higher magnetization values previously reported in the literature.[95] We also compared the r_1 values of $NaGdF_4$ NPs in both phases coated with different surface groups, *i.e.*, poly (acrylic acid) (PAA). Again, PAA-coated α-NPs showed superior r_1 values opposed to their β-analogues. Overall, this study showed that the crystalline phase of $NaGdF_4$ NPs influences r_1.

Surface effect. Surface properties of NPs also play an important role in MRI contrast enhancement based on interaction between NPs and water molecules, which happens primarily on the surface of NPs.[89] In principle, the more interaction between water protons and surface Gd^{3+} ions, the larger T_1 relaxivity will be obtained.[87] The effect of surface modification on T_1 relaxivity is summarized in Figure 1.10 D. It has been shown that ligand-free Gd_2O_3 NPs, the surface of which was not blocked by any chemical, had a higher r_1 value than the corresponding ligand-coated NPs.[96] It was believed that water protons get fairly close to the surface Gd^{3+} of the

ligand-free Gd_2O_3 NPs as compared to ligand-coated ones, ultimately resulting in the increase of the r_1 value. Yet, for such an effect to happen, ligand-free NPs must be stable in dispersion without any agglomeration in the aqueous medium. If the ligand-free NPs were aggregated (as is often the case), the r_1 value would be smaller than that of the ligand-coated NPs due to fewer water molecules interacting with surface Gd^{3+} ions.[97]

In addition, the ligand-size dependence of water proton relaxivities has been investigated for $NaGdF_4$ NPs with different types of ligands grafted to their surface. For example, van Veggel *et al.* reported that the r_1 value of NPs coated with shorter ligands was larger than that obtained for coating with longer ligands.[98] This phenomenon was attributed to a ligand-size effect on water accessibility to surface Gd^{3+} ions, that is, smaller ligands will allow more water molecules to access the surface Gd^{3+} ions.[99] In fact, the ligand-size also influences τ_R, and a longer ligand chain will slow the rotation of the NPs. In summary, a carefully designed surface modification of NPs is crucial for nanoparticulate T_1 CAs.

1.3.2.2 Mn^{2+}-Based T_1 Contrast Agents

Manganese (Mn^{2+}) ions have five unpaired d electrons, and have recently emerged as an alternative MRI T_1 CAs following the discovery of a strong relationship between Gd^{3+}-chelates and nephrogenic systemic fibrosis (NSF).[100] Mn^{2+} ions do not cause NSF and participate in many biological processes in humans, including processes involving regulatory cofactors and receptors.[101] However, the use of Mn^{2+} has been limited because of its toxicity, especially acute cardiovascular depression.[102] Hence, different kinds of design approaches have been introduced to resolve the toxicity issue and imbue further functionalities in Mn^{2+}-based CAs.[103] In this regard, Mn^{2+}-based inorganic materials, such as MnO, MnF_2, and $NaMnF_3$, might have the potential to overcome the toxicity issue.[104-106] Mn^{2+}-based particles also showed a size effect on T_1 relaxivity. For example, Hyeon and co-workers investigated the size-dependent T_1 relaxivity of MnO NPs and demonstrated that the smallest NPs (7 nm) exhibited greater r_1 values than that of the largest NPs (25 nm).[105] However, unlike the well-investigated Gd-based CAs, Mn^{2+}-particle-based T_1 CAs

are much less explored, thus, further investigation of the synthesis of these particles and their T_1 contrast performance will be addressed in this thesis (Chapter 6).

1.3.2.3 Ln-Based T_2 Contrast Agents

The T_2 relaxivity (r_2) of a CA is largely proportional to the square of effective magnetic moment (μ_{eff}) of the ion, as T_2 CAs show a reduced signal dependence on induced magnetic moment of these CAs.[107] Clinically used MRI T_2 CAs are based on iron oxides, which, however, suffer from magnetization saturation at high magnetic fields (greater than 3 T).[108] High-field MRI is gaining increasing attention due to its higher spatial resolution and signal-to-noise ratio, holding potential for more effective diagnostic imaging.[107, 109] Therewith comes the raising demand for suitable high-field T_2 CAs. Dy^{3+} is a suitable candidate for high-field T_2 CAs due to its relatively large magnetic moment (10.6 μ_B) and short relaxation time, without saturation of the magnetization even at high magnetic fields up to 11.7 T.[98, 109, 110] Dy^{3+}-based NPs, including dysprosium oxide (Dy_2O_3) and sodium dysprosium fluoride ($NaDyF_4$) have been explored as potential T_2 CAs, and the key parameters influencing the T_2 relaxivity are discussed in detailed in the following paragraphs.

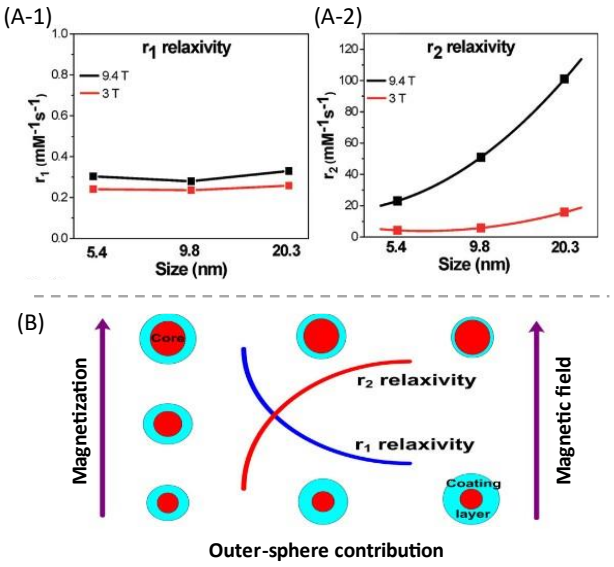

Figure 1.11. Parameters of (A) particle size and (B) surface influencing MRI T_2 relaxivity. Figure A taken from [111], figure B taken from [109] with permission.

Size effect. Unlike Gd^{3+}-based T_1 CAs, the relaxation enhancement for Dy^{3+}-based NPs is a bulk effect. Larger NPs generally have a higher contrast effect. The size-dependent properties of $NaDyF_4$ NPs under high magnetic fields (9.4 T) were first reported by van Veggel and co-workers,[111] demonstrating that the T_2 contrast was enhanced with increasing NP size (5 − 20 nm) and magnetic field strength (3 T and 9.4 T) (Figure 1.1111 A), while the r_1 value remained almost unchanged. This finding was ascribed to larger NPs possessing larger magnetization, which contributed to higher r_2 values.

Surface effect. In a follow-up study, van Veggel and co-workers further investigated the surface coating effect of $NaDyF_4$ on T_2 relaxivity (Figure 1.11 B).[109] The NPs were coated with different polymers, namely PMAO−PEG (poly(maleic anhydride-alt-1-octadecene)−polyethylene glycol) and DSPE-$mPEG_{2000}$ (1,2-Distearoyl-snglycero-3-phosphoethanolamine-N-[methoxy(polyethylene glycol)-2000], respectively. The NPs coated with thinner-layer DSPE-$mPEG_{2000}$ exhibited higher r_2 values than those coated with thicker layers of PMAO−PEG.

1.3.3 CT Contrast Agents

1.3.3.1 Basic Principles of CT Imaging

CT is one of the most widely used imaging modalities in clinical practice to diagnose disease and monitor treatment, owing to its high efficiency, deep penetration in biological tissue, and short scan duration.[112] A CT system consists of an X-ray source and X-ray detectors, between which the subject is placed. In clinical CT, the X-ray source and detector rotate around the subject to produce projections of X-ray attenuation through the body at many different angles (Figure 1.122). The X-ray projections acquired at each angle of rotation are then used to reconstruct tomographic images, which are visualized as 2D slices or 3D volumes of the specimen.[113]

The contrast in CT images originates from the different attenuation coefficients of various tissues. The ability of matter to attenuate X-rays is measured in Hounsfield units (HU). HU is defined by the following equation (**Eq. 1.5**)[114]:

$$HU = \frac{(\mu_{material} - \mu_{water})}{\mu_{water}} \times 1000 \qquad \textbf{(Eq. 1.5)}$$

where μ is the linear X-ray attenuation coefficient of a material, obtained from the following equation (**Eq. 1.6**):

$$I = I_0 \times e^{-\mu x} \quad \textbf{(Eq. 1.6)}$$

where *I* is the X-ray output intensity from the investigated object, I_0 is the X-ray incident intensity and x is the thickness of the object.

Therefore, the absorption of X-rays by a material is dependent on the thickness of the material and on the material-dependent attenuation coefficient. It has been reported that the photoelectric effect, which involves the interaction between X-ray photons and the inner shell electrons of objects, is the most dominant factor for X-ray attenuation.[115] The photoelectric effect is also proportional to the cube of a element's atomic number (Z^3), hence, high atomic weight materials exhibit a much stronger photoelectric effect than that of low atomic weight materials.[116]

Under X-ray irradiation, the hard body parts (*e.g.*, bones), soft tissues (*e.g.*, blood vessels, brain, muscles, and tumors), and air cavities in the body can be easily distinguished from each other, due to their differences in attenuation coefficients.[117] However, such a difference in attenuation coefficients between different soft tissues is quite small, as the CT values of most soft tissues range from 40 to 80 HU.[116]

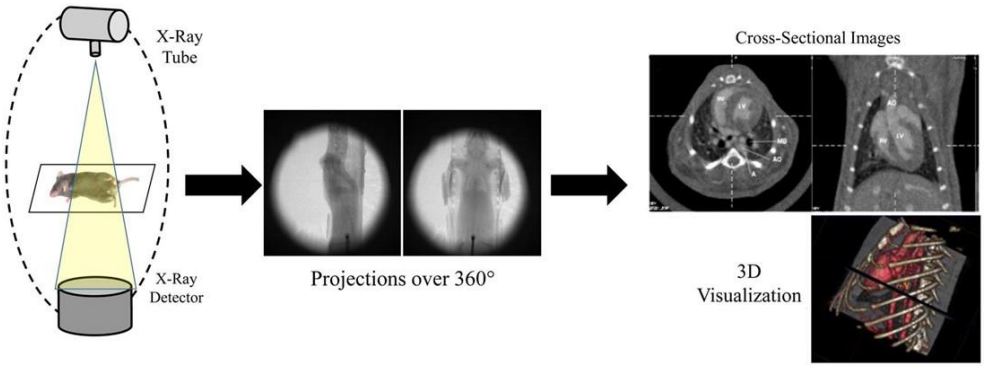

Figure 1.12. Schematic of a CT system. Multiple X-ray projections are acquired over a 360° rotation around the subject. These individual x-ray projections are then reconstructed to produce 2D cross-sectional images and 3D volumes. Figure taken from [113] with permission.

Therefore, CAs are often utilized to produce a reliable CT contrast. Different from MRI CAs, which indirectly enhance the contrast by accelerating the relaxation of water protons, the CT CAs can directly generate the contrast.[118] To date, two types of CT CAs have been clinically approved: barium sulfate suspensions (only for gastrointestinal tract imaging) and water-soluble aromatic iodinated CAs.[119] However, the iodinated CAs used in clinic have several limitations. Iodine has a relatively small atomic number (Z = 53) and low K-edge value (33.2 keV), resulting in less efficient attenuation of X-ray in CT scanning.[116] Therefore, to obtain images with good contrast, large doses (*e.g.*, hundreds of milligrams of iodine or more per kilogram of patient body weight) of iodinated CAs are needed, which may induce adverse effects (*e.g.*, nausea, and vomiting) in patients.[120] Moreover, these iodinated CAs are excreted through the kidney rapidly, allowing only short imaging times, which limits the long-term tracking activities (*e.g.*, tumor growth and metastasis).[120]

1.3.3.2 Ln^{3+}-Based NPs as CT Contrast Agents

Recently, several heavy metal elements, such as gold (Au), platinum (Pt), bismuth (Bi) and Ln have been investigated aiming as potential CT CAs.[121-126] Ln^{3+}-based NPs have been demonstrated as promising CT CAs, given their relatively high X-ray attenuation coefficients (*e.g.*, Gd: 3.1, Dy: 3.4, Yb: 3.9, Lu: 4.0 cm^2/g at 100 keV).[127] Combined with their unique optical and magnetic properties, Ln^{3+}-based NPs are excellent for multifunctional imaging probes (*vide infra*). The higher X-ray attenuation coefficient of these Ln-based NPs can confer higher efficacy than that of iodine-based CAs, thus, expected to provide an equivalent contrast at a lower dose compared to the iodine-based CAs. This reduced dose requirement is highly beneficial as it may reduce potential adverse effects in patients in clinical applications.[124]

Among all the Ln elements, Gd has been the most investigated because it can be used for both T_1-weighted MRI CAs and host matrix of Ln-NPs. The X-ray attenuation properties of different Gd-based NPs, with Gd as either the matrix (*e.g.*, Gd_2O_3, GdF_3, $NaGdF_4$)[121, 125, 126, 128] or the dopant[129, 130] have been well studied. Alternatively, Zhu *et al.* reported $NaLuF_4$ NPs as more efficient CT CA given that Lu has the highest atomic number among all Ln elements.[131]

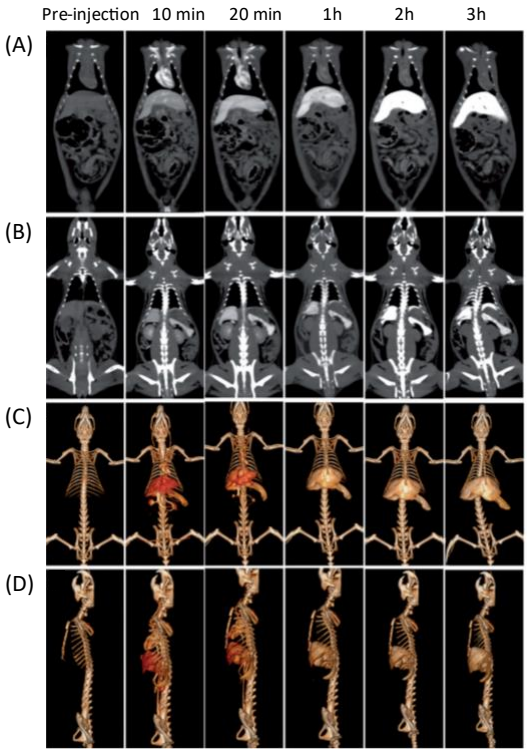

Figure 1.13. *In vivo* CT coronal view images of a rat after intravenous injection of 1 mL of Yb-NPs (70 mg Yb/mL) solution at timed intervals. (A) Heart and liver, (B) spleen and kidney. (C, D) Corresponding 3D renderings of *in vivo* CT images. Figures taken from [132] with permission.

The investigated $NaLuF_4$ NPs exhibited almost five-fold higher contrast enhancement than the commercial iodinated agent. Moreover, their long circulation time and low toxicity compared to commercial agents make them a highly promising CT agent. Besides Gd and Lu, Liu *et al.* reported the first Yb-based nanoparticulate CT CAs using Er^{3+}-doped $NaYbF_4$ NPs (Figure 1.13).[132]

These Yb-based NPs showed a higher CT contrast signal under the normal operating conditions of clinical CT scanners (120 kV), not only in comparison with a solution having the same concentration (g/mL) of iobitridol, but also with respect to heavy metals salts (Au, Pt, and Bi). The great advantage of Yb is its proper K-edge energy (61 keV), which locates just within the higher-energy region of the X-ray spectrum used in clinical CT (120 kV). This may indicate that Ln-based probes could be among the most effective CT *in vivo* CAs at 120 kV.

1.3.4 Ln^{3+}-Based NPs for Multimodal Bioimaging

It must be kept in mind that each diagnostic imaging technique, including optical imaging, MRI, and CT, has its own strengths and weaknesses as summarized in Table 1.1.[9] Optical imaging allows for the investigation of time-dependent biological phenomena with high spatial imaging resolution (100 – 300 nm) and sensitivity (pM – mM). Yet, one of its major drawbacks is the low penetration depth of light (UV-to-NIR) (up to 2 cm).[58] In contrast, MRI and CT imaging come with the advantage of providing physiological and anatomical information with unlimited penetration depth. However, their relatively low sensitivity remains a challenge.[60] Merging the advantages of each imaging technique on its own, multimodal approaches have been proposed. In this vein, multifunctional NPs exhibiting properties suitable for two or more imaging modalities bear great potential as bioprobes enabling multimodal imaging.[133-136] These multimodal imaging probes may provide more precise diagnosis and monitoring of disease progression through integrating several imaging modalities with different properties into one nanoparticle platform.[137]

Table 1.1. Pros and cons of imaging modalities described in this thesis.

Imaging Modality	Pros	Cons
Optical Imaging	high sensitivity fast acquisition time high spatial resolution	low penetration depth small field of view phototoxicity and photobleaching for organic dyes (UV excitation)
MRI	unlimited penetration depth high spatial resolution	low sensitivity long imaging acquisition time
CT	unlimited penetration depth high spatial resolution fast acquisition time	low sensitivity radiation risk

Probes combing optical and MRI imaging capabilities are the most reported, among which optical/T_1 imaging probes have been widely studied, by doping luminescent Ln^{3+} (*e.g.*, Er^{3+}, Tm^{3+}, Nd^{3+}, Ho^{3+}) ions into Gd^{3+}-based host matrix.[40, 135, 138, 139] However, there are only a few reports about multimodal probes that combine upconverting and T_2 imaging capabilities.[133, 134, 140, 141]

A main reason for the slow development of optical/T_2 probes based on Ln^{3+} ions may be the severe quenching effect of Dy^{3+} on the UC luminescence, thus, hampering the probe's optical performance.[142] One explanation for the Dy^{3+} quenching of Er^{3+} luminescence was previously proposed by Zhang *et al.*.[140] As shown in Figure **5.4**1.14, in close vicinity to Dy^{3+} ions, the $^2F_{5/2}$ excited state of Yb^{3+} and the $^2I_{11/2}$ excited state of Er^{3+} can be depopulated *via* resonant energy transfer to the excited $^6H_{5/2}$ level of Dy^{3+}. Dy^{3+} can receive energy from either the excited Yb^{3+} and Er^{3+}, or be directly excited by 980 nm photon, populating the $^6H_{5/2}$ excited state from the $^6H_{15/2}$ ground state. The life time of $^6H_{5/2}$ is short, and so back-energy transfer to Yb^{3+} is negligible.[143] The excited Dy^{3+} can either undergo radiative decay to the ground state or non-radiative decay to the $^6H_{9/2}$ level, of which the transition energy is transferred to the Er^{3+} for excitation from the ground level ($^4I_{15/2}$) to the first excitation level ($^4I_{13/2}$). This depopulation of the excited Yb^{3+} and intermediate Er^{3+} levels compromise efficient UC to the emitting Er^{3+} levels, ultimately resulted in loss of UC emission. However, this quenching process of Dy^{3+} was proposed based on monitoring the UC emission of Er^{3+} ions in Dy^{3+}/Gd^{3+}-based NPs, no further spectroscopic measurements were performed to confirm the mechanism.

In order to circumvent the UC poisoning effect of Dy^{3+} ions, some studies suggested to physically separate Dy^{3+} from the luminescent Ln^{3+} ions, *e.g.* Er^{3+} or Tm^{3+}.[133, 140-142, 144] For instance, Su *et al.* synthesized $NaGdF_4$:Yb^{3+},Er^{3+}/$NaDyF_4$ CS NPs and found that the UC emission intensity of Er^{3+} decreased upon shelling with $NaDyF_4$ because of the persistent quenching effect of the Dy^{3+} ions.[142] To overcome this issue, Biju *et al.* proposed a strategy based on a lower Dy^{3+} concentration in the shell by preparing $NaGdF_4$:Yb^{3+},Er^{3+}/$NaYbF_4$:Dy^{3+} NPs with 38 mol% Dy^{3+} doped into the shell. While UC emission could be partially restored, the emission intensity still dropped by 27 % compared to that of CS NPs with an undoped $NaGdF_4$ shell.[141] Moreover, reducing the amount of Dy^{3+} ions might not be advantageous when aiming for additional T_2 imaging capabilities.

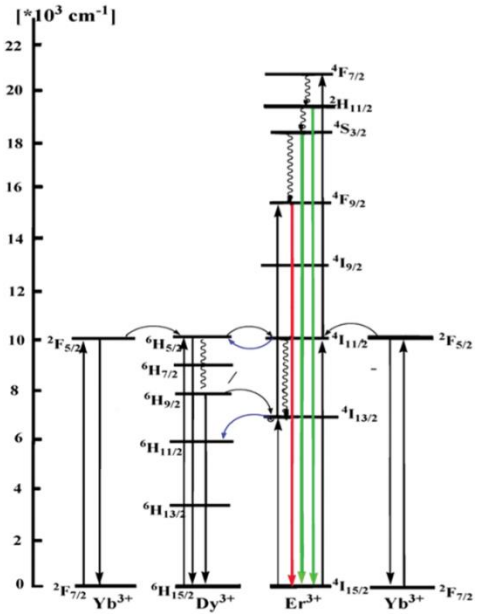

Figure 1.14. Proposed energy transfer processes for the quenching of UC emission caused by Dy^{3+} ions. Vertical and wavy arrows represent non-radiative transitions, curved arrows represent non-radiative energy transfer, green and red arrows represent green and red emissions. Figure taken from [140] with permission.

The introduction of an intermediate CaF_2 shell as a separating barrier between Dy^{3+} and the emitting Ln^{3+} ions was reported by Li *et al.*. A 2.3 nm thick inert shell between the upconverting Tm^{3+} ions in the core and the Dy^{3+} ions in the outer shell ($NaYbF_4$:Tm^{3+}/CaF_2/$NaDyF_4$ CSS architecture) allowed for UC emission intensities of Tm^{3+} as high as those from $NaYbF_4$:Tm^{3+}/CaF_2 CS NPs, although even higher emission intensities were expected from CSS NPs.[133]

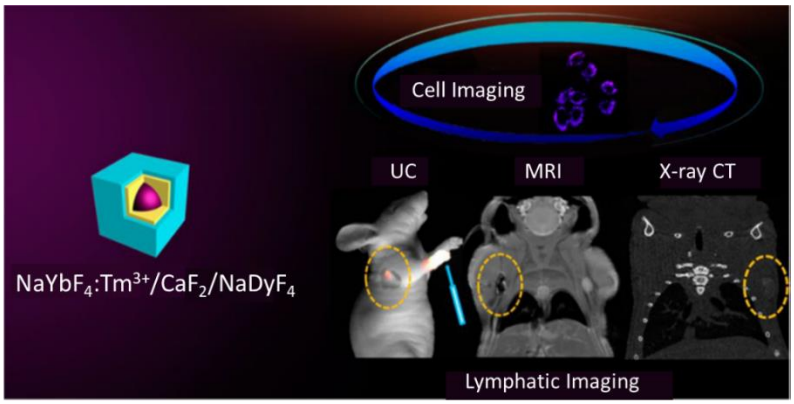

Figure 1.15. $NaYbF_4$:Tm^{3+}/CaF_2/$NaDyF_4$ CSS NPs used as multimodal UC/T_2-weighted MRI/CT imaging probes for lymphatic imaging. Figure taken from [133] with permission.

Despite the relatively small r_2 relaxivity and CT values, these CSS NPs were tested as potential *in vivo* optical/T_2/CT probes (Figure 1.15). This and related work demonstrated the high promise of the CSS architecture design as a strategy towards optical/T_2/CT probes based on upconverting Ln^{3+} and Dy^{3+} ions.[134] In order to better understand the mechanism of the Dy^{3+} quenching effect and optimize the imaging capabilities, a series of Dy^{3+}-based CSS NPs as multimodal imaging probes with superior UC, T_2, and CT imaging capabilities were introduced in this thesis (Chapter 5).

1.4 Synthesis of $NaREF_4$ Nanoparticles

1.4.1 Particle Formation: Growth Mechanism

Prior to introducing the synthesis of $NaREF_4$ NPs, it is important to understand the formation mechanism of nanoparticles, which can provide insights into controlling their size and morphology.[145, 146] Based on LaMer theory, there are two main processes, namely nucleation and particle growth, that must be considered (Figure 1.166).[147] The formation process primarily proceeds through three different stages.

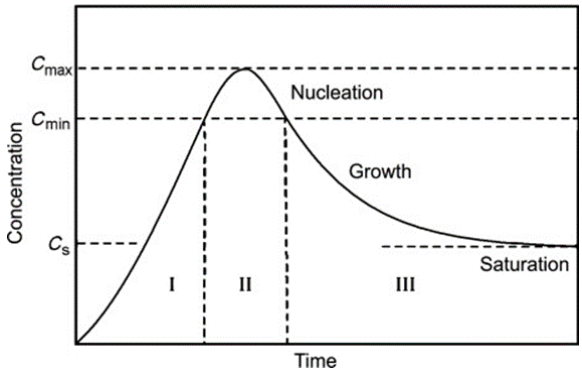

Figure 1.16. LaMer diagram: visualization of the three, timely separated growth and nucleation stages during a particle synthesis (I, II and III). C_s represents the saturation concentration of monomers in the reaction solution. C_{min} and C_{max} indicate the bottom limit (minimum) and the top limit (maximum) concentrations, respectively, that determine the range of supersaturation of the monomers. Figure taken from [148] with permission.

At stage I, the monomer concentration increases continually until it exceeds the saturation level of the solution (C_s). It should be noted that the nucleation of particles does not yet occur at this stage, even if the monomer concentration is above the saturated concentration.[148, 149] At stage II, as the monomer concentration further rises, supersaturation takes place when the monomer concentration surpasses the critical minimum concentration (C_{min}). During this phase, uniform formation of crystalline nuclei starts, and more monomers may also attach to already formed nuclei. This results in a quick drop of the monomer concentration in solution down to a level at which nucleation stops. Subsequently, the system goes to the growth stage (stage III) without any further nucleation processes taking place.

At this stage III, the existing nuclei form nanocrystals and will grow larger until the monomer concentration drops below C_s.[147, 150] From this point on, detachment of monomer from the particles and adsorption of monomer from the solution are in dissolution-recrystallization equilibrium, and no further growth occurs. To obtain uniform NPs, the nucleation stage and the growth stage must be separated distinctly. Otherwise, if the nucleation process continues throughout the synthesis, the growth process of the NPs will vary largely from one to another, thus resulting in NPs with broad size distribution.[147, 149]

1.4.2 Microwave-Assisted Synthesis of $NaREF_4$ Particles

This section was taken from the published work: Handbook on the Physics and Chemistry of Rare Earths, Elsevier, 2024, ISSN 0168-1273. Christian Homann, Nan Liu, Helliomar Barbosa and Eva Hemmer.

A well-known method to synthesize $NaREF_4$ NPs is the thermal decomposition approach,[22, 151] inspired by the synthesis of quantum dots discovered by M. G. Bawendi.[152] This approach involves the oxygen-free decomposition of organometallic precursors at high temperature.[153] RE^{3+}-based trifluoroacetates (RE-TFA) are commonly used as the organometallic precursors, while octadecene (ODE), oleic acid, and oleylamine (OAm) are employed as the high-boiling-point solvents. Oleic acid and OAm with polar groups can selectively adsorb to specific facets of the NPs. Therefore, they are usually used as capping reagents to control the size and shape of the

formed NPs. The thermal decomposition method allows for some control of the crystalline phase of the NPs (within specific size regions) and has been demonstrated as highly suitable for the synthesis of CS architectures.[38, 154] However, the preparation of $NaREF_4$ NPs – with high batch-to-batch and lab-to-lab reproducibility – is still a challenge.

Over the past two decades, the use of microwave (MW) energy to heat chemical reactions has gained considerable attention, due to its successful applications in organic synthesis, polymer chemistry, material science, and biochemical processes.[155-157] More recently, the MW-assisted approach has attracted attention for the preparation of Ln^{3+}-based nanomaterials as the advantages of MW-induced heating over conventional (conductive) heating methods were recognized. These include the significantly shorter reaction duration, uniform heating with limited thermal gradients, and high reproducibility.[157, 158] With the benefit of highly precise synthesis control, new approaches in material design, such as well-defined shells became accessible, allowing to create small and core/multi-shell NPs.[39, 159]

The heating mechanism of microwave radiation involves two main processes, namely dipolar polarization and ionic conduction (Figure 1.17).[160] In the event of dipole polarization, the oscillation of the microwave causes a realignment of the dipoles, which makes the polar molecule move. In turn, there is molecular friction and dielectric loss, which generates heat. By continuously irradiating the solution, enough energy to heat the solution is produced (Figure 1.17 A). Ionic conduction works similarly, but the charged molecule or ion can follow the microwave's oscillation more quickly than a polar molecule and is, thus, releasing more heat (Figure 1.17 B).

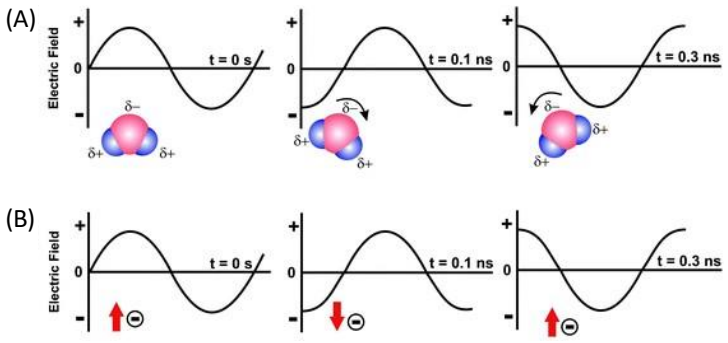

Figure 1.17. Two main heating mechanisms under microwave irradiation: (A) dipolar polarization; (B) ionic conduction mechanism. Figure taken from [160] with permission.

For the MW-assisted synthesis, reactions are typically carried out in tightly sealed, closed vessels, allowing reaction mixtures to be heated very rapidly to temperatures close to or above the boiling point of the solvent. Maximum temperatures of *ca.* 300 °C and pressure as high as 30 bar can be obtained with modern MW reactors.[161] Furthermore, efficient gas-jet cooling at the end of the heating cycle can be used to decrease temperatures to ambient conditions within a few minutes (thermal quenching).[162, 163] As introduced in the previous sections, crystalline phase and morphology control are key to optimize the particles' optical and magnetic properties. Over the past decade, special focus has been set on the selective synthesis of α- *versus* β-$NaREF_4$. As a synthesis method that is still in its infancy with respect to $NaREF_4$, recent achievements in MW-assisted approaches are mainly based on knowledge gained from thermal decomposition. This includes precursor and solvent choices. Yet, it must be mentioned that a simple transfer of protocols and reaction conditions from these established routes to a MW process is most often not possible. Rather, meticulous fine-tuning of reaction parameters is needed to synthesize the sought-after materials.

1.4.2.1 Microwave-Assisted Synthesis of $NaYF_4$

$NaYF_4$, as one of the most efficient host materials for upconversion, was the first material among alkali metal RE tetrafluorides that has been successfully synthesized using the MW-assisted approach.[163-166] One of the earliest reports was published in 2009 by Wang *et al.*.[163] Herein, metal-trifluoroacetate (M-TFA) precursors were used as starting materials dissolved in high-boiling point solvents oleic acid and ODE.[163] The subsequent synthesis of oleate-capped α-$NaYF_4$ NPs doped with Yb^{3+} and Er^{3+} (or Tm^{3+}) was achieved in a sealed vessel heated at 290 °C for only 5 min. This constituted a significant shortening in reaction time compared to other methods, such as conventional thermal decomposition and hydrothermal methods, which typically require hours to days. The resultant NPs were highly monodisperse with an average particle size of 10 nm (Figure 1.188 (A-1)) and exhibited the characteristic narrow UC bands of Er^{3+} (540 nm and 670 nm) and Tm^{3+} (800 nm) under 980 nm excitation.

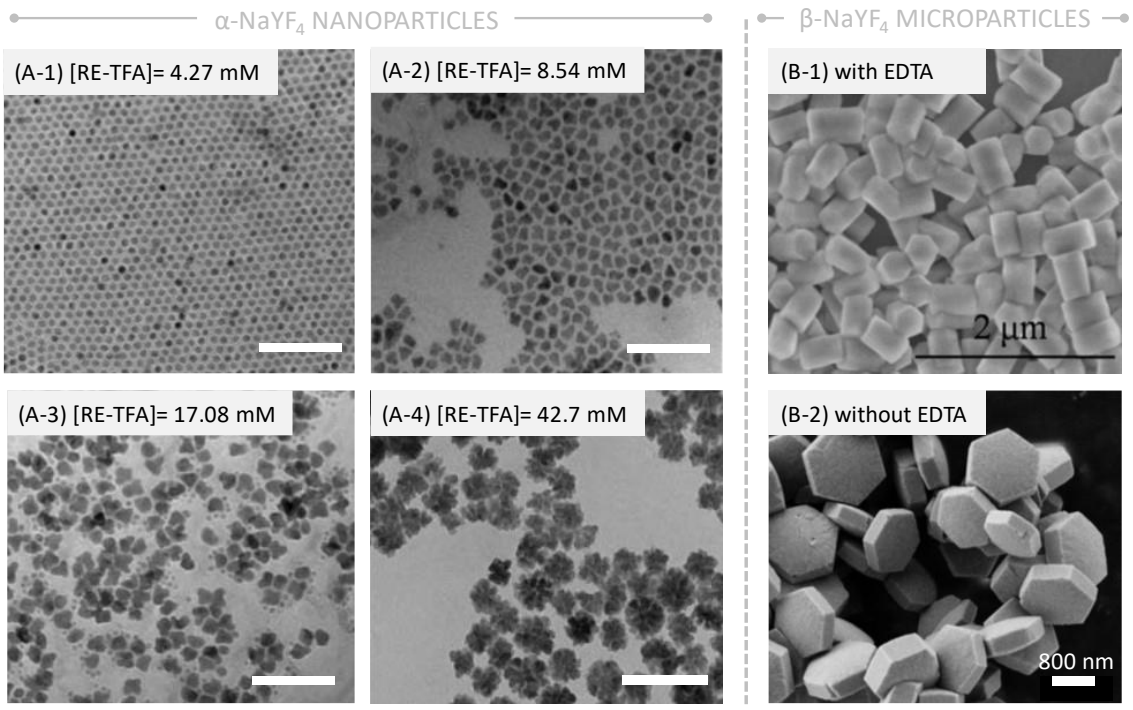

Figure 1.18. (A) TEM images of α-$NaYF_4$:Yb^{3+},Er^{3+} NPs prepared using a MW-assisted thermal decomposition approach with different RE-TFA precursor concentrations.163, 167 Scale bars: 100 nm. (B) SEM images of β-$NaYF_4$:Er^{3+},Yb^{3+} microparticles synthesized with a MW-assisted hydrothermal method with or without EDTA as an additive.165, 168 Figures adapted from [163, 165, 167, 168], with permission.

Importantly, Wang *et al.* further extended their work by investigating the effect of reaction parameters, such as reaction time and reactant concentrations on NP size and shape.[167] They observed an increase in particle size from 6 to 13 nm when the reaction time prolonged from 10 to 70 min, respectively. This early study is a good example showcasing the small NP size typical for MW-assisted approaches.

In contrast to size, no significant change in morphology was observed. All the obtained NPs were of spherical shape, irrespective of the reaction time. Conversely, the precursor concentration provided a more significant effect on both NP size and shape. At higher precursor concentrations, the NPs grew significantly, reaching sizes of 20 – 60 nm depending on the concentrations used Figure 1.188 (A-2) to (A-4). Furthermore, the morphology evolved to become flower-like when using extremely high precursor concentrations (20 times higher than those that yield sub-15 nm sized NPs), while the polydispersity also increased, including bimodal distributions. This seminal

work provides important insights into the interplay between reaction parameters and the resultant $NaREF_4$ size and morphology. Yet, it must be noted that these early MW-assisted protocols suffered from lack of tunability of the crystalline phase, *i.e.*, the phase-selective synthesis of hexagonal *versus* cubic $NaREF_4$, and only the synthesis of cubic $NaREF_4$ NPs was reported. Nonetheless, they act as an important stepping stone towards the establishment of protocols for the MW-assisted synthesis of similar materials of controlled phase, size, and morphology (*vide infra*).

In the quest for β-$NaYF_4$ NPs, researchers sought after alternative approaches and established a MW-assisted hydrothermal method using water as a solvent.[165] While the anticipated phase could be achieved, this strategy led to micron-sized β-$NaYF_4$ particles. For instance, Tong *et al.* synthesized β-$NaYF_4$:Yb^{3+},Er^{3+} microparticles, using rare-earth chlorides ($RECl_3$) and NaF as precursors (Figure 1.188 B).[165, 168] The resulting particles showed microrod shape when EDTA was used as an additive, while microplates were obtained without the addition of EDTA. The parallels to the conventional hydrothermal synthesis (*i.e.*, using an autoclave and conventional heating) of β-$NaREF_4$ in terms of morphological evolution are striking, though, might be expected given the similar reaction chemistry.[169] Interestingly though, the particle formation at 180 °C was completed within 30 min, opposed to 12 h in the conventional hydrothermal approach.[169, 170] Despite the successful MW-assisted synthesis of β-$NaYF_4$ *micro*particles, it is important to mention that up to date, there is no report on *nano*scale β-$NaYF_4$:Ln^{3+} via the MW-assisted approach. One difficulty in obtaining β-phase $NaYF_4$ NPs is possibly related to the high energy required for the α → β phase transformation.[151] Working with conventional thermal decomposition method, Mai *et al.* demonstrated that such phase transformation requires high temperatures of up to 330 °C, high Na^+-to-RE^{3+} ion ratios, and longer reaction times.[151] Despite the phase control of nanosized $NaYF_4$ particles by MW-assisted routes is still challenging, it could be achieved for $NaGdF_4$ NPs in our lab during my master's thesis. This phase control of $NaGdF_4$ NPs using the MW-assisted approach is discussed next.

1.4.2.2 Crystalline Phase Control of $NaREF_4$

$NaGdF_4$ constitutes an alternative, widely investigated host material for optically active Ln^{3+} ions, and efforts were undertaken to achieve its MW-assisted synthesis. Interestingly, $NaGdF_4$ is the first representative of the $NaREF_4$ family for which the controlled synthesis of β- over α-$NaGdF_4$ was achieved.[89] Yet, the beginnings of the MW-assisted synthesis of $NaGdF_4$ take us back to the year 2014, when Quintanilla *et al.* first reported the synthesis of ultrasmall α-$NaGdF_4$:Ln^{3+} (Ln = Yb, Er and Tm) NPs.[39] Following the seminal work on α-$NaYF_4$ NPs by Wang *et al.*,[163] similar M-TFA precursors were used, while OAm was added to the oleic acid/ODE solvent mixture. Inspired by the work of Quintanilla *et al.*, our group investigated and optimized the process parameters and precursor chemistry towards the first synthesis of β-$NaGdF_4$ NPs. Herein, the Na^+-to-Gd^{3+} ion ratio was identified as key parameter for the phase-selective synthesis of β- over α-$NaGdF_4$ NPs.[89] Sub-10 nm sized β-$NaGdF_4$ NPs were obtained when the Na^+-to-Gd^{3+} ratio was 2:1, while a 1:1 ratio resulted in the α-phase (Figure 1.19 (A-1)).

Irrespective of the sought-after crystalline phase, for NPs of homogenous size and morphology, it was deemed crucial to separate the nucleation and growth steps, as for the conventional thermal decomposition process. This was attained through a specific temperature profile used during the reaction, *i.e.*, heating up to 300 °C for 1 s to trigger nucleation, followed by particle growth at lower temperature (*e.g.*, 230 °C) for 10 min. While β-$NaGdF_4$ NPs of monodisperse and narrow size distributions were successfully obtained, doping with Ln^{3+} ions to endow the NPs with UC and NIR emitting properties, inevitably resulted in the formation of α-$NaREF_4$ or a phase mixture. Thus, additional adjustments to the synthesis protocol were deemed necessary to synthesize β-$NaGdF_4$ NPs doped with high amounts of heavier Ln^{3+} dopant ions, *e.g.*, Yb^{3+}. Further variation of the Na^+-to-RE^{3+} ion ratio and stringent adjustment of the precursor concentration were identified as key parameters for the phase-selective synthesis of β- over α- $NaGdF_4$:Ln^{3+} NPs. More specifically, when using RE-TFA and Na-TFA as precursors, a 3:1 Na^+-to-RE^{3+} ratio and a RE-TFA precursor concentration of 0.625 mmol (opposed to 0.125 mmol in case of undoped β-$NaGF_4$ or Ln^{3+}-doped α-$NaGdF_4$) led to sub-10 nm, phase-pure β-$NaGdF_4$:Yb^{3+}(20%),Er^{3+}(2%) NPs (Figure 1.199 (A-2) and (A-3)). Detailed reaction conditions are given in Chapter 3.

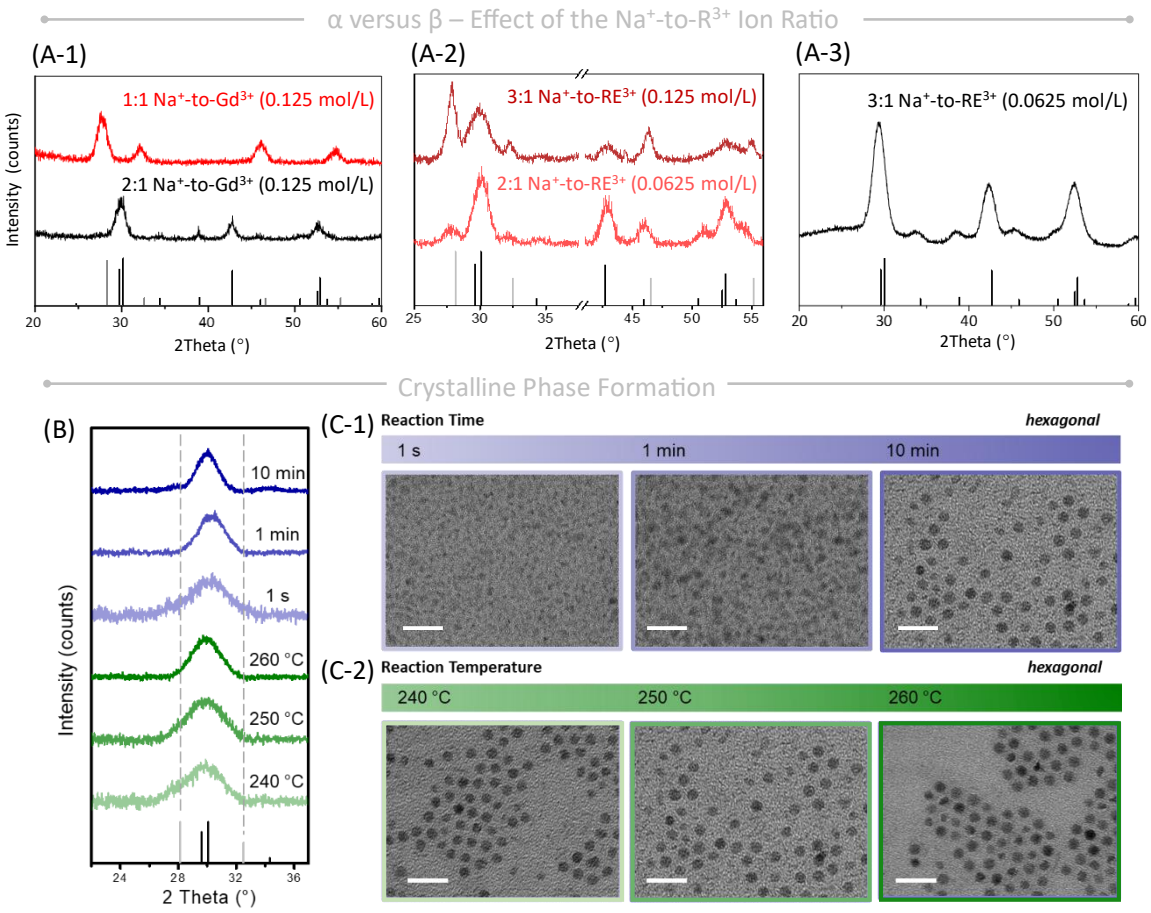

Figure 1.19. Crystalline phase control and phase formation mechanism of $NaREF_4$ NPs by MW-assisted synthesis. (A) Effect of the Na^+-to-RE^{3+} ion ratio and precursor concentration on phase formation. (1) XRD patterns revealed the obtained $NaGdF_4$ NPs were in α- or β-phase when the Na^+-to-Gd^{3+} ratio was 1:1 or 2:1 respectively, (precursor concentration: 0.125 mol/L). (2) NPs exhibiting a phase mixture were obtained for improper precursor concentration and Na^+-to-RE^{3+} ratio. (3) Pure β-phased NPs obtained when the Na^+-to-Gd^{3+} ratio was 3:1 at 0.625 mol/L precursor concentration. XRD patterns (B) and TEM images (C) of $NaRF_4$ NPs synthesized at different reaction time (C-1) and reaction temperature (C-2). XRD references: α-$NaGdF_4$ (PDF#: 00-027-0697, light grey lines), β-$NaGdF_4$ (PDF#: 01-080-8787, black lines).

Phase formation. In-depth investigations of $NaREF_4$ formation by thermal decomposition led to today's understanding that the β-phase is formed through a α → β phase transformation process, whereas phase-pure α-$NaREF_4$ NPs can be isolated if stopping the reaction at an early stage.[31] Given the significantly faster reaction times under MW-irradiation, such isolation of the α-phase was found difficult. In fact, XRD results indicated that the β-phase was formed from 1 s onwards at a targeted temperature of 250 °C (Figure 1.199 B).[159] As the reaction evolves, the crystallinity

of the NPs increased, along with particle growth from *ca.* 3 nm to 6 nm after 10 min (Figure 1.199 (C-1)). No significant change in crystalline phase, morphology or particle size was observed when lowering or increasing the reaction temperature 240 and 260 °C, respectively (Figure 1.199 (C-2)). These results suggested that, in the MW-assisted approach, the NPs likely crystallized in their hexagonal phase from the beginning and did not undergo any detectable α → β phase transformation.

1.4.2.3 Effect of Precursor Chemistry on Particle Size

While most studies on the MW-assisted synthesis of $NaREF_4$ NPs report the use of RE-TFAs as RE^{3+} ion source, RE-oleate (RE-OA) and RE-acetate (RE-OAc) are suitable alternative precursors, overall leading to smaller sized $NaREF_4$ NPs. For example, β-$NaGdF_4$:Yb^{3+},Er^{3+} NPs were 3 nm in size when RE-OA or RE-OAc were used as RE^{3+} source, with Na-OA or Na-OAc and NH_4F as Na^+ and F^- sources, compared to 6 nm for RE- and Na-TFA precursors.[159] The precursor-dependent size evolution was ascribed to the differences in the thermal stability of the precursors. TGA analysis unveiled that RE-TFA decomposed at lower temperature compared to RE-OA and RE-OAc, providing more material for the particle growth, resulting in larger particles. In another study, Amouroux *et al.* reported the MW-assisted decomposition of RE-OA into ultra-small heavily Yb^{3+}-doped NPs, namely β-$NaGdF_4$:Yb(53%),Tm NPs.[171] The authors conducted a comparison of the particle sizes obtained through conventional heating and MW-irradiation, observing a decrease in particle size from 10 nm to *ca.* 4 nm when changing the heating method from a heating mantle to a MW-reactor. The smaller size was ascribed to the faster heating rate induced by MW irradiation compared to convection heating by a mantle.

Although several efforts have been made to investigate the MW-assisted synthesis of $NaREF_4$ particles, as one of the newest methods, MW-assisted strategies are less explored than other methods, and challenges remain. For instance, the currently reported work for the synthesis of $NaREF_4$ mainly focuses on $NaYF_4$ and $NaGdF_4$ materials. Hence, a systematic investigation of the synthesis of other $NaREF_4$ (RE ≠ Y, Gd) NPs and the evaluation of their phase accessibility were topic of this thesis and are discussed in Chapter 4.

1.4.2.4 $NaREF_4$ Core/Multi-Shell NPs

Quintanilla *et al.* demonstrated for the first time that the MW-based approach was also suitable for the synthesis of core/multi-shell NPs (Figure 1.2020 A).[39] Despite the very thin shell thickness of only 0.5 – 1 nm, the overall shell growth was fast (*ca.* 10 min) compared to the conventional thermal decomposition (*ca.* 1 h), and the in-depth assessment of the UC behaviour of the Tm^{3+}- and Er^{3+} ions confirmed the existence of all Ln^{3+} ions in the NPs. Subsequently, our group reported that the solvent choice also played an important role for efficient shell growth.[159] While the presence of OAm as co-solvent in the reaction mixture was found necessary to guarantee monodisperse and homogeneous spherical core RE-NPs, OAm had to be omitted in the shelling step.[159] In the absence of OAm, shell growth around β-$NaREF_4$ core NPs was sufficiently efficient to protect the Ln^{3+} emitters in the core from surface quenching. Increasing the reaction time for shell growth from 10 to 30 min led to the increase in shell thickness from 2.5 to 4.1 nm (Figure 1.2020 B), ultimately resulting in small yet bright UCNPs.[159]

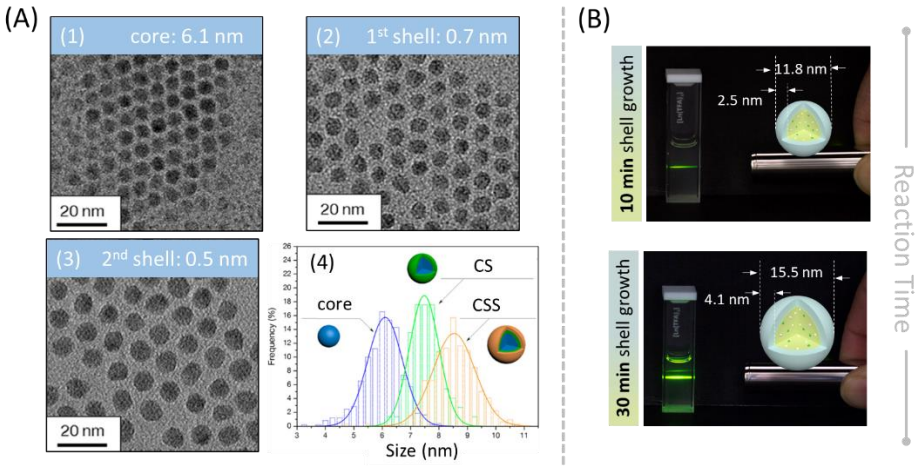

Figure 1.20. Strategies to $NaREF_4$ core/shell NPs by MW-assisted synthesis. (A) TEM images of core (1), CS (2), CSS NPs (3), and their corresponding size distributions (4) when OAm was used as co-solvent in the reaction mixture. (B) Effect of reaction time. Photographs of $NaREF_4$ CS NPs dispersed in toluene under excitation with a 980 nm 50 mW laser pointer. Brighter green upconversion emission was observed with thicker undoped shell (4.1 nm) yielding from 30 min shell growth compared to 10 min (2.5 nm shell thickness). Figure (A) adapted from [39], figure (B) adapted from [159] with permission.

Gaining the knowledge to grow a thicker shell for CS NPs was promising, yet achieving a tunable shell thickness for CSS NPs remained a challenge, which limited the multifunctional design of $NaREF_4$ NPs. In this thesis, we further optimized the MW-assisted approach to control the shell thickness of CSS NPs and explored their potential bioimaging applications (Chapter 5).

1.5 Surface Modification of Ln^{3+}-based NPs

Due to the hydrophobic nature of the capping ligands used such as OA and OAm during the synthesis, the obtained Ln^{3+}-based NPs with hydrophobic surfaces limit their biomedical applications in diverse fields such as drug delivery, biodetection and bioimaging where hydrophilicity is a prerequisite.[172] Therefore, various modification strategies have been developed, including ligand removal, ligand exchange, ligand attraction, ligand oxidation, layer-by-layer assembly, and surface silanization (Figure 1.2121) as summarized in several review papers.[21, 173-176] Hence, this section provides only a brief introduction to the ligand removal and ligand exchange methods used in this thesis.

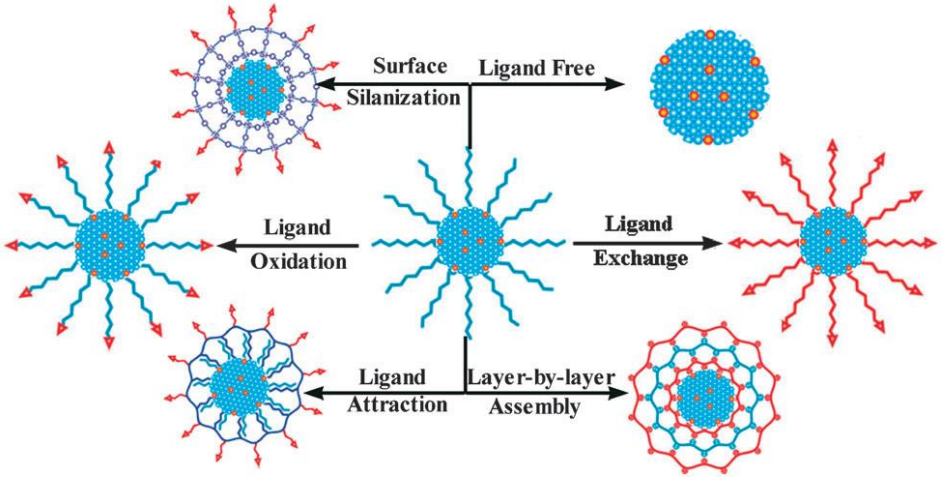

Figure 1.21. Typical surface modification strategies used for making hydrophilic Ln^{3+}-doped NPs with pendant functional groups. Figure taken from [176] with permission.

1.5.1 Ligand Removal

Removal of the organic ligands coordinated on the surface of the NPs is a simple way to disperse Ln-NPs into aqueous phase (also called ligand-free (LF) NPs).[177, 178] Ligand-free Ln-NPs can be obtained by treating the as-prepared hydrophobic NPs with strong acids.[177] At low pH, the oleate ligands (and OAm, depending on the chosen synthesis route) are re-protonated and thus detach from the NP surface.

Capobianco and coworkers first reported ligand removal of OA-capped $NaGdF_4$:Yb^{3+},Er^{3+} NPs with HCl solution.[177] When dispersing the NPs in the HCl solution (pH = 4) with the assistance of sonication, the carboxylate groups of the oleate ligand were gradually protonated to yield oleic acid, resulting in the release from the NP surface. The authors demonstrated that the obtained ligand-free NPs maintained the same size and shape as the OA-capped NPs. This approach not only achieves water-dispersible NPs, but also offers great flexibility with respect to subsequent application-specific surface modification and functionalization. The resulting abundant metal ions on the surface of the particles exhibit strong coordination capabilities. As a result, positively charged NPs allow for further surface conjugation with negatively charged functional groups, such as −COOH, $-NH_2$, −OH, by electrostatic interactions in aqueous solution for further biological applications.[179-181] However, pH values as low as 1 have also been reported for various β-phase $MREF_4$ NPs with sizes in the 10 to 30 nm range.[181-184] Subjected to such relatively harsh conditions, the chemical stability of the $NaREF_4$ might be at risk. A systematic investigation of the chemical stability of $NaREF_4$ NPs after acidic treatment (pH below 3) is discussed in Chapter 4.

1.5.2 Ligand Exchange

Ligand exchange is currently one of the most popular methods to modify the surface of hydrophobic NPs without affecting their shapes, compositions, and morphologies.[185] In a typical ligand exchange procedure, the original hydrophobic capping ligand such as OA and OAm anchored on the NP surface can be replaced with new hydrophilic ligands exhibiting stronger coordination abilities. Such hydrophilic ligands possess one functional group capable of binding

to the NP surface and another hydrophilic functional group at the other end so that the NPs can be well dispersed in water or can be further functionalized.[186] The hydrophilic ligands usually used in ligand exchange process include citrate,[174] polyethylene glycol (PEG) derivatives,[187] poly(acrylic acid) (PAA) derivatives,[188] and phosphate derivatives[189].

Chapter 2. Objectives

As highlighted in the Introduction, the development of MW-assisted approaches led to promising achievements for the synthesis of small Ln^{3+}-doped $NaREF_4$ (RE = Y and Gd) NPs within significantly shorter reaction times and at high reproducibility. Yet, when the research in the frame of this thesis kicked off, the MW-assisted synthesis lacked diversity in materials selection and architectural design compared to the much more established thermal decomposition approaches. Therefore, the objectives of this thesis were to expand the MW-assisted synthesis protocols towards other host materials ($NaREF_4$ and $NaMnF_3$) and CS architectures, and to investigate their potential applications. The specific objectives of this thesis were as follows:

1. **MW-assisted synthesis beyond Ln^{3+}-doped $NaGdF_4$?** – Synthesis of $NaREF_4$ (RE $\neq$ Gd) NPs to evaluate the accessibility of different crystalline phases (α *versus* β) as a function of RE ion choice (Chapter 4), followed by the optimization of the MW-assisted strategy to control the shell thickness of core/multi-shell NPs (Chapter 5) and the exploration of the MW-assisted approach for the synthesis of $NaMnF_3$ particles (Chapter 6).
2. **Is $NaREF_4$ really chemically stable?** – Assessment of the chemical stability of $NaREF_4$ NPs under the acidic treatment (pH at 1.5) required to render them water dispersible (Chapter 4).
3. **How can the properties of the $NaREF_4$ NPs be controlled?** Potential application of the core/multi-shell NPs for multimodal imaging, taking advantage of property control through architectural design (Chapter 5).
4. **Next steps** – Design of core/multi-shell NPs using the MW-assisted approach to investigate their thermometric properties in the NIR-III spectral range (Chapter 7).

Chapter 3. Experimental Details and Characterization Techniques

3.1 Chemicals

All reagents were used as received without any further purification. Yttrium oxide (Y_2O_3, 99.999%), praseodymium oxide (Pr_2O_3, 99.9%), neodymium oxide (Nd_2O_3, 99.999%), samarium oxide (Sm_2O_3, 99.9%), europium oxide (Eu_2O_3, 99.996%), gadolinium oxide (Gd_2O_3, 99.999%), holmium oxide (Ho_2O_3, 99.995%), erbium oxide (Er_2O_3, 99.99%), ytterbium oxide (Yb_2O_3, 99.9%) and lutetium oxide (Lu_2O_3, 99.995%) were purchased from Alfa Aesar. Terbium oxide (Tb_2O_3, 99.99%), dysprosium oxide (Dy_2O_3, 99.9%) and manganese oxide (MnO, 99.99%) were purchased from Sigma Aldrich. Trifluoroacetic acid (CF_3COOH, TFA, 98%), sodium trifluoroacetate (CF_3COONa, Na-TFA, 98%), potassium trifluoroacetate (CF_3COOK, K-TFA, 98%), oleic acid ($CH_3(CH_2)_7CH=CH(CH_2)_7COOH$, 90%), oleylamine ($CH_3(CH_2)_7CH=CH(CH_2)_7CH_2NH_2$, OAm, 70%) and 1-octadecene ($CH_3(CH_2)_{15}CH=CH_2$, ODE, 90%) were purchased from Sigma Aldrich. Sodium citrate dihydrate ($C_6H_9Na_3O_9$, 99%) and poly(acrylic acid) (PAA, #323667) were purchased from Sigma Aldrich. Trypsin and ethidium homodimer-1 were purchased from Sigma Aldrich. Ethanol (99%) was purchased from Commercial Alcohols. Acetone, dimethyl sulfoxide (DMSO), and hexane (analytical grade) were purchased from Fischer Chemicals. Toluene (99.8%), phenol, nitric acid (HNO_3), hydrochloric acid (HCl, 36.5 %), and phosphate-buffered saline (PBS) were purchased from Fisher Scientific.

3.2 Microwave-Assisted Synthesis of $NaREF_4$ NPs

3.2.1 Synthesis of Rare Earth Trifluoroacetate Precursor

The synthesis of the $NaREF_4$ NPs was performed using a MW-assisted approach as previously reported by our group.[89, 159] The optimized synthesis parameters for the core-only NPs were applied in this thesis without further variation. In this synthesis method, rare earth trifluoroacetate, $RE(TFA)_3$, (RE = Y, Pr, Nd, Sm, Eu, Gd, Tb, Dy, Ho, Er, Yb, Lu), were used as precursors. $RE(TFA)_3$ precursors were prepared by mixing a certain amount of RE_2O_3 (0.625 mmol for α-NPs, 0.3125 mmol for β-NPs) with 10 mL of a 1:1 TFA-to-H_2O mixture in a 50 mL round bottom flask. The slurry was refluxed at 95 °C until it became clear. The solvent was evaporated by drying the product overnight at 60 °C in an open atmosphere. The powder $RE(TFA)_3$ was obtained with no further purification (equation 3.1).

$$RE_2O_3 + 6\ CF_3COOH \xrightarrow[95\ °C,\ reflux]{H_2O} 2\ RE(OOCCF_3)_3 + 3\ H_2O \qquad \textbf{(Eq. 3.1)}$$

3.2.2 Synthesis of α/β-$NaREF_4$ Core NPs

$$RE(OOCCF_3)_3 + Na(OOCCF_3) \xrightarrow[\substack{1\text{-octadecene}\\ \text{oleic acid, oleylamine}}]{T_a\text{: 1 s; } T_b\text{: 10 min}} NaREF_4 + CO_2 + CO + (CF_3CO)_2O \qquad \textbf{(Eq. 3.2)}$$

The scheme of the synthesis of $NaREF_4$ core NPs is shown in Figure 3.1 A. Na-TFA was first added to the flask containing the $RE(TFA)_3$ precursor (equation 3.2).[190] Detailed $RE(TFA)_3$ and Na-TFA precursor amounts as well as RE^{3+}-to-Na^+ ratios used to phase-selectively synthesize each $NaREF_4$ NP composition are given in Table 3.1. Irrespective of the choice of RE ions or crystalline phase of the $NaREF_4$ NPs, 10 mL of high-boiling point solvents ODE, OAm, and oleic acid in a ratio of 2:1:1 were added to the $RE(TFA)_3$ and Na-TFA precursor mixture, and the solution was degassed under vacuum at 120 °C for 30 min to remove oxygen and residual water/TFA.

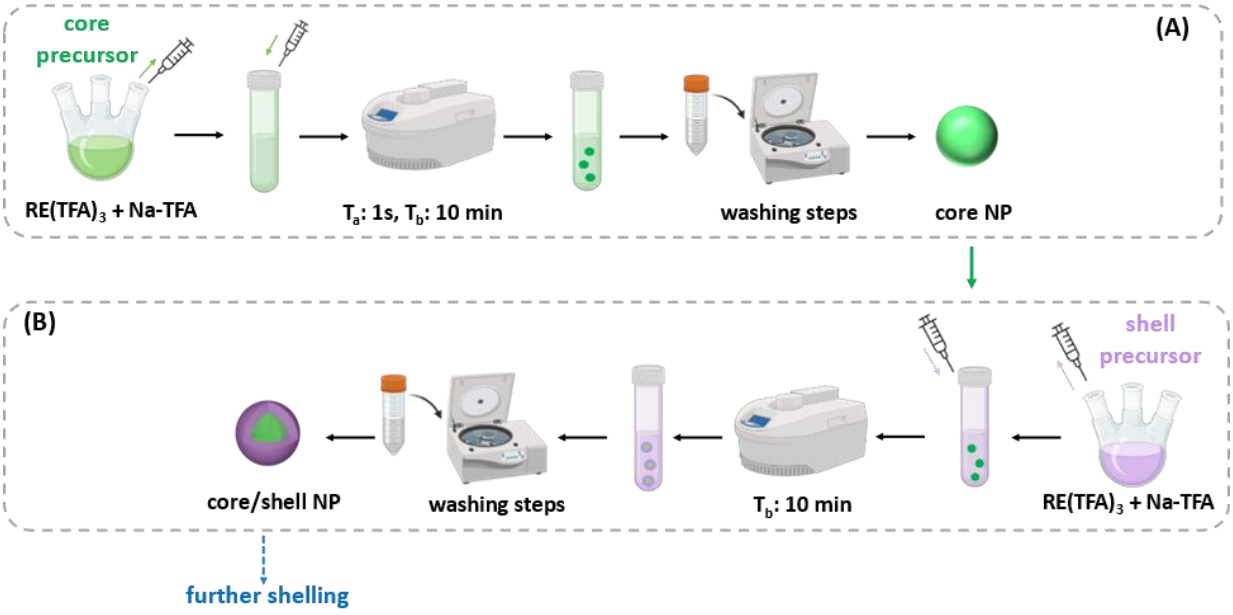

Figure 3.1. Schematic representation of the synthesis of $NaREF_4$ (A) core and (B) core/shell NPs. This figure was made in BioRender (www.biorender.com).

Subsequently, 10 mL of the degassed precursor solution were transferred to a 35 mL MW glass vessel, purged with N_2 and tightly sealed. The vessel was inserted into a CEM Discovery SP microwave reactor, and the $NaREF_4$ NPs were grown under constant stirring. The temperature profiles used for the NP synthesis are given in Table 3.1. Following the synthesis, the reaction mixture was washed with a 1:3 hexane-to-ethanol mixture and centrifuged at 6595 RCF for 20 min. The product was then washed with a 1:3 toluene-to-acetone mixture and centrifuged using the same conditions reported above. After purification, the NPs were dispersed and stored in 5 mL of toluene for further use. For the synthesis of β-NPs, solid NaF as a potential by-product can be removed by redispersing the NPs in 5 mL of ethanol prior to the addition of 5 mL of water, followed by precipitation via centrifugation. Obtained NPs were washed one more time with 10 mL of ethanol before being stored in 5 mL of toluene for further characterization. In case of loss of dispersion stability of the NPs following this washing procedure, dispersibility in toluene can be restored by adding 0.2 mL of oleic acid to the NP dispersion and subsequent stirring at room temperature overnight.

Table 3.1. Overview of the experimental conditions used in the microwave-assisted synthesis of OA-capped α/β-$NaREF_4$ NPs as well as the representative average NP size (± standard deviation).

$NaREF_4$	Ion Ratio (RE^{3+}-to-Na^+)	Ln^{3+} Precursor Amount (mmol)	T_a [1] (°C)	T_b [2] (°C)	$NaREF_4$ Crystalline Phase	$NaREF_4$ Size (nm)
$NaYF_4$	1:1	1.250	300	230	α	8.6 ± 0.5
$NaPrF_4$	1:1	1.250	300	230	α	5.3 ± 0.5
	1:3	0.625	260	250	β	5.3 ± 0.6
$NaNdF_4$	1:1	1.250	300	230	α	4.8 ± 0.6
	1:3	0.625	260	250	β	6.5 ± 0.3
$NaSmF_4$	1:1	1.250	300	230	α	6.5 ± 0.6
	1:3	0.625	260	250	β	6.3 ± 0.2
$NaEuF_4$	1:1	1.250	300	230	α	7.8 ± 0.3
	1:3	0.625	260	250	β	6.4 ± 0.1
$NaGdF_4$: Nd (10%)	1:1	1.250	300	230	α	7.3 ± 0.4
	1:3	0.625	260	250	β	5.6 ± 0.2
$NaGdF_4$: Eu (10%)	1:1	1.250	300	230	α	8.1 ± 0.4
$NaGdF_4$	1:1	1.250	300	230	α	7.4 ± 0.4
	1:2		260	250	β	5.9 ± 0.5
$NaGdF_4$: Tb (10%)	1:1	1.250	300	230	α	7.2 ± 0.5
$NaGdF_4$: Er/Yb (2%/20%)	1:1	1.250	300	230	α	8.4 ± 0.3
	1:1[c]	0.625	-	230	α	11.7 ± 0.9
	1:3	0.625	260	250	β	6.5 ± 0.4
	1:3[c]	0.625	-	230	β	7.4 ± 0.5
$NaTbF_4$	1:1	1.250	300	230	α	6.3± 0.8
	1:3	0.625	260	250	β	6.5 ± 0.6
$NaDyF_4$	1:1	1.250	300	230	α	5.2 ± 0.8
	1:3	0.625	260	250	β	6.8 ± 0.2
$NaHoF_4$	1:1	1.250	300	230	α	5.6 ± 0.8
$NaErF_4$	1:1	1.250	300	230	α	6.3 ± 1.0
$NaYbF_4$	1:1	1.250	300	230	α	7.6 ± 1.0
$NaLuF_4$	1:1	1.250	300	230	α	6.3 ± 1.0

[1] Holding time at T_a = 1 s

[2] Reaction time at T_b = 10 min

[c] Reaction conditions for growing an undoped $NaGdF_4$ shell

3.2.3 Synthesis of β-$NaGdF_4$:Yb^{3+},Er^{3+}/$NaREF_4$ (RE = Gd, Dy) Core/Shell NPs

A shell layer was grown onto the doped core NPs to prevent surface quenching effects by subjecting the NPs to a second MW-assisted treatment, adding [$RE(TFA)_3$] as a shell precursor (Figure 3.1 B). For instance, an undoped $NaGdF_4$ shell was often used as the passivating shell grown on $NaGdF_4$:Yb^{3+},Er^{3+} core NPs. To grow a $NaGdF_4$ shell, 0.625 mmol of the shell precursor was prepared as described above, using Gd^{3+} as sole lanthanide. Subsequently, 1.875 mmol of Na-TFA (3:1 Na^+-to-Gd^{3+} ratio), 4 mL of ODE and 5 mL of oleic acid were added to the shell precursor. The reaction mixture was degassed under vacuum at 120 °C for 30 min. The shell thickness was controlled by adjusting the ratio between the core NPs acting as seeds for shell growth and the shell precursor (Figure 3.2). More specifically, 100 mg, 40 mg, or 30 mg of the core NPs, prepared in the previous step, were used as seeds to grow shells of *ca.* 3, 4, and 6 nm, respectively (resulting CS NPs are labelled ^{3nm}CS, ^{4nm}CS, and ^{6nm}CS). Therefore, the respective amount of core NPs was firstly dispersed in 1 mL of ODE (note: in contrast to the core synthesis, no OAm was used to grow the $NaGdF_4$). Subsequently, this 1 mL of ODE containing core NPs and 9 mL of the degassed shell precursor solution were transferred to a 35 mL microwave vessel, purged with N_2, and tightly sealed. The vessel was inserted into a CEM Discover SP microwave reactor, and the mixture was heated to 250 °C and held for 10 min under stirring. The cooling and washing procedure as well as storage of the obtained CS NPs were as described above for the core NPs.

However, when the ratio between core NPs and shell precursor in the reaction mixture dropped below a critical value (*i.e.*, a mass of core NPs of less than 30 mg), flower-like NPs were formed (Figure 3.3). The relatively high concentration of shell precursor is proposed to lead to the nucleation and subsequent growth of individual undoped $NaGdF_4$ NPs at the surface of the core NPs.[191] This ultimately results in heterogeneous structures that resemble flower petals.

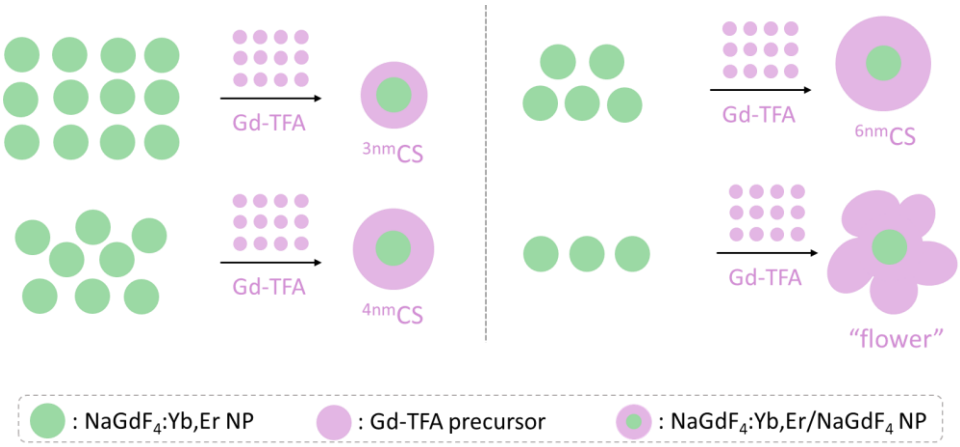

Figure 3.2. Schematic representation of MW-assisted shell thickness control in CS NPs. The nominal ratio between $NaGdF_4$:Yb^{3+},Er^{3+} core NPs, and the amount of shell precursors was used to illustrate the shell thickness control.

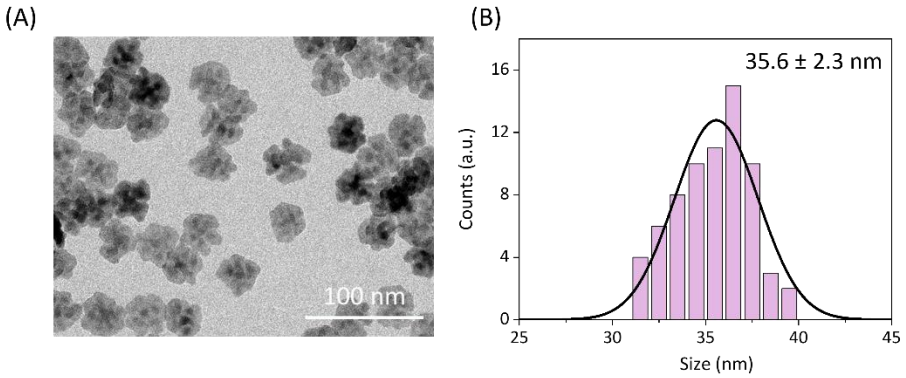

Figure 3.3. (A) TEM image of "flower-like" CS NPs and (B) their corresponding size distribution.

3.2.4 Synthesis of β-$NaREF_4$:Yb^{3+},Er^{3+}/$NaGdF_4$/$NaDyF_4$ Core/Shell/Shell NPs

The procedure to grow the second shell was similar to that used for the synthesis of the CS NPs. For instance, to grow a $NaDyF_4$ shell to obtain magnetic properties, the shell precursor, 0.625 mmol of [$Dy(TFA)_3$], was prepared as described above, using Dy^{3+} as sole lanthanide. Then, 1.25 mmol of Na-TFA (2:1 Na^+-to-Dy^{3+} ratio), 4 mL of ODE and 5 mL of oleic acid were added to the precursor. The reaction mixture was degassed under vacuum at 120 °C for 30 min. The shell thickness was controlled by adjusting the ratio between the CS NPs acting as seeds for shell

growth and the shell precursor (Figure 3.4). More specifically, 160 mg, 120 mg, or 90 mg of the CS NPs, prepared in the previous step, were used as seeds to grow shells of *ca.* 1, 3, and 4 nm (resulting CSS NPs are labelled CSS^{1nm}, CSS^{3nm} and CSS^{4nm}), respectively. Subsequently, 1 mL of ODE containing the CS NPs and 9 mL of the degassed shell precursor solution were transferred to a 35 mL MW glass vessel, purged with N_2, and tightly sealed. The vessel was inserted into a CEM Discover SP microwave reactor, the mixture was heated to 250 °C and held for 10 min under stirring. The cooling and washing procedure as well as storage of the obtained CSS NPs were as described above for the core NPs. Of note, throughout many different batches of CS and CSS NPs synthesized in the frame of this thesis and by co-workers in the HemmerLab, the batch-to-batch variability was found to be small, indicating excellent reproducibility of the MW-assisted approach.

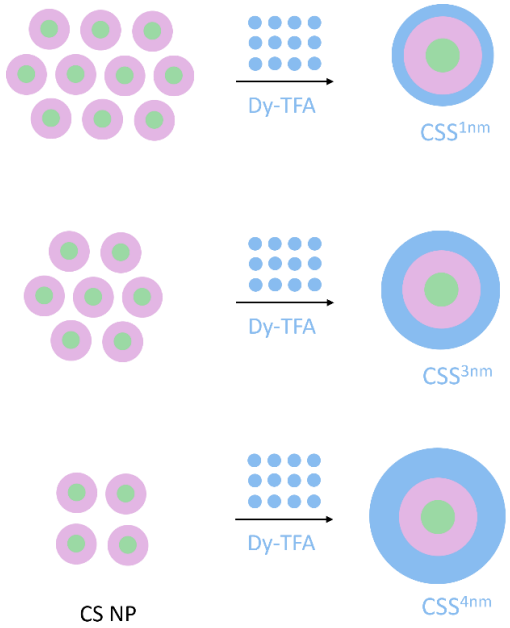

Figure 3.4. Schematic representation of MW-assisted shell thickness control in core/shell/shell NPs.

3.3 Microwave-Assisted Synthesis of $MMnF_3$ (M = Na and K) Particles

3.3.1 Microwave-Assisted Synthesis of $NaMnF_3$ Particles

The procedure to synthesize $NaMnF_3$ particles was similar to that used for the synthesis of α-$NaREF_4$ core NPs. The precursor, 1.25 mmol of manganese trifluoroacetate ($Mn(CF_3COO)_2$, $Mn(TFA)_2$), was prepared as described above, using Mn^{2+} as sole metal ion (equation 3.3).

$$MnO + 4\ CF_3COOH \xrightarrow[95\ °C,\ reflux]{H_2O} 2\ Mn(OOCCF_3)_2 + 2\ H_2O \qquad \textbf{(Eq. 3.3)}$$

Subsequently, a stoichiometric amount of Na-TFA was added to the synthesized $Mn(TFA)_2$ along with 2.5 mL of oleic acid, 2.5 mL of OAm and 5 mL of ODE. To investigate the effect of the Na^+-to-Mn^{2+} ion ratio on particle formation, different amounts of Na-TFA were added as following: 1.25 mmol, 1.875 mmol, 2.5 mmol, and 3.75 mmol, yielding Na^+-to-Mn^{2+} ratios of 1:1, 1.5:1, 2:1, and 3:1, respectively. This mixture was degassed at 120 °C under vacuum for 30 min. Subsequently, the degassed precursor solution was transferred to a 35 mL MW glass vessel, purged with N_2 and tightly sealed. The vessel was inserted into a CEM Discovery SP microwave reactor, and the particles were grown by subjecting the reaction mixture under constant stirring to the following temperature profile: (i) slow stirring with rapid increase in temperature to a set nucleation temperature T_a (7 min), (ii) rapid cooling to the growth temperature T_b (15 s), (iii) static heating at T_b (10 min) under slow stirring , and (iv) gradual cooling to 50 °C (6 min). In a typical synthesis, T_a and T_b were 300 °C and 240 °C, respectively. To assess the effect of reaction temperature and time on particle formation and growth, T_a and T_b as well as the holding time at T_b were varied (equation 3.4). An overview of all reaction parameters is given in Chapter 6. The washing procedure as well as storage of the obtained particles were as described above for the $NaREF_4$ NPs.

$$Mn(OOCCF_3)_2 + Na(OOCCF_3) \xrightarrow[\substack{1\text{-octadecene}\\ \text{oleic acid, oleylamine}}]{T_a\text{: 1 s; } T_b\text{: 10 min}} NaMnF_3 + CO_2 + CO + (CF_3CO)_2O \qquad \textbf{(Eq. 3.4)}$$

3.3.2 Microwave-Assisted Synthesis of $KMnF_3$ Particles

The synthesis of the $KMnF_3$ particles followed the same protocol as described above for the $NaMnF_3$ particles, by replacing Na-TFA by K-TFA. The $Mn(TFA)_2$ precursor was prepared following the aforementioned protocol. Subsequently, different amounts of K-TFA (1.25 mmol or 2.5 mmol, yielding K^+-to-Mn^{2+} ratios of 1:1 and 2:1, respectively) were added to the synthesized precursor along with 2.5 mL of oleic acid, 2.5 mL of OAm, and 5 mL of ODE. This mixture was degassed at 120 °C under vacuum for 30 min. The T_a and T_b used in the microwave reactor were 300 °C and 240 °C (holding time: 10 min), respectively. The subsequent washing procedure was the same as described above for the $NaMnF_3$ particles.

3.4 Surface Modifications of the Particles Towards Water Dispersibility

3.4.1 Ligand-Free NPs

Ligand-free NPs (LF-NPs) were obtained through acidic treatment of the OA-capped $NaREF_4$ NPs following a modified version of previously reported protocols.[177,178] In brief, approximately 150 mg of OA-capped $NaREF_4$ NPs were dispersed in 15 mL of hexane and transferred to a 125 mL Erlenmeyer flask. To this suspension, 15 mL of an aqueous solution of HCl (pH = 1.0, 1.5, 2.0, 2.5, and 3.0, respectively) was added, resulting in a 1:1 (v:v) ratio between the organic and aqueous phase and a 5 mg/mL NP concentration. The flask was closed, and the mixture was vigorously stirred at room temperature for pre-determined times, namely: 1 h, 4 h, 8 h, and 20 h. Further details of the different pH conditions as well as stirring time studies are discussed in Chapter 4. To obtain successful LF-$NaREF_4$ NPs, a HCl solution of pH 1.5 and 20 h stirring time were deemed necessary. Subsequently, irrespective of the pH and stirring time, the bi-phasic system (acidic aqueous phase and organic hexane phase) was separated using a separation funnel. The organic phase was discarded, while the aqueous phase was transferred to a centrifuge tube, diluted with a 1:3 ratio of a water-to-acetone mixture and centrifuged at 8346 RCF for 20 min. This washing procedure was repeated twice after which the LF-NPs were stored in 5 mL of water for posterior characterizations.

3.4.2 Surface Modification with Citrate Groups

70 mg of OA-capped NPs was dispersed in 5 mL of hexane, and the dispersion was mixed with 5 mL of 0.2 M trisodium citrate buffer (pH = 2.5). The resulting mixture was stirred for 3 h at 40 °C.[192] The aqueous/organic mixture was poured into a separatory funnel, and the aqueous phase now containing the NPs was isolated. The NPs were precipitated with 25 mL of acetone (1:5 aqueous phase:acetone) and centrifuged for 15 min (6595 RCF). The organic solvent was removed, and the recovered solids were redispersed in 5 mL of trisodium citrate buffer (pH = 7). The dispersion was stirred for 2 h, followed by three washing steps using water (5 mL) and acetone (25 mL) (1:5 water:acetone) for precipitation and subsequent centrifugation under aforementioned conditions. The obtained citrate (Cit)-capped NPs were stored in 5 mL of water.

3.4.3 Surface Modification with Poly(acrylic acid)

To prepare PAA-coated NPs, 120 mg PAA were dispersed in 10 mL of ethanol, and 100 mg OA-capped NPs were dispersed in 5 mL of chloroform. The two solutions were mixed together and stirred overnight.[193] Subsequently, the NPs were precipitated with 120 mL of acetone (8:1 acetone:NP dispersion) and centrifuged for 20 min (6595 RCF). The recovered solids were dispersed in 5 mL of water and washed with acetone twice. The obtained PAA-coated NPs were stored in 5 mL of water.

3.5 Characterizations Techniques

3.5.1 Powder X-Ray Diffraction (XRD)

To determine the crystalline phase of the NPs, powder X-ray diffraction (XRD) analysis was performed on all samples using a Rigaku Ultima IV Diffractometer or a Bruker D8 Endeavor (Cu Kα, λ = 1.5401 Å), operating at 44 kV and 40 mA (step size: 0.02°, scan speed: 1°min^{-1}). Therefore, the NPs were deposited on a glass slide from their suspension.

To distinguish the morphology-specific assignment between LF-α-$NaREF_4$ and orthorhombic LF-REF_3 (RE = Ho and Lu) phase (Chapter 4.2.4), the interplanar distances obtained from XRD patterns, d_{XRD}, were calculated by direct application of Bragg equation:

$$n\lambda = 2d_{XRD}sin\theta \quad \textbf{(Eq. 3.5)}$$

where, n = 1 (first order diffraction); λ = 1.5401 Å; $sin\theta \cong \theta$, for small θ.

The crystallite size (L) of LF-GdF_3 particles (Chapter 4.2.1) estimated from the XRD pattern was calculated by the Scherrer equation:

$$L = \frac{K\lambda}{\beta cos\theta} \quad \textbf{(Eq. 3.6)}$$

Where K is a dimensionless shape factor, with a value close to unity. The shape factor of spheres has a typical value of about 0.9, but varies with the actual shape of the crystallite; λ is the X-ray wavelength; β is the line broadening at half the maximum intensity (FWHM), after subtracting the instrumental line broadening, in radians; θ is the Bragg angle.

3.5.2 Transmission Electron Microscopy (TEM)

The morphology and size distribution of all obtained NPs were investigated by transmission electron microscopy (TEM, FEI Tecnai Spirit). The samples were dispersed on a Formvar/carbon film supported on a 300-mesh copper TEM grid. Size distributions (mean size ± standard deviation) of the samples were derived from TEM images using the software ImageJ. The respective size distributions were obtained by analyzing 200 particles per sample and plotted with Gaussian fit using Origin software. The spatial resolution of the TEM instrument is *ca.* 0.4 nm.

3.5.3 Selected Area Electron Diffraction (SAED) Measurements

The morphology-specific phase of the samples (LF-HoF_3, LF-$NaHoF_4$, LF-LuF_3, and LF-$NaLuF_4$, see the discussion in Chapter 4.2.4) was determined by selected area electron diffraction (SAED) analysis. The SAED patterns were obtained using a JEOL (JEM 2100F) TEM operating at 200 kV.

The camera length was calibrated using a gold foil as standard. The samples were prepared as described above for TEM analysis.

The interplanar distances (d_{SAED}) were calculated based on the camera length calibration with a standard Au sample (Au foil, d_{Au} = 0.204 Å for the first ring) using a derivation of Bragg´s equation:

$$d = \frac{\lambda L}{R} \quad \textbf{(Eq. 3.7)}$$

where, d = interplanar distance; λ = wavelength of the diffracted electrons; L = camera length. and by adopting the ratio between the radius of the first ring of the SAED image of the Au standard and that of the sample:

$$\frac{d_{sample}}{d_{Au}} = \frac{R_{Au}}{R_{sample}} \quad \textbf{(Eq. 3.8)}$$

where, R_{Au} = radius of the SAED ring of the Au standard; R_{sample} = radius of the SAED ring for the sample; d_{Au} = interplanar distance of the Au foil for the corresponding ring.

3.5.4 Scanning Electron Microscopy (SEM)

The morphology of $NaMnF_3$ particles was investigated by scanning electron microscopy (SEM, JEOL JSM-7500F FESEM). The SEM analysis was conducted on samples drop-casted on a 5 mm x 5 mm silicon wafer after gold-sputtering (3 nm gold layer thickness) in a vacuum coater (Leica EM ACE200).

3.5.5 Energy Dispersive X-ray (EDX) Measurements

The elemental composition of the obtained $NaMnF_3$ particles was investigated by energy dispersive X-ray (EDX) spectroscopy analysis. The EDX measurements were performed on a Zeiss Gemini SEM 500 equipped with a Bruker EDX detector.

3.5.6 Fourier Transform Infrared (FTIR) Spectroscopy

In order to confirm the successful surface modification of the NPs, the presence of the functional groups at the particles' surface was investigated by Fourier-transform infrared (FTIR) spectroscopy, using a Cary 630 FTIR spectrometer in ATR mode (Diamond ATR crystal), with acquisition of 128 scans and resolution of 4 cm^{-1}.

3.5.7 Thermogravimetric Analyses (TGA)

Thermogravimetric analysis (TGA) of the surface modified samples was carried out using a TGA Q500/Discovery instrument, heating from 30 to 800 °C at a heating rate of 10 °C min^{-1} under N_2 atmosphere, allowing to estimate the degree of surface modification in each sample.

3.5.8 Dynamic Light Scattering (DLS)

The hydrodynamic diameter and the zeta potential of the water-dispersible NPs were measured with a Malvern Zetasizer Nano-ZS instrument. The measurements were carried out on NPs dispersed in water at room temperature. Three measurements were performed for each sample.

3.5.9 Inductively Coupled Plasma Optical Emission Spectroscopy (ICP-OES)

The metal ion concentration in the samples for MRI relaxivity and CT measurements was determined with an Agilent ICP-OES spectrometer. Therefore, 10 mg of particles was added to a mixture of 0.5 mL of concentrated HNO_3 and 1.5 mL of concentrated HCl, followed by heating at 80 °C for 5 h ensuring that all NPs were digested. Flow conditions of the Agilent ICP-OES spectrometer were as follows: nebulizer flow = 0.7 L/min, plasma flow = 12 L/min, auxiliary flow = 1 L/min.

3.5.10 Time-Domain Nuclear Magnetic Resonance (NMR) Relaxivity Measurements

The proton relaxation times of PAA-capped $NaMnF_3$ and $KMnF_3$ suspensions were measured using a time domain NMR relaxometer. R_1 and R_2 relaxation rates (in s^{-1}) were obtained from T_1 and T_2 relaxation times (in s) determined at 40 °C on a Bruker Minispec mq20 instrument (Bruker, Billerica, MA, School of Nutrition Sciences, University of Ottawa) operating at 0.47 T and 20 MHz, equipped with a temperature control unit. T_1 was obtained with an inversion-recovery sequence with the following parameters: first pulse separation time = 40 ms, final pulse separation time = 10000 ms, fifteen data points separated by exponentially increasing intervals were recorded, acquisition scans = 4. T_2 was obtained by a Carr-Purcell-Meiboom-Gill sequence with the following parameters: 90° – 180° pulse separation time (tau) = 5 ms, 3000 data points were acquired, acquisition scans = 4. Relaxivities r_1 and r_2 and their statistical difference (p-value) were obtained from the linear fit of the plots of R_1 and R_2 against the molar concentration of Mn^{2+} ions of the tested particle dispersions (ICP-OES), carried out with Minitab 19 (Minitab LLC, State College, PA).

3.5.11 Magnetic Resonance Imaging (MRI) Relaxivity Measurements

MRI relaxivity measurements were performed on a 7.0 T preclinical MRI instrument (Discovery MR901, Agilent/General Electric, Pre-clinical Imaging Core Facility (PCIC), Faculty of Medicine, University of Ottawa). Samples were prepared by dispersing NPs in water with different concentrations. T_1 measurements were performed using a classical inversion recovery method with the following parameters: repetition time TR = 15000 ms, echo time TE = 6.4 ms, eight inversion recovery times (TI = 50, 100, 400, 800, 1200, 2000, 3000 and 4000 ms), field of view (FOV) = 8 × 8 mm^2, slice thickness = 3 mm, matrix = 128 × 128. T_2 measurements were performed using a Carr-Purcell-Meiboom-Gill (CPMG) sequence with the following parameters: TR = 5000 ms, FOV = 10 × 10 mm^2, slice thickness = 3 mm, matrix = 128 × 256, TE = 13, 26.1, 39.1, 52.2, 65.2, 78.2, 91.3 and 104 ms. T_2-weighted images were obtained on the same MR instrument using the following parameters: TR = 5000 ms, FOV = 10 × 10 mm^2, slice thickness = 3 mm, matrix = 128 × 256, TE = 52 ms. T_1 and T_2 relaxation times (R_1 and R_2) were calculated using single exponential

fitting of the data extracted from mapping images for different concentrations of particles in water.

3.5.12 Photoluminescence Spectroscopy

Investigation of the steady-state photoluminescence properties of the NPs in suspension (in toluene or water) was carried out in a quartz cuvette (suitable spectral range from 200 to 2500 nm, 1 cm optical path) inserted into the Peltier temperature sample holder of a QuantaMaster 8075-21 spectrofluorometer from HORIBA, equipped with double grating emission monochromators, a red-extended photomultiplier detector R13456 PMT (185 to 980 nm), a liquid nitrogen cooled InGaAs detector (800 to 1550 nm) for the emission acquisition of Nd^{3+}-based sample, and an InAs detector (1000 to 3450 nm) for the emission acquisitions of Er^{3+} and Tm^{3+}-based samples. The UV continuous excitation of the Eu- and Tb-doped samples was performed with a Xenon lamp (75 W). The NIR continuous excitation was performed using 980 nm and 808 nm continuous-wave laser diodes with a maximum power of 2 W.

Power-dependent studies were performed using the same setup described above, including different neutral density filters to stepwise reduce the incident laser power. The slopes of the fitted curves of the log-log power plots (which reflect the number of photons involved in the UC process) were determined by the power-dependent measurements.

For temperature-dependent studies, the temperature of the sample was changed from 15 °C to 50 °C (following a heating regiment of 15, 20, 25, 30, 35, 40, 45, 50 °C), using the Peltier temperature sample holder with a liquid cooling system. At each step, the temperature was allowed to stabilize for 15 min prior to the measurements.

Excited state lifetimes were obtained by time-resolved spectroscopy, using the Xenon lamp or 980 nm laser diode in pulsed mode. Lifetime values were obtained by integration of the area under the normalized decay curves. For all the optical measurements, filters were placed in front of detectors. A long-pass 400 nm filter was used for the UV excitation, a short-pass 775 nm filter was used for upconversion acquisition, while a long-pass 1025 nm filter was used for NIR emission detection.

3.5.13 X-Ray Absorption Spectroscopy

X-ray absorption spectroscopy measurements were conducted using a Hamamatsu L12161-07 tungsten source collimated to a 1 mm beam. A 0.6 mm Cu filter was used to harden the beam. The source current was 150 µA, and the source voltage was 150 kV. An Amptek Cd-Te 25 mm^2 spectrometer was used in combination with an Amptek PX-5 Digital Pulse Processor (Department of Earth and Environmental Sciences, University of Ottawa). Each spectrum had an acquisition time of 120 s. Samples were prepared by dispersing different amounts of NPs (5 – 30 mmol of Ln^{3+} ions as determined by ICP) in 1 mL of water in 1 cm of plastic cuvettes.

3.5.14 Radiograph Imaging

Radiograph imaging measurements were performed with a PXS MicroCT system (Pinnacle X-ray Solutions Inc.) consisting of a Hamamatsu L12161-07 source coupled with a Varian PaxScan 1313DX digital image detector (Department of Earth and Environmental Sciences, University of Ottawa). Conditions of the source were 150 µA current with different voltages, *i.e.,* 70, 80, 90, 100, 110 and 120 kV. The X-ray beam was hardened using a 3.3 mm Al filter. Each image consists of the average of 20 frames taken at 2 frame per second for a total acquisition time per image of 10 s. ImageJ 1.52c was used to determine an average attenuation value from an area within the frame. Images of water and an empty (air) cuvette were obtained as reference to calculate the HU values. Samples were prepared by dispersing different amounts of NPs (5 – 30 mmol of Ln^{3+} ions determined by ICP) in 1 mL of water in 1 cm of plastic cuvettes.

3.5.15 Computed Tomography Imaging

The CT images were collected using a Hamamatsu L12161-97 source coupled with a Varian PaxScan 1313DX flat panel detector. Conditions of the source were 110 kV voltage and 250 µA current. The X-ray beam was hardened using a 3.3 mm Al filter. Data acquisition was done using PXS iRAD software (v7.0.0.12) with each image consisting of the average of 10 frames, each frame

being captured at 15 fps (or 0.067 s exposure per frame). Prior to the acquisition, flat field correction of the panel was obtained as well as a bright (X-ray on, no target) and a dark file (X-ray off) for reconstruction calibration. A total of 360 images were taken with a 1° clockwise stepping. The obtained images were imported using VGS-studio-max software for the reconstruction. Average values of a volume within water-filled and the empty vials were obtained with ImageJ 1.52c and used to determine the HU values. Samples were prepared by dispersing different amounts of NPs (5 – 30 mmol of Ln^{3+} ions determined by ICP) in 1 mL of water in 1 cm of plastic cuvettes.

3.6 Cytotoxicity of Ln-NPs

Human lung adenocarcinoma (A549) cells were seeded (75,000 cells) in a 6-well plate to a final volume of media of 1 mL. After 48 h the media was removed from wells, and fresh media containing Ln-NPs (50 µg/mL, 250 µg/mL, 500 µg/mL) was added. The Ln-NPs were incubated at 37 °C with the cells for 24 h. After the incubation, the cells were washed 3 times with PBS, followed by the addition of 250 µL of trypsin, diluted with 750 µL phenol red-free media and centrifuged (1000 RCF, 6 min). After the cells were decanted, 1 mL of PBS with 0.2% DMSO, 1 µM calcein-AM, and 2 µM ethidium homodimer-1 were added. The mixture was vortexed briefly three times. All cell experiments including controls were performed in triplicates. Flow cytometry (Beckman Coulter Gallios Flow Cytometer, Center for Chemical and Synthetic Biology, University of Ottawa) was performed doing standard compensation and gating. The flow cytometry data analysis was performed with Kaluza software.

Chapter 4. Water Dispersible Ligand-Free Rare Earth Fluoride Nanoparticles: Water Transfer *versus* $NaREF_4$-to-REF_3 Phase Transformation

This Chapter is based on published work in Dalton Transactions: Nan Liu, Nicholas Gobeil, Parrish Evers, Isabel Gessner, Emille M. Rodrigues and Eva Hemmer, Dalton Trans., 2020, 49, 16204-16216.

Author contributions: E. H. and N. L. conceptualized the study. N. L. and N. G. synthesized OA-capped $NaREF_4$ NPs, and P. E. performed ligand-removal experiments. I. G. optimized the conditions for ligand-removal. N. L. did structural characterizations, E. M. R. conducted the optical measurements. N. L., E. M. R., and E. H. co-wrote the manuscript.

Abstract:

The chemical stability of OA-capped sub-10 nm α- and β-$NaREF_4$ NPs (RE = Y, Pr, Nd, Sm, Eu, Gd, Tb, Dy, Ho, Er, Yb, Lu for α- and RE = Pr, Nd, Sm, Eu, Gd, Tb, Dy for β-phase NPs) was evaluated under the acidic conditions used for ligand removal towards water dispersibility. It was found that for such small NPs, a pH lower than 3 was necessary for the water transfer to be efficient and to yield well-dispersed LF-NPs. In stark contrast to the generally considered good chemical stability of $NaREF_4$, these conditions were observed to pose a risk to phase transformation of the $NaREF_4$ NPs into much larger, hexagonal- or orthorhombic-phase REF_3, depending on the NP composition. A correlation between the thermodynamic stability of the α/β-$NaREF_4$ and the hexagonal/orthorhombic REF_3 phases – dictated by the RE ion choice – and the chemical stability of the NPs was found. For instance, β-$NaGdF_4$ NPs remained stable, while α-$NaGdF_4$ NPs underwent phase transformation into hexagonal GdF_3. More general, $NaREF_4$ NPs based on lighter RE ions were more prone towards phase transformation, while those based on heavier RE ions exhibited stability. Herein, within the RE series, the borderline for phase transformation was identified as Tb/Dy for α-$NaREF_4$ NPs and Sm/Eu for β-$NaREF_4$ NPs, respectively. Also, given the large interest in luminescent NPs for, *e.g.*, biomedical applications, optically active Ln^{3+} ions (Ln = Nd, Eu, Tb, Er/Yb) were doped into α/β-$NaGdF_4$ host NPs, and the dopant influence on the chemical stability was evaluated. Steady state and time-resolved spectroscopy unveiled spectral features characteristic for Ln^{3+} f-f transitions, *i.e.*, downshifting and upconversion, before and after ligand removal. Overall, the results herein described emphasise the importance of minding the chemical procedure used for ligand removal of $NaREF_4$ NPs of different crystalline phases and RE compositions.

4.1 Introduction

As introduced in Chapter 1.5.1, ligand removal is a simple and efficient way to obtain water-dispersible $MREF_4$ (M = Li and Na) NPs for their biomedical applications. Typically, pH values of 3 to 4 are used for the acidic treatment of OA-capped NPs.[177, 178, 194, 195] However, pH values as low as 1 have also been reported for various β-phase $MREF_4$ NPs with sizes in the 10 to 30 nm range.[181-184] In fact, pH values < 3 were deemed necessary for an efficient organic-to-aqueous phase transfer of most of the sub-10 nm sized NPs presented in this work. Subjected to such relatively harsh conditions, the chemical stability of the $NaREF_4$ constitutes a crucial aspect. Indeed, one of the advantages of $NaREF_4$ NPs over their oxide counterparts is their generally claimed superior chemical stability.[19, 196, 197] As such, good chemical stability of β-$NaREF_4$ NPs in acidic environments (pH 3 to 6) has been demonstrated.[178, 181, 182, 195] Conversely, Lahtinen *et al.* reported the disintegration of β-$NaYF_4$:Er^{3+}/Yb^{3+} NPs in very diluted aqueous suspensions (pure water and different buffers at pH 7.7 and 8.0).[198] The authors demonstrated that the disintegration of these NPs was concentration-dependent, namely, most of the NPs completely dissolved in diluted suspensions (μg/mL). According to the solubility product (K_{sp}), the fluoride ion has been proven to play a major role in NP disintegration. Work by Lisjak *et al.* unveiled the instability of α/β-$NaYF_4$:Tm^{3+}/Yb^{3+} NPs under neutral physiological conditions.[199,200] They found that the degree of dissolution increased with decreasing particle size, increasing temperature, and increasing concentration of HPO_4^{2-} in the aqueous media.

Given the outstanding application potential of water-dispersible $NaREF_4$ NPs, crystallized in either the β or α lattice, more careful analysis of their chemical stability seemed overdue, specifically at pH < 3 required for the removal of OA/OAm surface groups from our small NPs. With this in mind, we systematically evaluated the outcome of the ligand removal procedure for both crystalline phases of small $NaREF_4$ NPs, α and β. More specifically, we carefully assessed the influence of the chosen RE^{3+} ions, either being used to form the host lattice (RE = Y, Pr, Nd, Sm, Eu, Gd, Tb, Dy, Ho, Er, Yb, and Lu for α- $NaREF_4$; RE = Pr, Nd, Sm, Eu, Gd, Tb, and Dy for β-$NaREF_4$) or constituting the optically active Ln^{3+} ion doped into α- or β-$NaGdF_4$ (Ln = Nd, Eu, Tb, Er/Yb). In short, those NPs that were based on the heavier RE ions exhibited superior stability, while $NaREF_4$

NPs based on the lighter RE ions were more prone to suffer from chemical instability, this trend being more pronounced for the α-phase of $NaREF_4$ than its β polymorph. Interestingly, instead of mere NP disintegration,[198-200] we observed phase transformation from ternary $NaREF_4$ to binary REF_3, either in its orthorhombic or hexagonal crystal phase. Based on these findings, a correlation was established between the chemical and thermodynamic stability of the crystalline phase of $NaREF_4$ – α *versus* β [31, 151, 200, 201] – as a function of the RE ion. A similar correlation was found with respect to the crystalline phase of the formed REF_3 materials – hexagonal *versus* orthorhombic.[201-203]

In the solid state, $NaREF_4$ systems have been described as eutectic mixtures between NaF and REF_3 at high temperatures.[204] As such, the interconversion between REF_3 and $NaREF_4$ is known for bulk materials in solid state and micro-sized particles.[204-206] With respect to the synthesis of REF_3, various methods using different RE^{3+} and F^- precursors have been proposed, often involving high temperatures and long reaction times (*e.g.*, solvothermal processes),[203, 207-212] while only a few examples of room temperature reactions exist.[213-215] Herein, special attention is paid to the hexagonal REF_3 phase, which is considered to be the more efficient host material for optically active Ln^{3+} ions compared to the orthorhombic REF_3 phase.[210, 214, 216, 217] In addition to phosphors[218, 219] and MRI CAs[125, 219], *e.g.*, based on Eu^{3+}- and Gd^{3+}, various other applications have been described for REF_3 materials, such as PrF_3 as bactericidal,[220] NdF_3 as glass ceramic for band pass filters,[221] SmF_3 for Li-ion batteries,[222] or TbF_3 and DyF_3 in magnets[223]. While a $NaREF_4$-to-REF_3 phase transformation at the nanoscale has been observed under the influence of an electron beam,[224] it has not been reported so far for NPs dispersed in aqueous media, at room temperature, and under ambient pressure. Hence, foremost, our findings came as a warning to mind the chemical procedure used for ligand removal of $NaREF_4$ NPs of different crystalline phases and RE compositions, but also as an alternative method to obtain REF_3 from $NaREF_4$ NPs.

4.2 Results and Discussion

4.2.1 Formation of GdF_3 as a Function of the Crystalline Phase of the OA-Capped $NaGdF_4$ NPs

$NaGdF_4$ being a good host for doping with optically active Ln^{3+} ions and offering MRI capabilities, α- and β-phase NPs of this material are of great interest for various biomedical applications, including multimodal imaging.[89, 225-228] Thus, the $NaGdF_4$-based system constitutes an important candidate to investigate in detail the effects of ligand removal under acidic conditions on the NPs' structural integrity. OA-capped $NaGdF_4$ NPs in the β and α crystalline phases were successfully synthesized by a previously established MW-assisted protocol (Figure 4.1, (A/B-1/2)).[159] Both samples exhibited a narrow size distribution with similar sizes in the sub-10 nm realm (Figure 4.1, (A/B-4)).

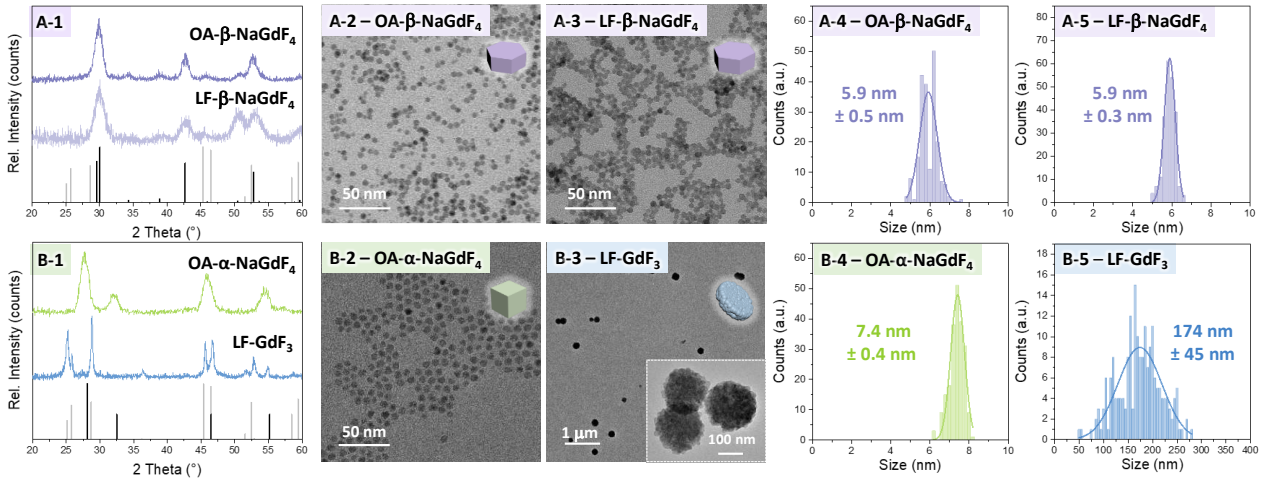

Figure 4.1. Formation of hexagonal GdF_3 upon treatment of $NaGdF_4$ NPs at pH 1.5 (20 h) as a function of their crystalline phase: (A-1) XRD patterns of β-$NaGdF_4$ NPs before (OA-capped) and after treatment at pH 1.5 (ligand-free, LF). (B-1) XRD patterns of OA-capped α-$NaGdF_4$ NPs and resulting LF-hexagonal GdF_3 particles. References: α-$NaGdF_4$, PDF card [00-027-0697] (black line, B); β-$NaGdF_4$, PDF card [01-080-8787] (black line, A); hexagonal EuF_3, PDF card [00-032-0373] (light grey line, A and B; this card was used as no reference for hexagonal GdF_3 is available). (A-2) and (B-2): TEM images of OA-capped β- and α-$NaGdF_4$ NPs obtained by MW-assisted synthesis approach. (A-3) and (B-3): TEM images of LF-NPs obtained upon stirring of the respective OA-NPs shown in (A/B-2) at pH 1.5 for 20 h. The inset shown in (B-3) is the higher magnification image, note the different scale bars for (B-3). (A-4/5) and (B-4/5): Average particle sizes and size distributions of OA-capped β- and α-$NaGdF_4$ NPs as well as their respective LF-NPs.

The as-synthesized, OA-capped NPs were submitted to a ligand removal procedure, modified from those reported in the literature.[177,178] Most importantly, it was found that commonly applied pH 3-4 was not efficient in case of such small NPs capped with OA and OAm. In contrast, lower pH, *e.g.*, pH 1.5, was necessary to transfer the hydrophobic NPs into the aqueous phase at good yield (*vide infra* for further discussion of the effect of pH on ligand removal and phase transformation). As expected, following stirring of OA-capped β-$NaGdF_4$ NPs in a HCl solution of pH 1.5 for 20 h, LF-β-$NaGdF_4$ NPs were successfully obtained, size and morphology not undergoing any significant variation (Figure 4.1 A).

Conversely, in the case of α-$NaGdF_4$ NPs, the same treatment triggered a phase transformation of the initial small α-$NaGdF_4$ NPs into significantly larger (*ca.* 174 nm in diameter) hexagonal-phase GdF_3 NPs (Figure 4.1 (B-3)). The NPs' plate-like morphology is commonly reported for hexagonal-phase GdF_3 (*vide infra* for TEM and SEM images taken on various REF_3 structures confirming their plate-like character).[201] The higher magnification TEM image (Figure 4.1 (B-3)) unveiled a granular structure of the formed GdF_3 plates, being built up by smaller NPs of about 17 nm in size. The crystallite size estimated from the XRD pattern shown in Figure 4.1 (B-1) was about 20 nm, which is in line with TEM observations and provides further evidence that the larger structures are formed by self-assembly of smaller GdF_3 NPs.

Previous reports demonstrated the dissolution of $NaREF_4$-type NPs in diluted (1 mg/mL and below) aqueous suspensions at pH 5-7.[199, 200] These studies revealed quantitatively more Na^+ and F^- ions being released into solution than RE^{3+} ions, and the possibility of REF_3 crystallization was hypothesized. However, to the best of our knowledge, this is the first time that the phase transformation of $NaREF_4$ to REF_3 is reported during a ligand removal procedure, specifically as a function of the crystalline phase of the starting $NaGdF_4$ NPs. While the concentration of the NP suspensions used in this study (*ca.* 5 mg/mL) was significantly higher than the critical concentration reported in the literature (1 mg/mL and below), the low pH fosters the dissolution of the NPs, resulting in leaching of Na^+, RE^{3+}, and F^- ions into the solution. Herein, the very high solubility product of NaF (K_{sp} = 7.1 × 10^{-1}) compared to that of REF_3 (*e.g.*, $K_{sp}(LaF_3)$ = 3.26 × 10^{-21})[199, 229] is proposed to result in dissolution of Na^+ and F^- ions, while promoting the precipitation of REF_3. In other words, the presence of dissolved F^- ions in solutions of very low pH

containing RE^{3+} ions has been reported to favour the precipitation of REF_3 NPs, for instance by a hydrothermal method.[203] Indeed, in our study, the presence of NaCl – formed between Na^+ ions dissolved from the NPs and Cl^- ions from the acid – in the dried supernatant after the ligand removal was confirmed by XRD (data not shown), corroborating this hypothesis.

4.2.2 Assessment of pH for Successful Ligand Removal

As discussed previously, a pH < 3 was deemed necessary to transfer OA/OAm-capped α-$NaGdF_4$ NPs from the organic into the aqueous phase. Conversely, in case of β-$NaGdF_4$ NPs, the synthesis of which also included oleic acid and OAm as solvent and capping agent, LF-β-$NaGdF_4$ NPs could be transferred at pH 3 (samples shown in Figure 4.2 (A-1) are the same batch of NPs as those used for ligand removal at pH 1.5, Figure 4.1 A). The crystalline phase of the LF-NPs was confirmed by XRD analysis (Figure 4.2 (A-3)). Yet, as evident from Figure 4.2 (A-2), the LF-NPs suffered from severe aggregation and lost their crisp spherical morphology. Based on these findings, a pH value of 3 was deemed unsuitable for the successful preparation of LF-β-$NaGdF_4$ NPs.

Effect of surface chemistry. The use of both OAm and oleic acid during NP synthesis is expected to result in NPs capped with OA and OAm groups. FTIR spectra shown in Figure 4.2 D confirmed the presence of OA. The peaks at 2926 cm^{-1} and 2850 cm^{-1} can be assigned to the asymmetric and symmetric stretching of $-CH_2$ groups while the peaks at 1550 cm^{-1} and 1460 cm^{-1} originate from the asymmetric (δ_{as}) and symmetric (δ_s) $-COO^-$ stretching. [230] The presence of OAm could not be unambiguously confirmed by FTIR spectroscopy given the overlap of the spectral features for both compounds, neither can its presence be ruled out.

In order to investigate the influence of surface chemistry, *i.e.*, the presence of OAm on the NP surface, a batch of β-$NaGdF_4$ NPs of comparable size was synthesized without OAm. As the MW-assisted approach requires the presence of OAm as a surfactant in addition to oleic acid to yield NPs of homogeneous morphology, it was not possible to simply omit OAm during the reaction. Conveniently, no OAm is used for the MW-assisted growth of a thin shell onto the NPs.

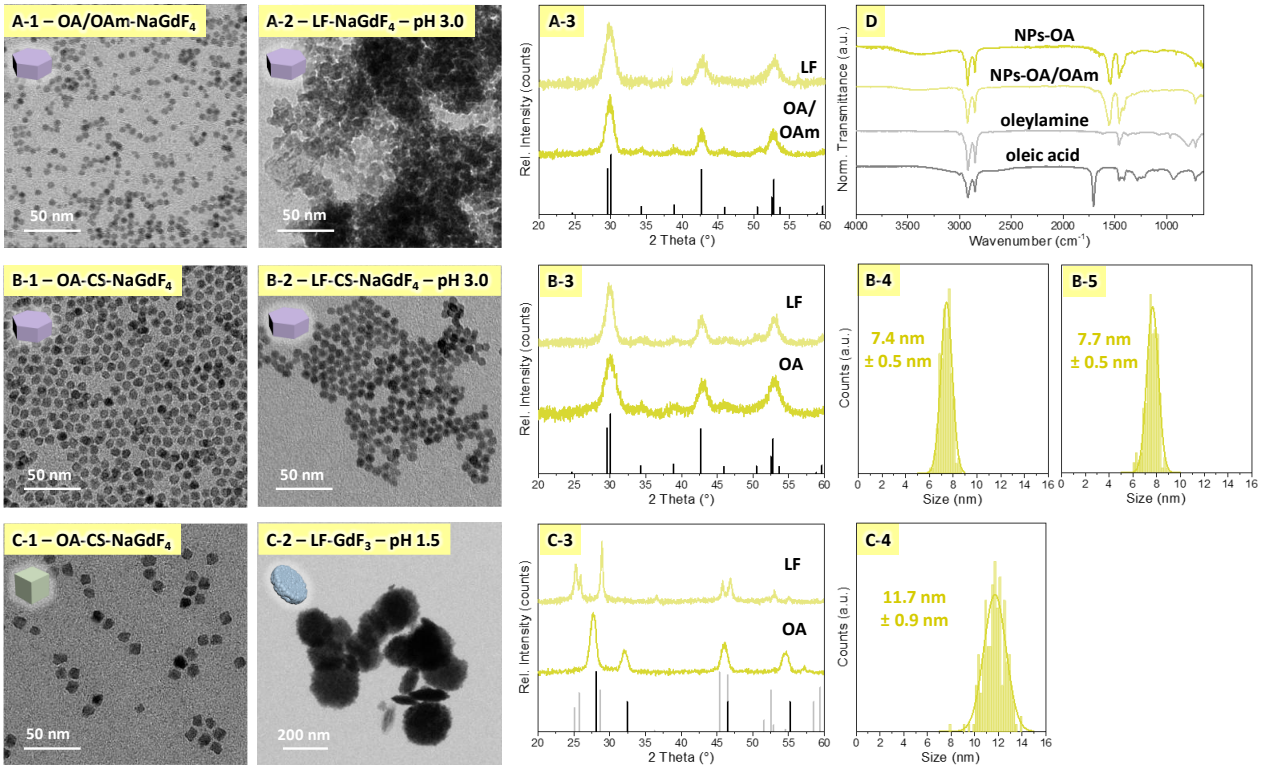

Figure 4.2. Effect of (A) the $NaREF_4$ crystalline phase on the pH necessary for ligand removal, (B) surface chemistry on ligand removal, and (C) particle size on phase transformation upon ligand removal. (A-1/2) TEM images of β-$NaGdF_4$ NPs synthesized using oleic acid and OAm before and after ligand removal at pH 3 (20 h) reveal the poor quality of LF-NPs obtained under these conditions. XRD patterns of both samples are shown in (A-3). Reflections at 39° due to NaF (a possible by-product of NP synthesis)[159] were removed for clarity. Size and size distribution of (A-1) are given in Figure 4.1 (A-4). (B-1/2) TEM images of β-$NaGdF_4$:Er^{3+},Yb^{3+}/$NaGdF_4$ CS NPs (only OA was used during shell growth) before and after ligand removal at pH 3 (20 h) demonstrate the successful transfer of the NPs into the aqueous phase. XRD patterns of both samples are shown in (B-3). Size and size distribution are given in (B-4/5). (C-1/2) TEM images of larger α-$NaGdF_4$:Er^{3+},Yb^{3+}/$NaGdF_4$ CS NPs before and after ligand removal at pH 1.5 (4 h) indicate phase transformation into hexagonal GdF_3 (see C-3 for XRD patterns) despite the larger particle size (no OAm was used for shell growth). (C-4) Size and size distribution of (C-1). (D) Representative FTIR spectra recorded of $NaGdF_4$ NPs grown in the presence (NPs-OA/OAm) and absence (NPs-OA) of OAm, respectively. Spectra obtained of pure oleic acid and OAm used in the synthesis are also shown. References: β-$NaGdF_4$, PDF card [01-080-8787] (black line in A/B-3); α-$NaGdF_4$, PDF card [00-027-0697] (black line in C-3); hexagonal EuF_3, PDF card [00-032-0373] (light grey line in C-3).

Hence, first, OA/OAm-capped NPs were synthesized (in this case: β-$NaGdF_4$:Er^{3+},Yb^{3+}), followed by a washing step to remove any OAm from the reaction mixture prior to subsequent shell growth (pure $NaGdF_4$) using solely oleic acid in addition to ODE as solvent. This strategy allowed to obtain β-$NaGdF_4$:Er^{3+},Yb^{3+}/$NaGdF_4$ NPs, most likely being only capped with OA (Figure 4.2: TEM – B-1;

XRD – B-3; Size – B-4, FTIR – D). The thickness of the shell was estimated to be 0.7 nm, based on TEM images recorded of the core-only NPs before the addition of the shell precursor (data not shown).

Obtained OA-capped CS NPs were treated with a HCl solution at pH 3 for 20 h to assess the ligand removal. The NPs were transferred successfully to the aqueous phase, without any phase transformation (Figure 4.2 B). It should be noted that this was the only sample that underwent an organic-to-aqueous phase transfer retaining morphology at pH 3. These observations indicate the importance of surface chemistry for ligand removal, *i.e.*, the presence of OAm groups requiring lower pH. In light of this, the use of pH 3-4 for ligand removal reported in the literature may be related to the fact that many of these studies revolve around NPs that – based on their synthesis method – are only OA-capped.[177, 178, 194, 195] In addition, it is notable that successful ligand removal at pH 4 is typically achieved on $NaREF_4$ NPs crystallized in the β-phase and of larger size.[178, 194] Consequently, it is hypothesized that both surface chemistry and particle size (the latter being briefly addressed in the following paragraph) have an influence on conditions required for ligand removal. Further investigation of a broad range of NPs exhibiting various sizes and surface chemistries may provide clarification yet is beyond the scope of this study.

Besides the potential influence of the ligand on pH requirements, phase transformation itself is thought not to be governed (neither prevented nor fostered) by the presence of OA/OAm ligands. In case of stable NPs, upon re-protonation, oleic acid migrates into the organic phase, while LF-NPs are dispersed in the (still acidic) aqueous phase. Even under prolonged stirring (*e.g.*, 20 h), these LF-NPs did not undergo phase transformation, despite lack of any protecting OA/OAm ligands on their surface. In case of instable NPs, the phase transformation takes place in the aqueous phase of the bi-phasic mixture used for ligand removal: The dissolution and re-precipitation processes are ruled by the relative thermodynamic stability of each $NaREF_4$ and REF_3, which in turn, depends on the equilibrium of the solvated ions and the precipitated NPs in the aqueous phase. Hence, the (in)stability of $NaREF_4$ NPs is rather due to the intrinsic materials properties than due to the synthesis-related OA/OAm ligands.

Size effect. In addition, it was investigated whether larger NP size may prevent phase transformation from α-$NaGdF_4$ into GdF_3 upon treatment at pH 1.5 (4 h). Given that surface grows significantly over volume upon decreasing particle size, the larger surface of small NPs – as used in this study – may enhance the interaction with H^+ ions in the acidic solution, thus, challenging chemical stability. As the MW-assisted approach generally provides access to small NPs at the sub-10 nm realm, the CS strategy was applied to obtain larger NPs, namely α-$NaGdF_4$:Er^{3+},Yb^{3+}/$NaGdF_4$ NPs of almost 12 nm in size (Figure 4.2 C). Yet, TEM and XRD analysis revealed that phase transformation into GdF_3 took place. Hence, while larger sizes may endow the NPs with chemical stability, size effects at the size scale accessible by our MW-assisted approach can be ruled out. Finally, it should be mentioned that the obtained LF-GdF_3 NPs exhibited a hexagonal crystalline phase. This is in contrast to GdF_3:Er^{3+},Yb^{3+} obtained from α-$NaGdF_4$:Er^{3+},Yb^{3+} core-only NPs, which crystallized in the orthorhombic phase. The presence of the undoped shell, *i.e.*, α-$NaGdF_4$, may explain this behaviour as pure α-$NaGdF_4$ was shown to transform into hexagonal GdF_3.

4.2.3 Formation of GdF_3 from OA-Capped α-$NaGdF_4$

Interestingly, the $NaGdF_4$-to-GdF_3 phase transformation took place only for the metastable α-phase of $NaGdF_4$, yet, not for the thermodynamically more stable β-phase. It is important to keep in mind that both samples only differed in their crystalline phase, while NP size and surface chemistry were intentionally kept constant to rule out any effect related to size or surface. Hence, the observed phase-selective behaviour can be correlated with the thermodynamic stability of the crystalline phase of the initial material. Overall, under the given conditions (low pH, room temperature), β-$NaGdF_4$ NPs were found to be chemically and thermodynamically stable enough to resist phase transformation into the hexagonal GdF_3 phase. In contrast, the metastability of the α-phase drove the transformation into the thermodynamically more stable GdF_3 phase.

Lastly, it should be mentioned that, in general, the orthorhombic phase of GdF_3 is thermodynamically favoured over the hexagonal polymorph at room temperature.[201, 212, 214, 216] Consequently, synthetic efforts are undertaken to stabilize the hexagonal phase as the more

efficient host lattice when aiming for optically active materials. For instance, Li *et al.* tuned hydrothermal reaction times and solvent compositions to selectively obtain either the hexagonal or orthorhombic phase of Eu^{3+}-doped GdF_3.[212] Zhao *et al.* achieved the hexagonal phase of GdF_3 via a hydrothermal approach through doping with Sr^{2+} and Ca^{2+}.[216] Thus, the here observed favoured crystallization of well-formed hexagonal GdF_3 NPs at room temperature is noteworthy with respect to the potential formation of their luminescent, Ln^{3+}-doped analogues (*vide infra*).

pH dependence. As mentioned above, treatment of sub-10 nm sized OA-capped α-$NaGdF_4$ at pH 3 did not result in any efficient transfer of the NPs from the organic into the aqueous phase. While lowering the pH to 1.5 led to LF-NPs in good yield, the crystalline α-$NaGdF_4$ phase could not be preserved. In order to investigate whether a pH higher than 1.5 but lower than 3 would grant access to LF-α-$NaGdF_4$ NPs, the ligand removal experiment was repeated at pH values 2.5, 2.0, and 1.0 (Figure 4.3). The large particle sizes of approximately 150-180 nm (Figure 4.4, Table 4.1) and the granular structure observed in TEM (Figure 4.3 (A-C)) indicate the formation of GdF_3, even at higher pH (2.5 and 2.0).

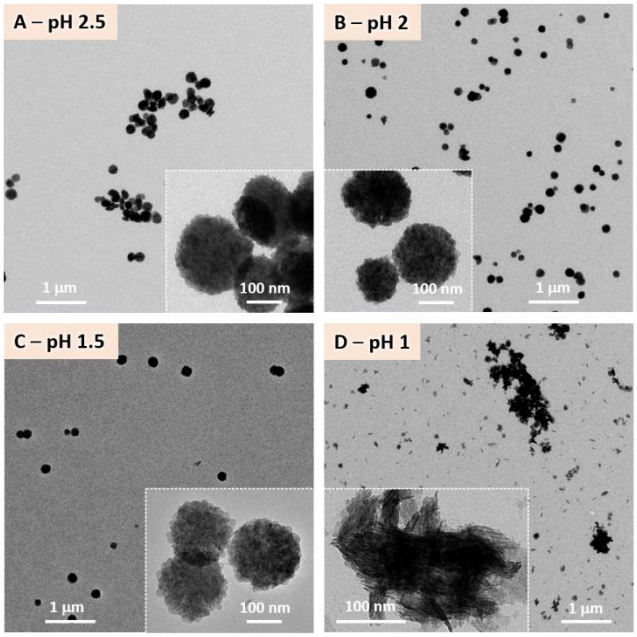

Figure 4.3. The effect of pH on ligand removal and phase transformation of OA-capped α-$NaGdF_4$ NPs. TEM images (higher magnification images are shown as insets) of LF particles obtained upon treatment of OA-capped α-$NaGdF_4$ NPs at (A) pH 2.5, (B) pH 2, (C) pH 1.5, and (D) pH 1. Treatment at pH 3 did not yield any particle transfer from the organic into the aqueous phase.

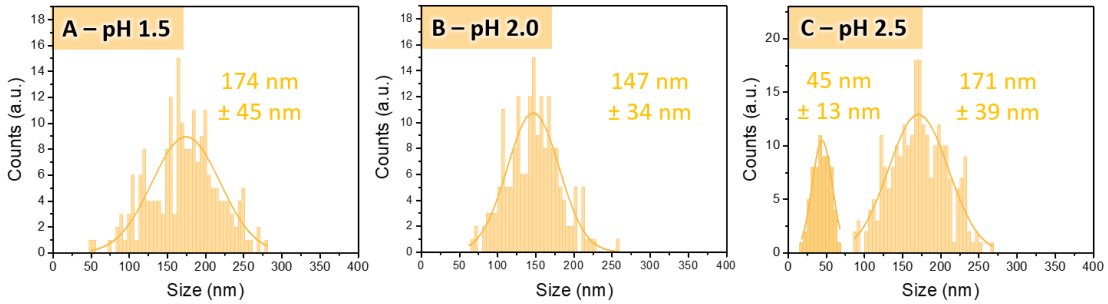

Figure 4.4. Average sizes and size distributions of particles obtained upon treatment of α-$NaGdF_4$ NPs for 20 h at (A) pH 1.5, (B) pH 2.0, and (C) pH 2.5, respectively. (C) In addition to the diameter, the average thickness of the plate-like structures is given as determined from plates that self-arranged perpendicular to the TEM grid. Similar dimensions were observed for the other GdF_3 structures.

Table 4.1. Overview of the experimental conditions used for the evaluation of the pH dependence of the ligand removal for α-$NaGdF_4$ NPs and size of the resulting GdF_3 NPs.

pH	Stirring Time (h)	Transfer into Aqueous Phase	GdF_3 Formation	GdF_3 Crystalline Phase	GdF_3 NP Diameter (nm)	GdF_3 NP Thickness (nm)
1		Yes	Yes	hexagonal	[a]	-
1.5		yes	Yes	hexagonal	174 ± 45	-
2	20	yes	Yes	hexagonal	147 ± 34	-
2.5		yes	Yes	hexagonal	171 ± 39	45 ± 13
3		no	No	no	[b]	-

[a] Due to the non-defined morphology of the obtained NPs, it was not possible to obtain any size distribution.
[b] At this pH, no product was found in the aqueous phase, yet, the OA-capped α-$NaGdF_4$ NPs could be easily recovered from the organic phase after precipitation with ethanol.

Phase transformation was further confirmed by XRD analysis (Figure 4.5). While some material was transferred from the organic into the aqueous phase upon treatment at pH 1.0, the resultant structures exhibited a poorly defined morphology that may be described as aggregates of small plate- and rod-like structures. According to XRD analysis, again, hexagonal GdF_3 was formed, yet of poor crystallinity as indicated by the broad and weak reflections.

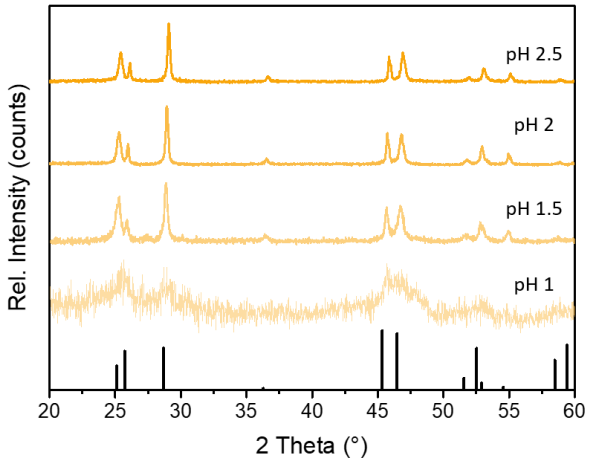

Figure 4.5. XRD patterns of particles obtained upon treatment of α-$NaGdF_4$ NPs for 20 h at pH 1, 1.5, 2, and 2.5, respectively. Reference**:** hexagonal EuF_3, PDF card [00-032-0373].

Time dependence. When developing a modified protocol for efficient ligand removal for sub-10 nm OA-capped α-$NaREF_4$ NPs, in addition to lowering pH, prolonging reaction times (20 h versus 2 h reported in the original work)[21] was found to increase the yield in LF-NPs. However, given the observed α-$NaGdF_4$-to-GdF_3 transformation, reaction times were reduced to assess the time dependence of the phase transformation. Therefore, α-$NaGdF_4$ NPs were stirred at pH 1.5 for different times: 1 h, 4 h, 8 h, and 20 h. Subsequent analysis by TEM (Figure 4.6) and XRD (Figure 4.7) did not reveal any significant time effect on the formation of GdF_3. Irrespective of the stirring time, the crystalline phase, morphology, *i.e.*, granularly structured plates, and size (Figure 4.6) of the GdF_3 NPs were retained. Based on these observations, a 4-h time frame was chosen for the following investigation of the chemical stability of α-$NaREF_4$ NPs and their possible transformation into REF_3 as a function of the RE^{3+} ion. Yet, as our phase-dependent study (Figure 4.1) revealed better stability for β-$NaGdF_4$ NPs, *i.e.*, stronger resistance towards phase transformation, the 20-h time frame was kept for all further studies on β-$NaREF_4$ NPs (*vide infra*).

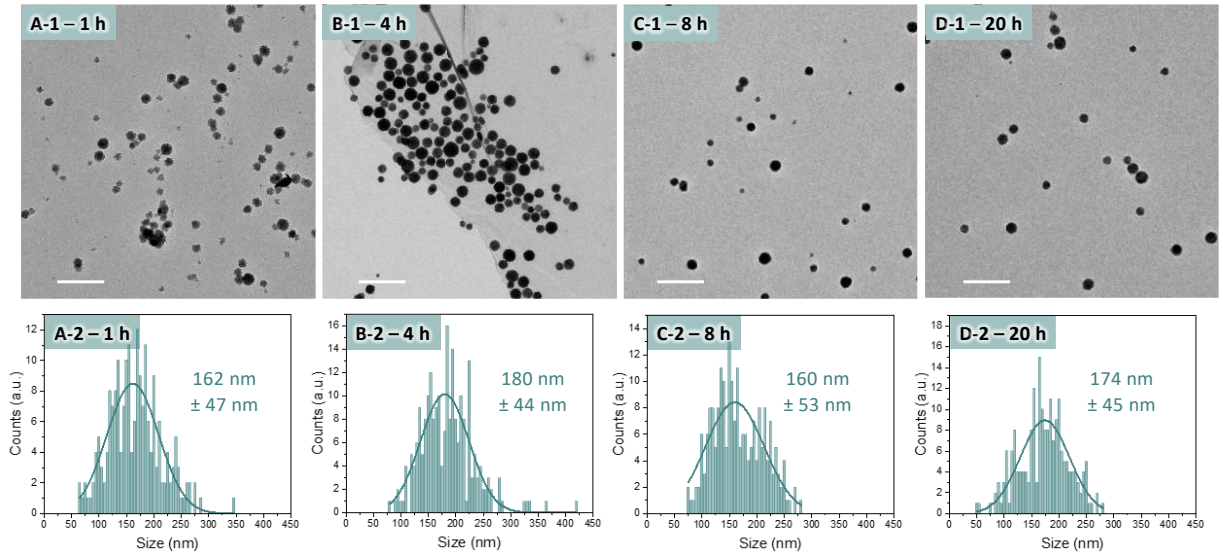

Figure 4.6. (1) TEM images and (2) size distributions of hexagonal GdF_3 particles obtained by stirring of α-$NaGdF_4$ NPs at pH 1.5 for (A) 1 h, (B) 4 h, (C) 8 h, and (D) 20 h, respectively. Scale bars: 1 μm.

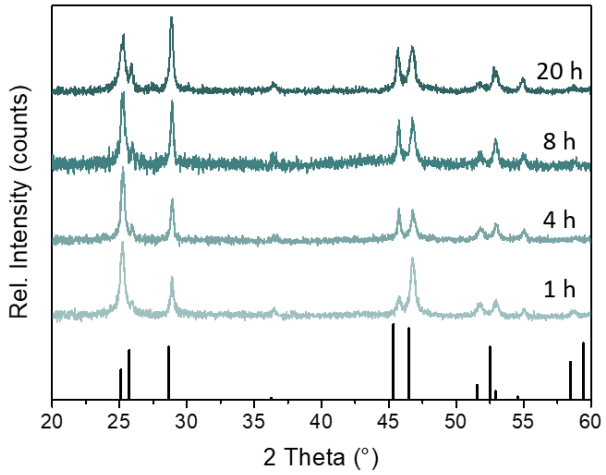

Figure 4.7. XRD patterns revealing hexagonal GdF_3 as the sole crystalline phase upon treatment of α-$NaGdF_4$ NPs at pH 1.5 for 1, 4, 8, and 20 h, respectively. Reference**:** hexagonal EuF_3, PDF card [00-032-0373].

4.2.4 RE^{3+} Ion Dependence of the Chemical Stability and Phase Transformation of $NaREF_4$ NPs

As already briefly mentioned, there is a strong influence of the RE^{3+} ion on the stability of the $NaREF_4$ phase, α or β. While the lighter RE^{3+} ions, Pr to Gd, favour the crystallization of β-$NaREF_4$, heavier RE^{3+} ions, Tb to Lu, tend to form α-$NaREF_4$.[31, 151] Y ion belongs to the class that preferentially crystallize in the α-phase, while La is mostly found in form of its binary fluoride, LaF_3 (which is the reason why the latter was excluded from this study).[31, 151] Similarly, different RE^{3+} ions favour either the hexagonal or the orthorhombic REF_3 phase, whereas the hexagonal phase is preferentially found for the lighter and the orthorhombic phase for the heavier RE^{3+} ions.[203] Given the interest in the various $NaREF_4$ materials beyond $NaGdF_4$ (*e.g.*, $NaDyF_4$ and $NaHoF_4$ for application as T_2 MRI CAs, $NaYF_4$ as host matrix for UCNPs, $NaNdF_4$ for use as photothermal therapy temperature probes, and $NaSmF_4$ for mass cytometry applications, among others)[109, 231-237], we stepped forward to investigate the chemical stability and possible $NaREF_4$-to-REF_3 phase transformation for a series of RE^{3+} ions and as a function of the $NaREF_4$ crystalline phase, α *versus* β.

α-$NaREF_4$ NPs; RE = Y, Pr, Nd, Sm, Eu, Gd, Tb, Dy, Ho, Er, Yb and Lu. The α-$NaREF_4$ NPs (RE ≠ Gd) were synthesized following the same MW-assisted method as used for α-$NaGdF_4$. XRD analysis confirmed that all obtained OA-capped NPs were phase-pure α-$NaREF_4$ (Figure 4.8). Across the series, the NPs exhibited a spherical morphology with comparable sizes in the sub-10 nm realm (Figure 4.9 (A-1) to (L-1) and Figure 4.10). Interestingly, TEM images obtained on NPs after ligand removal revealed a strong influence of the chosen RE^{3+} ion on morphology and size of the LF-NPs (Figure 4.9 (A-2) to (L-2) and Figure 4.11). From Pr to Eu, plate-like structures of granular morphology were obtained, similar to those found for GdF_3. Indeed, XRD analysis confirmed that those structures consisted of REF_3 crystalized in the hexagonal phase of the binary RE fluoride (Figure 4.12). For the light RE ions, α-$NaREF_4$ is not the most thermodynamically stable crystalline phase at room temperature. This relates to the here observed complete transformation of α-$NaREF_4$ NPs (RE = Pr to Gd) into hexagonal REF_3 – which, in turn, is thermodynamically more stable for these RE ions when compared to orthorhombic REF_3.

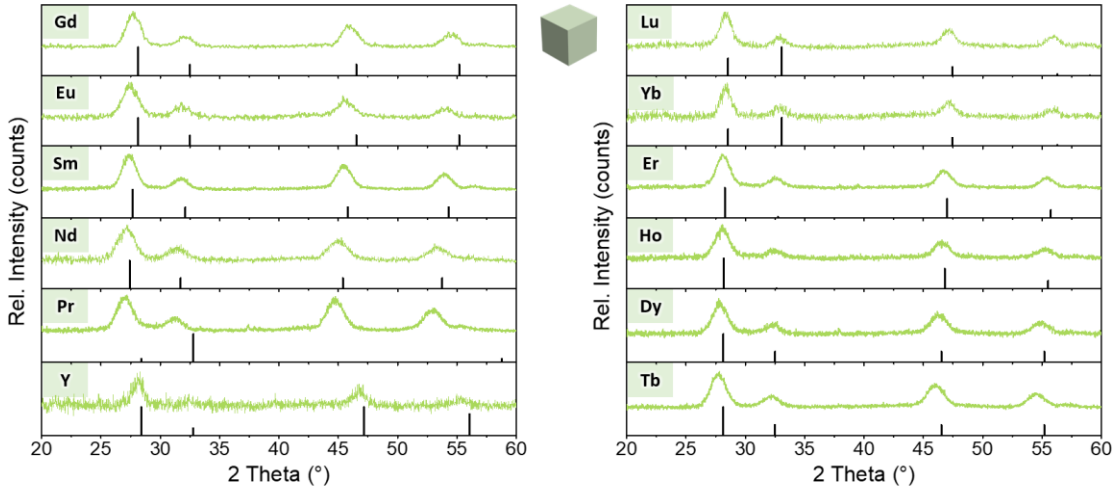

Figure 4.8. XRD patterns of α-$NaREF_4$ NPs obtained by microwave-assisted thermal decomposition. RE refers to the rare earth ions studied as labelled for each pattern. References: α-$NaYF_4$, PDF card [00-006-0342]; α-$NaPrF_4$, PDF card [00-022-1393]; α-$NaNdF_4$, PDF card [00-028-1114]; α-$NaSmF_4$, PDF card [00-027-0778]; α-$NaGdF_4$, PDF card [00-027-0697] (this card was also used for RE = Eu, Tb, Dy); α-$NaHoF_4$, PDF card [01-077-2040]; α-$NaErF_4$, PDF card [01-077-2041]; α-$NaYbF_4$, PDF card [01-077-2043] (this card was also used for RE = Lu).

Moreover, the K_{sp} of REF_3 is lower for RE at the beginning of the RE series, which further facilitates the nucleation of these NPs during the phase transformation process.[199] Noteworthy, there is a clear size trend for the transformed REF_3 NPs, showing a decrease in diameter and thickness of the plate-like structures from GdF_3 to PrF_3 (approximate diameters: Gd – 180 nm, Eu – 84 nm, Sm – 44 nm, Nd – 42 nm, Pr – 22 nm; see Figure 4.11 for size distributions and estimated thicknesses). Such trend in size as a function of the RE ion was previously observed for REF_3 NPs synthesized by a co-precipitation method.[238] A possible explanation was proposed based on the fact that the larger the radii of the RE, the higher is the stabilization of the surface charge of the starting REF_3 nuclei. This stabilization prevents their aggregation into super-structures of larger sizes, ultimately resulting in smaller REF_3 NPs.

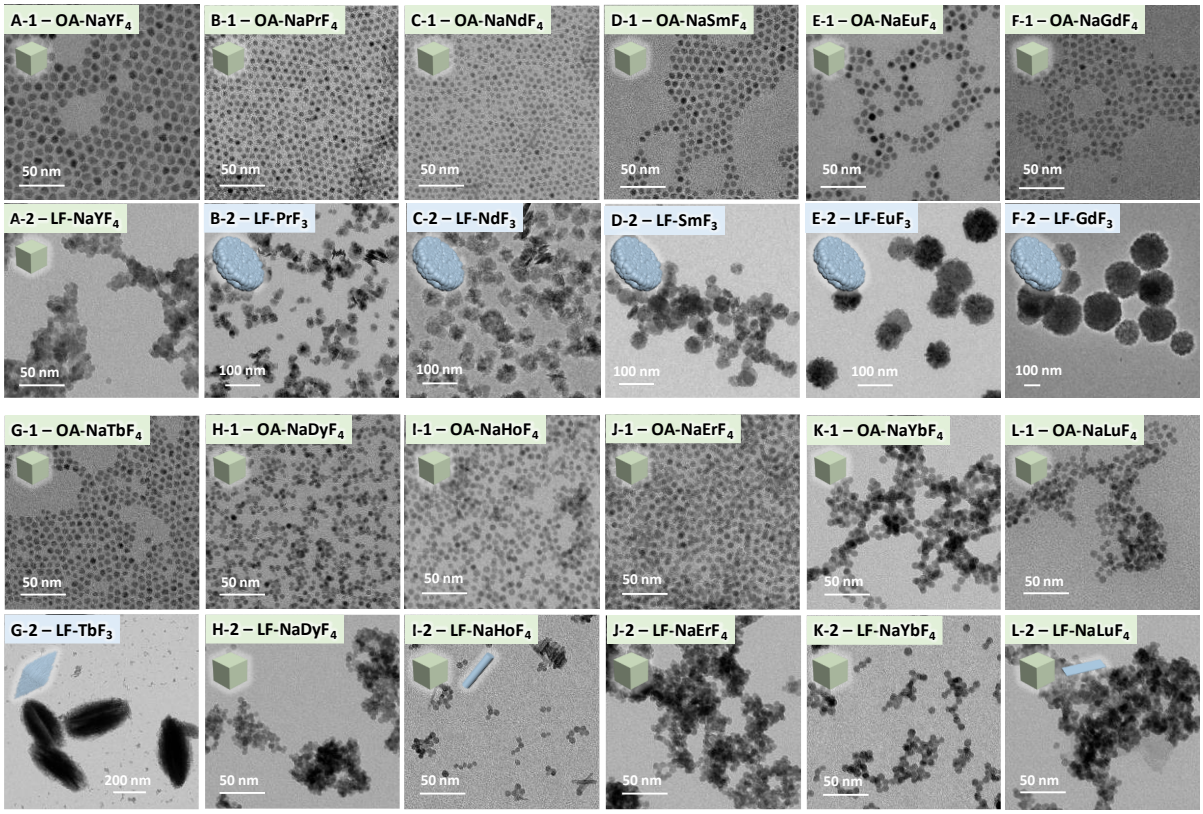

Figure 4.9. TEM images of (1) OA-capped α-$NaREF_4$ NPs as well as (2) LF particles obtained after treatment of the NPs shown in (1) at pH 1.5 for 4 h. RE refers to the rare earth ions studied as labelled in each image, A to L.

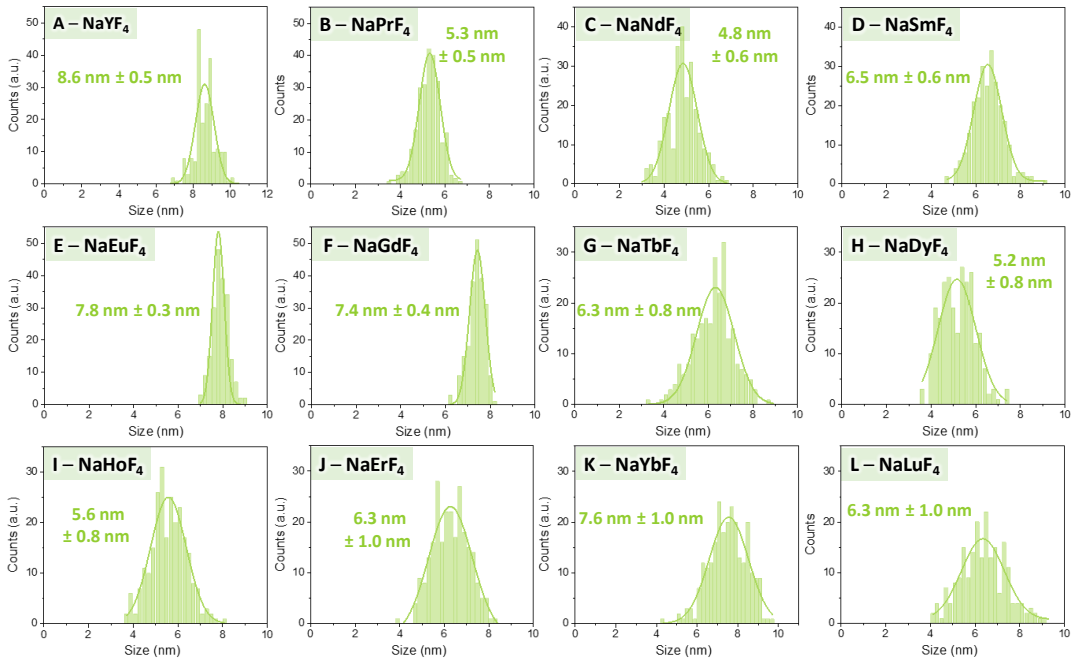

Figure 4.10. Average sizes and size distributions of the OA-capped α-$NaREF_4$ NPs used for ligand removal (pH 1.5, 4 h).

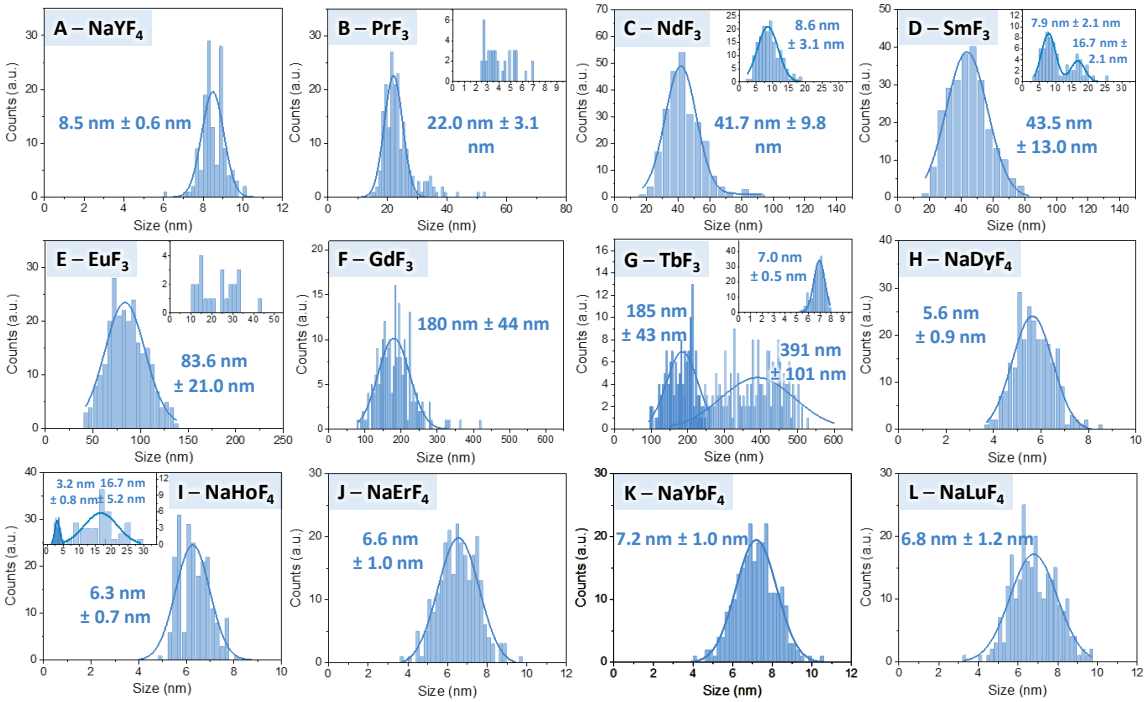

Figure 4.11. Average sizes and size distributions of the LF-NPs shown in Figure 4.9 (A2 to L2) obtained by treatment of the OA-capped α-$NaREF_4$ NPs at pH 1.5 for 4 h. The insets in B to E provide an estimated value for the thickness of the obtained plates. Dimensions given in G correspond to the length, width and thickness of the TbF_3 bundle-like structures. The inset in I shows the length and width of the nanorods ascribed to HoF_3 as minor, secondary phase.

For the RE from Tb to Lu, including Y, α-$NaREF_4$ is known as the thermodynamically stable phase. In line with this, LF-α-$NaREF_4$ NPs were obtained when choosing RE ions from Dy to Lu as well as Y (Figure 4.9 and Figure 4.12). Herein, the particle size of the LF-NPs did not significantly differ from that of the starting OA-capped NPs (Figure 4.10 and Figure 4.11). Yet, it must be noted that in case of Ho and Lu, both XRD and TEM provided evidence for at least minor presence of HoF_3 and LuF_3 in their orthorhombic crystalline phase. For Ho, this is supported by the X-ray reflection at a 2θ value of 30.4 °, which can be ascribed to orthorhombic HoF_3. The observation of orthorhombic HoF_3 rather than its hexagonal analogue is not surprising given Ho's position within the RE series favouring orthorhombic REF_3 as stable phase. In addition, the rod-like morphology of structures seen in TEM along with spherical NPs coincides with that reported elsewhere for orthorhombic REF_3.[211, 238] For Lu, unambiguous phase assignment to α-$NaLuF_4$ or orthorhombic LuF_3 was challenging due to the overlap of the characteristic X-ray reflections for both phases in

combination with the broadness of the reflections in the recorded pattern due to small particle size. Nevertheless, reflections in the 2θ range from 25° to 35° indicated the formation of LuF_3 in addition to α-$NaLuF_4$ (most intense LuF_3 reflections at 23.48° and 25.74°). The observation of ribbon-like structures as secondary morphology in TEM provided further evidence for the presence of orthorhombic LuF_3 (note that prolonged pH treatment of α-$NaLuF_4$, *i.e.*, 20 h, strongly promoted the formation of these ribbons as shown in Figure 4.13).[208, 211]

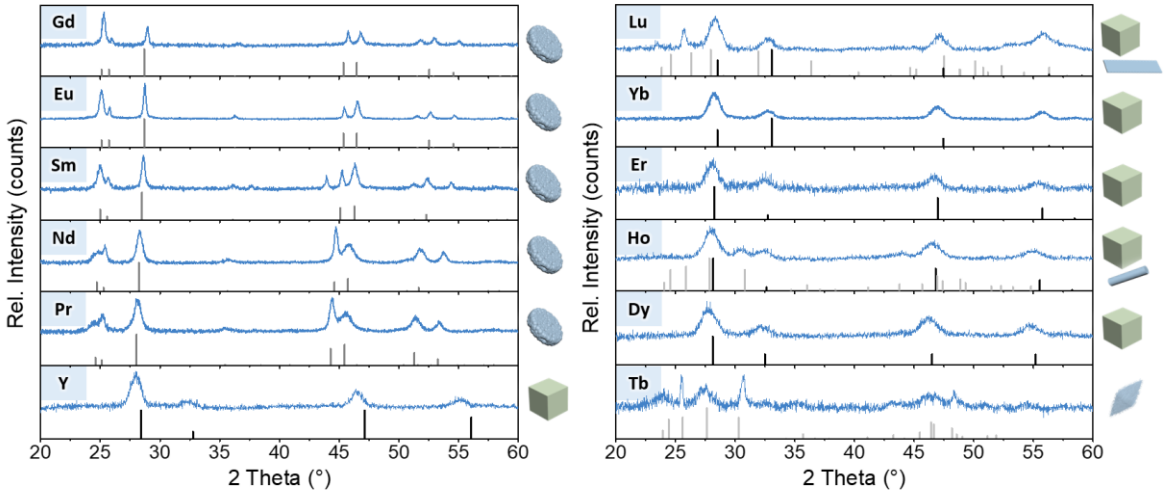

Figure 4.12. XRD patterns of LF-NPs obtained from α-$NaREF_4$ NPs upon stirring at pH 1.5 for 4 h. References: black lines – α-$NaYF_4$, PDF [00-006-0342]; α-$NaGdF_4$, PDF card [00-027-0697], used for α-$NaDyF_4$; α-$NaHoF_4$, PDF card [01-077-2040]; α-$NaErF_4$, PDF card [01-077-2041]; α-$NaYbF_4$, PDF card [01-077-2043] (this card was also used for α-$NaLuF_4$); grey lines – hexagonal PrF_3, PDF card [00-046-1167]; hexagonal NdF_3, PDF card [00-009-0416]; hexagonal SmF_3, PDF card [00-012-0792]; hexagonal EuF_3, PDF card [00-032-0373] (this card was also used for hexagonal GdF_3); orthorhombic TbF_3, PDF card [00-037-1487]; orthorhombic HoF_3, PDF card [00-023-0284]; orthorhombic LuF_3, PDF car [00-032-0612].

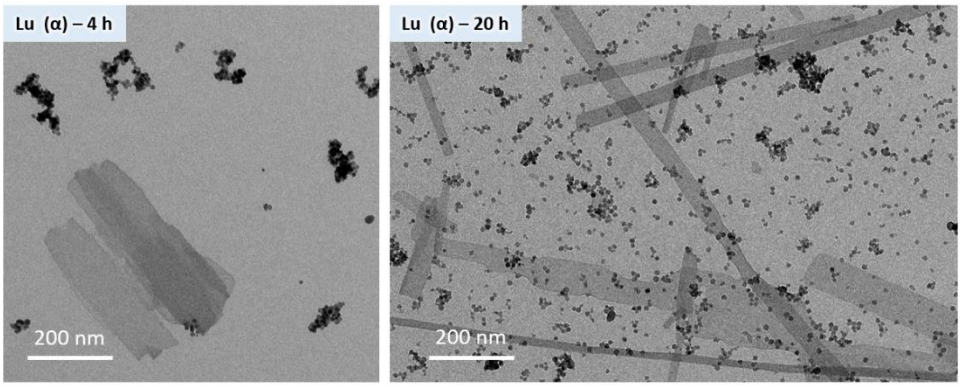

Figure 4.13. TEM image of LF-NPs and ribbon-like structures obtained upon stirring OA-capped α-$NaLuF_4$ NPs at pH 1.5 for 4 and 20 h, respectively.

To further validate the assignment of the crystalline phases to specific morphologies, SAED analysis was performed in the selected regions highlighted in Figure 4.14. The interplanar distances obtained from the SAED patterns (calculations are shown in Chapter 3.5.3) for the small spherical NPs of the Ho-based sample (Figure 4.14, (A/B-2)) reveal an interplanar distance of 3.15 Å attributed to the α-$NaHoF_4$ (1 1 1) planes (Table 4.2, highlighted in green). These findings confirm that α-$NaHoF_4$ partially resisted the phase transformation into HoF_3. Further, the size of the small spherical LF-NPs (Figure 4.11 I) was very close to the size of the used OA-capped NPs (Figure 4.10 I), which corroborates the suggested phase/morphology assignment. SAED patterns of the rod-like structures of the same sample (Figure 4.14, (A/B-1)) correspond to an interplanar distance of 3.02 Å, which can be assigned to the (2 1 0) planes of the orthorhombic HoF_3 crystalline structure (Table 4.2, highlighted in green). Overall, these observations show that a phase transformation started to take place in this sample, with a clear morphological difference between the two phases as confirmed by SAED and TEM analysis.

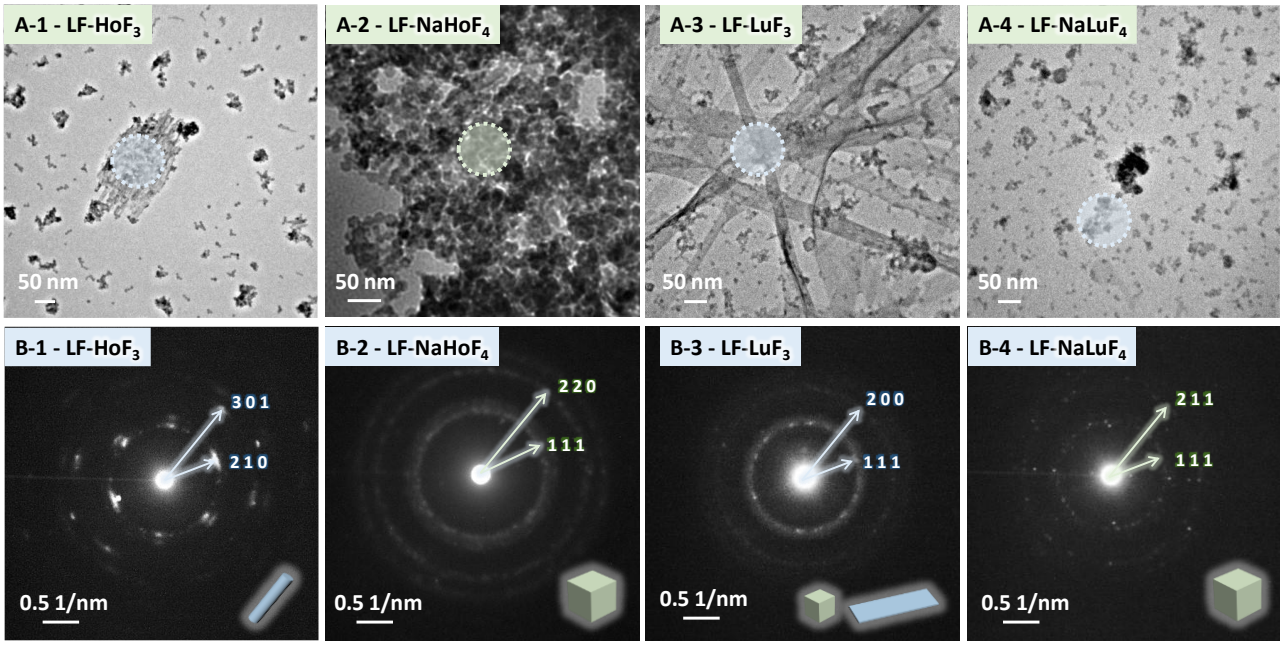

Figure 4.14. (A) TEM images showing the highlighted areas from which the SAED patterns shown in (B) were obtained. (1) LF-HoF_3 structures of rod-like morphology, (2) LF-$NaHoF_4$ NPs, (3) LF-LuF_3 band-like structures; (4) LF-$NaLuF_4$ NPs.

Table 4.2. Comparison between the values of the interplanar distances (d) calculated from Scherrer equation using the main reflections in the recorded XRD patterns shown in Figure 4.12, those obtained from the first and second rings of the SAED patterns shown in Figure 4.14, and the standard values from the PDF cards for the Ho- and Lu-based samples.

Sample	2θ (°)	d_{XRD} (Å)	d_{SAED} (Å)	d_{PDF} (Å)	*h k l*	Crystalline Phase	PDF #
LF-$NaHoF_4$	27.94	3.19	3.15	3.17	1 1 1	α-$NaHoF_4$	01-077-2040
	30.40	2.94	3.02	2.90	2 1 0	HoF_3	00-023-0284
	32.36 *	2.77	-	2.74	2 0 0	α-$NaHoF_4$	01-077-2040
	46.42 †	1.95	1.91	1.94	2 2 0	α-$NaHoF_4$	01-077-2040
			1.90	1.94	1 3 1	HoF_3	00-023-0284
LF-$NaLuF_4$	25.74 *	3.46	-	3.38	0 2 0	LuF_3	00-032-0612
	28.34	3.15	3.09	3.19	1 1 1	LuF_3	00-032-0612
			3.10	3.13	1 1 1	α-$NaLuF_4$	01-077-2043
	32.80 *	2.73	-	2.70	2 0 0	α-$NaLuF_4$	01-077-2043
	47.20 †	1.92	1.88	1.91	2 2 0	α-$NaLuF_4$	01-077-2043
			1.90	1.91	1 3 1	LuF_3	00-032-0612

* These diffractions were present in the XRD patterns but were not observed by SAED analysis.
† These diffractions were present both in the XRD patterns and SAED analysis, however, they are common to both crystalline phases and, therefore, are not suitable to distinguish between the α-$NaREF_4$ and REF_3 phases.

For the Lu-based samples, however, both the SAED patterns of the small spherical NPs (Figure 4.14, (A/B-4)) and of the ribbon-like structures (Figure 4.14, (A/B-3)) showed very similar interplanar distances of 3.09 and 3.10 Å, respectively, which can be attributed to the (1 1 1) planes from either the α-$NaLuF_4$ or the orthorhombic LuF_3 crystalline phases (Table 4.2). Therefore, an unambiguous attribution of the planes was not possible, as the interplanar distances found from the SAED patterns and the respective standards are too close to both the α-$NaLuF_4$ and orthorhombic LuF_3 reflections. This observation is in line with the XRD patterns shown in Figure 4.12, where the presence of the cubic-phase $NaLuF_4$ is clear but a phase mix with the orthorhombic LuF_3 cannot be ruled out. Nevertheless, having been able to clearly ascribe a crystalline phase to each of the morphologies in the Ho-based samples, we propose a similar case for the Lu-based samples. As such, the size of the small LF-NPs was again in good agreement with

that of the initial OA-capped $NaLuF_4$ NPs, indicating a certain resistance of the sample to phase transformation. Moreover, the ribbon-like structures shown in Figure 4.13 and Figure 4.14 (A-3) have been described by Becerro *et al.* as a possible morphology adopted by orthorhombic LuF_3 as reported.[208]

Lastly, Tb takes a special position in the here discussed RE series. According to TEM, sub-micron sized bundle-like structures were formed through self-assembly of smaller NPs upon stirring of α-$NaTbF_4$ at pH 1.5 for 4 h. As obvious from XRD analysis, these structures consist of pure orthorhombic TbF_3, the most stable REF_3 phase for the heavier RE ions.

To provide a first conclusion, these results demonstrate that the stability of α-$NaREF_4$ NPs under acidic conditions used for efficient ligand removal (pH 1.5) and a possible phase transformation into REF_3 are highly dependent on RE ion choice. Generally speaking, the more thermodynamically stable the respective α-$NaREF_4$ phase is in comparison to its β-counterpart, the more resistant it will be to the referred phase transformation; hence, allowing the synthesis of LF-α-$NaREF_4$ NPs with RE = Dy to Lu and Y. Yet, some care must be taken with regard to the formation of secondary REF_3 phases, as observed in case of Ho and Lu. Less thermodynamically stable α-$NaREF_4$ phases tend to undergo phase transformation, herein resulting in crystalline hexagonal (Pr to Gd) or orthorhombic (Tb) REF_3, depending on the preferred binary fluoride phase for the respective RE ion.

β-$NaREF_4$ NPs; RE = Pr, Nd, Sm, Eu, Gd, Tb, and Dy. As shown above, for α-$NaREF_4$ NPs, phase transformation to REF_3 upon ligand removal strongly depended on the thermodynamic stability of the crystalline phase of the fluorides, being determined by RE^{3+} ion choice. It was also shown that the crystalline phase of $NaGdF_4$ – α *versus* β – had a strong influence on whether or not LF-$NaGdF_4$ NPs could be obtained (namely, only in case of β, yet not in case of α due to phase transformation).

To further elucidate this phase and RE ion dependence, we extended our study towards a series of β-$NaREF_4$ NPs with RE = Pr, Nd, Sm, Eu, Gd, Tb, and Dy. The selection of these RE ions was determined by the $NaREF_4$ compositions accessible in the hexagonal crystalline phase by MW-assisted synthesis. Successful synthesis of β-$NaREF_4$ NPs was confirmed by XRD (Figure 4.15) and

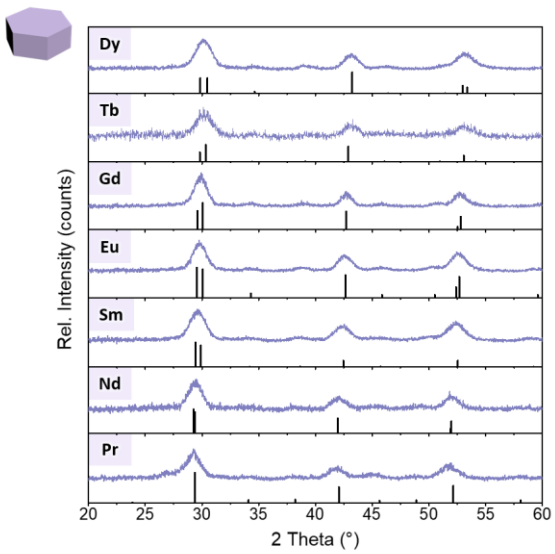

Figure 4.15. XRD patterns of β-$NaREF_4$ NPs obtained by MW-assisted approach. RE refers to the rare earth ions studied as labelled for each pattern. References: β-$NaPrF_4$, PDF card [01-082-4240]; β-$NaNdF_4$, PDF card [00-027-0756]; β-$NaSmF_4$, PDF card [00-027-0779]; β-$NaEuF_4$, PDF card [00-028-1085]; β-$NaGdF_4$, PDF card [01-080-8787]; β-$NaTbF_4$, PDF card [00-027-0809]; β-$NaDyF_4$, PDF card [00-027-0687].

TEM (Figure 4.16 (A-1) to (G-1)). The latter revealed spherical particles of homogeneous sizes at the sub-10 nm level with narrow size distributions (Figure 4.17). TEM images and XRD patterns of each of the compositions after ligand removal are presented in

Figure **4.16** (A-2) to (G-2) and 6H. Accordingly, β-$NaREF_4$ with RE = Pr, Nd, and Sm were the only compositions that underwent phase transformation, resulting in hexagonal-phase REF_3 plate-like particles, similar to those obtained from the α-$NaREF_4$ polymorphs. Conversely, in case of the other RE (Eu to Dy), LF-β-$NaREF_4$ were successfully transferred into the aqueous phase. The very weak reflection at 25.12° in the XRD pattern of LF-$NaEuF_4$ (Figure 4.16 H) may indicate an early stage of phase transformation to hexagonal EuF_3, making Eu the borderline RE ion with respect to phase transformation.

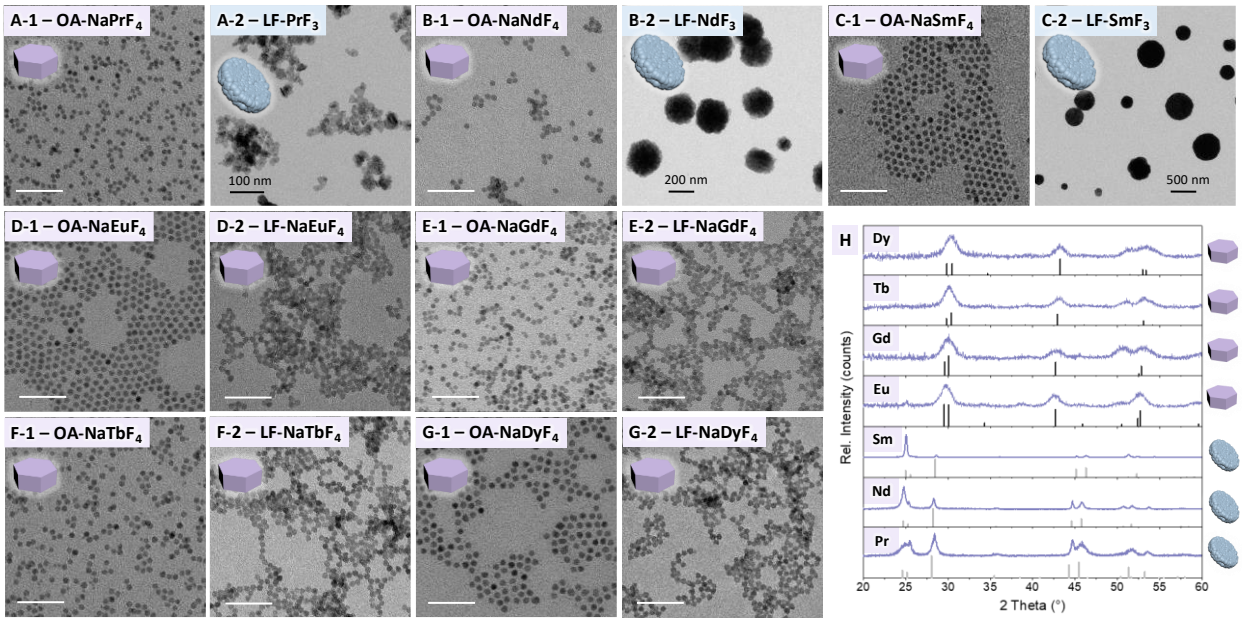

Figure 4.16. (A-G) TEM images of (1) OA-capped β-$NaREF_4$ NPs and (2) their respective LF particles obtained by stirring at pH 1.5 for 20 h. RE = (A) Pr, (B) Nd, (C) Sm, (D) Eu, (E) Gd, (F) Tb, and (G) Dy. Scale bars: 50 nm (unless noted otherwise). (H) XRD patterns of LF β-$NaREF_4$ (RE = Eu, Gd, Tb, Dy) and hexagonal REF_3 (RE = Pr, Nd, Sm) NPs, respectively. References: grey lines – hexagonal PrF_3, PDF card [00-046-1167]; hexagonal NdF_3, PDF card [00-009-0416]; hexagonal SmF_3, PDF card [00-012-0792] ; black lines – β-$NaEuF_4$, PDF card [00-028-1085]; β-$NaGdF_4$, PDF card [01-080-8787]; β-$NaTbF_4$, PDF card [00-027-0809]; β-$NaDyF_4$, PDF card [00-027-0687].

Overall, two trends were observed. First, β-$NaREF_4$ NPs exhibited a higher chemical stability and resistance towards phase transformation than their cubic counterparts when approaching the lighter RE ions – down to Eu *versus* Dy in case of α-$NaREF_4$ NPs. Second, despite their good thermodynamic stability, the lightest β-phase ternary fluorides (RE= Pr to Sm) transformed into hexagonal REF_3. This speaks for a competition in terms of stability between the binary and the ternary fluorides of these RE ions, the hexagonal REF_3 phase becoming most stable when choosing a sufficiently light RE ion.

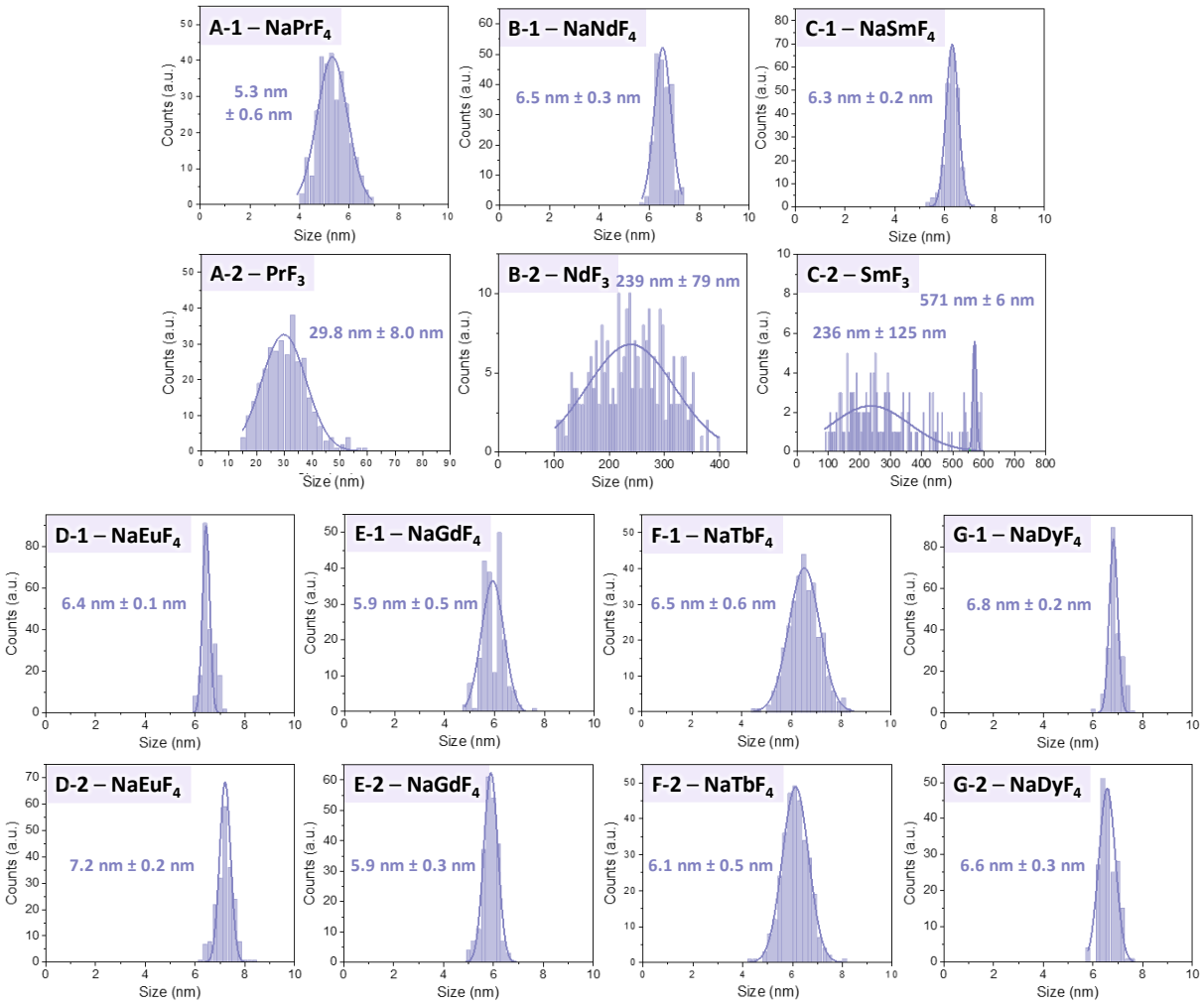

Figure 4.17. Average particle sizes and size distributions of (1) OA-capped β-$NaREF_4$ NPs and (2) their respective LF counterparts obtained by stirring at pH 1.5 for 20 h. RE = (A) Pr, (B) Nd, (C) Sm, (D) Eu, (E) Gd, (F) Tb, and (G) Dy.

4.2.5 Ln^{3+} Dopant Influence on the Formation of REF_3 From OA-Capped Ln^{3+}-Doped α/β-$NaGdF_4$ (Ln = Nd, Eu, Tb, Er/Yb)

$NaGdF_4$ is receiving attention as host matrix for optically active Ln^{3+} ions, particularly at the nanoscale. Excitation in NIR-I (700-950 nm) and emission in NIR-II (1000-1350 nm) or NIR-III (1550-1870 nm) biological windows as well as in the UV-visible is particularly significant for a gamut of biomedical applications. [197, 232, 239] For instance, when doped into a host lattice such as $NaGdF_4$, the dopant pair Er^{3+}/Yb^{3+} gives rise to UC and NIR-III emission under 980-nm excitation.

Nd^{3+} constitutes an excellent choice when seeking NIR-II emission. [233, 239, 240] Being excited with 808-nm light, the Nd^{3+} dopant has further been established as an interesting alternative to 980-nm excited Yb^{3+}, reducing sample heating and increasing penetration depth into biological tissue. [240, 241] Doping with Eu^{3+} or Tb^{3+} ions enables downshifting properties, yielding visible emission under UV excitation, and resulting nanomaterials have been proposed for applications ranging from in vitro tumour marker detection[242] to aptamer sensors[243]. As many of the aforementioned applications require water-dispersibility or, more generally, tuning of the NP surface chemistry, we included Ln^{3+}-doped α-and β-$NaGdF_4$ NPs in this study and evaluated the influence of the Ln^{3+} dopant on the $NaGdF_4$-to-GdF_3 phase transformation. A set of OA-capped Ln^{3+}-doped α- and β-$NaGdF_4$ NPs were successfully synthesized as confirmed by XRD and TEM analysis (Figure 4.18 (A- 1) to (E-1) and Figure 4.19-1). Nd, Eu, and Tb (dopant concentration: 10 mol%) as well as Er/Yb (dopant concentration: 2 and 20 mol%, respectively) were chosen as dopants for α-phase NPs for two reasons: (i) due to their significance for optical applications (*vide infra*) and (ii) as constituting representative candidates of the lighter and heavier ions of the RE series, that have different impact on phase transformation as previously described (*vide supra*). Similarly, this was our rational for choosing Nd and Er/Yb as exemplary dopants for β-$NaGdF_4$ NPs.

For ligand removal, all samples were stirred at pH 1.5 for 20 h. XRD analysis and electron microscopy of the NPs before and after the treatment clearly showed phase transformation from α-$NaGdF_4$:Ln^{3+} to GdF_3:Ln^{3+}, along with morphological changes, irrespective of dopant choice. The Eu, Tb, and Nd-doped α-$NaGdF_4$ NPs, respectively, transformed into pure hexagonal Ln^{3+}-doped GdF_3 NPs, which exhibited a plate-like morphology with a mean diameter of *ca.* 86, 144 and 185 nm, respectively (Figure 4.18 (A-2) and B/E(3-4)). The thickness of Tb-doped GdF_3 plates was estimated by SEM as *ca.* 38.5 nm (Figure 4.20).

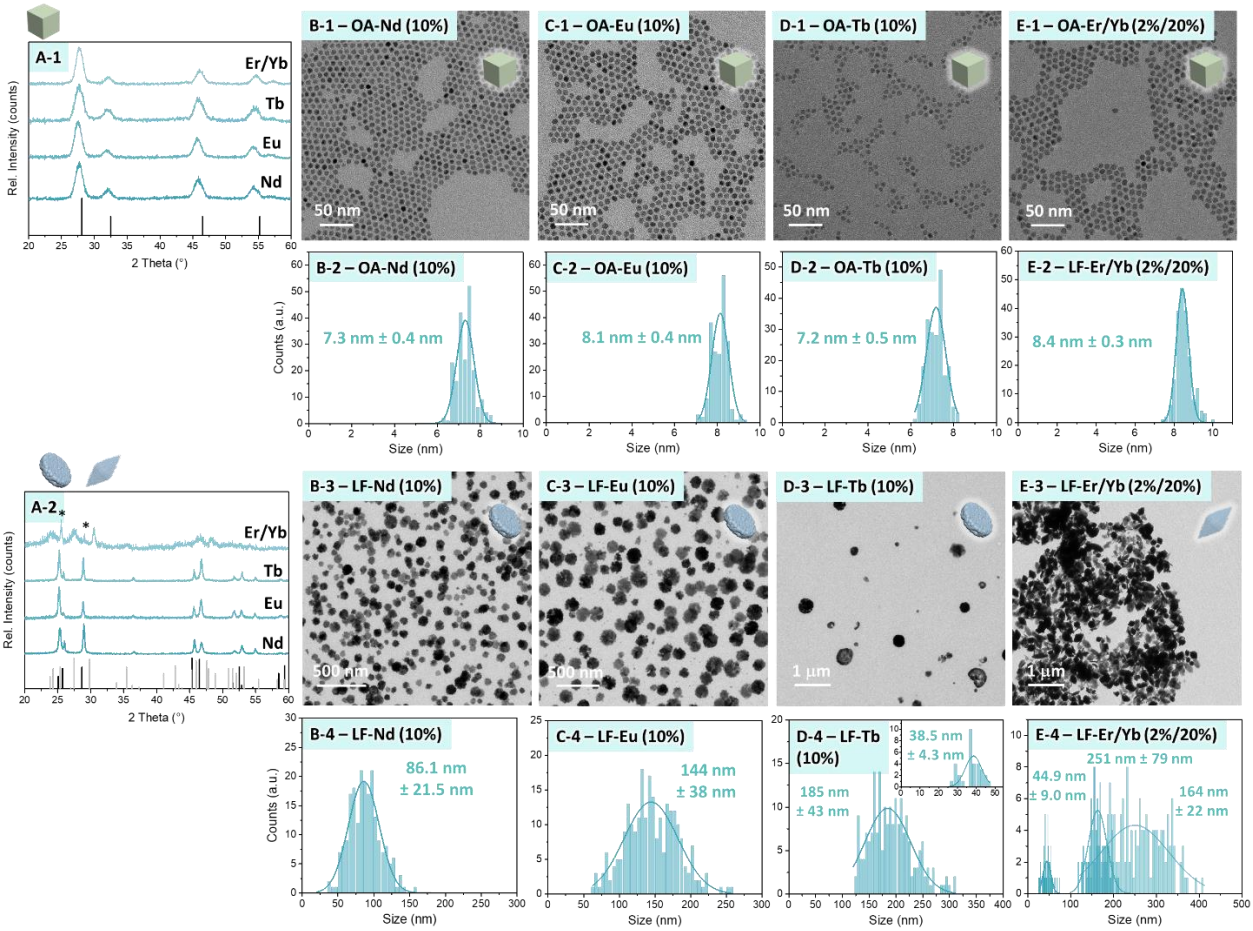

Figure 4.18. (A-1) XRD patterns of OA-capped α-$NaGdF_4$ NPs doped with 10% Nd^{3+}, 10% Eu^{3+}, 10% Tb^{3+}, and 2%/20% Er^{3+}/Yb^{3+}, respectively. (A-2) XRD patterns of hexagonal LF-GdF_3 doped with 10% Nd^{3+}, Eu^{3+}, and Tb^{3+}, respectively, as well as GdF_3 doped with 2%/20% Er^{3+}/Yb^{3+} exhibiting an orthorhombic crystalline phase (the sharp reflections at 25.5° and 29.1° [marked by *] point toward the presence of hexagonal GdF_3 as secondary phase). References: α-$NaGdF_4$, PDF card [00-027-0697] (black lines in A-1); hexagonal EuF_3 (for GdF_3), PDF card [00-032-0373] (black lines in A-2); orthorhombic GdF_3, PDF card [00-049-1804] (light grey lines). (B-E) TEM images and their corresponding size distributions of (1-2) OA-capped α-$NaGdF_4$ and (3-4) LF-GdF_3 particles doped with (B) 10% Nd^{3+}, (C) 10% Eu^{3+}, (D) 10% Tb^{3+}, and (E) 2%/20% Er^{3+}/Yb^{3+}, respectively.

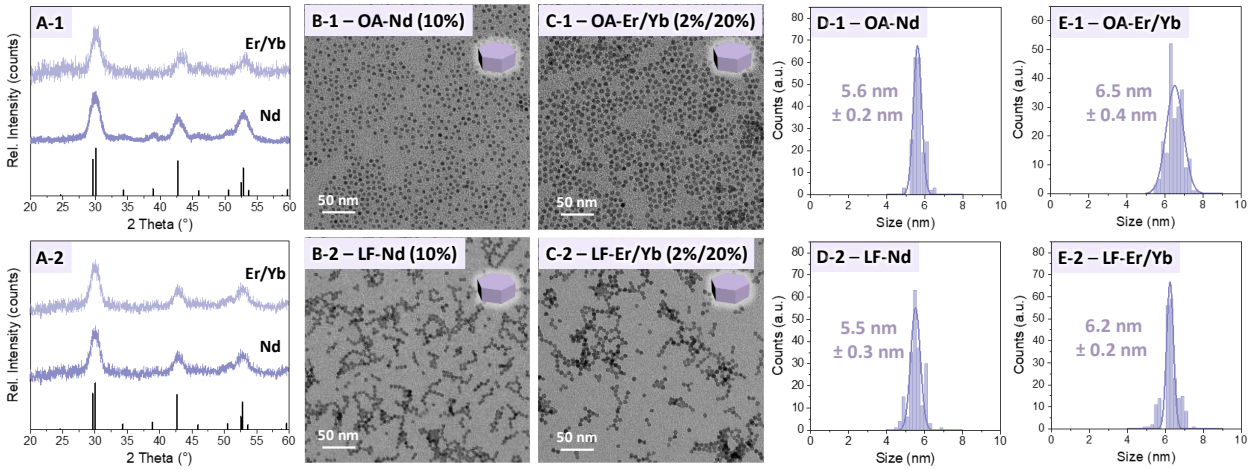

Figure 4.19. XRD patterns of (A-1) OA-capped and (A-2) LF-β-$NaGdF_4$ NPs doped with 10% Nd^{3+} and 2%/20% Er^{3+}/Yb^{3+}, respectively. References: β-$NaGdF_4$, PDF card [01-080-8787]. (B-C) TEM images of (1) OA-capped and (2) LF-β-$NaGdF_4$ NPs doped with (B) 10% Nd^{3+}, and (C) 2%/20% Er^{3+}/Yb^{3+}, respectively. All LF-NPs were obtained by stirring at pH 1.5 for 20 h. The respective average sizes and size distributions are shown in (D) and (E).

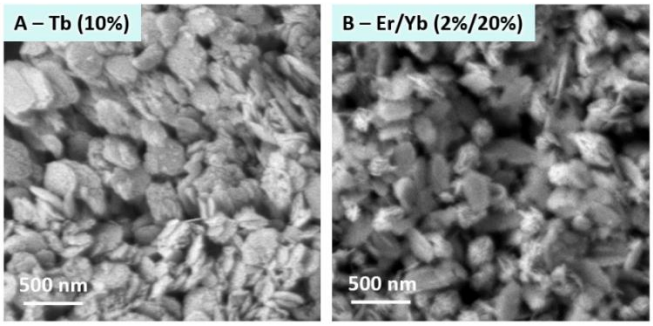

Figure 4.20. SEM images of LF- (A) hexagonal GdF_3 doped with 10% Tb^{3+} and (B) orthorhombic GdF_3 co-doped with 2% Er^{3+} and 20% Yb^{3+}. Both samples were obtained upon stirring of the respective Ln^{+}-doped α-$NaGdF_4$ NPs at pH 1.5 for 20 h.

In agreement with results obtained on REF_3 particles deduced from α-$NaREF_4$ (*vide supra*), a size trend was noticeable for the formed hexagonal GdF_3 NPs depending on dopant ion choice: while the OA-capped α-$NaGdF_4$:Ln^{3+} NPs exhibited comparable sizes ranging from 7.2 to 8.1 nm, the size of the GdF_3:Ln^{3+} plates increased from Nd^{3+} to Tb^{3+}. Consequently, phase and morphology evolvement of the Ln^{3+}-doped α-$NaREF_4$ NPs (RE = Eu, Tb, Nd) upon ligand removal coincided with that of the undoped α-$NaREF_4$ NPs; hence, following the dominant behaviour of the host

material with respect to stability and phase transformation. For the hexagonal phase, XRD patterns and TEM images confirmed that Ln^{3+}-doped β-$NaGdF_4$ NPs were successfully transferred into the aqueous phase, with no morphology or phase transformation and irrespective of Ln^{3+} ion choice, thus, corroborating results obtained on undoped NPs (Figure 4.17). In contrast, orthorhombic GdF_3 was formed when Er/Yb-doped α-$NaGdF_4$ NPs underwent the same procedure (Figure 4.18 (A-2)). Recalling that Er and Yb belong to the heavier RE ions that foster crystallization of orthorhombic REF_3, the Er/Yb dopant concentration of 22 mol% in total was high enough to drive the crystallization of the Gd-based host towards the orthorhombic GdF_3 phase. It should be noted that some hexagonal phase GdF_3 impurity may be present as evidenced by the sharp X-ray reflections at 25.5° and 29.1°. Nevertheless, TEM and SEM images showed irregularly shaped GdF_3 structures at the nano- and sub-micron scale, some of which exhibited the characteristic bundle-like structure of orthorhombic REF_3 (Figure 4.18 (E-1) and Figure 4.20).[203]

The relative stability of the $NaREF_4$ and REF_3 crystalline phases depending on the RE ion is summarized in Figure 4.21. These findings unveil the importance to carefully consider the entire NP composition and not only the major RE component of the host lattice when choosing an adequate procedure for surface modification of $NaREF_4$-type NPs.

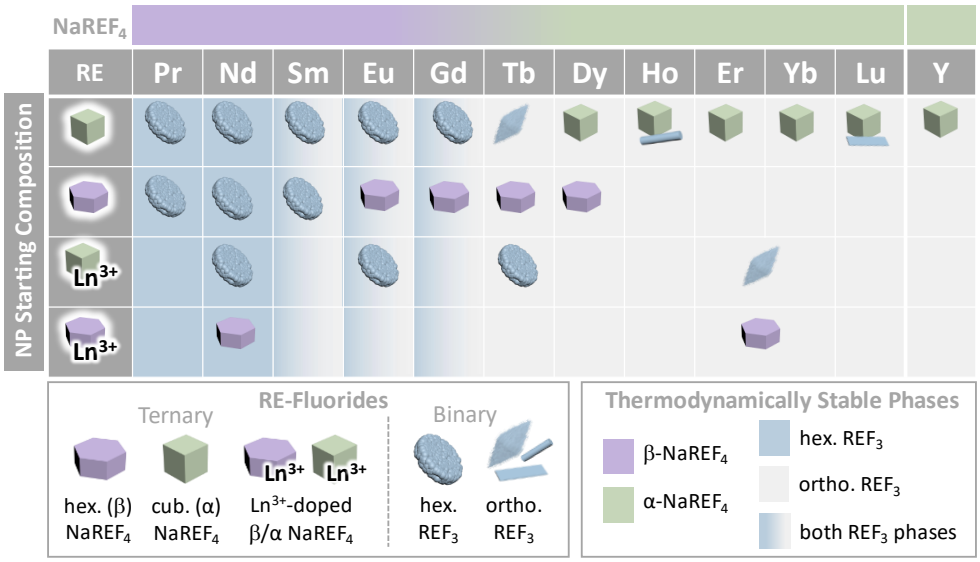

Figure 4.21. Representation of the relative stability of the $NaREF_4$ and REF_3 crystalline phases depending on the RE ion.

4.2.6 Optical Properties

The intrinsic spectroscopic features of optically active Ln^{3+} are a consequence of the intra-configurational 4f transitions, that experience a low influence of the crystal field. Therefore, regardless of the host matrix the Ln^{3+} is doped into, the ion's characteristic emission bands will appear at the same wavelengths.[244] However, the change in the symmetry of the site where the Ln^{3+} ion is placed in a host matrix can lead to different splitting and intensity ratios between these emission bands.

UV-Excited OA-α-$NaGdF_4$ and LF-GdF_3 NPs Doped with Eu^{3+} or Tb^{3+}. Excitation and emission spectra recorded for Eu^{3+}- and Tb^{3+}-doped NPs are given in Figure 4.22 (A-1/2) and (B-1/2), respectively. The corresponding energy level diagrams are shown in Figure 4.23. Characteristic excitation lines of the Gd^{3+} ion indicate a possible indirect excitation of Eu^{3+} and Tb^{3+}, respectively, through the Gd^{3+} ions of the host matrix. Indeed, for Tb^{3+}, the most efficient excitation was at 311 nm, corresponding to the Gd^{3+} $^6P_{5/2}$ level. Yet, in case of Eu^{3+}, the direct excitation pathway was found more efficient, as the band at 393 nm (Eu^{3+} $^7F_0 \rightarrow {}^5L_6$) was the most intense. Interestingly, the excitation spectra of the OA-α-$NaGdF_4$:Ln^{3+} doped with either Eu^{3+} or Tb^{3+} showed a large excitation band from 290 to 350 nm, which is not present in the excitation spectra of the respective LF-GdF_3 NPs. This broad band can be attributed to the presence of OA/OAm surface groups anchored to the surface of the as-synthesized NPs. [245]

All Eu^{3+}- and Tb^{3+}-doped samples showed emission in the red and green wavelength region, respectively, which is characteristic for the f–f transitions of these Ln^{3+} ions and which can be ascribed to the Eu^{3+} $^5D_0 \rightarrow {}^7F_J$ (J = 1-4) and Tb^{3+} $^4D_4 \rightarrow {}^7F_J$ (J = 6-3) transitions. Eu^{3+} is frequently used as an optical probe to assess the local symmetry of Ln^{3+} ions in a host matrix. [246] The forced electric-dipole allowed $^5D_0 \rightarrow {}^7F_2$ transition (613 nm) is sensitive to the symmetry around the ion. Therefore, comparison of its intensity with that of the internal reference transition – *i.e.*, the magnetic-dipole allowed transition $^5D_0 \rightarrow {}^7F_1$ (592 nm) – allows to monitor changes in the Eu^{3+} environment. Hence, Eu^{3+} exhibiting an O_h symmetry when doped into α-$NaGdF_4$ and a C_2 symmetry in the hexagonal GdF_3 lattice explains the differences in the emission profiles before and after phase transformation.[31, 216]

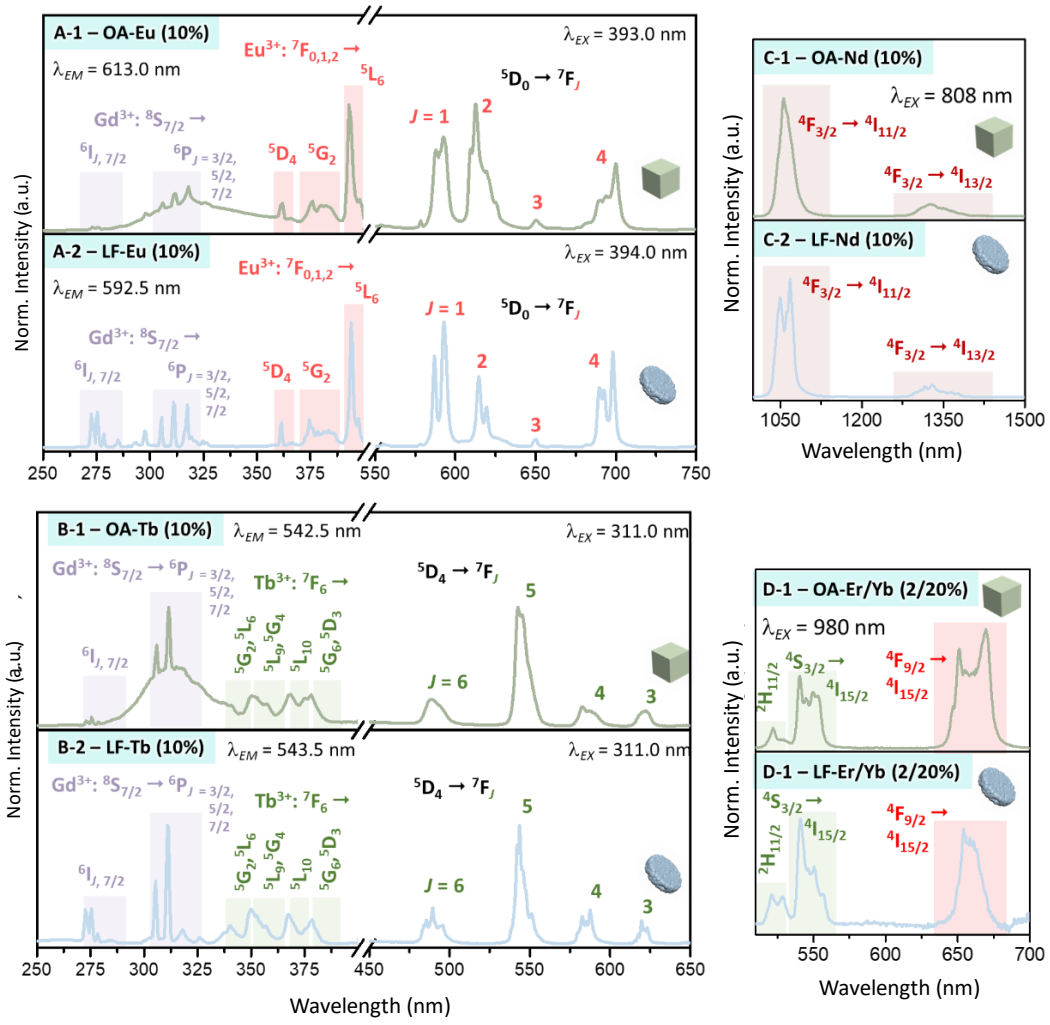

Figure 4.22. (A/B-1) Excitation and emission spectra of OA-capped α-$NaGdF_4$ NPs doped with (A-1) 10% of Eu^{3+} and (B-1) 10% of Tb^{3+}. (A/B-2) Excitation and emission spectra of hexagonal LF-GdF_3 NPs doped with (A-2) 10% of Eu^{3+} and (B-2) 10% of Tb^{3+}. (C-1/2) NIR emission spectra obtained under 808 nm laser excitation of (1) OA-capped α-$NaGdF_4$ and (2) LF-GdF_3 NPs doped with 10% of Nd^{3+}. (D-1/2) Upconversion emission spectra obtained under 980 nm laser excitation of (1) OA-capped α-$NaGdF_4$ and (2) LF-GdF_3 NPs co-doped with 2% Er^{3+} and 20% Yb^{3+}. Excitation wavelengths, λ_{EX}, and monitored emission wavelengths, λ_{EM}, are indicated in the respective figures (A) to (D).

In addition, narrowing of the emission bands and more pronounced Stark splitting for the Eu^{3+} and Tb^{3+} transitions are a consequence of the larger size and crystallinity of the GdF_3 particles in comparison with the small α-$NaGdF_4$ NPs.

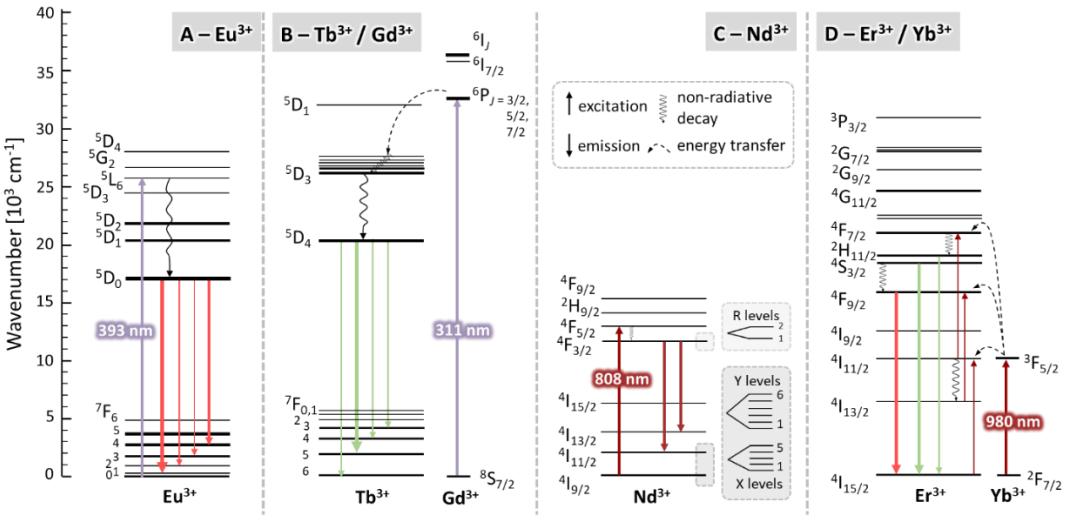

Figure 4.23. Energy level schemes for (A) the Eu^{3+}/Gd^{3+}, (B) the Tb^{3+}/Gd^{3+}, (C) Nd^{3+}, and (D) Er^{3+}/Yb^{3+} showing the respective f-f transitions.

Fluorescence decay curves and the corresponding lifetimes for the Eu^{3+} $^5D_0 \rightarrow {}^7F_2$ and the Tb^{3+} $^5D_4 \rightarrow {}^7F_5$ transitions in OA-capped and LF samples are given in Figure 4.24. Due to the complex nature of the upconversion emission process in Ln-NPs, the luminescence decay curves shown below do not have a clear single-exponential character.[247] Therefore, lifetime values were obtained by integration of the area under the normalized decay curves. The determined lifetime values of the emitting states were *ca.* 4 ms (Table 4.3), close to the reported values for comparable NP sizes and compositions. [214, 234, 248]

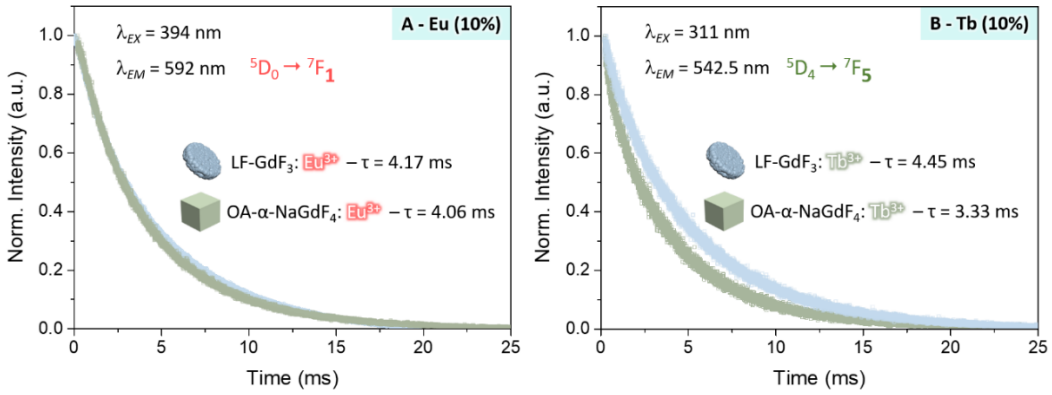

Figure 4.24. Fluorescence decay curves and respective lifetime values for the indicated transitions of samples doped with (A) Eu^{3+} (10%), (B) Tb^{3+} (10%).

Table 4.3. Overview of all obtained lifetime values.

Ln^{3+} Dopant	Monitored Transition	$NaGdF_4$ Crystalline Phase	GdF_3 Crystalline Phase	Lifetime	
				OA-NPs	LF-NPs
Eu (10%)	$^5D_0 \rightarrow {}^7F_1$	α	hexagonal	4.06 ms	4.17 ms
Tb (10%)	$^5D_4 \rightarrow {}^7F_5$	α	hexagonal	3.33 ms	4.45 ms
Er/Yb (2%/20%)	$^4S_{3/2} \rightarrow {}^4I_{15/2}$	α	orthorhombic	22 μs	– [a]
		β		41 μs	38 μs
	$^4F_{9/2} \rightarrow {}^4I_{15/2}$	α	orthorhombic	12 μs	– [a]
		β		56 μs	49 μs
Nd (10%)	$^4F_{3/2} \rightarrow {}^4I_{11/2}$	α		19 μs	– [a]
		β		< 10 μs [b]	– [a]

[a] Emission intensity too weak.
[b] Based on the experimentally determined decay curve and the instrument response function (IRF), a lifetime of *ca.* 4 μs was obtained, yet, such short value must be taken with care due to instrumental limitations.

NIR-Excited OA-α-$NaGdF_4$ and LF-GdF_3 NPs Doped with Nd^{3+} or Er^{3+}/Yb^{3+}. Emission spectra of Nd^{3+}-doped α-$NaGdF_4$ and GdF_3 NPs under 808 nm excitation are shown in Figure 4.22 (C-1/2). Two Nd^{3+} emission bands were observed in the NIR spectral region, *i.e.*, at 1056 nm and 1328 nm, corresponding to the $^4F_{3/2} \rightarrow {}^4I_{11/2}$ and $^4F_{3/2} \rightarrow {}^4I_{13/2}$ transitions (Figure 4.23), respectively. Again, increase in particle size that came along with the phase transformation resulted in narrowing and clearer Stark splitting of the emission bands. Upon doping with Er^{3+}/Yb^{3+}, OA-α-$NaGdF_4$ and LF-GdF_3 NPs exhibited upconversion emission under 980 nm excitation (Figure 4.22 (D-1/2)). Characteristic Er^{3+} emissions in the green (520/540 nm) and red (650 nm) spectral regions were observed in both samples, with a small difference in the relative intensities of these emissions – OA-α-$NaGdF_4$ NPs showing a slightly more intense red emission, as is typically found for the cubic $NaREF_4$ phase.[211]

Table 4.4. Overview of NP concentrations, excitation wavelength (λ_{EX}), and power of the excitation source used for steady state and time-resolved spectroscopy of OA-capped and LF-Ln^{3+}-doped $NaGdF_4$ and GdF_3 NPs.

Ln^{3+} Dopant	$NaGdF_4$ Crystalline Phase	OA-NP Concentration (mg/mL)	LF-NP Crystalline Phase [a]	LF-NP Concentration (mg/mL)	λ_{EX} (nm)	Power OA / LF [b] (W)
Nd (10%)	α	33	h-GdF_3	13	808	1.30
	β	15	β-$NaGdF_4$	3		
Eu (10%)	α	42	h-GdF_3	18	394	75 [c]
Tb (10%)	α	54	h-GdF_3	11	311	75 [c]
Er/Yb (2%/20%)	α	5	o-GdF_3	5	980	1.35 / 1.83
	β	2	β-$NaGdF_4$	6		1.35

[a] h = hexagonal, o = orthorhombic

[b] The same laser power was used for OA-capped and LF-NPs, unless stated otherwise.

[c] 75 W Xenon lamp

Noteworthy, for the Er^{3+}/ Yb^{3+} dopant pair, phase transformation resulted in the crystallization of orthorhombic GdF_3 in opposite to hexagonal GdF_3 that was observed for all other Ln^{3+}-doped samples. As previously mentioned, the orthorhombic crystalline phase is considered the less efficient host material when seeking luminescence-based applications. [201, 214, 216, 249] In good agreement with this, relatively high excitation power (Table 4.4) was deemed necessary to induce detectable UC emission. Emission spectra of Nd^{3+}- and Er^{3+}/Yb^{3+}-doped OA-capped and LF-β-$NaGdF_4$ NPs exhibited similar spectral features as those obtained for their cubic counterparts and are shown in Figure 4.25.

Fluorescence decay curves and corresponding lifetimes obtained for the green $^4S_{3/2} \rightarrow {}^4I_{15/2}$ and red $^4F_{9/2} \rightarrow {}^4I_{15/2}$ Er^{3+} emissions as well as the NIR $^4F_{3/2} \rightarrow {}^4I_{11/2}$ Nd^{3+} transition (Figure 4.23) are given in Figure 4.26 and Table 4.3. For OA-capped Er^{3+}/Yb^{3+}-doped α- and β-$NaGdF_4$ NPs, lifetimes of both the green ($^4S_{3/2} \rightarrow {}^4I_{15/2}$) and the red ($^4F_{9/2} \rightarrow {}^4I_{15/2}$) emission were found to be in a similar range as previously reported, namely around 50 µs (Figure 4.26 A/B/C).[159]

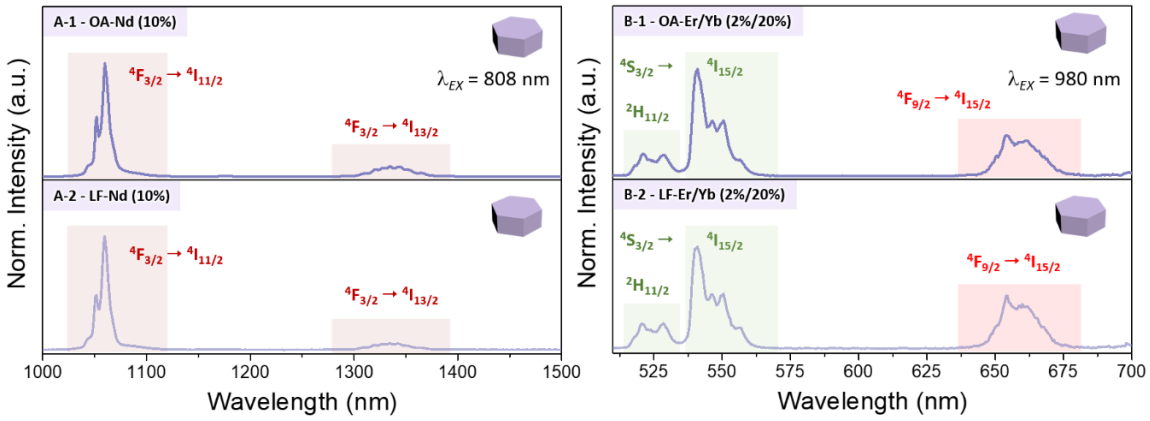

Figure 4.25. NIR emission spectra for (A-1) OA-capped and (A-2) ligand-free Nd^{3+}-doped β-$NaGdF_4$ as well as upconversion emission spectra for (B-1) OA-capped and (B-2) ligand-free Er^{3+}/Yb^{3+}-doped β-$NaGdF_4$.

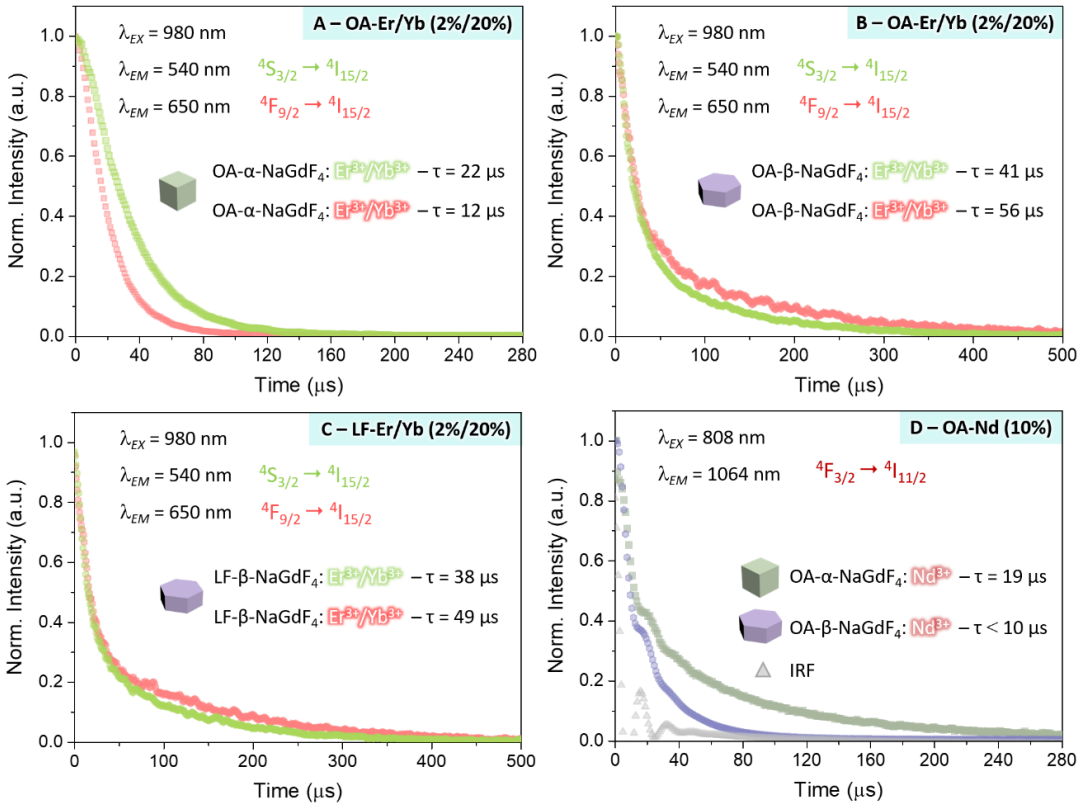

Figure 4.26. Fluorescence decay curves and respective lifetime values for the indicated transitions of (A) OA-capped α-$NaGdF_4$ doped with Er^{3+}/Yb^{3+}, (B) and (C) OA-capped and LF-β-$NaGdF_4$ doped with Er^{3+}/Yb^{3+}, and (D) α- and β-$NaGdF_4$ doped with Nd^{3+} (10%). IRF: instrument response function of the InGaAs detector.

Not surprisingly, lifetime shortening was observed for LF-Er^{3+}/Yb^{3+}-doped β-$NaGdF_4$ NPs when compared to their OA-capped counterparts (Figure 4.26 C), indicating stronger contribution of non-radiative processes, *e.g.*, due to interaction with the solvent, *i.e.*, water. As discussed previously, the α-$NaGdF_4$-to-GdF_3 phase transformation resulted in orthorhombic ligand-free Er^{3+}/Yb^{3+}-doped GdF_3 NPs. Their weak upconversion emission intensity did not allow to obtain an emission decay curve for this sample.

Relatively short lifetimes were determined for the $^4F_{3/2} \rightarrow {}^4I_{11/2}$ NIR emission of Nd^{3+}-doped OA-capped α- and β-$NaGdF_4$ NPs; namely 19 µs for the α-NPs, while even shorter values of less than 10 µs were estimated for the β-NPs (Figure 4.26 D). Such short lifetimes may be ascribed to the relatively high Nd^{3+} dopant concentration of 10%: it is known that higher concentrations foster cross-relaxation processes, which can result in shorter lifetime values.[250] The corresponding ligand-free Nd^{3+}-doped β-$NaGdF_4$ NPs exhibited too weak emission when dispersed in water, not allowing for reliable lifetime measurements. The growth of a passive shell on core-only NP is an efficient strategy to enhance the emission intensity, which will be further investigated in Chapter 5.

4.3 Conclusions

A series of $NaREF_4$ NPs were synthesized using a MW-assisted approach. Herein, the accessibility of $NaREF_4$ in the α and β phase as a function of the RE ion was investigated. Furthermore, an adapted ligand removal procedure was developed, suitable to efficiently render OA- and OAm-capped $NaREF_4$ NPs of sub-10 nm in size water dispersible. Importantly, pH < 3 was deemed necessary, which was found to pose a risk with respect to the chemical stability of some of the investigated samples. More precisely, under acidic conditions, phase transformation of α- and β-$NaREF_4$ NPs into hexagonal or orthorhombic REF_3 NPs during ligand removal was systematically studied as a function of RE ion choice. As the parameters playing a key role in the likelihood of phase transformation to occur, we identified (*i*) the starting α/β-$NaREF_4$ composition, and (*ii*) the relative thermodynamic stability of the $NaREF_4$ (α or β) *versus* the REF_3 (hexagonal or

orthorhombic) crystalline phases. For the lighter RE^{3+} ions, Pr to Sm, higher stability of hexagonal REF_3 *versus* α/β-$NaREF_4$ resulted in a phase transformation, regardless of the starting phase of the $NaREF_4$ NPs (α or β). Moving to the middle of the series, Eu to Dy, phase transformation occurred only in case of the less thermodynamically stable α-$NaREF_4$. Finally, for the heavier RE^{3+} ions, Ho to Lu as well as Y, the α-$NaREF_4$ phase is known as the most stable $NaREF_4$ phase, and indeed, these compositions were more resistant towards phase transformation. Crystallization of the formed REF_3 either in the hexagonal or orthorhombic crystalline phases followed the expected tendency predicted by the type of RE ions present in the starting α/β-$NaREF_4$ NPs compositions (Figure 4.21).

Overall, these findings offer an alternative route to hexagonal-phase REF_3 NPs at room temperature and under ambient pressure. Most important though, they unveil unaddressed chemical stability concerns for the large family of $NaREF_4$ NPs. As such, it comes as an alert to the community working with small $NaREF_4$-type NPs: Water dispersibility can be achieved by ligand removal under acidic conditions, yet, may come along with a morphologic and crystallographic transformation into significantly larger REF_3 particles. Nevertheless, we are pleased to refer to alternative approaches to render small α- and β-$NaREF_4$ NPs water dispersible, *i.e.*, *via* ligand exchange with stabilizing and hydrophilic groups, such as citrate or PAA [89, 186, 195, 251, 252] which will be used in Chapter 5 and Chapter 6, respectively.

Chapter 5. Core-Multi-Shell Design: Unlocking Multimodal Capabilities in Lanthanide-based Nanoparticles as Upconverting, T_2-Weighted MRI and CT Probes

*This Chapter is based on published work in Nanoscale: Nan Liu, Christian Homann, Samuel Morfin, Meghana Kesanakurti, Nicholas D. Calvert, Adam J. Shuhendler, Tom Al, and Eva Hemmer, Nanoscale, **2023**, 15, 19546-19556.*

Author contributions: E. H. and N. L. conceptualized the study. N. L. synthesized all the samples and characterized their structural (TEM and XRD) and optical properties. C. H. provided guidelines for lifetime measurements, and S. M. did X-ray absorption and CT measurements. T. A. helped to design the experiment setup for the CT measurements. M. K. and N. D. C. did the cell toxicity experiments under the guidelines of A. J. S.. N. L. and E. H. co-wrote the manuscript with input from A. J. S. and T. A..

Abstract:

Multimodal bioimaging probes merging optical imaging, MRI, and CT capabilities have attracted considerable attention due to their potential biomedical applications. Lanthanide-based nanoparticles are promising candidates for multimodal imaging because of their optical, magnetic and X-ray attenuation properties. We prepared a set of β-phase $NaGdF_4$:Yb,Er/$NaGdF_4$/$NaDyF_4$ CSS NPs (Dy-CSS NPs) and demonstrated their optical/T_2-weighted MRI/CT multimodal capabilities. A known drawback of multimodal probes that merge the upconverting Er^{3+}/Yb^{3+} ion pair with magnetic Dy^{3+} ions for T_2-weighted MRI is the loss of UC emission due to Dy^{3+} poisoning. Particular attention was paid to controlled nanoparticle architectures with tuned inner shell thicknesses separating Dy^{3+} and Er^{3+}/Yb^{3+} to shed light on the distance-dependent loss of UC due to $Yb^{3+} \rightarrow Dy^{3+}$ energy transfer. Based on the Er^{3+} UC spectra and the excited state lifetime of Yb^{3+}, a 4 nm thick $NaGdF_4$ inner shell did not only restore but enhanced the UC emission. We further investigated the effect of the outer $NaDyF_4$ shell thickness on the particles' magnetic and CT performance. MRI T_2 relaxivity measurements *in vitro* at a magnetic field of 7 T performed on citrate-capped Dy-CSS NPs revealed that NPs with the thickest outer shell thickness (4 nm) exhibited the highest r_2 value, with a superior T_2 contrast effect compared to commercial iron oxide and other Dy-based T_2 contrast agents. In addition, the citrate-capped Dy-CSS NPs were demonstrated suitable for CT in *in vitro* imaging phantoms at X-ray energies of 110 keV, rendering them interesting alternatives to clinically used iodine-based agents that operate at lower energies.

5.1 Introduction

As introduced in Chapter 1.3, Ln^{3+}-based NPs are promising candidates used as multimodal (*e.g.*, optical, MRI and CT) imaging probes.[136] CSS architecture design as a strategy holds promise towards optical/T_2/CT probes based on upconverting Ln^{3+} and Dy^{3+} ions.[134] The overarching goal of this work was to design Ln^{3+}-based nanoparticle probes that merge the manifold properties of the Ln^{3+} ions into one multimodal imaging agent that has UC, T_2-modulating, and CT capabilities. Inspired by previous work, here, we designed a set of CSS NPs, *i.e.*, β-phase $NaGdF_4$:Yb,Er/$NaGdF_4$/$NaDyF_4$ (Dy-CSS, Figure 5.1 A). Particular attention was paid to the establishment of new protocols for the controlled shell growth *via* a rapid and straightforward MW-assisted route. The adjustment of the inner and outer shell thicknesses allowed to (i) shed light on distance-dependent Dy^{3+} quenching effects and energy transfer mechanisms as well as (ii) assess the effect of shell thickness on T_2 MRI and CT performance. As a result, Dy-CSS NPs were obtained with not only restored but enhanced UC emission as well as superior T_2 and CT capabilities compared to previously reported nanoparticle architectures and common CAs, holding potential as a multimodal imaging probe.

5.2 Results and Discussion

5.2.1 Synthesis and Structural Characterization of Dy-CSS NPs

A set of OA-capped Dy-CSS NPs was successfully synthesized using a modified version of the MW-assisted protocol as introduced in Chapter 3.[89, 159] Control over the shell thickness in multi-shell Ln-NPs is crucial to optimize their performance and to understand structure-property relationships. While the MW-assisted route was previously reported as suitable for simple CS architectures, stringent control over shell thicknesses and the synthesis of core/multi-shell systems remained a challenge. Here, we demonstrate that adjustment of the ratio between the core NP seeds and the shell precursor in the reaction mixture was found to be key, as discussed in Chapter 3.2.

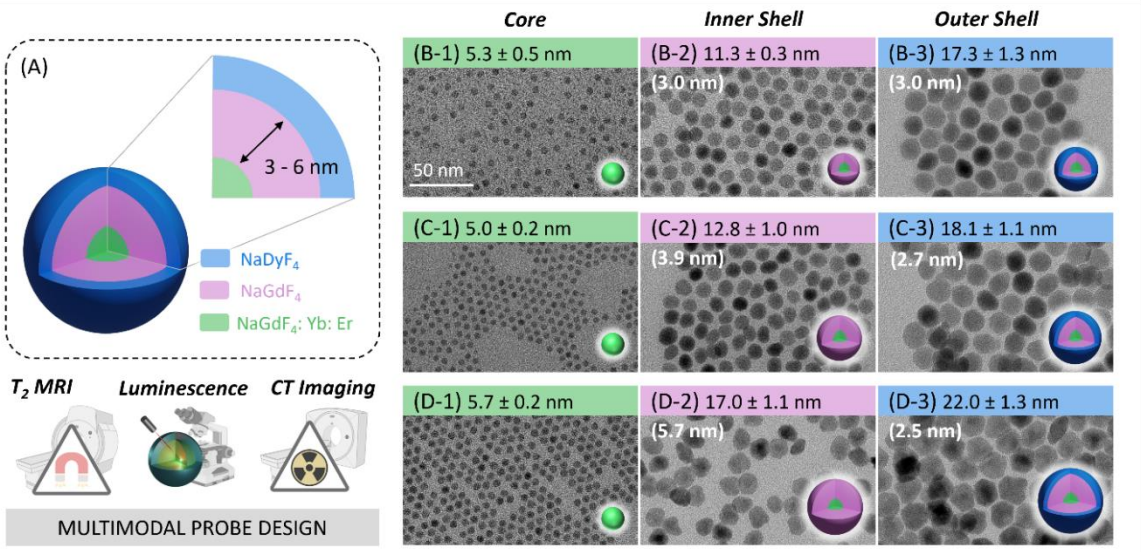

Figure 5.1. (A) Schematic illustration of the CSS Dy-NP architecture proposed as multimodal optical/T_2/CT probe. (B-D) TEM images and sizes of OA-capped (1) core β-$NaGdF_4$:Yb^{3+},Er^{3+}, (2) β-$NaGdF_4$:Yb^{3+},Er^{3+}/$NaGdF_4$ CS, and (3) β-$NaGdF_4$:Yb^{3+},Er^{3+}/$NaGdF_4$/$NaDyF_4$ CSS NPs. The $NaGdF_4$ inner shell thickness and $NaDyF_4$ outer shell thickness are indicated in brackets. Core sizes and outer shell thicknesses were kept comparable, while the thickness of the inner shell increased from B to D. The 50 nm scale bar applies to all TEM images.

Decreasing the number of core NPs, while keeping the amount of shell precursor constant allowed to tune the thickness of the undoped $NaGdF_4$ shell on the Er^{3+}/Yb^{3+}-co-doped core from *ca.* 3 to 4 and 6 nm (^{3nm}CS, ^{4nm}CS, and ^{6nm}CS), respectively (Figure 5.1 and Table 5.1). Similarly, during the synthesis of CSS Dy-NPs, the thickness of the outer $NaDyF_4$ shell could be tuned by controlling the ratio of CS NP seeds and the Dy-TFA precursor in the reaction mixture from *ca.* 1 to 3 and 4 nm (^{4nm}Dy-CSS^{1nm}, ^{4nm}Dy-CSS^{3nm}, and ^{4nm}Dy-CSS^{4nm}, whereas the first and second superscript indicate the thickness of the inner and outer shell), respectively. XRD analysis confirmed that all the Dy-CSS NPs were of pure hexagonal phase of $NaGdF_4$ and $NaDyF_4$ (Figure 5.2). The morphology and size of core, CS and CSS NPs were examined by TEM. As shown in Figure 5.1 (B-D) and Figure 5.3, all NPs were monodisperse with narrow size distributions. The obtained $NaGdF_4$ core NPs, co-doped with 2 mol% Er^{3+} and 20 mol% Yb^{3+} to induce luminescent properties, exhibited a spherical morphology with an average diameter of *ca.* 5.4 nm. Growing an undoped $NaGdF_4$ shell resulted in CS NPs of 11.3 ± 0.3 nm, 12.8 ± 1.0 nm, and 17.0 ± 1.1 nm, with controlled shell thicknesses of *ca.* 3, 4, and 6 nm.

Table 5.1. Overview of the compositions and dimensions of the core, CS, and CSS NPs used in this study. Green shaded samples were used to study the effect of inner shell thickness on UC. Blue shaded samples were used to study the effect of outer shell thickness on MRI and CT performance. Sample ^{4nm}Dy-CSS^{3nm} was used in both studies, the first and second superscript indicate the thickness of the inner and outer shell.

Sample Code	$NaGdF_4$:Yb,Er Core Size (nm)	$NaGdF_4$ Inner Shell Thickness (nm)	$NaDyF_4$ Outer Shell Thickness (nm)	Overall Particle Size (nm)	Surface Chemistry	Investigated Performance
Dy-CS	5.3 ± 0.5	-	3.4	12.1 ± 1.0	oleate	UC
^{3nm}CS	5.3 ± 0.5	3.0	-	11.3 ± 0.3	oleate	UC
^{3nm}Dy-CSS^{3nm}			3.0	17.3 ± 1.3		
^{4nm}CS	5.0 ± 0.2	3.9	-	12.8 ± 1.0	oleate	UC
^{4nm}Dy-CSS^{3nm}			2.7	18.1 ± 1.1	oleate, citrate	
^{6nm}CS	5.7 ± 0.2	5.7	-	17.0 ± 1.1	oleate	UC, MRI
^{6nm}Dy-CSS^{3nm}			2.5	22.0 ± 1.3	oleate, citrate	
^{4nm}CS	5.4 ± 0.2	4.4	-	14.2 ± 0.9	oleate	UC
^{4nm}Dy-CSS^{1nm}			1.3	16.9 ± 1.0	oleate, citrate	UC, MRI, CT
^{4nm}CS	5.0 ± 0.2	3.9	-	12.8 ± 1.0	oleate	UC
^{4nm}Dy-CSS^{3nm}			2.7	18.1 ± 1.1	oleate, citrate	UC, MRI, CT
^{4nm}CS	5.1 ± 0.3	4.3	-	13.8 ± 1.0	oleate	UC
^{4nm}Dy-CSS^{4nm}			4.0	21.9 ± 1.3	oleate, citrate	UC, MRI, CT

Further growth of a *ca.* 2.7 nm thick $NaDyF_4$ outer shell to introduce Dy^{3+} ions for T_2-weighted MRI led to overall NP sizes of 17.3 ± 1.3 nm, 18.1 ± 1.1 nm, and 22.0 ± 1.3 nm for ^{3nm}Dy-CSS^{3nm}, ^{4nm}Dy-CSS^{3nm}, and ^{6nm}Dy-CSS^{3nm}, respectively. Importantly, the core size and outer shell thickness of the obtained Dy-CSS NPs were kept comparable among the three NP architectures, while three different inner shell thicknesses were introduced. Such control of the CSS architecture allows for the investigation of the efficiency of the inner barrier layer between the Er^{3+}/Yb^{3+} ions in the core and the Dy^{3+} ions in the outer shell.

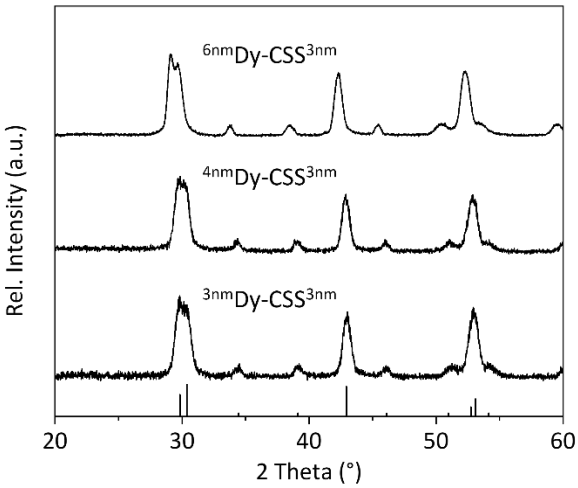

Figure 5.2. XRD patterns of OA-capped CSS β-$NaGdF_4$:Yb,Er/$NaGdF_4$/$NaDyF_4$ (Dy-CSS) with different inner shell thicknesses of 3.0 nm (^{3nm}Dy-CSS^{3nm}), 3.9 nm (^{4nm}Dy-CSS^{3nm}), and 5.7 nm (^{6nm}Dy-CSS^{3nm}), respectively. Reference: β-$NaGdF_4$, PDF card [01-080-8787].

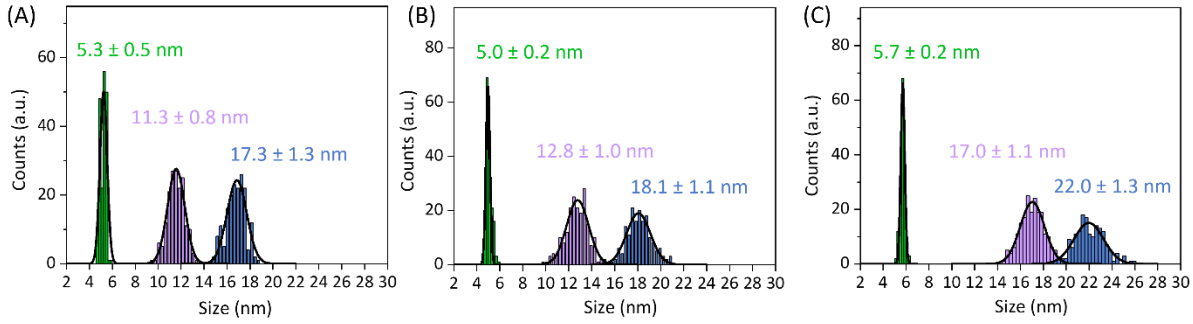

Figure 5.3. Size distributions of (A) ^{3nm}Dy-CSS^{3nm}, (B) ^{4nm}Dy-CSS^{3nm}, as well as (C) ^{6nm}Dy-CSS^{3nm} NPs and their corresponding CS (^{3nm}CS, ^{4nm}CS, ^{6nm}CS) and core NPs, demonstrating the varying thickness of the inner shell, while keeping core size and outer shell thickness constant.

5.2.2 Optical Properties of Dy-CSS NPs

The UC luminescence properties of the obtained NPs, dispersed in toluene, were investigated under 980 nm excitation. As shown in Figure 5.4 (A-1), the emission spectra of ^{3nm}Dy-CSS^{3nm} and their corresponding core/shell (^{3nm}CS) and core NPs exhibited characteristic UC emission peaks in the green and red spectral regions ascribed to the $^2H_{11/2} \rightarrow {}^4I_{15/2}$ (520 nm), $^4S_{3/2} \rightarrow {}^4I_{15/2}$ (540 nm), and $^4F_{9/2} \rightarrow {}^4I_{15/2}$ (650 nm) Er^{3+} transitions.

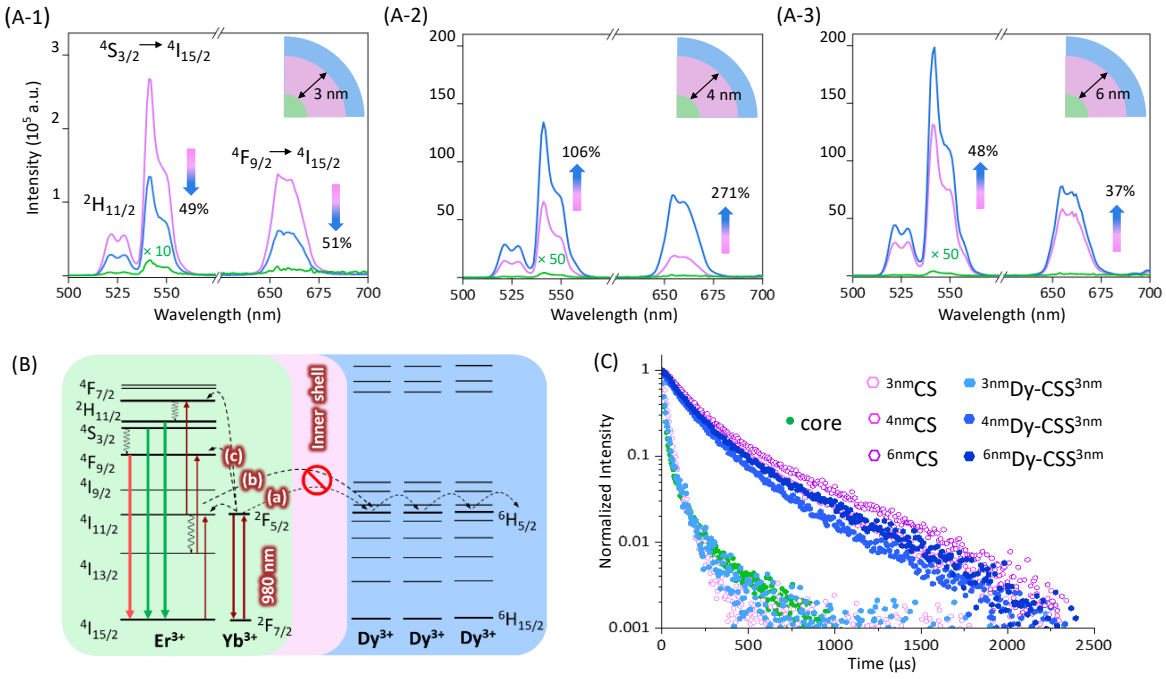

Figure 5.4. (A) UC spectra of OA-capped ^{3nm}Dy-CSS^{3nm} (1), ^{4nm}Dy-CSS^{3nm} (2), and ^{6nm}Dy-CSS^{3nm} (3) NPs (blue) as well as their corresponding core (green) and CS (pink) NPs. All spectra were obtained under 980 nm laser excitation. Power density = 6.0 W/cm^2, [NP] = 5 mg/mL in toluene. (B) Partial energy level diagram for Er^{3+}/Yb^{3+} and Dy^{3+}, schematically showing how the addition of an inner shell physically separates Er^{3+}/Yb^{3+} from Dy^{3+} ions, thus, preventing Dy^{3+}-induced loss of the UC. Solid lines are radiative transitions, dotted lines indicate energy transfer, and wavy lines are non-radiative transitions. (C) Luminescence decay curves of the Yb^{3+} emission under 980 nm excitation obtained from core, CS, and CSS NPs.

The low emission intensity obtained from core NPs was no surprise given the very small NP size (*ca.* 5 nm) resulting in severe surface quenching. When adding a 3 nm undoped $NaGdF_4$ shell, as expected, the emission intensity increased, reducing surface quenching effects.[41] However, the addition of an additional outer $NaDyF_4$ shell (^{3nm}Dy-CSS^{3nm} NPs) resulted in lower UC emission intensities than obtained for ^{3nm}CS NPs without the $NaDyF_4$. The observed loss (*ca.* 50 % for both the green and red emissions) indicated that an inner shell of 3 nm thickness was not sufficient to protect the emitter pair Er^{3+}/Yb^{3+} from the Dy^{3+} quencher. Previous studies reported that an inner CaF_2 shell as thin as 2.3 nm was suitable to restore the UC emission,[133] while in our study, emission loss was observed with a 3 nm inner $NaGdF_4$ shell. This might be explained by potential cation intermixing in the Dy-CSS NPs taking place during shell growth, resulting in the distribution of Ln^{3+} dopant ions (*i.e.*, Er^{3+} and Dy^{3+}) into the nominally undoped shell.[41, 42] As expected,

growing a thicker inner shell of 4 nm on core NPs significantly increased the UC emission intensity, ^{4nm}CS NPs showing an overall 2000 times higher UC intensity than core NPs (Figure 5.4 (A-2)).

Most interestingly, no loss of UC was observed upon the addition of an outer $NaDyF_4$ shell. The obtained ^{4nm}Dy-CSS^{3nm} NPs exhibited not only restored UC emission but an UC enhancement by more than 100 % for the green and by *ca.* 270 % for the red emission compared to their respective ^{4nm}CS NPs. This result indicated that an inner $NaGdF_4$ shell of at least 4 nm in thickness was required to overcome the Dy^{3+}-induced loss of UC.

Possible quenching processes caused by Dy^{3+} were previously proposed by Zhang *et al.* based on steady-state UC spectroscopy.[140] As schematically shown in Figure 5.4 B, in close vicinity to Dy^{3+} ions, the $^2F_{5/2}$ excited state of Yb^{3+} and the $^2I_{11/2}$ excited state of Er^{3+} can be depopulated via resonant energy transfer to the excited $^6H_{5/2}$ level of Dy^{3+} (steps (a) and (b)). This depopulation of the excited Yb^{3+} and intermediate Er^{3+} levels compromise efficient UC to the emitting Er^{3+} levels (step (c)), ultimately resulting in loss of UC emission. The added inner shell acts as a barrier hampering the Yb^{3+} (and Er^{3+}) → Dy^{3+} energy transfer, restoring Er^{3+} UC. In order to confirm the UC loss mechanism, two reference samples were synthesized, namely, α-phase $NaDyF_4$:Yb,Er core NPs and β-phase $NaGdF_4$:Yb,Er/$NaDyF_4$ NPs (Dy-CS) (Figure 5.5).

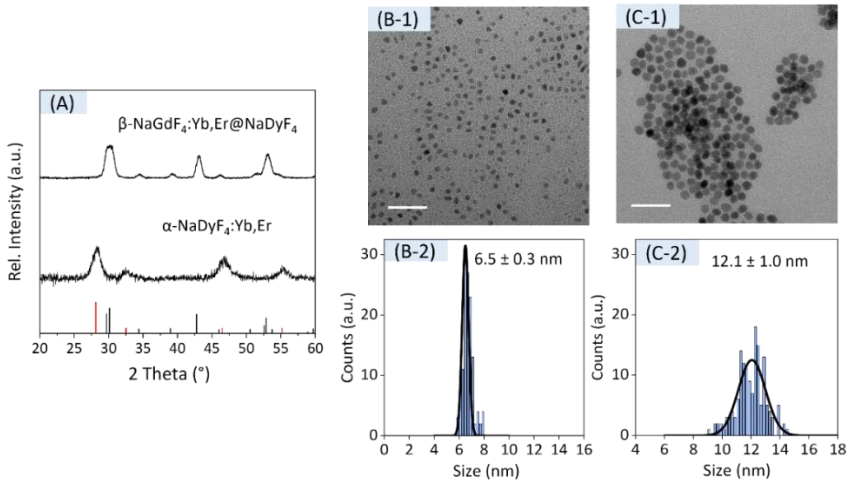

Figure 5.5. (A) XRD patterns of OA-capped α-$NaDyF_4$:Yb,Er core and β-$NaGdF_4$:Yb,Er/$NaDyF_4$ (Dy-CS) core-shell NPs. References: red line – α-$NaDyF_4$, PDF card [00-027-0697]; black line – β-$NaGdF_4$, PDF card [01-080-8787]. (B and C) (1) TEM images and (2) their corresponding size distributions of OA-capped (B) α-$NaDyF_4$:Yb,Er and (C) β-$NaGdF_4$:Yb,Er/$NaDyF_4$ NPs. Scale bars: 50 nm. Note that β-$NaDyF_4$:Yb,Er is not accessible *via* our MW-assisted synthesis.[253] Therefore, α-$NaDyF_4$:Yb,Er was used as a similar-sized reference core sample.

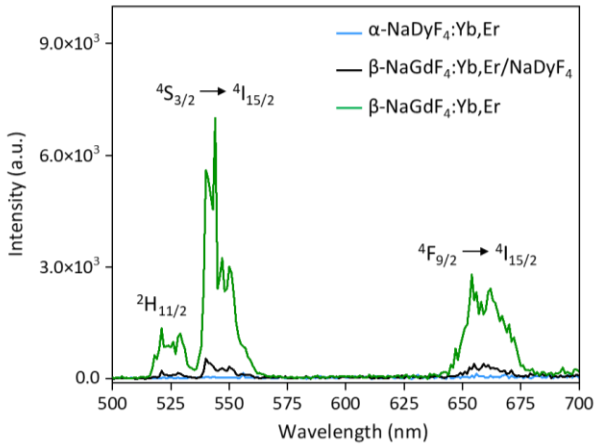

Figure 5.6. UC spectra of OA-capped α-$NaDyF_4$:Yb,Er, β-$NaGdF_4$:Yb,Er, and β-$NaGdF_4$:Yb,Er/$NaDyF_4$ CS NPs. All spectra were obtained under 980 nm laser excitation. Power density = 6.0 W/cm^2, [NP] = 5 mg/mL in toluene.

As shown in Figure 5.6, not surprisingly, the emission of Er^{3+} was completely lost when the emitting Ln^{3+} ions were co-doped into the $NaDyF_4$ host. UC loss still took place upon separation of Er^{3+}/Yb^{3+} and Dy^{3+} into the β-$NaGdF_4$:Yb^{3+},Er^{3+} core and a $NaDyF_4$ shell (Dy-CS).

Confirmation of the proposed quenching mechanism was obtained by determining the excited state lifetime of Yb^{3+} in the series of core, CS and CSS NPs under investigation. Therefore, the time-dependent emission of Yb^{3+} under 980 nm excitation was monitored at the shoulder of the ion's emission at 940 nm.[254, 255] The decay curves and respective lifetime values (obtained by integrating the area under the decay curves) are given in Figure 5.4 C and Table 5.2. The small core NPs exhibited a relatively short lifetime of 25.5 µs due to surface quenching, which was slightly prolonged to 33.3 µs when an undoped shell of 3 nm was added (^{3nm}CS). Yet, growth of an additional $NaDyF_4$ shell shortened the lifetime to 26.1 µs (^{3nm}Dy-CSS^{3nm}). This decrease in lifetime is in line with the reduced Er^{3+} emission (Figure 5.4 (A- 1)). As expected, the addition of a thicker undoped $NaGdF_4$ shell on the doped core led to a significantly longer lifetime (^{4nm}CS: 207.6 µs). The observed increase in UC emission intensity upon growth of an additional outer $NaDyF_4$ shell (^{4nm}Dy-CSS^{3nm}) suggests efficient shielding of the Yb^{3+}/Er^{3+} ion pair from Dy^{3+} (Figure 5.4 (A-2)) as well as additional protection against surface loss processes. Hence, a prolonged Yb^{3+} lifetime might be expected.

Table 5.2. Lifetime values extracted from the decay curves of the Yb^{3+} emission under 980 nm.

Sample	Inner Shell Thickness (nm)	Lifetime (µs)
Core	NA	25.5
^{3nm}CS	*ca.* 3	33.3
^{3nm}Dy-CSS^{3nm}		26.1
^{4nm}CS	*ca.* 4	207.6
^{4nm}Dy-CSS^{3nm}		175.8
^{6nm}CS	*ca.* 6	251.3
^{6nm}Dy-CSS^{3nm}		207.6

Conversely, the decay time decreased to 175.8 µs for ^{4nm}Dy-CSS^{3nm} NPs, indicating continuous depopulation of the $^2F_{5/2}$ Yb^{3+} level by Dy^{3+} ions. To assess whether an even thicker undoped shell could fully overcome energy transfer to Dy^{3+}, the optical properties of ^{6nm}Dy-CSS^{3nm} NPs with a *ca.* 6 nm thick inner shell were analyzed. As expected, emission spectra did not indicate any UC poisoning effect of Dy^{3+}, and the sample exhibited the strongest emission intensity among all the investigated NPs due to its overall thick shell ($NaGdF_4$ + $NaDyF_4$: 8.2 nm) (Figure 5.4 (A-3)). Still, time-dependent measurements revealed that energy transfer to Dy^{3+} was not fully suppressed, as indicated by the shortening of the Yb^{3+} lifetime upon shelling with $NaDyF_4$ (251.3 µs for ^{6nm}CS *versus* 207.6 µs for ^{6nm}Dy-CSS^{3nm}).

The influence of the $NaDyF_4$ shell on the UC emission was further demonstrated by power-dependent photoluminescence spectroscopy. As shown in Figure 5.7, regardless of the architecture of the NPs, the slopes of the fitted curves of the log-log power plots (which reflect the number of photons involved in the UC process[256]) were larger than 1 for both the green ($^4S_{3/2}$ → $^4I_{15/2}$) and red ($^4F_{9/2}$ → $^4I1_{5/2}$) Er^{3+} UC emissions. Thus, a 2-photon process took place, as expected for the Yb^{3+}/Er^{3+} UC ion pair. Nonetheless, the presence of Dy was found to have an influence on the UC process. Interestingly, the addition of a $NaDyF_4$ shell on the Er^{3+}/Yb^{3+}-doped core lowered the slope values of the double logarithmic power plots from 1.88 to 1.49 and 1.75 to 1.68 for the green and red emissions, respectively (Figure 5.7 (A-B)).

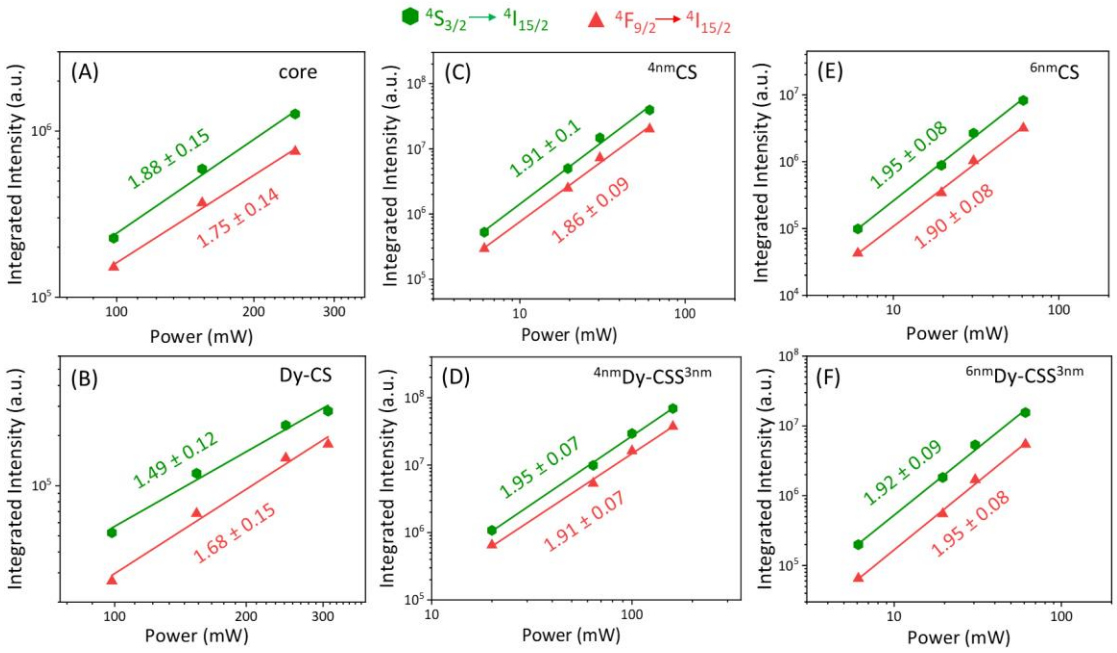

Figure 5.7. Integrated $^4S_{3/2} \rightarrow {}^4I_{15/2}$ and $^4F_{9/2} \rightarrow {}^4I_{15/2}$ Er^{3+} emission intensities versus 980 nm excitation power for OA-capped (A) β-$NaGdF_4$:Yb,Er (core), (B) Dy-CS, (C) ^{4nm}CS, (D) ^{4nm}Dy-CSS^{3nm}, (E) ^{6nm}CS, and (F) ^{6nm}Dy-CSS^{3nm} NPs.

This decrease in the slope values indicated a perturbation of the classical UC process for which a slope close to 2 would be expected, along with energy transfer from Er^{3+}/Yb^{3+} to Dy^{3+} as a competing process. Moreover, this observation agrees with the reduced Er^{3+} UC emission (Figure 5.6) and shortened lifetime of the Yb^{3+} excited state (Figure 5.4 C). When adding a 4 nm undoped $NaGdF_4$ shell on the Er^{3+}/Yb^{3+}-doped core (^{4nm}CS NPs), the values slightly increased to 1.91 and 1.86 for the green and red emission (Figure 5.7 C), approaching the theoretical value of 2. This increase was ascribed to the prevention of surface quenching *via* inner shelling. Upon further growth of a $NaDyF_4$ outer shell (^{4nm}Dy-CSS^{3nm} NPs), minor additional increase of the slope values to 1.95 and 1.91 was observed (Figure 5.7 D). This might indicate that the energy transfer process from Er^{3+}/Yb^{3+} to Dy^{3+} was not dominant anymore but that recovery of classical 2-photon UC process took place. The same trend in terms of slope values was observed for ^{6nm}CS NPs (green: 1.95, red: 1.90) and ^{6nm}Dy-CSS^{3nm} NPs (green: 1.92, red: 1.95) (Figure 5.7 E/F). Overall, based on the Er^{3+} emission spectra and Yb^{3+} lifetimes of ^{4nm}Dy-CSS^{3nm} and ^{6nm}Dy-CSS^{3nm}, a 4 nm inner shell

thickness was deemed sufficiently efficient to suppress the most severe Dy^{3+}-induced UC loss, resulting in bright UC emitters, despite some remaining energy transfer from Yb^{3+} to Dy^{3+}.

Herein, the increased shell thickness is suggested to play a dual role. First, the $Yb^{3+} \rightarrow Dy^{3+}$ energy transfer is hindered by the barrier layer, resulting in more efficient UC to the Er^{3+} emitting levels. Second, the overall shell ($NaGdF_4$ + $NaDyF_4$) around the emitting core reaches a thickness that was previously reported as highly efficient in reducing non-radiative depopulation of the emitting Er^{3+} levels, which is supported by increasing lifetimes of the green ($^4S_{3/2}$) and red ($^4F_{9/2}$) emitting excited states (Figure 5.8 and Figure 5.9).[257] Fluorescence decay curves and the corresponding lifetimes of the green and red Er^{3+} emissions at 540 nm ($^4S_{3/2} \rightarrow {}^4I_{15/2}$) and 650 nm ($^4F_{9/2} \rightarrow {}^4I_{15/2}$) under 980 nm excitation are shown in Figure 5.8. As expected, the small core NPs exhibited relatively short lifetimes for the green (62.1 µs) and red (66.4 µs) emissions due to surface quenching. The slightly longer lifetime for the red emission is in agreement with previous studies.[159, 250] Growth of a passivating shell is expected to increase the lifetimes of the green and red emissions, along with increased photoluminescence intensities, due to reduced surface quenching.

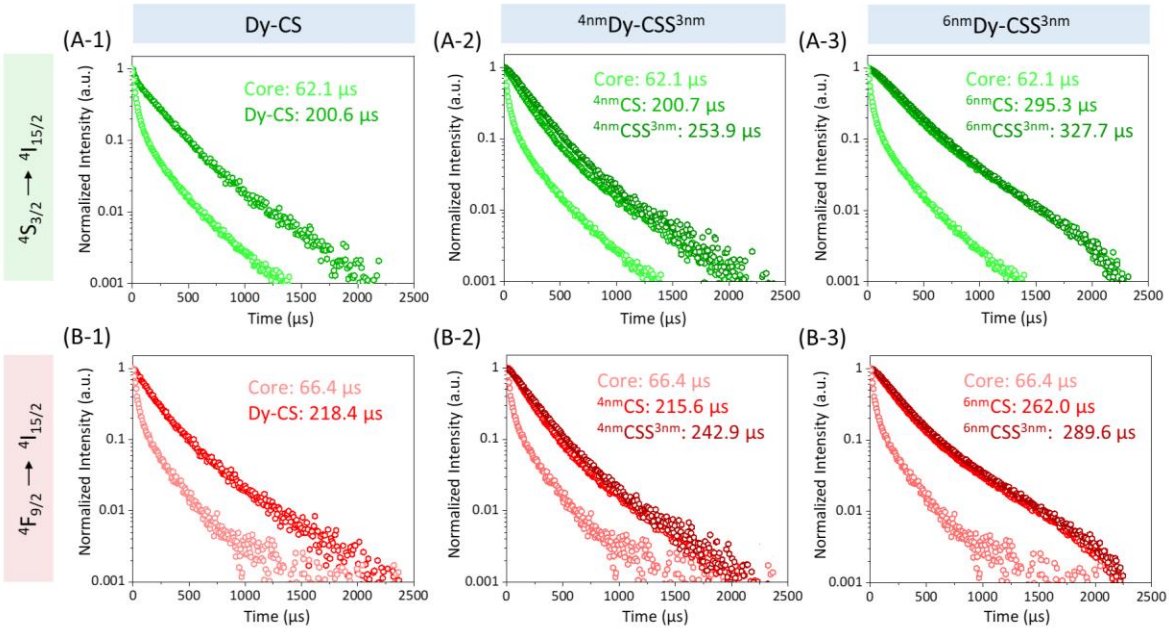

Figure 5.8. Luminescence decay curves of the (A) $^4S_{3/2} \rightarrow {}^4I_{15/2}$ (540 nm) and (B) $^4F_{9/2} \rightarrow {}^4I_{15/2}$ (650 nm) Er^{3+} transitions for (1) Dy-CS, (2) ^{4nm}Dy-CSS^{3nm}, and (3) ^{6nm}Dy-CSS^{3nm} NPs and their corresponding core and CS NPs in toluene. λ_{ex} = 980 nm.

In line, lifetimes prolonged to more than 200 µs upon growth of an undoped $NaGdF_4$ shell (^{4nm}CS and ^{6nm}CS NPs, Figure 5.8 (A/B-2/3)), whereas increased shell thickness resulted in longer lifetimes.

Shelling of an Er^{3+}/Yb^{3+}-doped $NaGdF_4$ core with $NaDyF_4$ resulted in severe loss of UC emission (Figure 5.6). Yet, noteworthy, the Er^{3+} lifetime values of Dy-CS NPs (Figure 5.8 (A/B-1)) were comparable to those obtained for ^{4nm}CS and ^{6nm}CS NPs with a $NaGdF_4$ shell (green emission: 200.6 µs, red emission: 218.4 µs). This indicated that Dy^{3+} ions in the shell do not significantly contribute to UC emission loss *via* non-radiative depopulation of the excited Er^{3+} levels. Rather, both shell types – $NaGdF_4$ and $NaDyF_4$ – protect the Er^{3+} emitters from surface quenching, leading to similar lifetimes. To recall, lifetime measurements of the Yb^{3+} emission provided evidence for energy transfer from Yb^{3+} in the core to Dy^{3+} ions in the shell, depopulating the excited Yb^{3+} state and hence, hampering efficient UC of Er^{3+} to the ion's emitting levels. Thus, while radiative decay of Er^{3+} ions once excited to the green- and red-emitting levels took place upon shelling with $NaDyF_4$, the Yb^{3+}-sensitized population of these emitting levels was hampered by Dy^{3+} ions (reflected in the shortened lifetime of Yb^{3+}, Figure 5.4). Consequently, only a few Er^{3+} ions undergo efficient UC excitation followed by radiative decay, resulting in overall poor UC emission when Dy^{3+} ions are in proximity to the emitters. Growth of an outer $NaDyF_4$ shell resulted in even longer Er^{3+} lifetimes for both the green and red emissions (Figure 5.8 (A/B2/3)), reaching lifetimes from *ca*. 240 to *ca*. 330 µs for ^{4nm}Dy-CSS^{3nm} and ^{6nm}Dy-CSS^{3nm} NPs, respectively, providing overall efficient protection from surface quenching. Figure 5.9 summarizes the interplay between the $Yb^{3+} \rightarrow Dy^{3+}$ energy transfer hampering efficient UC excitation of Er^{3+} and UC emission intensity as a function of NP architecture. Ultimately, both aspects together result in not only restored but enhanced UC emission, demonstrated here – to the best of our knowledge – for the first time.

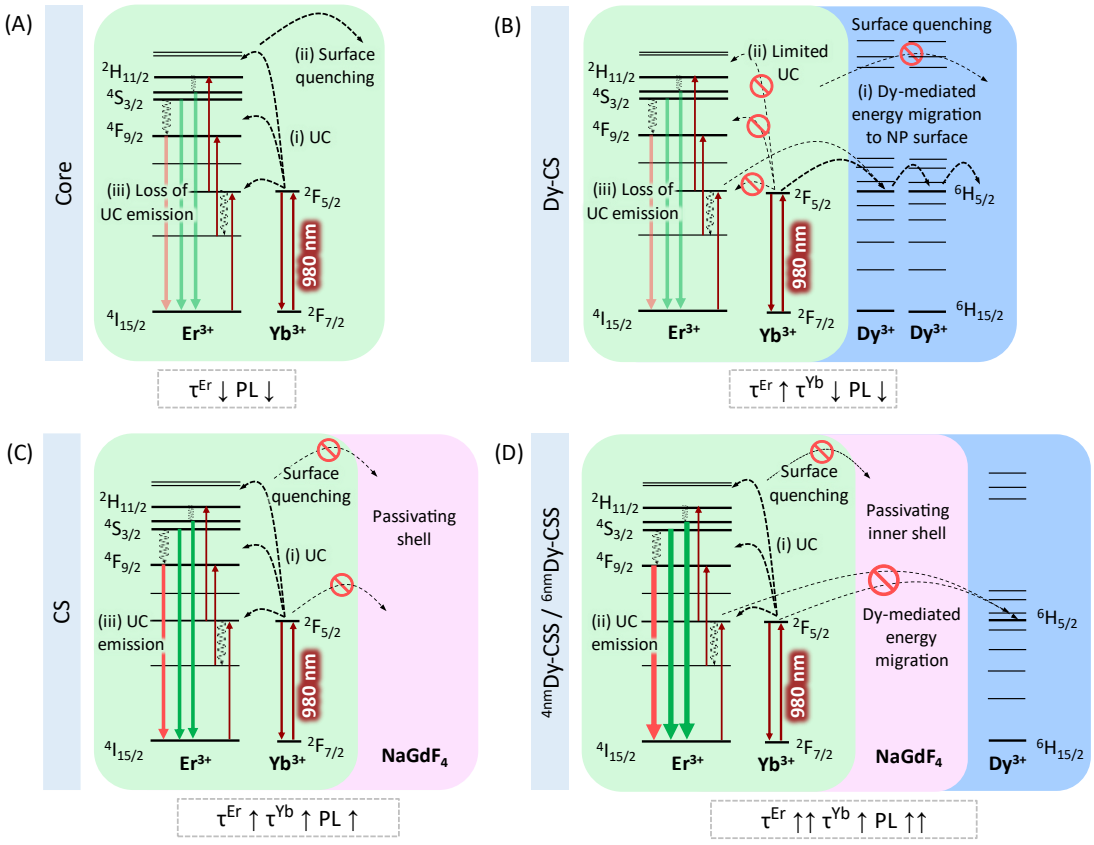

Figure 5.9. Partial energy level diagrams for UC pair Yb^{3+}/Er^{3+} and Dy^{3+} as well as mechanisms resulting in the observed architecture-dependent green and red UC emission intensities of (A) core, (B) Dy-CS, (C) CS, and (D) Dy-CSS NPs. The following dominating mechanisms are proposed based on UC emission intensities as well as Yb^{3+} and Er^{3+} excited state lifetimes: (A) Loss of UC emission due to surface quenching. (B) Loss of UC emission due to Dy^{3+}-mediated energy migration to the NP surface. (C) Enhancement of UC emission due to prevention of surface quenching. (D) Restoration and enhancement of UC emission due to prevention of Dy^{3+}-mediated energy migration and protection of the Er^{3+} excited states from surface quenching.

To explore the effect of the $NaDyF_4$ shell on the probes' performance, particularly MRI T_2 and CT capabilities (*vide infra*), additional Dy-CSS NPs were synthesized. Given the good optical performance of ^{4nm}Dy-CSS^{3nm}, exhibiting a *ca.* 4 nm thick inner shell, two samples with an outer $NaDyF_4$ shell of varying thickness on ^{4nm}CS NPs were synthesized. This resulted in a total set of three samples of comparable core size and inner shell thickness, yet, varying outer shells of *ca.* 1 nm (^{4nm}Dy-CSS^{1nm}), 3 nm (^{4nm}Dy-CSS^{3nm}), and 4 nm (^{4nm}Dy-CSS^{4nm}), respectively (Table 5.1). The morphology, size and crystalline phase of these samples are shown in Figure 5.10 and Figure 5.11.

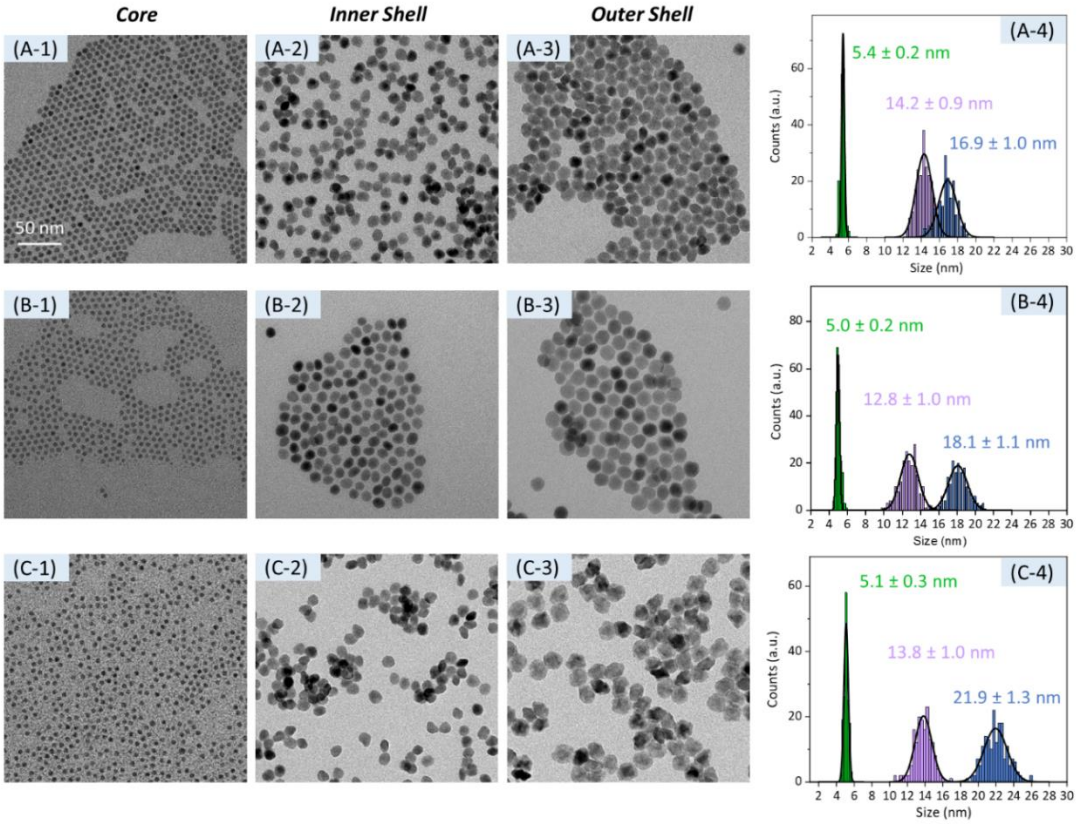

Figure 5.10. Dy-CSS NPs with tuned outer shell thickness: (1-3) TEM images and (4) their corresponding size distributions of OA-capped (A) ^{4nm}Dy-CSS^{1nm}, (B) ^{4nm}Dy-CSS^{3nm} and (C) ^{4nm}Dy-CSS^{4nm} NPs. The core diameter and the thickness of the inner shell were kept constant. The 50 nm scale bar applies to all TEM images.

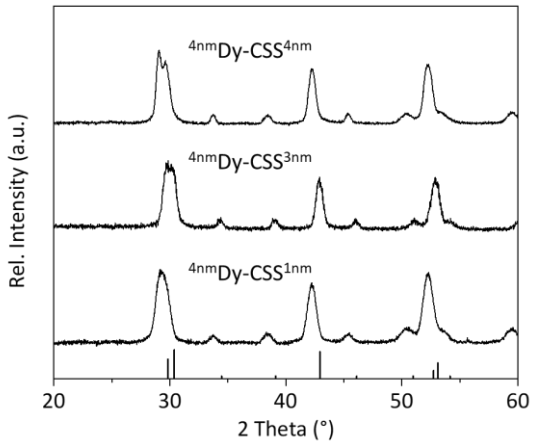

Figure 5.11. XRD patterns of OA-capped ^{4nm}Dy-CSS^{1nm}, ^{4nm}Dy-CSS^{3nm} and ^{4nm}Dy-CSS^{4nm} NPs with tunable outer shell thickness. Reference: β-$NaGdF_4$, PDF card [01-080-8787].

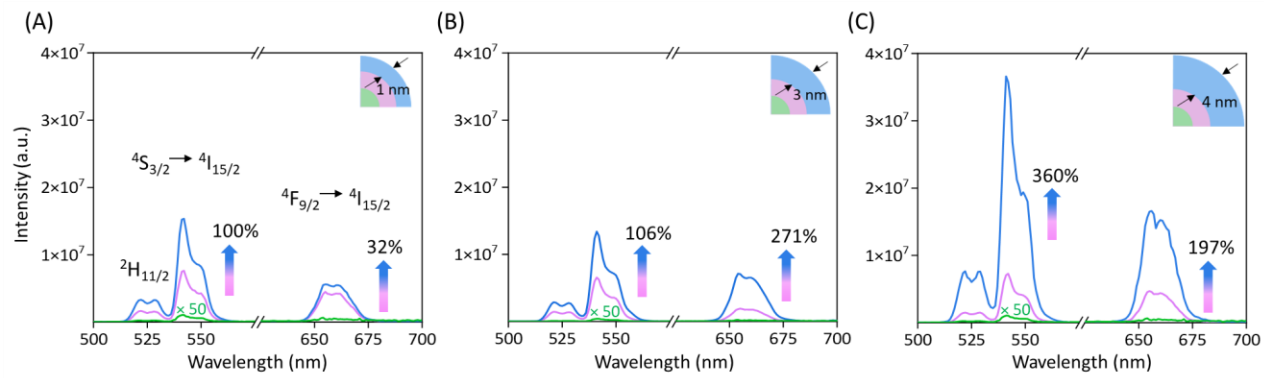

Figure 5.12. UC spectra of OA-capped (A) ^{4nm}Dy-CSS^{1nm}, (B) ^{4nm}Dy-CSS^{3nm} and (C) ^{4nm}Dy-CSS^{4nm} NPs (blue) as well as their corresponding core (green) and CS (pink) NPs. All spectra were obtained under 980 nm laser excitation. Power density = 6.0 W/cm^2, [NP] = 5 mg/mL in toluene.

Figure 5.12 shows the UC spectra of Dy-CSS NPs with comparable inner shell thickness (*ca.* 4 nm), yet, different outer shell thicknesses, 1 nm, 3 nm, and 4 nm, respectively. Due to the efficient inner shell protection, the emission intensities of Dy-CSS NPs in all the three samples were higher than those of their corresponding CS NPs. With the thinnest $NaDyF_4$ outer shell growth, the obtained ^{4nm}Dy-CSS^{1nm} NPs exhibited an enhancement of 100 % for the green and by *ca.* 32 % for the red emission compared to their respective ^{4nm}CS NPs (Figure 5.12 A). The enhancement obtained between ^{4nm}Dy-CSS^{3nm} NPs and their corresponding ^{4nm}CS NPs (Figure 5.12 B) was 106 % for the green and 271 % for the red emission, due to the thicker outer shell thickness. When the $NaDyF_4$ shell thickness increased to *ca.* 4 nm, the obtained ^{4nm}Dy-CSS^{4nm} NPs showed the strongest intensity among all the samples due to its overall thick shell ($NaGdF_4$ + $NaDyF_4$: 8.4 nm) (Figure 5.12 C). Once having a set of Dy-CSS NPs with different inner and outer shell thicknesses in hand, their MRI and CT imaging performances were assessed.

5.2.3 Rendering the NPs Water-Dispersible: Citrate-Capping

Prior to explore MRI and CT capabilities, the NPs had to be rendered hydrophilic and water dispersible. Citrate (Cit) groups were chosen as a model capping agent to transfer the as-obtained, hydrophobic OA-capped NPs into water. The surface modification of OA-capped NPs

with citrate groups was obtained through a ligand exchange process described in Chapter 3.4.[89, 192]

^{3nm}Dy-CSS^{3nm} NPs were disregarded given their inferior optical performance. The morphology of the citrate-capped Dy-CSS NPs was confirmed by TEM analysis (Figure 5.13 A), showing the same morphology and size comparing to their OA-capped counterparts. A representative Cit-^{4nm}Dy-CSS^{3nm} sample was selected for further characterizations by FTIR, XRD, and DLS. As shown in Figure 5.13 B, the successful citrate capping was confirmed by Fourier transform infrared (FTIR) spectroscopy. The crystallinity of the Cit-^{4nm}Dy-CSS^{3nm} NPs was confirmed by XRD analysis (Figure 5.13 C), showing that the pure hexagonal phase was retained. The hydrodynamic diameter of the Cit-^{4nm}Dy-CSS^{3nm} NPs was determined to 23.4 ± 4.7 nm (PDI: 0.27) (Figure 5.13 D), while the NPs exhibited a negative zeta potential of -32.4 ± 0.4 mV. In order to evaluate the potential bioimaging applications of these Cit-Dy-CSS NPs, the cytotoxicity of Cit-^{4nm}Dy-CSS^{3nm} NPs against human lung adenocarcinoma cells (A549) was firstly assessed using the flow cytometry assay.

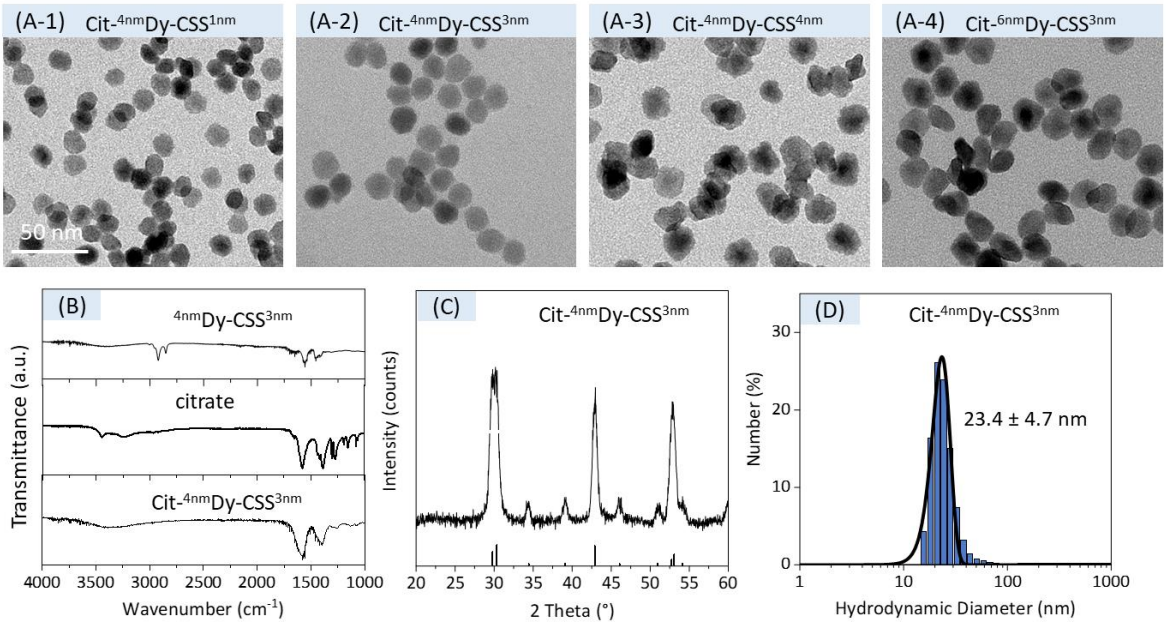

Figure 5.13. (A) TEM images of Cit-^{4nm}Dy-CSS^{1nm} (1), Cit-^{4nm}Dy-CSS^{3nm} (2), Cit-^{4nm}Dy-CSS^{4nm} (3) and Cit-^{6nm}Dy-CSS^{3nm}. The 50 nm scale bar applies to all TEM images. (B) FTIR spectra of citrate- and OA-capped ^{4nm}Dy-CSS^{3nm} NPs as well as citrate used as a reference. (C) XRD pattern of Cit-^{4nm}Dy-CSS^{3nm} NPs. Reference: β-$NaGdF_4$, PDF card [01-080-8787]. (D) DLS curve of Cit-^{4nm}Dy-CSS^{3nm} NPs dispersed in water. DLS data revealed a hydrodynamic diameter of 23.4 nm (polydispersity index, PDI: 0.27).

As shown in Figure 5.14, the cell viability remained 95 % for all NP concentrations, indicating low cytotoxicity of citrate-capped NPs at concentrations below 500 µg/mL in line with the reported results for the $NaREF_4$ NPs.[258]

Despite some expected loss of photoluminescence intensity upon dispersion of the NPs in water compared to their OA-capped counterparts in toluene, Cit-^{4nm}Dy-CSS^{3nm} NPs still showed bright UC emission and NIR emission at 1570 nm, which stems from the $^4I_{13/2} \rightarrow {}^4I_{15/2}$ Er^{3+} transition (Figure 5.15). Understanding the nano-bio interactions (interactions between NPs and complex biological systems) is critical for developing NPs for *in vivo* applications. Therefore, with respect to future applications of the studied NPs, the photoluminescence stabilities in different media were investigated. As shown in Figure 5.16, the NPs exhibited good luminescence stability after incubation in water and phosphate-buffered saline (PBS) for 24 h at 37° C. The photoluminescence stability of Cit-^{4nm}Dy-CSS^{3nm} NPs was assessed by monitoring the Er^{3+} UC emission intensity of the NPs in water and PBS buffer, respectively, at room temperature and 37 °C as a function of time. As shown in Figure 5.16 A, at room temperature, the UC emission intensity of Cit-^{4nm}Dy-CSS^{3nm} NPs in water remained after 24 h incubation, while a slight decrease of 10% was observed in PBS buffer. The emission intensities retained 80 % when incubating the NPs in water and PBS at 37°C after 24 h (Figure 5.16 B).

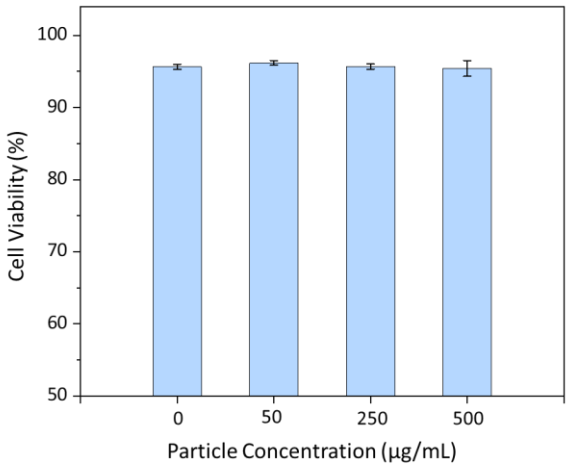

Figure 5.14. Cell viability of A549 cells incubated with Cit-^{4nm}Dy-CSS^{3nm} NPs at different concentrations (0, 50, 250, and 500 µg/mL) for 24 h at 37 °C.

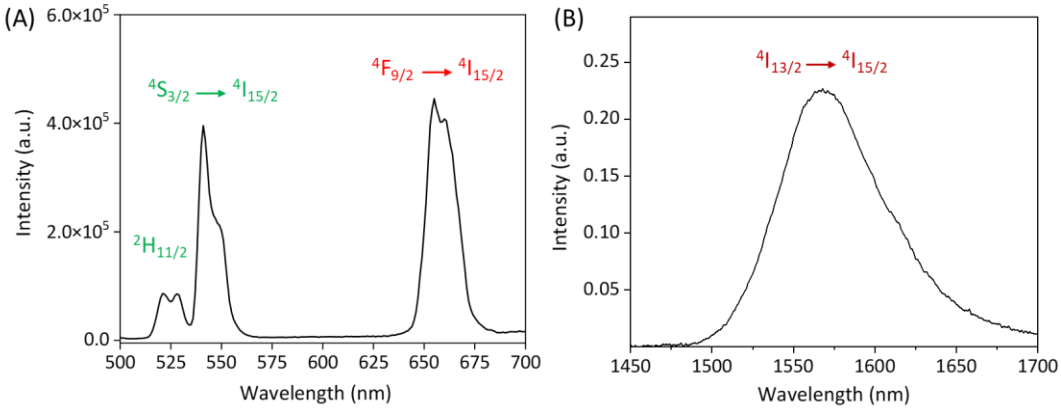

Figure 5.15. Upconversion (A) and downshifting (B) luminescence spectra of Cit-^{4nm}Dy-CSS^{3nm} NPs (5 mg/mL in water for UC emission, 10 mg/mL in water for NIR emission) obtained under 980 nm laser excitation. Power densities used to trigger UC and NIR emission were 6.0 W/cm^2 and 33.3 W/cm^2, respectively.

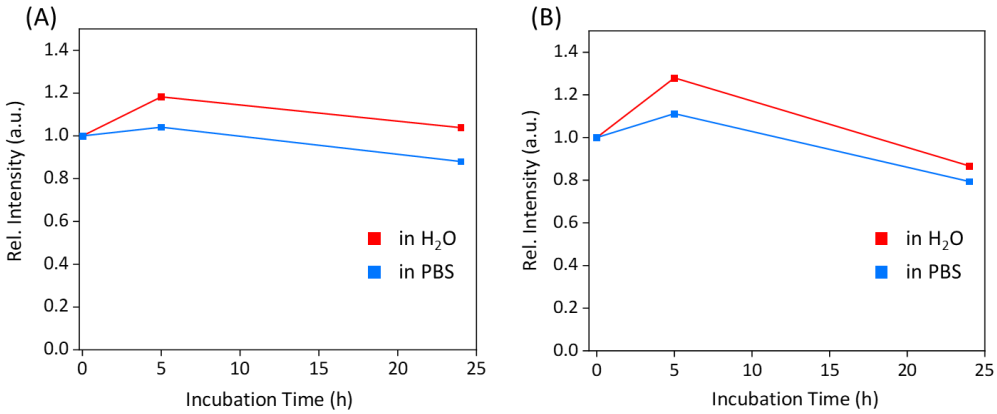

Figure 5.16. Overall UC emission intensity of Cit-^{4nm}Dy-CSS^{3nm} NPs as a function of incubation time in H_2O and PBS at (A) room temperature and (B) 37 °C.

Er^{3+}-based upconverting NPs are well known for their thermometric sensing capabilities, whereas the temperature-induced change in luminescence intensity ratio (LIR) – LIR being the ratio between the $^2H_{11/2} \rightarrow {}^4I_{15/2}$ (525 nm) and $^4S_{3/2} \rightarrow {}^4I_{15/2}$ (540 nm) emission intensities – is a suitable and popular thermometric parameter.[47, 259] While nanothermometry was not the major focus of this study, we stepped forward to briefly explore this avenue, assessing the potential of the prepared NPs for thermal sensing and imaging. In order to assess the performance of Cit-^{4nm}Dy-CSS^{3nm} NPs dispersed in water as nanothermometers, temperature-dependent UC spectra were

recorded from 15 to 50 °C, including the physiologically relevant range from 35 to 45 °C. As shown in Figure 5.17 A, an increase of the emission intensity at 525 nm ($^2H_{11/2} \rightarrow {}^4I_{15/2}$) relative to that at 540 nm ($^4S_{3/2} \rightarrow {}^4I_{15/2}$) was observed upon temperature increase. This is expected as higher temperatures provide the energy required for the population of the higher laying $^2H_{11/2}$ Er^{3+} level. The thermometric parameter, LIR = I_{525}/I_{540}, was calculated using the two integrated spectral regions of I_{525} (500 – 535 nm) and I_{540} (535 – 575 nm). The obtained LIR values as a function of temperature are shown in Figure 5.17 B.

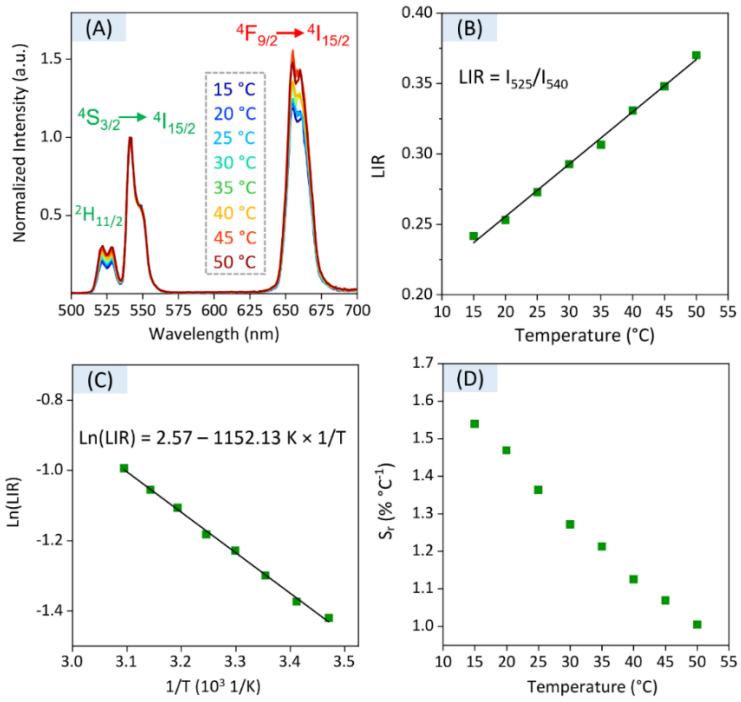

Figure 5.17. (A) Temperature-dependent emission spectra of Cit-^{4nm}Dy-CSS^{3nm} NPs dispersed in water. (B) Luminescence intensity ratio (LIR) between the two green emission bands stemming from the $^2H_{11/2}$ and $^4S_{3/2}$ excited levels plotted against temperature. (C) Natural logarithm of LIR plotted as a function of the inverse absolute temperature (Boltzmann's plot). (D) Relative thermal sensitivity, S_r, plotted as a function of the temperature.

The temperature governed population of the two closely spaced energy levels of Er^{3+} follows a Boltzmann's distribution, and LIR can be expressed by equation 5.1:

$$LIR = \frac{I_{525}}{I_{540}} = B \times \exp\left(-\frac{\Delta E}{k_B T}\right) \qquad \textbf{(Eq. 5.1)}$$

where ΔE is the energy gap between the emitting levels in close proximity, I_{525} and I_{540}, and B is a constant that depends on the experimental system and the intrinsic spectroscopic parameters of the dopant/host pair. T is given in Kelvin. k_B is the Boltzmann factor. The Boltzmann's plot and its linear fits for Cit-^{4nm}Dy-CSS^{3nm} are shown in Figure 5.17 C.

As shown in Figure 5.17 D, the S_r values obtained for the Dy-CSS NPs were larger than 1% °C^{-1} over the assessed temperature range, with S_r values of *ca.* 1.1 to 1.2% °C^{-1} at physiologically relevant temperatures. The obtained S_r values were in line with the reported values of Er^{3+} based upconversion nanothermometry.[10]

5.2.4 Citrate-Capped Dy-CSS NPs for MR Imaging

The Dy^{3+} ion has the potential to be a T_2-weighted MRI contrast agent due to its high magnetic moment. To study the effect of the $NaDyF_4$ shell thickness of the obtained Cit-Dy-CSS NPs on T_2 contrast performance, T_2 and T_1 relaxivities (r_2 and r_1) were measured at 7 T. As shown in Figure 5.18 A, the T_2-weighted MRI signals obtained from Cit-Dy-CSS NPs changed from brighter to darker when the concentration of Dy^{3+} increased, indicating the potential of these NPs to act as T_2 contrast agents.

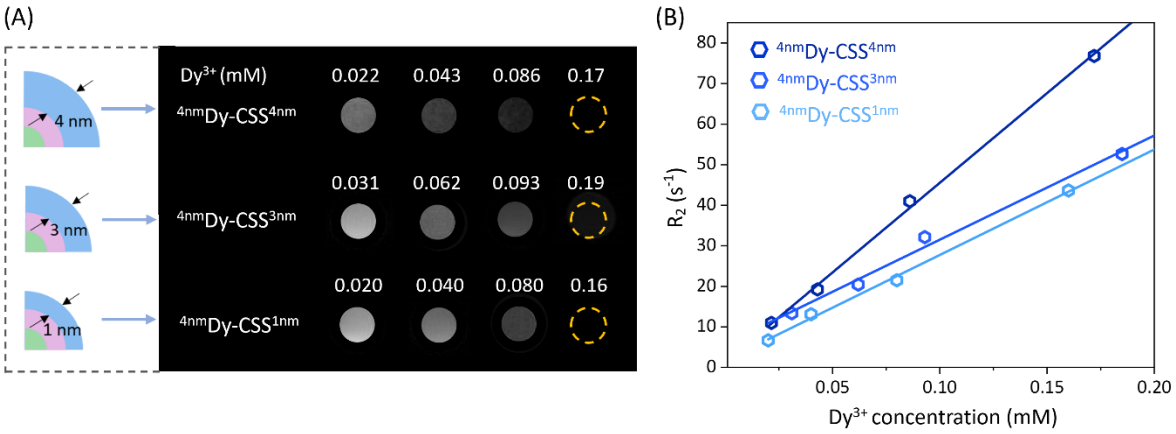

Figure 5.18. (A) T_2-weighted MR images of Cit-Dy-CSS NPs with varying $NaDyF_4$ outer shell thickness (Cit-^{4nm}Dy-CSS^{1nm}, Cit-^{4nm}Dy-CSS^{3nm} and Cit-^{4nm}Dy-CSS^{4nm}) as a function of the Dy^{3+} concentration. (B) Relaxation rate R_2 (= $1/T_2$) of water protons plotted against the molar concentration of Dy^{3+} at 7 T. Solid lines are linear fits.

The relaxivity values were extracted from the slopes of the linear fits of the relaxation rates R_2 and R_1 (= $1/T_2$ and $1/T_1$) against the molar concentration of Dy^{3+} ions of the NP dispersions as obtained from ICP-OES (Figure 5.18 B – r_2; Figure 5.19 – r_1; all values are summarized in Table 5.3). Similar r_2 values were obtained for Cit-^{4nm}Dy-CSS^{1nm} (260.0 $mM^{-1}\,s^{-1}$) and Cit-^{4nm}Dy-CSS^{3nm} NPs (256.9 $mM^{-1}\,s^{-1}$), while a significant increase of r_2 to 442.1 $mM^{-1}\,s^{-1}$ was observed when the $NaDyF_4$ shell thickness increased to 4 nm (Cit-^{4nm}Dy-CSS^{4nm}). This increase in r_2 was ascribed to the increasing amount of Dy^{3+} ions in the sample upon growth of a thicker outer shell, resulting in a higher Dy^{3+}-to-Gd^{3+} ratio (Figure 5.20). Larger particle sizes have previously been reported to result in more pronounced T_2 contrast enhancement, as demonstrated for different-sized $NaDyF_4$ NPs.[109, 111] Even though the direct comparison with data from the literature is difficult given the different NP architectures under investigation (CSS in this study *versus* previously investigated core-only NPs), the larger size of the Cit-^{4nm}Dy-CSS^{4nm} NPs might also contribute to the observed T_2 contrast enhancement.

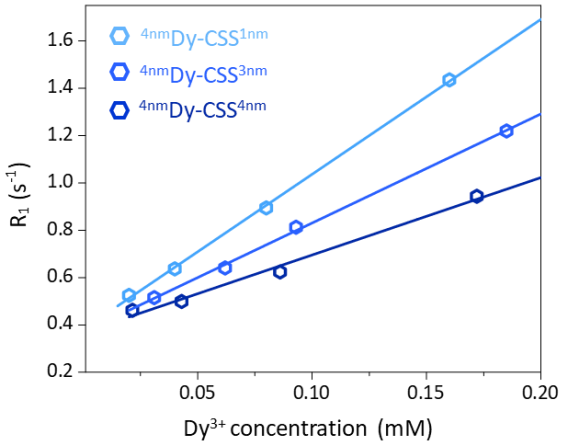

Figure 5.19. Relaxation rate R_1 (= $1/T_1$) of water protons plotted against the molar concentration of Dy^{3+} for Cit-^{4nm}Dy-CSS^{1nm}, Cit-^{4nm}Dy-CSS^{3nm} and Cit-^{4nm}Dy-CSS^{4nm} NPs at 7 T. The solid lines are linear fits.

Table 5.3. Relaxivity values r_2 and r_1 of Cit-Dy-CSS NPs at 7 T. Relaxivity values and the associated errors were obtained from the linear fitting procedure of the data sets reported in Figure 5.18, Figure 5.19, and Figure 5.21.

Sample	Size (nm)	r_2 (mM^{-1} s^{-1})	r_1 (mM^{-1} s^{-1})	r_2/r_1
^{4nm}Dy-CSS^{1nm}	16.9	260.0 ± 9.8	6.5 ± 0.1	40.0
^{4nm}Dy-CSS^{3nm}	18.1	256.9 ± 17.7	4.6 ± 0.1	55.8
^{4nm}Dy-CSS^{4nm}	21.9	442.1 ± 22.1	3.3 ± 0.2	134.0
^{6nm}Dy-CSS^{3nm}	22.0	116.0 ± 10.0	2.5 ± 1.1	46.4

On the contrary, the r_1 values decreased with increasing $NaDyF_4$ shell thickness (Figure 5.19, Table 5.3). It is important to recall that $NdGdF_4$ was used as host matrix for the core and inner shell of the CSS-NPs. Gd^{3+} ions are well known for their T_1 MRI capabilities when in close vicinity to water protons. Thus, the Gd^{3+} ions in the core and inner shell might influence the overall MRI performance of the CSS-NPs. Indeed, the highest r_1 value was obtained for Cit-^{4nm}Dy-CSS^{1nm} NPs with a very thin outer shell. Such thin shelling might be less efficient and prone to cation intermixing, resulting in Gd^{3+} ions close to the NP surface where they can interact with water protons, contributing to higher r_1 value. Thicker $NaDyF_4$ shells provided greater shielding of the Gd^{3+} ions in the inner shell, resulting in lower r_1 values. Overall, the resultant r_2/r_1 ratios increased from 40.0 to 55.8 and 134.0 with increasing $NaDyF_4$ shell thickness. As larger r_2/r_1 ratios provide for higher signal-to-noise and more robust contrast enhancement in T_2-weighted images,[111] Cit- ^{4nm}Dy-CSS^{4nm} NPs with the thickest outer shell are the most promising among the studied T_2 MRI CA candidates.

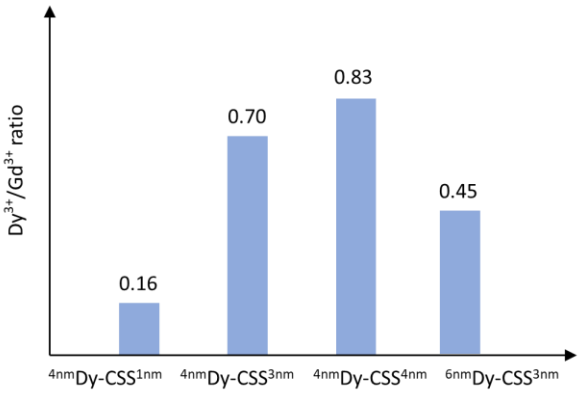

Figure 5.20. Dy^{3+}-to-Gd^{3+} ion ratio in the Dy-CSS NPs obtained from ICP measurements.

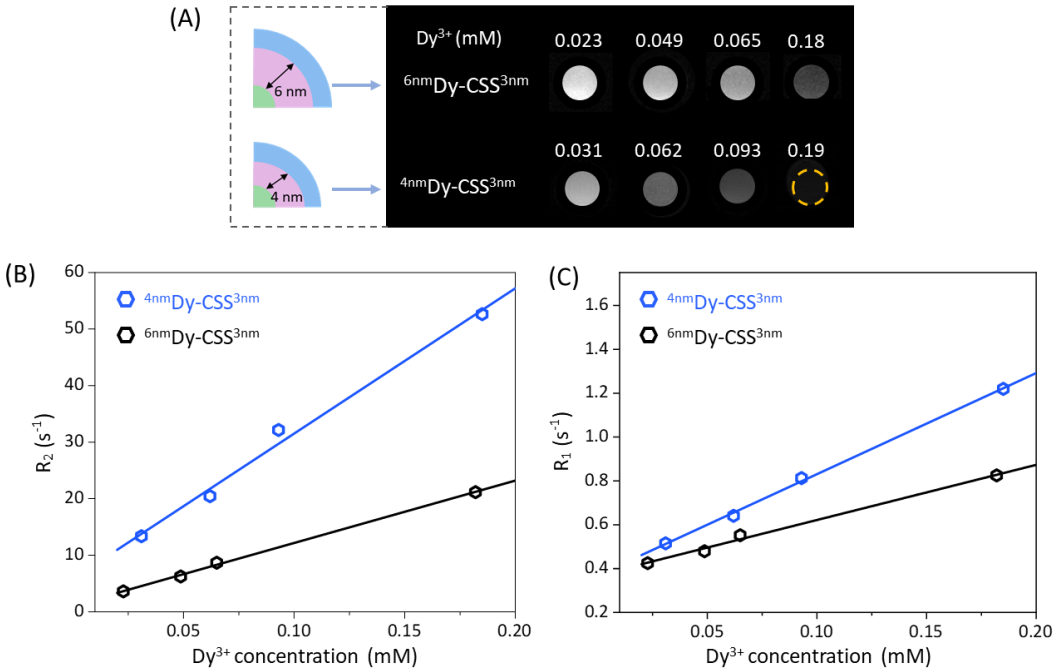

Figure 5.21. (A) T_2-weighted MR images of Cit-Dy-CSS NPs with varying $NaGdF_4$ inner shell thickness (Cit-^{4nm}Dy-CSS^{3nm} and Cit-^{6nm}Dy-CSS^{3nm}) as a function of the Dy^{3+} concentration. (B) Relaxation rate R_2 (= $1/T_2$) and (C) R_1 (=$1/T_1$) of water protons plotted against the molar concentration of Dy^{3+} for Cit-^{6nm}Dy-CSS^{3nm} and Cit-^{4nm}Dy-CSS^{3nm} at 7 T. Solid lines are linear fits.

The effect of the inner $NaGdF_4$ shell thickness on the T_2 contrast behaviour was also investigated. As shown in Figure 5.21, Cit-^{4nm}Dy-CSS^{3nm} NPs exhibited a higher r_2 value (256.9 $mM^{-1}\,s^{-1}$) than Cit-^{6nm}Dy-CSS^{3nm} NPs (116.0 $mM^{-1}\,s^{-1}$), which can be ascribed to the relatively higher Dy^{3+} content in the sample (Figure 5.20). In line, a larger r_2/r_1 ratio was obtained for Cit-^{4nm}Dy-CSS^{3nm} (55.8)

than for Cit-^{6nm}Dy-CSS^{3nm} (46.4) NPs, demonstrating the importance to not only tune the outer $NaDyF_4$ but also inner $NaGdF_4$ shell. Noteworthy, all the r_2 values of Cit-Dy-CSS NPs are higher than those of commercial iron oxide-based T_2 contrast agents (Combidex: 60.0 mM^{-1} s^{-1}, Feridex: 93.0 mM^{-1} s^{-1}) and other comparable sized Dy-based NPs (Table 5.4) [111, 133, 144, 260-269]. These observations are promising with respect to the potential use of Dy-CSS NPs T_2 CAs. Particularly, high relaxivity CAs are generally considered beneficial as they can allow for the administration of lower doses, ultimately contributing to lower toxicity risks. [270]

5.2.5 Citrate-Capped Dy-CSS NPs for CT Imaging

Owing to the relatively high K-edge values and X-ray attenuation coefficients of the Ln ions, Cit- Dy-CSS NPs hold potential for CT imaging. To assess their CT contrast performance, we first used X-ray spectrometry (Figure 5.22) to compare the X-ray absorption efficacy of Cit-Dy-CSS NPs to that of Iohexol (a widely used clinical CT CA). With the iodine K-edge at 33.3 keV, Iohexol absorbs X-ray photons most effectively in the range 35-50 keV.[271] In comparison, Cit-Dy-CSS NPs absorb more photons in a higher energy region (50-120 keV) due to the higher K-edge values of Gd (50.2 keV) and Dy (53.8 keV). In an alternative approach to demonstrate the X-ray absorption behaviour of Iohexol and Cit-Dy-CSS NPs (Cit-^{4nm}Dy-CSS^{3nm}, Cit-^{6nm}Dy-CSS^{3nm}), radiography imaging was performed across a range of X-ray source voltages from 70 to 120 kV. These voltages are consistent with conditions used in clinical applications.

As shown in Figure 5.23 A, CT values (Hounsfield units, HU) for Iohexol were highest at a source voltage of 70 kV, followed by a continuous decrease with voltage increase to 120 kV. This is expected given the optimized performance of Iohexol at lower energies.[272] On the contrary, the CT values of Cit-Dy-CSS NPs displayed an initial increase in CT values when the voltage increased from 70 to 110 kV, followed by a decrease at 120 kV (Figure 5.23 B/C). This decrease in CT values at higher voltage was caused by the mismatch of the K-edge values of Gd and Dy in the high-energy region. The highest CT value obtained for Cit-^{6nm}Dy-CSS^{3nm} NPs at 110 kV was 1080 HU (Ln^{3+} ion concentration, *i.e.*, sum of Gd^{3+}, Dy^{3+}, Yb^{3+} and Er^{3+} = 94.2 mM) compared to 850 HU of Iohexol (I^- ion concentration = 157.6 mM).

Table 5.4. Comparison of MRI T_2 relaxivity values of clinically used iron oxide NPs, Dy-based chelates, and Dy-based NPs. The table also shows examples for multimodal CAs for additional optical and CT imaging.

Contrast Agents	Size (nm)	Surface Coating	r_2 (mM^{-1} s^{-1})	r_1 (mM^{-1} s^{-1})	r_2/r_1	Magnetic Field (T)	Other Imaging Capabilities	Ref.
Clinically Used CAs								
Combidex (Fe_3O_4)	5.9	dextran	60.0	10	6.0	1.5		260
Feridex (Fe_3O_4, γ-Fe_2O_3)	5.0	dextran	93.0	4.1	22.7	3	-	261
Resovist (Fe_3O_4)	4.0	carboxy-dextran	146.0	4.6	31.7	3		261
Dy-Based Chelates								
Dy-DOTA	-	-	20.0	-	-	9.4	-	262
Dy-DTPA-PcHexPh$_2$			3.0	0.1	30	7		263
Dy-Based Nanoparticles								
$NaDyF_4$:Tb	30×35	CTAB[a]	22.3	-	-	7	optical	273
$NaDyF_4$	20.3	PMAO-PEG[b]	101.0	-	-	9.4	-	111
$NaGdF_4$:Dy	7.5	PEG[c]	10.6	5.2	2.0	9.4	CT	265
$NaGdF_4$:Yb,Er /$NaYbF_4$:Dy(38 %)	31.0	citrate	70.0	0.5	140	9.4	optical	141
$NaLuF_4$:Yb,Tm /$NaLuF_4$/$NaDyF_4$	21×39	PC[d]	40.0	-	-	7	optical CT	144
$NaYbF_4$:Tm /CaF_2/$NaDyF_4$	16.0	citrate	41.0	-	-	7	optical CT	133
$NaYF_4$:Nd /$NaDyF_4$	15.7	liposome	44.0	-	-	11.7	optical	267
Dy_2O_3	70.0	dextran	190	-	-	7	-	268
Dy-doped γ-Fe_2O_3	4.2	PEG	123.3	-	-	1.5	-	269
Cit-^{4nm}Dy-CSS^{1nm}	16.9	citrate	260.0	6.5	40.0	7	optical CT	this work
Cit-^{4nm}Dy-CSS^{3nm}	18.1	citrate	256.9	4.6	55.8	7	optical CT	this work
Cit-^{4nm}Dy-CSS^{4nm}	21.9	citrate	442.1	3.3	134	7	optical CT	this work
Cit-^{6nm}Dy-CSS^{3nm}	22.0	citrate	116.0	2.5	46.4	7	optical	this work

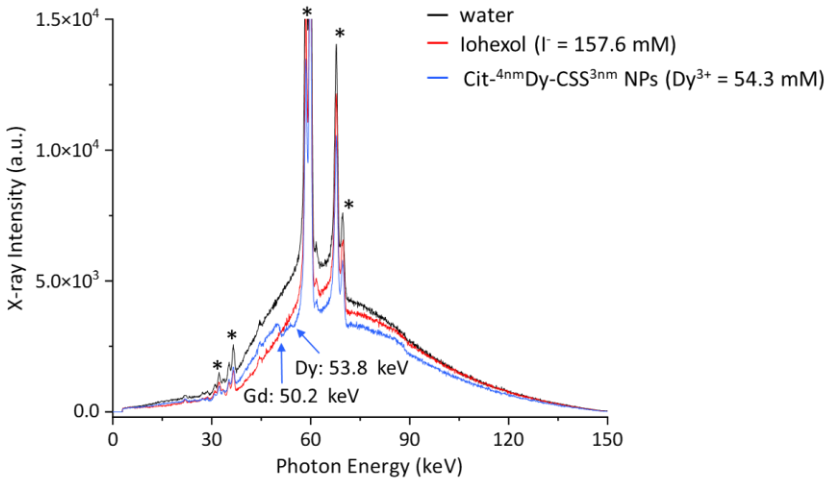

Figure 5.22. X-ray absorption spectra for water, Iohexol, and Cit-^{4nm}Dy-CSS^{3nm} NPs using a tungsten X-ray tube operating at 150 kV. Peaks marked with stars belong to the X-ray source, tungsten.

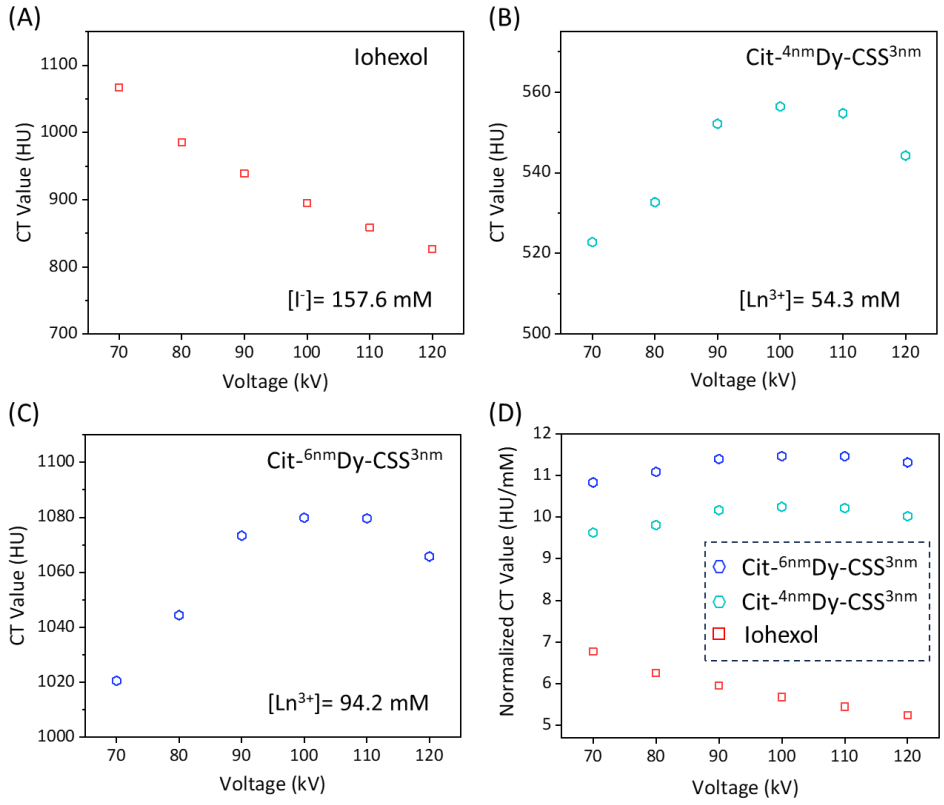

Figure 5.23. CT values of (A) Iohexol, (B) Cit-^{4nm}Dy-CSS^{3nm} NPs, (C) Cit-^{6nm}Dy-CSS^{3nm} NPs, and (D) their corresponding normalized values as a function of X-ray source peak voltage.

Normalization of the CT values to the concentration of the corresponding contrast agent, revealed more than two-times higher values for the Cit-Dy-CSS NPs than for Iohexol between 100 and 120 kV (Figure 5.23 D). These findings demonstrate the potential of Cit-Dy-CSS NPs as CT CA candidates with higher contrast efficacy compared to Iohexol at 110 kV and the advantage that X-rays optimized for the K-edge of the Ln^{3+} have lower potential for tissue damage than those optimized for the K-edge of iodine.[132]

Encouraged by the results of radiography imaging, CT phantom imaging measurements of Cit-Dy-CSS NPs and Iohexol were performed at 110 kV. Herein, samples with thinner and thicker $NaDyF_4$ shells were investigated to assess any potential effect that the outer shell thickness might have on CT performance. As shown in Figure 5.24 A, with similar CA concentrations, all Cit-Dy-CSS NPs produced brighter CT signals than Iohexol. The obtained CT values increased linearly with the concentration for Cit-Dy-CSS NPs and Iohexol (Figure 5.24 B), and the slopes extracted from the linear fits are shown in Table 5.5. Among the three Cit-Dy-CSS samples, the slope values increased with the $NaDyF_4$ shell thickness increasing from 1 nm to 4 nm (9.4 ± 1.3 HU mM^{-1} for Cit-^{4nm}Dy-CSS^{1nm}, 11.4 ± 0.5 HU mM^{-1} for Cit-^{4nm}Dy-CSS^{3nm} and 13.1 ± 0.05 HU mM^{-1} for Cit-^{4nm}Dy-CSS^{4nm}). These findings can be ascribed to the relatively larger amount of Dy^{3+} with increasing $NaDyF_4$ shell thickness, resulting in a higher Dy^{3+}-to-Gd^{3+} ratio (Figure 5.20), ultimately allowing for higher X-ray attenuation. Noteworthy, all the slope values obtained from Cit-Dy-CSS NPs were higher than that of Iohexol (5.8 ± 1.3 HU mM^{-1}), indicating that Cit-Dy-CSS NPs exhibit higher contrast efficacy than Iohexol.

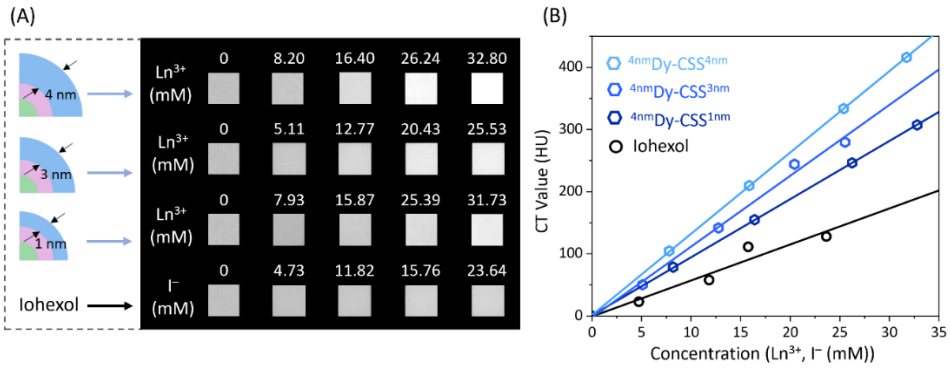

Figure 5.24. (A) CT images of Cit-Dy-CSS (Cit-^{4nm}Dy-CSS^{1nm}, Cit-^{4nm}Dy-CSS^{3nm}, and Cit-^{4nm}Dy-CSS^{4nm}) NPs and clinically used CT CA Iohexol at different concentrations. (B) CT values for different concentrations of Cit-Dy-CSS NPs dispersed in water and Iohexol solutions. Solid lines are linear fits.

Table 5.5. CT capabilities of Cit-Dy-CSS NPs and Iohexol solution measured at 110 kV.

Sample	Size (nm)	Slope of the linear fit (HU mM^{-1})
^{4nm}Dy-CSS^{1nm}	16.9	9.4 ± 0.03
^{4nm}Dy-CSS^{3nm}	18.1	11.4 ± 0.5
^{4nm}Dy-CSS^{4nm}	21.9	13.1 ± 0.05
Iohexol	-	5.8 ± 1.3

5.3 Conclusions

With the goal to design a NP candidate to act as multimodal probe that merges upconversion and T_2 MRI capabilities, a set of Dy-CSS NPs doped with Er and Yb was synthesized using a microwave-assisted approach. Careful tuning of the microwave reaction conditions allowed for tuning of the inner shell thickness from *ca*. 3 to 6 nm. Such control is crucial to physically separate the luminescent Er^{3+}/Yb^{3+} ion pair in the core from the magnetic Dy^{3+} ions in the outer shell, ultimately preventing UC loss. The mechanism of UC loss was investigated in detail by evaluating the Er^{3+} upconversion intensities and the excited state lifetimes of Yb^{3+} and Er^{3+} as a function of the inner shell thickness. Based on the Er^{3+} emission spectra and Yb^{3+} lifetimes, an isolating 4 nm inner shell between the emitting core and the $NaDyF_4$ outer shell suppressed energy transfer from Yb^{3+} to Dy^{3+}, followed by Dy^{3+}-mediated energy migration and loss at the NP surface. As a result, UC excitation of the Er^{3+} ions was restored, and enhanced UC emission was observed upon addition of the outer $NaDyF_4$ shell. Noteworthy, the microwave-assisted strategy led to CSS architectures, while keeping the overall NP size close to 20 nm. In addition, the effect of the outer $NaDyF_4$ shell thickness on the particles' magnetic and CT performance was investigated. MRI T_2 relaxivity measurements performed *in vitro* at 7 T on Cit-Dy-CSS NPs revealed that the Cit-^{4nm}Dy-CSS^{4nm} NPs with the thickest outer shell (4 nm) exhibited the highest r_2 value and r_2/r_1 ratio, indicating a superior T_2 contrast effect compared to commercial iron oxide-based CAs and other Dy-based T_2 CAs. In addition, the CT values of Cit-Dy-CSS NPs increased with increasing outer

$NaDyF_4$ shell thickness. Interestingly, all investigated Cit-Dy-CSS NPs exhibited advanced CT contrast efficacy compared to commercially used Iohexol at an X-ray energy of 110 keV. Our results demonstrate the promise of the designed Dy-CSS NPs to act as potential multimodal imaging probe. However, it is important to note that the concentrations of the Dy-CSS NPs examined in this study need further testing to meet the requirements for clinical applications. The concept of fabricating multilayer NPs by use of microwave-assisted routes that offer control over shell thicknesses also provides insights for the future architecture design of Ln-based materials for their *e.g.,* biomedical applications and beyond.

Chapter 6. Microwave-Assisted Synthesis of $NaMnF_3$ Particles with Tuneable Morphologies

*This Chapter is based on published work in Chemical Communications: Nan Liu, Jessica Holmes, Nicolas Bordenave, and Eva Hemmer, Chem. Common., **2021**, 57, 11799-11802.*

Author contributions: E. H. and N. L. conceptualized the study and co-wrote the manuscript. N. L. and J. H. synthesized $NaMnF_3$ samples. N. L. also performed surface coating experiments and ran all the relaxivity measurements under the guidance of N. B.

Abstract:

Here, the synthesis of sub-micron $MMnF_3$ (M = Na or K) particles by a rapid microwave-assisted approach is reported. Adjustment of the N^{a+}-to-Mn^{2+} ratio in the reaction mixture yielded tuneable morphologies, *i.e.*, rods, ribbons, and plates. Relaxometric results indicated that poly(acrylic acid)-capped $MMnF_3$ particles exhibited characteristic magnetic properties, which endows them with potential T_1-weighted contrast agent capabilities.

6.1 Introduction

Complex metal fluorides of general stoichiometry ABF_3, where A and B stand for metal cations, have received considerable attention because of their unique ferroelectric, magnetic, electrochemical, and optical properties.[274-277] $MMnF_3$ (M = Na, K) as important members of the ABF_3 family, have been studied for their potential applications as bioimaging contrast agents, ferromagnets, and active material for batteries.[278-281] In order to obtain $MMnF_3$ materials with controlled size and morphology, solvothermal and thermal decomposition methods are commonly used.[279, 282-284] However, these established strategies relying on conventional heating are time-consuming (typical reaction times up to 24 h). Given the application potential, it is highly desirable to develop a more straightforward strategy for the preparation of $MMnF_3$ particles of controlled size and morphology. In this regard, MW-assisted approaches provide faster and more homogenous heating, thus, significantly shorter reaction durations with excellent reproducibility.[253] Recently, Wang and Chun proposed a MW-assisted solvothermal method towards $NaMnF_3$ nanopowders.[285] The reported reaction time of 1 h constitutes a significant shortening as compared to conventional, convection-based methods. As introduced in Chapter 4, our group developed a MW-assisted approach yielding reproducibly $NaREF_4$ NPs of narrow size distribution within a few minutes.[89, 253] In this work, we report the rapid synthesis of $NaMnF_3$ sub-micron sized particles by a MW-assisted thermal decomposition approach. Especially, we report for the first time the morphology-selective synthesis of $NaMnF_3$ particles by varying the Na^+-to-Mn^{2+} metal ion ratio, yielding rods and ribbons in addition to the commonly seen plate-like structures. The particle growth mechanism suggests that this ratio as well as reaction temperature and time are key factors controlling crystallographic phase and morphology of the particles. Poly (acrylic acid) (PAA)-capped $NaMnF_3$ particles exhibited characteristic relaxometric properties under a magnetic field of 0.47 T, indicating that they may be used as MRI CAs, for example. Overall, this study offers an alternative way to synthesize $NaMnF_3$ sub-micron particles with tuneable morphology and gives insight into their growth mechanism. In addition, the versatility of the established approach was demonstrated by its successful adoption for the synthesis of the potassium-based analogue, $KMnF_3$.

6.2 Results and Discussion

6.2.1 Synthesis of $NaMnF_3$ Particles

Effect of the Na^+-to-Mn^{2+} ratio. In order to uncover the optimal conditions for the formation of $NaMnF_3$ particles of various yet controlled morphologies, a stringent adjustment of the reaction conditions under MW-induced heating was conducted, including the Na^+-to-Mn^{2+} metal ion ratio (using sodium and manganese trifluoroacetate as precursors), nucleation and growth temperatures (T_a and T_b, respectively), as well as reaction time (see Table 6.1 for an overview of all reaction conditions).

Table 6.1. Overview of the experimental conditions used in the microwave-assisted synthesis of $NaMnF_3$ particles, as well as their resulting products and morphologies.

Parameter Studied	Ion Ratio (Na^+-to-Mn^{2+})	T_a [1]	T_b	t (Tb)	Product	Predominant Morphology
Ion Ratio (Na^+-to-Mn^{2+})	1:1	300 °C	240 °C	10 min	$NaMnF_3$ [2]	Rods
	1.5:1					Ribbons
	2:1					Plates
	3:1					Plates
Reaction Temperature	2:1	260 °C 270 °C	240 °C	10 min	NaF	/
		280 °C 290 °C 300 °C			$NaMnF_3$	Irregular Shape
						Plates
		300 °C	240 °C 250 °C 280 °C	10 min	$NaMnF_3$	Plates
						Irregular Shape
Reaction Time	1:1	300 °C	240 °C	1 min 5 min 10 min 20 min	$NaMnF_3$	Rods + Increasing Number of Plates
	2:1			1 min	$NaMnF_3$ $NaMn_3F_7$	Plates + Nanoparticles
				5 min 10 min 20 min	$NaMnF_3$	Plates

[1] Holding time at growth temperature T_a: 1 s

[2] All $NaMnF_3$ particles listed in this table crystallized in the orthorhombic phase

In the context of complex metal fluorides synthesis, the metal ion ratio has significant influence on the crystalline phase, size, and morphology of the targeted material, for example, $NaREF_4$ NPs.[286] Therefore, the effect of the Na^+-to-Mn^{2+} ratio on the crystalline phase formation and morphology of $NaMnF_3$ particles was investigated, setting it to 1:1, 1.5:1, 2:1, and 3:1, while nucleation and growth temperatures as well as reaction time were kept constant (T_a = 300 °C, T_b = 240 °C; t = 10 min – *vide infra* for a rationale for this parameter choice and discussion of the influence of temperature and time on $NaMnF_3$ formation).

The XRD patterns shown in Figure 6.1 confirmed that all $NaMnF_3$ samples crystallized in orthorhombic phase (space group: *Pnma*) irrespective of the chosen Na^+-to-Mn^{2+} ratio. The formation of sodium fluoride (NaF) as a by-product was observed when Na^+ ions were in excess due to non-stoichiometric metal ion ratios (1.5:1, 2:1, and 3:1). This by-product was also observed previously in the microwave-assisted synthesis of β-phase $NaREF_4$ NPs and could be washed away using an ethanol/water mixture.[159] The elemental composition of the particles obtained was further confirmed by EDX spectroscopy analysis (Figure 6.2). It should be noted that the XRD pattern observed for the (1:1) sample differed from those obtained for the other samples: the reflections at 31.07° and 32.22° were missing. This is indicative of a preferential direction for particle growth, ultimately influencing particle morphology.

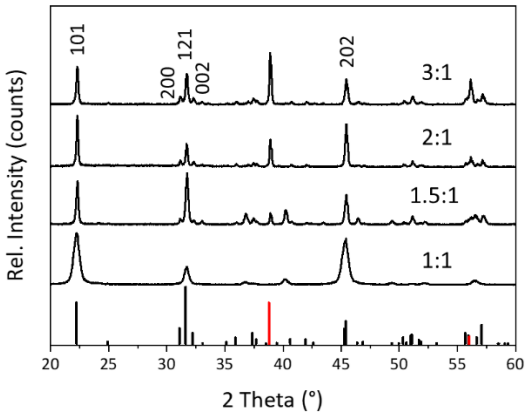

Figure 6.1. XRD patterns of orthorhombic $NaMnF_3$ particles obtained by a MW-assisted thermal decomposition approach using different Na^+-to-Mn^{2+} ratios: 1:1, 1.5:1, 2:1, and 3:1. T_a = 300 °C, T_b = 240 °C; t = 10 min. References: black line – orthorhombic $NaMnF_3$, PDF card [01-072-0291]; red line – NaF, PDF card [00-001-1184].

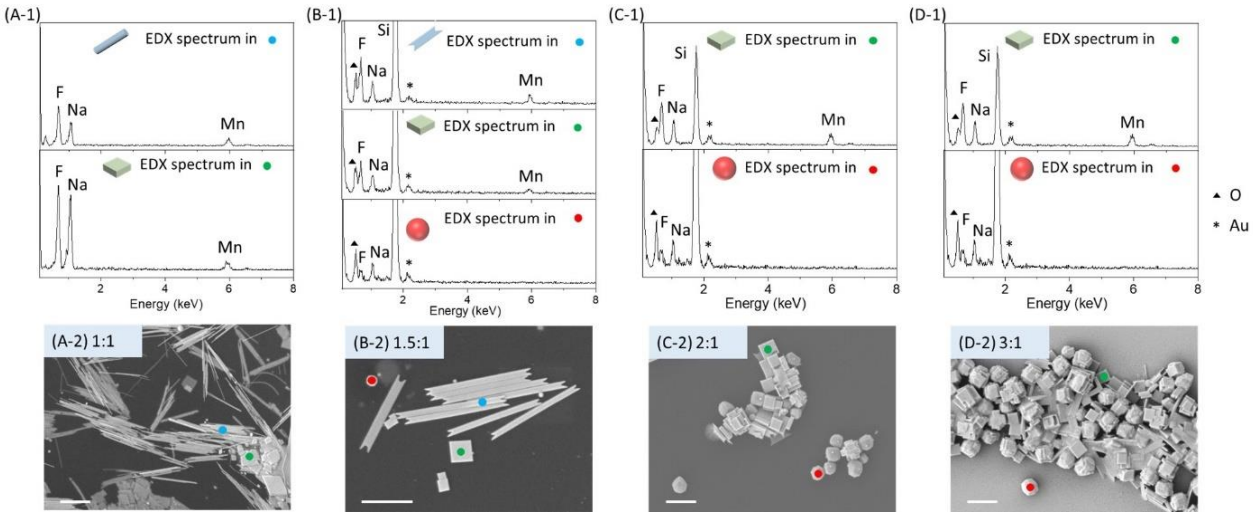

Figure 6.2. EDX spectra (1) and the corresponding SEM images (2) of the particles obtained using different Na^+-to-Mn^{2+} ratios: (A) 1:1, (B) 1.5:1, (C) 2:1, and (D) 3:1. Reaction temperature: T_a = 300 °C, T_b = 240 °C; reaction time = 10 min. Scale bars: 1 µm.

Indeed, SEM and TEM (Figure 6.3) showed very different morphologies for $NaMnF_3$ particles obtained with increasing Na^+-to-Mn^{2+} ratios (see Figure 6.4 for particle size distributions). The particles produced with a 1:1 ratio exhibited a dominant nanorod morphology of 1.3 ± 0.1 µm in length and 19.5 ± 2.7 nm in width (resulting in an aspect ratio of *ca.* 65), and a minor secondary plate-like morphology (Figure 6.3 A). A similar morphology of nanorods was previously reported for $NaMgF_3$, and the preferred growth direction of the nanorods was determined to be along the (0 1 0) crystallographic high-energy facet direction (overlapping with the (1 0 1) reflection in the XRD pattern).[280, 282]

The EDX spectrum in Figure 6.2 (A-1) corroborated that these nanorods were composed of Na, F, and Mn. Upon increase of the amount of Na^+ ions in the reaction mixture to a metal ion ratio of 1.5:1, the particles obtained showed a ribbon-like morphology (Figure 6.3 B). These ribbons were *ca.* 1.7 ± 0.1 µm long and 120 ± 18 nm wide, resulting in an aspect ratio of *ca.* 14, and exhibited hourglass-shaped tips (Figure 6.3 B).

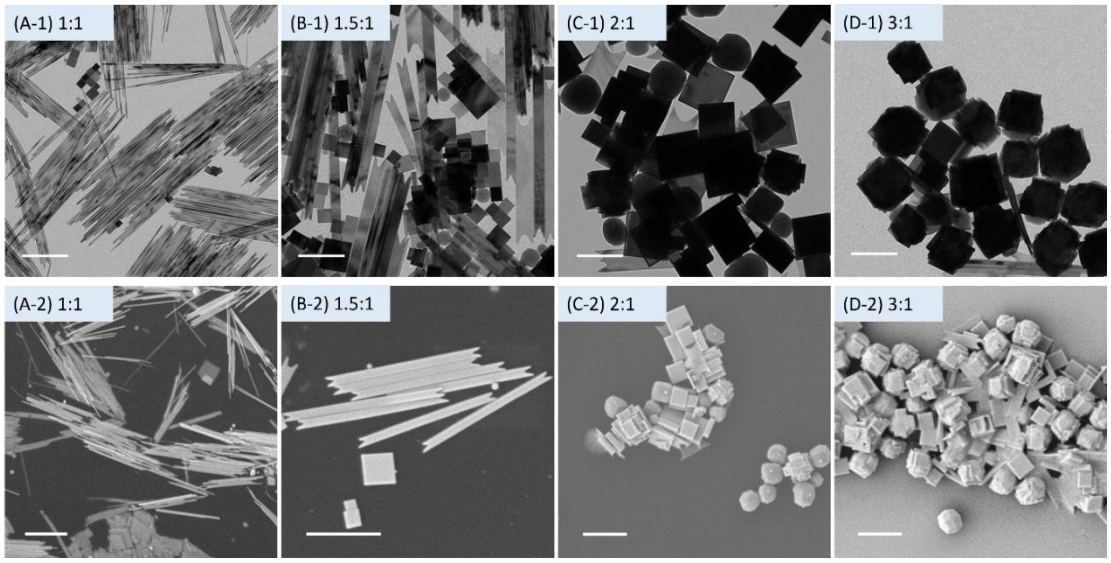

Figure 6.3. (1) TEM and (2) SEM images of $NaMnF_3$ particles synthesized using different Na^+-to-Mn^{2+} ratios: (A) 1:1, (B) 1.5:1, (C) 2:1 and (D) 3:1. Reaction temperature: T_a = 300 °C, T_b = 240 °C, reaction time = 10 min. Scale bars: 1 µm.

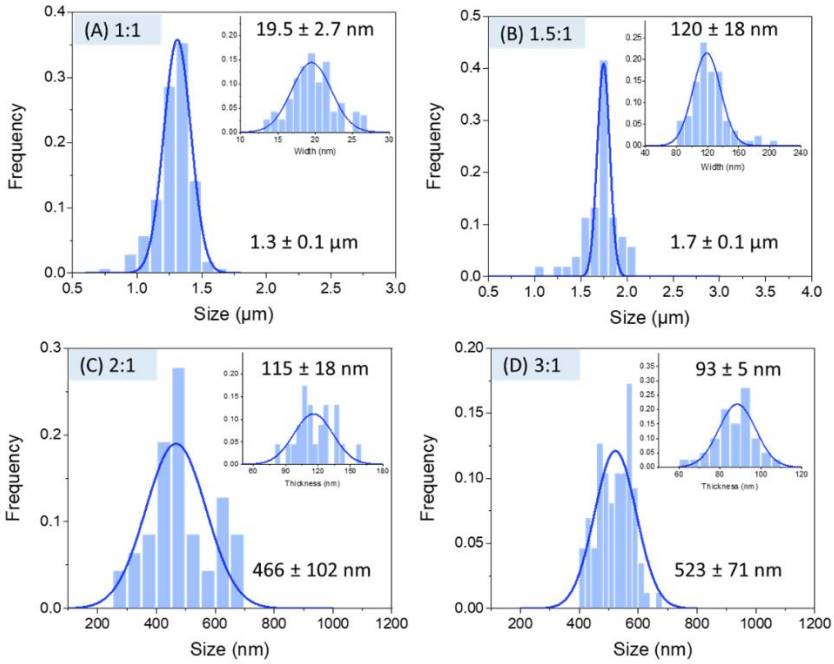

Figure 6.4. Size distributions of $NaMnF_3$ particles synthesized using different Na^+-to-Mn^{2+} ratios: (A) 1:1, (B) 1.5:1, (C) 2:1, and (D) 3:1. The insets in (A) and (B) provide the width distributions for the rods and ribbons obtained; insets in (C) and (D) provide the thickness distributions for the plates obtained. Reaction temperature: T_a = 300 °C, T_b = 240 °C; reaction time = 10 min.

In addition to the ribbons, the fraction of plate-shaped particles increased compared to the (1:1) sample, and a new spherical morphology appeared (*ca.* 220 nm in diameter). The onsetting NaF secondary phase observed in the sample's XRD pattern (Figure 6.1) was attributed to these spherical particles through EDX analysis (Figure 6.2 B). Upon further addition of Na^+ to increase the metal ion ratio to 2:1 (Figure 6.3 C), the ribbon-shaped morphology almost disappeared, forming only few hourglass-shaped structures resembling the ribbons formed at a 1.5:1 ratio. Instead, the particles exhibited a dominating plate morphology with a relatively broad size distribution (edge length: 466 ± 102 nm, thickness: 115 ± 18 nm). Interestingly, with an increasing fraction of NaF in the product, some of the $NaMnF_3$ plates were found to arrange on the surface of the spherical NaF particles. In that regard, careful inspection of the SEM images suggests that the NaF spheres may act as scaffolds for the assembly of $NaMnF_3$ plates into box-like structures (Figure 6.5).

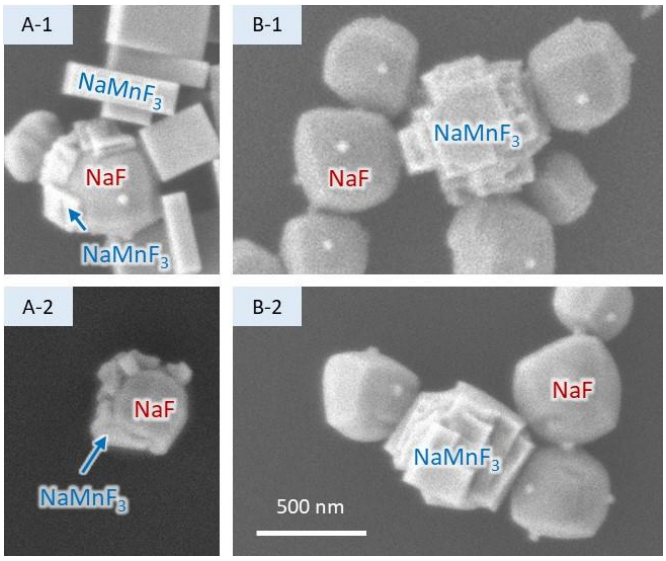

Figure 6.5. SEM images of the particles obtained using a 2:1 Na^+-to-Mn^{2+} ratio providing evidence for the proposed assembly of $NaMnF_3$ plates around NaF spheres – (A) partial and (B) full coverage of the spheres. The scale bar given in (B-2) applies to all four images. Upon further increase of the metal ion ratio to 3:1, SEM and TEM images showed an increasing number of these box-like assemblies.

Finally, at the highest metal ion ratio that was tested (3:1), the plates obtained showed a narrow size distribution (edge length: 439 ± 23 nm, thickness: 93 ± 5 nm; Figure 6.3 D). The corresponding XRD pattern indicated an increasing amount of NaF, thus, a potentially larger number of NaF

particles that may act as scaffolds for $NaMnF_3$ self-assembly. Indeed, at a 3:1 ratio, an increasing number of box-like assemblies of *ca.* 500 nm in size was observed (Figure 6.3 D). It is noteworthy that, at high metal ion ratios, the NaF spheres exhibited a truncated morphology and their size increased to *ca.* 500 nm (*versus ca.* 220 nm at 1.5:1). The good size match between NaF spheres and $NaMnF_3$ box-like structures provides further support for the proposed self-assembly mechanism.

Particle shape may be controlled by reaction kinetics, thereby explaining the different morphologies of $NaMnF_3$ particles obtained – nanorods, ribbons, and plates.[287] Increasing Na^+-to-Mn^{2+} ratio resulted in increased NaF monomer concentration, which may have in turn resulted in high supersaturation. Such high monomer concentration will favour restricted Ostwald ripening, limiting particle growth and disfavouring growth in a preferred direction.[288] Thus, in case of the formation of $NaMnF_3$ particles, the increasing Na^+-to-Mn^{2+} ratio is suggested to restrict the growth of the high-energy facet (0 1 0) so that the (0 1 0)-confined plate-shaped particles can be formed.[282] To the best of our knowledge, this is the first example of a morphology-selective synthesis of $NaMnF_3$ particles, controlled by varying the metal ion ratio, beyond the common plate morphology obtained by solvothermal or thermal decomposition methods.[282, 289] Therefore, the current work not only provides a fast route to making $NaMnF_3$ particles, but also a convenient and simple approach to controlling particle morphology.

Effect of reaction temperature and time. In order to gain additional insight into the MW-assisted formation of $NaMnF_3$, the effect of nucleation and growth temperature (temperatures T_a and T_b) on particle morphology and crystalline phase was investigated (Na^+-to-Mn^{2+} ratio: 2:1; reaction time: 10 min). First, nucleation temperature T_a was varied between 260 °C and 300 °C, while keeping growth temperature T_b constant at 240 °C. As shown by the XRD patterns in Figure 6.6 A, at lower T_a, 260 °C and 270 °C, the predominant product was NaF. Increasing nucleation temperature up to 300 °C yielded $NaMnF_3$.

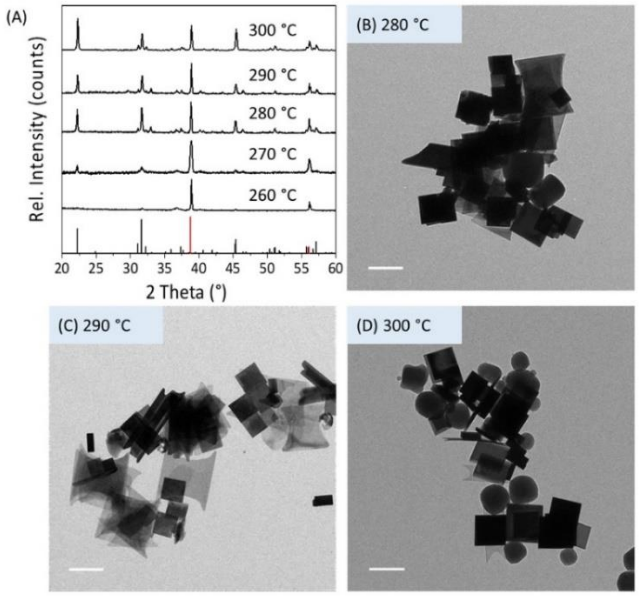

Figure 6.6. (A) XRD patterns of $NaMnF_3$ particles obtained by a microwave-assisted thermal decomposition using a 2:1 Na^+-to-Mn^{2+} ratio and a nucleation temperature T_a of 260 °C, 270 °C, 280 °C, 290 °C, and 300 °C, respectively (growth temperature T_b = 240 °C; reaction time = 10 min). References: black line – orthorhombic $NaMnF_3$, PDF card [01-072-0291]; red line – NaF, PDF card [00-001-1184]. (B-D) Transmission electron microscopy (TEM) images of particles obtained at T_a of (B) 280 °C, (C) 290 °C, and (D) 300 °C. Scale bars: 500 nm.

The co-formation of NaF observed is in line with the mechanism reported in the literature, namely, the separation of NaF monomer out of the reaction mixture, followed by transformation into $NaMnF_3$ upon reaction with MnF_2 monomer at higher temperature.[282] From 280 °C to 300 °C, the particles' morphology trends towards relatively well-defined plates of sub-micron size (Figure 6.6 (B-D)). Thus, T_a was kept at 300 °C for the subsequent assessment of the effect of growth temperature T_b (reaction time: 10 min; Na^+-to-Mn^{2+} ratio: 2:1). As indicated by XRD analysis, T_b had no influence on the crystalline phase of the particles obtained (Figure 6.7 A). TEM images of the corresponding $NaMnF_3$ samples showed irregularly shaped particles at higher T_b, 250 °C and 280 °C, while a lower T_b of 240 °C favoured the growth of well-defined plates (Figure 6.7 (B-D)). Therefore, 300 °C and 240 °C were chosen for T_a and T_b, respectively, for the subsequent assessment of reaction time from 1 to 20 min, while the Na^+-to- Mn^{2+} ratio was set to 1:1 or 2:1. XRD results (Figure 6.8 A) demonstrated that a 1:1 ratio yielded $NaMnF_3$ from 1 min onwards.

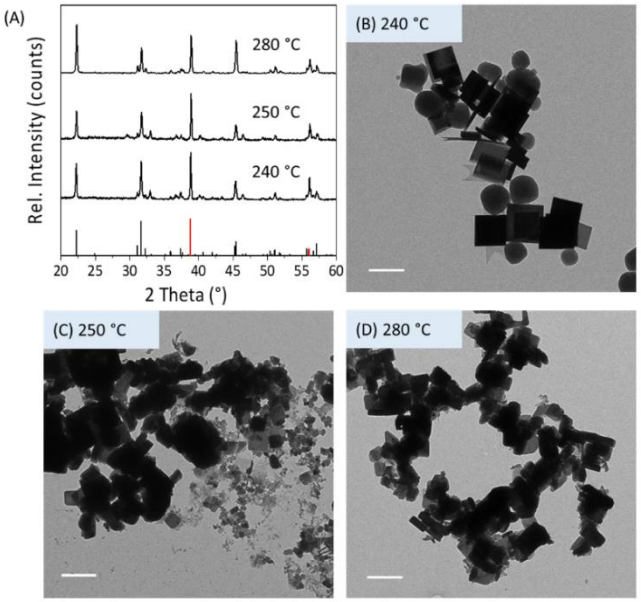

Figure 6.7. (A) XRD patterns of $NaMnF_3$ obtained by a microwave-assisted thermal decomposition using a 2:1 Na^+-to-Mn^{2+} ratio and a particle growth temperature T_b of 240 °C, 250 °C, and 280 °C, respectively (nucleation temperature T_a = 300 °C; reaction time = 10 min). Reference: black line – orthorhombic $NaMnF_3$, PDF card [01-072-0291]; red line – NaF, PDF card [00-001-1184]. (B-D) TEM images of materials obtained at (B) 240 °C, (C) 250 °C, and (D) 280 °C. Scale bars: 500 nm.

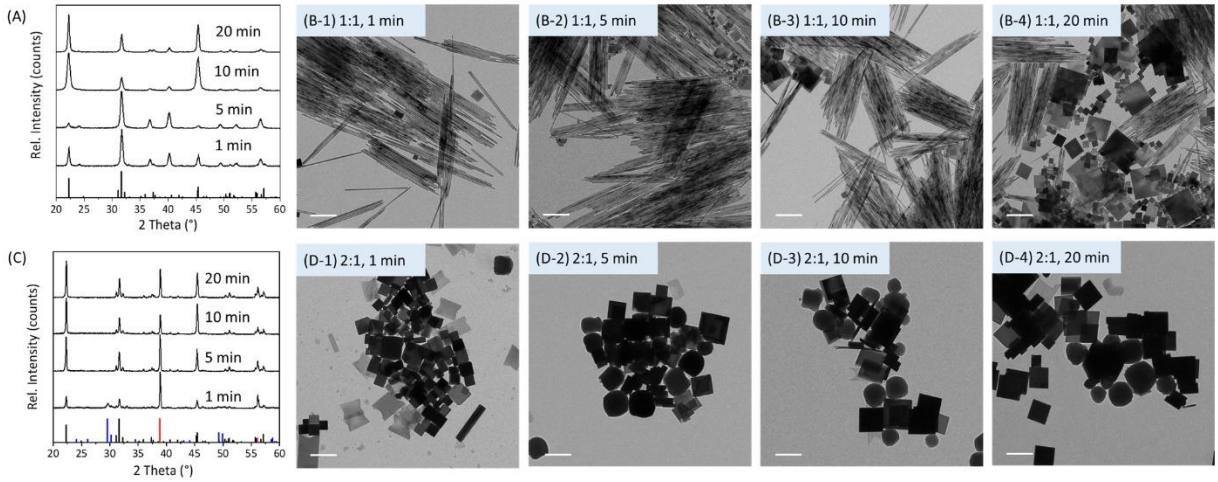

Figure 6.8. (A and C): XRD patterns of $NaMnF_3$ particles synthesized at different reaction times: 1 min, 5 min, 10 min, and 20 min, using Na^+-to-Mn^{2+} ratios of (A) 1:1 and (C) 2:1, respectively. Reaction temperature: T_a = 300 °C, T_b = 240 °C. References: black line – orthorhombic $NaMnF_3$, PDF card [01-072-0291]; blue line – $NaMn_3F_7$, PDF card [00-027-0745]; red line – NaF, PDF card [00-001-1184]. (B and D): TEM images of the corresponding $NaMnF_3$ particles obtained using Na^+-to-Mn^{2+} ratios of (B) 1:1 and (D) 2:1 and reaction times of (1) 1 min, (2) 5 min, (3) 10 min, and (4) 20 min. Scale bars: 500 nm.

As already discussed for the sample obtained at 10 min (Figure 6.1), reflections at 31.07° and 32.22° were missing for any of the reaction times. In agreement, TEM analysis confirmed the formation of nanorods (Figure 6.8 B). After 20 min, plate-like structures appeared as a secondary morphology (Figure 6.8 (B-4)), likely stemming from a nanorod-to-plate transformation. In contrast, at a 2:1 ratio, a short reaction time of 1 min resulted in the formation of $NaMn_3F_7$ as a secondary phase (Figure 6.8 C). This phase was ascribed to the small nanoparticles visible in the respective TEM image (Figure 6.8 (D-1)). Upon longer microwave treatment, the intermediate $NaMn_3F_7$ phase disappeared, leaving $NaMnF_3$ in a plate-like morphology as expected for this metal ion ratio (Figure 6.8 D). No significant change in morphology and size was observed when the reaction time increased from 5 to 20 min.

The yield of $NaMnF_3$ particles obtained using different metal ion ratios and reaction times are summarized in Table 6.2. Using a 1:1 Na^+-to-Mn^{2+} ratio resulted in a lower yield (50.6 %) compared to higher Na^+-to-Mn^{2+} ratios yielding 78 % to 83.6 %. In the MW-assisted synthesis, Na-TFA not only acts as a reagent but also to enrich the reaction medium with ions able to absorb microwave energy providing the system the energy required for $NaMnF_3$ crystallization (oleic acid/ODE/OAm alone being rather poor microwave absorbers).[2, 3] Therefore, excess Na-TFA will likely increase the energy intake from the microwave into the reaction, ultimately yielding more product. Moreover, the yield was assessed in light of reaction time. At a 2:1 Na^+-to-Mn^{2+} ratio, the yield increased when the reaction time was prolonged from 5 to 10 min, without further increase after 20 min. No significant change in morphology and size was observed under these conditions (Figure 6.8 D).

These findings indicate that, at sufficiently high metal ion ratio, time is the key aspect to increase the reaction's yield at a 5-10 min scale and once the phase mixture observed after 1 min was transformed into a phase-pure product. In contrast, at a metal ion ratio of only 1:1, no obvious correlation between reaction time and yield was observed, with yields not exceeding 60 % even after 20 min of microwave irradiation. The lack of increase in yield with time indicates that formation of rod-like particles takes place at the initial stages of the reaction, followed by their subsequent transformation into plate-like structures upon longer reaction times (Figure 6.8 B).

Table 6.2. Overview of the yield of $NaMnF_3$ particles obtained using different metal ion ratios and reaction times. The yields were determined by calculating the ratio of Mn^{2+} ions in the supernatant after the reaction compared to those in the initial reaction mixture (nominal concentration). The Mn^{2+} ion concentration was determined by ICP-OES.

Parameter Studied	Ion Ratio (Na^+-to-Mn^{2+})	T_a	T_b	t (Tb)	Yield
Ion Ratio (Na^+-to-Mn^{2+})	1:1	300 °C	240 °C	10 min	50.6 %
	1.5:1				81.3 %
	2:1				78.1 %
	3:1				83.6 %
Reaction Time	1:1	300 °C	240 °C	1 min	48.9 %
				5 min	56.2 %
				10 min	50.6 %
				20 min	59.0 %
	2:1			1 min [a]	/
				5 min	51.6 %
				10 min	78.1 %
				20 min	76.8 %

[a] After 1 min, a phase-mixture of $NaMnF_3$ and $NaMn_3F_7$ was obtained, hence, no yield for $NaMnF_3$ could be determined.

Lastly, following the optimization of the $NaMnF_3$ synthesis parameters, the suitability of the protocol for K-based particles as an alternative member of the $MMnF_3$ family was tested to demonstrate the versatility of the synthesis route established. As shown in Figure 6.9, plate-like $KMnF_3$ particles were successfully obtained at a 1:1 K^+-to-Mn^{2+} ratio (*ca.* 70 nm in size), while a 2:1 ratio yielded $KMnF_3$ of bimodal morphology, including plates and smaller nanoparticles.

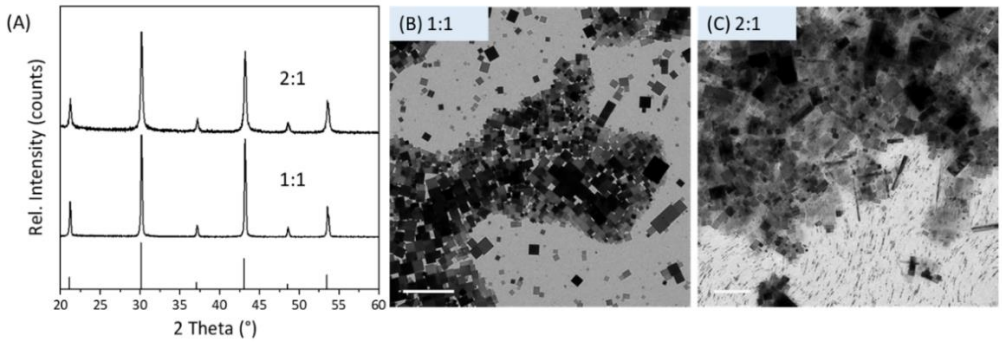

Figure 6.9. (A) XRD patterns of cubic-phase $KMnF_3$ particles synthesized by a microwave-assisted approach using K^+-to-Mn^{2+} ratios of 1:1 and 2:1. Reference: black line – cubic $KMnF_3$, PDF card [00-017-0116]. (B) and (C) show the corresponding TEM images of $KMnF_3$ particles obtained at K^+-to-Mn^{2+} ratios of (B) 1:1 and (C) 2:1. Reaction temperature: T_a = 300 °C, T_b = 240 °C; reaction time = 10 min. Scale bars: 500 nm.

6.2.2 Poly(acrylic acid)-Capped $MMnF_3$ Particles for T_1 Relaxivity

Mn^{2+}-based complexes have been applied as MRI T_1 contrast agents given the five unpaired d electrons present in the Mn^{2+} ion.[264, 275] To study the effect of morphology and elemental composition on the magnetic properties of the $MMnF_3$ particles presented here, two representative $NaMnF_3$ samples synthesized using the 1:1 and 3:1 Na^+-to-Mn^{2+} ratios as well as the $KMnF_3$ sample obtained at a 1:1 K^+-to-Mn^{2+} ratio were selected for magnetic measurements. Poly(acrylic acid) (PAA) was used as surface ligand to transfer the as-obtained oleate (OA)-capped particles into water as required for relaxometry studies. PAA was chosen due to its good biocompatibility and strong binding to the particles enabling good colloidal stability.[275] Successful PAA-capping was confirmed by FTIR spectroscopy (Figure 6.10) and TGA (Figure 6.11).

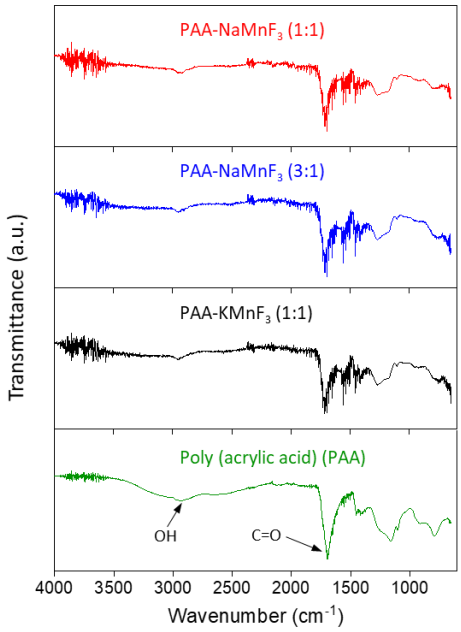

Figure 6.10. FTIR spectra of PAA-capped $MMnF_3$ (M = Na, K) particles and PAA used as reference.

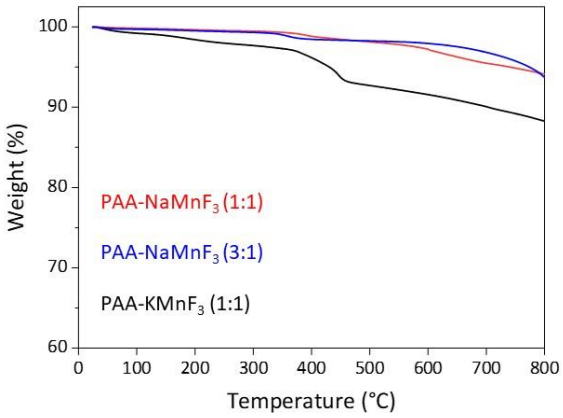

Figure 6.11. TGA profiles of PAA-capped $MMnF_3$ (M = Na, K) particles showing mass loss ascribed to PAA surface groups at temperatures up to *ca*. 500 °C. Comparable amounts of PAA were found for $NaMnF_3$ needles and plates obtained at Na^+-to-Mn^{2+} ratios of 1:1 and 3:1, exhibiting a mass loss of 2.4 % and 2.0 %, respectively. A larger amount of PAA (4.7 %) was observed for $KMnF_3$ particles, which may be explained by the particles' smaller size, thus, larger surface area.

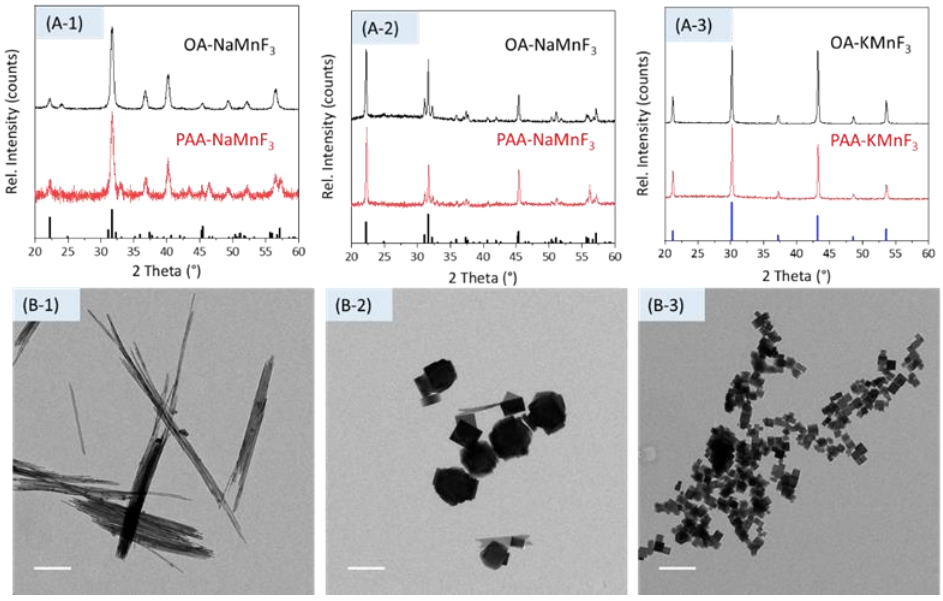

Figure 6.12. (A-1) and (A-2): XRD patterns of oleate (OA)-capped $NaMnF_3$ particles (black lines) obtained by the microwave-assisted approach using Na^+-to-Mn^{2+} ratios of (A-1) 1:1 and (A-2) 3:1 and their respective PAA-capped samples (red lines). (A-3): XRD patterns of OA-$KMnF_3$ synthesized using a 1:1 K^+-to-Mn^{2+} ratio (black line) and the corresponding PAA-capped particles (red line). Reference: black line – orthorhombic $NaMnF_3$, PDF card [01-072-0291]; blue line – cubic $KMnF_3$, PDF card [00-017-0116]. Reaction temperature: T_a = 300 °C, T_b = 240 °C; reaction time: 10 min. (B-1) to (B-3) show the corresponding TEM images of the PAA-capped samples. Scale bars: 500 nm.

The crystallinity and morphology of the PAA-capped particles were confirmed by XRD and TEM analysis (Figure 6.12). T_1 and T_2 relaxivities (r_1 and r_2) of the PAA-capped particles were determined under a magnetic field of 0.47 T (Figure 6.13). As shown in Figure 6.13 A, both $NaMnF_3$ samples exhibited T_1-weighted contrast effects. The r_1 value of the nanorods (1:1) (7.28 ± 0.06 mM^{-1} s^{-1}) was significantly higher by 19 % (statistical difference p-value, p = 0.025) than that of the plates (3:1) (6.14 ± 0.45 mM^{-1} s^{-1}), which may be ascribed to their larger surface-to-volume ratio.[85] The by-produce NaF presented in $NaMnF_3$ synthesized with 2:1 Na^+-to-Mn^{2+} ratios (Figure 6.12 (B-2)) may also influence r_1 relaxivity, and should be washed away with water.

The r_1 value of the PAA-capped $KMnF_3$ particles was determined as 7.23 ± 0.20 mM^{-1} s^{-1} (Figure 6.14). Of note, the r_1 values obtained were all higher than that of the clinically used T_1-contrast agent Magnevist (Gd-DTPA, 3.4 mM^{-1} s^{-1}, under 0.47 T, 40 °C).[261] Higher r_1 values of 6.8 and 12.7 $mM^{-1}s^{-1}$ were previously reported for $NaMnF_3$ nanoparticles,[2,20] yet, due to their smaller size, different surface chemistries, and higher magnetic fields under which these values were obtained (11.7 and 7 T, respectively), a direct comparison should be taken with care.

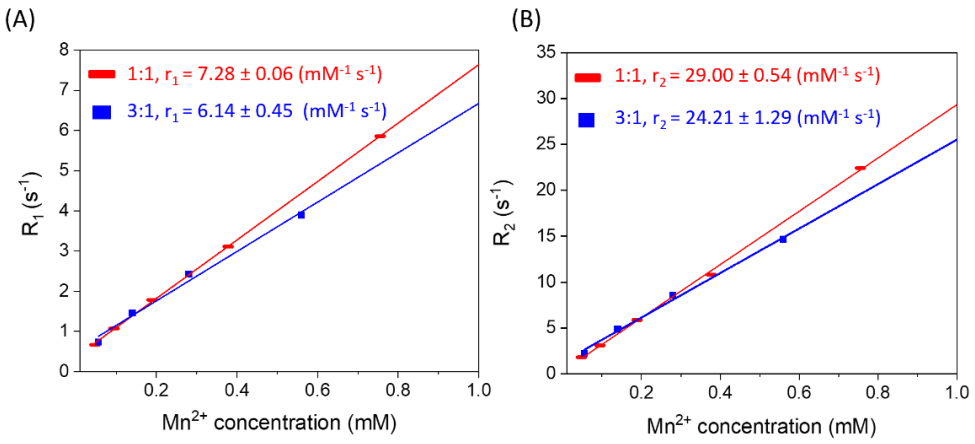

Figure 6.13. Relaxation rate R_1 (A) and R_2 (B) of water protons plotted against the molar concentration of Mn^{2+} for PAA-capped $NaMnF_3$ synthesized using 1:1 (red data points) and 3:1 (blue data points) Na^+-to-Mn^{2+} ratios under 0.47 T. Solid lines are linear fits.

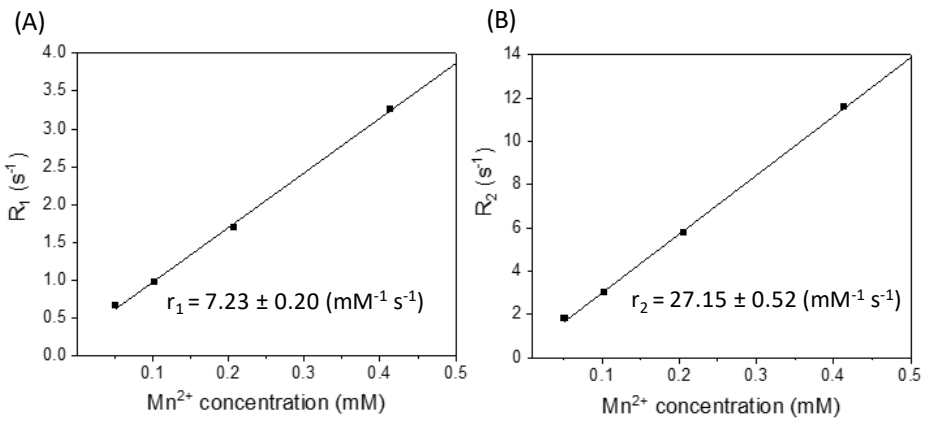

Figure 6.14. Relaxation rates R_1 (A) and R_2 (B) of water protons plotted against the molar concentration of Mn^{2+} for PAA-capped $KMnF_3$ particles (synthesized using a 1:1 K^+-to-Mn^{2+} ratio) under 0.47 T. Solid lines are linear fits.

6.3 Conclusions

In conclusion, a rapid microwave-assisted synthesis method was developed yielding orthorhombic $NaMnF_3$ particles. This method enabled the production of particles with specific morphologies (nanorods and ribbons) beyond well-established plates by varying the Na^+-to-Mn^{2+} metal ion ratio. The protocol was further adjusted to another member of the ABF_3 family, *i.e.*, $KMnF_3$. Moreover, PAA-capped $MMnF_3$ particles (M = Na, K) exhibited relaxometric properties, making them potential candidates for application as MRI T_1 contrast agents. Yet, nano-bio interaction must also be taken into account given the non-spherical shape of the $NMnF_3$ particles. Further extension of these studies – for instance, seeking particle size control from micro to nano through variation of precursor concentrations or solvent-to-capping agent ratio and further assessment of size-dependent relaxometry behaviour – is expected to provide knowledge valuable for the future design of these and related fluoride materials for their diverse applications.

Chapter 7. Summary and Outlook

7.1 Summary

In conclusion, building on preliminary work in our lab, the MW-assisted approach was demonstrated to provide several advantages, such as significantly shorter reaction time and high reproducibility, for the synthesis of $NaREF_4$ NPs. The work presented here aimed to expand the MW-assisted approach towards the synthesis of the whole family of $NaREF_4$ NPs and to carefully assess their accessibility in the two known crystalline phases. Stringent optimization of the synthesis parameters allowed to control the shell thickness of core/multi-shell $NaREF_4$ NPs, important for tuning the optical properties and generating new functionalities. The versatility of the developed MW-assisted approach was further applied to the synthesis of $NaMnF_3$ particles. Looking back at the initially posed research questions, the corresponding answers are described in the following.

MW-assisted synthesis beyond Ln^{3+}-doped $NaGdF_4$? A series of $NaREF_4$ NPs were prepared and their crystalline phase accessibility as a function of RE ion choice was investigated. Using the MW-assisted approach, α-$NaREF_4$ NPs could be obtained for the whole RE family, while the β- $NaREF_4$ NPs were only accessible for the lighter RE ions (Pr to Dy) (Chapter 4). The developed MW-assisted approach was further extended to the synthesis of $NaMnF_3$ particles. By adjusting the reaction parameters, the Na^+-to-Mn^{2+} ratio in the reaction mixture yielded $NaMnF_3$ particles with tuneable morphologies. Moreover, the obtained $NaMnF_3$ particles exhibited promising contrast effects as MRI T_1 contrast agents.

Is $NaREF_4$ really chemically stable? Given the potential biomedical applications, the dispersibility of the $NaREF_4$ NPs in water is a prerequisite. However, the established ligand removal protocols using a HCl solution of pH 4 were not efficient in removing the ligands from the NPs synthesized by the MW-assisted method. Therefore, an adapted ligand removal protocol using a HCl solution of pH 1.5 was developed to render the NPs water dispersible. The chemical stability of the

obtained NPs under the acidic treatment was investigated (Chapter 4). Upon acidic treatment, the phase transformation from $NaREF_4$ to REF_3 was observed for some of the α/β $NaREF_4$ NPs. More precisely, for the lighter RE^{3+} ions, Pr to Sm, higher stability of hexagonal REF_3 *versus* α/β-$NaREF_4$ resulted in a phase transformation, regardless of the starting phase of the $NaREF_4$ NPs (α or β). Moving to the middle of the series, Eu to Dy, phase transformation occurred only in case of the less thermodynamically stable α-$NaREF_4$. Finally, for the heavier RE^{3+} ions, Ho to Lu as well as Y, the α-$NaREF_4$ phase is known as the most stable $NaREF_4$ phase, and indeed, these compositions were more resistant towards phase transformation. These findings unveiled unaddressed chemical stability concerns for the larger family of $NaREF_4$ NPs. As such, it came as an alert to the community working with small $NaREF_4$-type NPs: Water dispersibility could be achieved by ligand removal under acidic conditions, yet, might come along with a morphologic and crystallographic transformation into significantly larger REF_3 particles. Alternatively, water dispersible NPs could be achieved by ligand exchange approaches.

How can the properties of $NaREF_4$ NPs be controlled? β-$NaGdF_4$:Yb^{3+},Er^{3+}/$NaGdF_4$/$NaDyF_4$ CSS NPs were prepared to be used as UC/T_2/CT multimodal imaging probes (Chapter 5). Careful tuning of the microwave reaction conditions allowed for tuning of the inner shell thickness from *ca.* 3 to 6 nm. Such control is crucial to investigate the mechanism of UC loss between Yb^{3+}/Er^{3+} pair and Dy^{3+}. Based on the Er^{3+} emission spectra and Yb^{3+} lifetimes, an isolating 4 nm inner shell between the emitting core and the $NaDyF_4$ outer shell suppressed energy transfer from Yb^{3+} to Dy^{3+}, followed by Dy^{3+}-mediated energy migration and loss at the NP surface. As a result, a 4 nm thick $NaGdF_4$ inner shell did not only restore but enhanced the UC emission of Er^{3+}. This was the first report showing UC enhancement when Er^{3+} and Dy^{3+} ions were incorporated into one NP. The further investigation of the effect of outer $NaDyF_4$ shell thickness on the particles' magnetic and CT performance showed that, the NPs with the thickest outer shell possessed superior T_2 and CT contrast effects compared to those of other MRI and CT contrast agents. Our results demonstrated the promise of the designed Dy-CSS NPs to act as potential multimodal imaging probes. More importantly, the concept of fabricating multilayer NPs provided insights for the future architecture design of Ln-based materials for their *e.g.*, biomedical applications and beyond.

Overall, the MW-assisted approach led to promising achievements for the synthesis of $NaREF_4$ NPs and could be extended to other fluoride materials. However, as it is currently one of the newest synthetic approaches to lanthanide-based nanomaterials, some challenges remain. For instance, there is still a lack of diversity of materials accessible via MW-assisted routes, and the degree of cation intermixing of core/shell NPs is still unknown. These challenges are currently being addressed in our lab and will be described in more detail in the following sections.

7.2 Outlook

7.2.1 Expanding Material Choice

As introduced in Chapter 1, β-phase $NaYF_4$ is efficient for the UC of Ln^{3+} emitters. However, the synthesis of β-$NaYF_4$ NPs or nano-sized $LiYF_4$ particles using the MW-assisted approach remains a challenge. By carefully tuning the reaction parameters, such as the ratio of metal-to-RE^{3+}, the concentration of the precursors, and the choice of precursors, β-$NaYF_4$ and $LiYF_4$ NPs might be possible to obtain. Moreover, exploring other host materials beyond fluorides is also worth investigating. For instance, Gd_2O_2S has been reported as a suitable host material for NIR (*e.g.*, 1550 nm excitation)-NIR (*e.g.*, 1000 nm emission) UC of Er^{3+}, which has the potential to enhance the efficiency of solar cells.[290] However, the synthesis methods of Gd_2O_2S are very limited, resulting in mainly micro-sized materials.[291] Given the potential application of Gd_2O_2S, one of our group members is currently exploring the MW-assisted synthesis of Gd_2O_2S. By adjusting the ratio of Gd^{3+} and S, different morphologies of nanomaterials were obtained. Moreover, when doping with Yb^{3+} and Er^{3+} ions, the particles showed promising optical properties, holding potential for thermal sensing applications.

7.2.2 Understanding Core/Shell Cation Intermixing

The synthesis of CS NPs is of particular interest as a shell of inert material can increase the quantum yield of the NPs by decreasing energy losses on the particle surface. Moreover, the

design of CS architecture allows engineering different Ln^{3+} ions in separate layers in one NP, optimizing their optical properties, and also generating new functionalities.[41] One crucial aspect in the synthesis of CS NPs is the intermixing of core and shell material during the formation of the shell. The effects of precursor choice and NP size on the cation intermixing in the thermal decomposition method have recently been investigated.[41] However, cation intermixing remains a hot topic within the UC community, and is still unstudied in NPs obtained by the MW-assisted approach. The use of advanced imaging techniques (*e.g.*, high-resolution TEM and EDS) is expected to shed light on cation intermixing in CS NPs. With the advantage of MW-induced uniform heating with limited thermal gradients, the degree of the cation intermixing is expected to be minimized in the CS NPs synthesized by the MW-assisted method.

In addition to the previously mentioned challenges, microwave reactors have very limited dimensions, thus, upscaling may require a costly upgrade of the whole setup.

7.2.3 Er^{3+}/Tm^{3+}-Based core/shell/shell NPs as NIR-III Nanothermometers

Ln^{3+}-NPs can be excited with and emit in the NIR regions. Of particular interest for biomedical applications is their capability to emit light of wavelengths longer than 1000 nm, matching the NIR-II/III (1000 – 1900 nm) transparency windows.[23] The use of longer wavelengths is favourable as it can reach greater penetration depths into tissues, and generate higher signal-to-noise ratios for optical imaging and thermal sensing.[292] Therefore, NIR-NIR luminescence thermometry is gaining increasing attention within the Ln community.

Having successfully established the synthesis of CSS NPs using the MW-assisted approach, we can now explore various applications of Ln^{3+}-based NPs. For instance, we previously reported a type of Pr^{3+}/Ho^{3+}-based CSS NPs as novel NIR-II nanothermometers.[293] We compared the thermometric performances of various Pr^{3+}/Ho^{3+}-based NPs in different architectures, either in CS or CSS structure. Pr^{3+}/Ho^{3+}-based CSS NPs, where emitters Ho^{3+} ions and Pr^{3+} ions separated in different layers, showed superior thermometric performances than the CS NPs (where all dopants were co-localized in the core). This finding was ascribed to the reduced unwanted cross-relaxation between emitters in CSS NPs.

When seeking NIR-NIR nanothermometers operating in longer wavelength regions, Tm^{3+} is a promising candidate for its NIR-III emission centered at 1850 nm, ascribed to the $^3F_4 \rightarrow {}^3H_6$ transition. While few examples of the NIR-III emission of Tm^{3+} have been reported,[294] there are even fewer studies exploring nanothermometry in this spectral range.[i] This motivated us to develop the first Tm^{3+}-based NIR-III nanothermometer.

We designed Er^{3+}/Tm^{3+}-based CSS ($^{Er/Tm}$CSS) NPs and explored their thermometric performance as NIR-III nanothermometers. One Honour's student, Lucas Crozier (co-supervised by me) conducted the synthesis of the $^{Er/Tm}$CSS NPs and temperature-dependent photoluminescence measurements under my guidance. The composition of the $^{Er/Tm}$CSS NP was β-$NaGdF_4$:Yb^{3+} (20%),Er^{3+} (2%)/$NaGdF_4$: Tm^{3+} (10%)/$NaGdF_4$. The preliminary results are briefly described in the following.

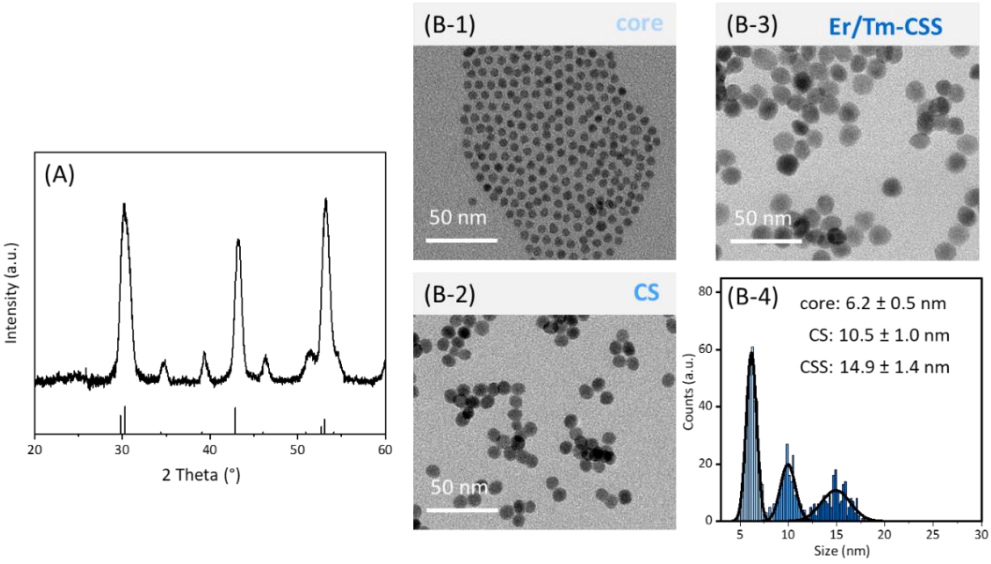

Figure 7.1. (A) XRD pattern of Er^{3+}/Tm^{3+}-based CSS NPs. Reference: β-$NaGdF_4$, PDF card [01-080-8787]. (B) TEM images of (1) core, (2) CS and (3) CSS NPs as well as (4) their corresponding size distributions.

[i] I worked on designing Ho^{3+}-based nanothermometers operating at an even longer wavelength, 2000 nm emission from Ho^{3+}. However, instead of an exciting new nanothermometer, the result was a lesson learned on the proper need of optical filters all students and researchers shall be reminded of.

XRD analysis confirmed that all NPs crystallized in the β-phase $NaGdF_4$ (Figure 7.1 A). The morphology and size of the NPs were examined using TEM. As shown in Figure 7.1 B, the core NPs exhibited a spherical morphology with an average size of 6.2 ± 0.5 nm. Growing a Tm^{3+}-doped shell resulted in CS NPs of 10.5 ± 1.0 nm. Further growth of a protecting 2.2 nm undoped $NaGdF_4$ shell led to the overall NP size of 14.9 ± 1.4 nm.

The downshifting luminescence properties of the obtained $^{Er/Tm}$CSS NPs, dispersed in toluene, were investigated under 980 nm excitation (Figure 7.2). Upon 980 nm excitation, the Er^{3+}-and Tm^{3+}-doped CSS NPs exhibited decent NIR emission in the NIR-III range (Figure 7.2 A). The well-studied NIR-III emission of Er^{3+}, centered at 1550 nm, corresponds to the ion's $^4I_{13/2} \rightarrow {}^4I_{15/2}$ radiative f-f transition (Figure 7.2 B).[295] In addition, a NIR-III emission peak was observed at 1850 nm, ascribed to the Tm^{3+} $^3F_4 \rightarrow {}^3H_6$ radiative f-f transition.[296]

The capability of the $^{Er/Tm}$CSS NPs to act as ratiometric nanothermometer operating in the NIR-III spectral region was assessed by temperature-dependent photoluminescence spectroscopy on their dispersions in toluene. Elevating the temperature from 20 to 50 °C resulted in a decrease in the intensity of Er^{3+} emission (Figure 7.3 A). Such intensity decrease has previously been ascribed to the thermal quenching by promoting the non-radiative transitions when increasing the temperature.[297] The intensity of the Tm^{3+} emission was relatively unchanged with increasing temperature. The different intensity changes between the Er^{3+} and Tm^{3+} NIR-III emission band pair allowed for an optical temperature readout via a double-band ratiometric approach. Therefore, the luminescence intensity ratio (LIR, I_{Tm}/I_{Er}) between the Tm^{3+} (I_{Tm}: 1700 – 2000 nm) and the Er^{3+} (I_{Er}: 1230 – 1700 nm) emission was determined as a function of the dispersions' temperature. The LIR values obtained for the $^{Er/Tm}$CSS-NPs exhibited an exponential temperature dependence in the investigated thermal range (Figure 7.3 B).

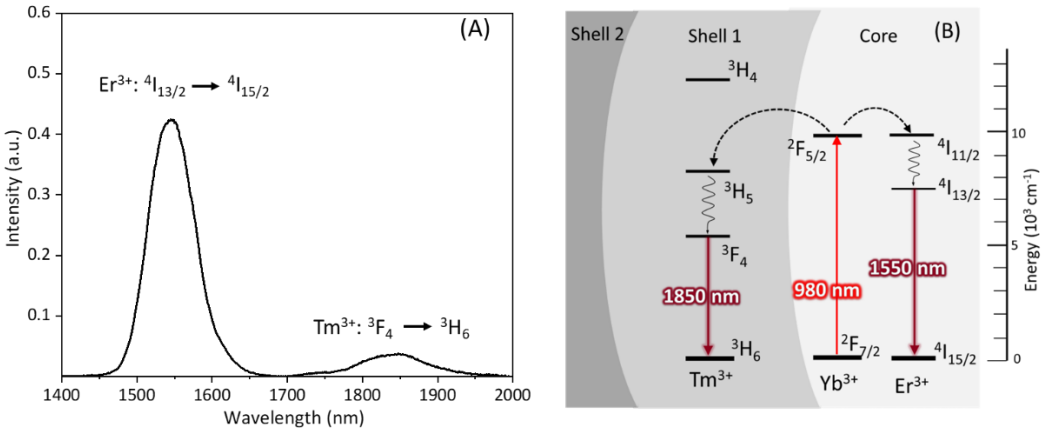

Figure 7.2. (A) NIR emission spectrum of $^{Er/Tm}$CSS NPs under 980 nm excitation and (B) the corresponding energy diagram.

The relative thermal sensitivity, S_r, exhibited the greatest maximum value of 2.50 ± 0.22 % °C^{-1} at 50 °C (Figure 7.3 C). This value is greater than most of reported Ln^{3+}-based NIR-III nanothermometers.[53] The preliminary thermometric results obtained from these $^{Er/Tm}$CSS-NPs are very promising. Further investigations (e.g., different concentrations of emitters and compositions) on these NPs are currently in progress.

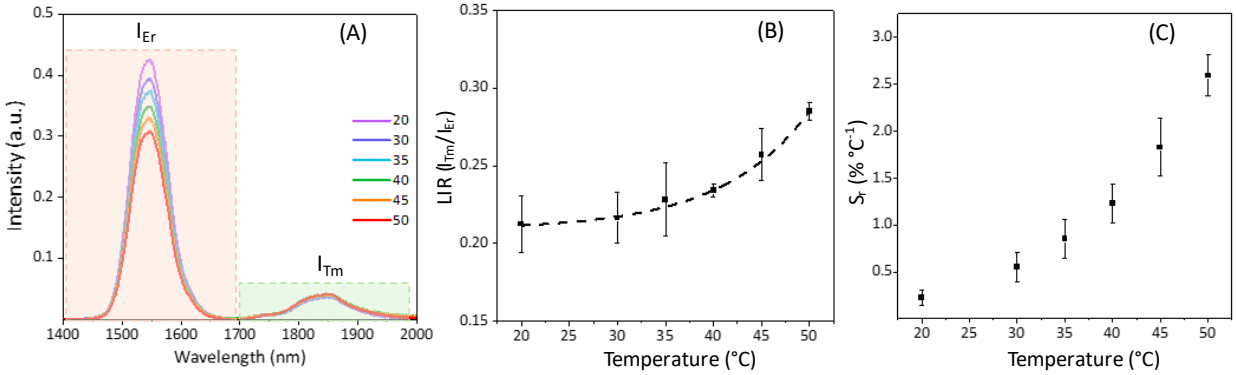

Figure 7.3. (A) Temperature-dependent emission spectra recorded on $^{Er/Tm}$CSS NPs under 980 nm excitation. Laser power density: 33 W/cm^2, shaded orange and green areas were used to calculate LIR. (B) Temperature-dependent LIR values and (C) relative thermal sensitivities of the $^{Er/Tm}$CSS NPs.

7.2.4 Challenges of Ln^{3+}-Based Nanothermometry

Despite significant advancements over the recent years, Ln^{3+}-based nanothermometers still face key limitations that impede their implementation in real-life, *e.g.*, *in vivo* applications.[53] For instance, recent studies have identified bias as the main limitation of luminescent nanothermometers for intracellular thermal measurement.[50] Although not exclusive to intracellular thermal measurements, biases are exacerbated by the extreme complexity of the intracellular medium.[298] This makes it necessary to acquire calibration curves in live cells, where multiple parameters change dynamically with temperature. Nonetheless, appropriate interpretation of such complex calibration datasets is impossible with traditional analysis methods. Moreover, the presence of bias caused by cell activity is superimposed on the signal distortions caused by tissues during the transition to *in vivo* applications.[299] Lifetime-based nanothermometers are expected to achieve more reliable thermal measurements *in vivo*, with the indispensable use of advanced analytical tools, *e.g.*, artificial intelligence.

7.2.5 Challenge of Enhancing the Quantum Yield of Upconverting Nanoparticles

One crucial aspect limiting the transition of UCNPs into real-life applications, *e.g.*, photodynamic therapy, photocatalysis, and photovoltaics, is their low quantum yield (QY). Photoluminescence QY constitutes a direct measure of a material's efficiency in converting absorbed photons into emitted photons.[300] Although there have been attempts to enhance the QY of UCNPs, the highest value reported is 9% for 45 nm-sized CS NPs,[257] while typical reported values remain far below 1%.[34] Therefore, by rational design of CS architecture, tuning the emitter concentrations, exploring new host materials, as well as optimizing the synthesis parameters, hopefully UCNPs with relatively higher QY can be realized.

7.2.6 Challenges Related to Nanomaterials for Biomedical Applications

Research in nanomedicine spans a multitude of areas, including drug delivery, vaccine development, antibacterial, diagnosis and imaging tools. Many of these developments are

starting to be translated into viable clinical products. Although nanomedicine has raised exciting expectations for many medical problems, scientific challenges have arisen as well, mainly due to the lack of knowledge about the behavior of nanomaterials inside living organisms.[301] One major concern is the safety of nanomaterials. Safety issues for nanomedicine are complex. A detailed assessment of the safety is necessary for clinical translation, but currently there is a lack of methods and standards for evaluation of the safety of nanomaterials. Moreover, physicochemical properties of nanomaterials, such as size, morphology, surface area, and aggregation induced at larger scales may alter biodistribution and interactions with cells and biomolecules, complicating safety issues.[258] Therefore, understanding the toxicity and physicochemical properties of nanomaterials is essential for increasing the odds of success in clinical translation. In addition, another major challenge that should be addressed is the low targeting efficiency of current nanoprobes.

References

1. Cotton, S., *Lanthanide and actinide chemistry*. John Wiley & Sons, 2006.
2. Piguet, C., Extricating erbium. *Nat. Chem.* **2014,** *6*, 370.
3. Balaram, V., Rare earth elements: A review of applications, occurrence, exploration, analysis, recycling, and environmental impact. *Geosci. Front.* **2019,** *10*, 1285.
4. Rodriguez, J. A.; Liu, P.; Hrbek, J.; Evans, J.; Perez, M., Water gas shift reaction on Cu and Au nanoparticles supported on CeO_2(111) and ZnO(0001): intrinsic activity and importance of support interactions. *Angew. Chem. Int. Ed.* **2007,** *46*, 1329.
5. Zhang, J.; Huang, Y.; Jin, L.; Rosei, F.; Vetrone, F.; Claverie, J. P., Efficient upconverting multiferroic core/shell photocatalysts: visible-to-near-infrared photon harvesting. *ACS Appl. Mater. Interfaces* **2017,** *9*, 8142.
6. Deng, R.; Qin, F.; Chen, R.; Huang, W.; Hong, M.; Liu, X., Temporal full-colour tuning through non-steady-state upconversion. *Nat. Nanotechnol.* **2015,** *10*, 237.
7. Park, B. J.; Hong, A. R.; Park, S.; Kyung, K. U.; Lee, K.; Seong Jang, H., Flexible transparent displays based on core/shell upconversion nanophosphor-incorporated polymer waveguides. *Sci. Rep.* **2017,** *7*, 45659.
8. Dong, H.; Du, S. R.; Zheng, X. Y.; Lyu, G. M.; Sun, L. D.; Li, L. D.; Zhang, P. Z.; Zhang, C.; Yan, C. H., Lanthanide nanoparticles: from design toward bioimaging and therapy. *Chem. Rev.* **2015,** *115*, 10725.
9. Smith, B. R.; Gambhir, S. S., Nanomaterials for in vivo imaging. *Chem. Rev.* **2017,** *117*, 901.
10. Brites, C. D. S.; Balabhadra, S.; Carlos, L. D., Lanthanide‐based thermometers: at the cutting‐edge of luminescence thermometry. *Adv. Opt. Mater.* **2018,** *7*, 1801239.
11. Zheng, B.; Fan, J.; Chen, B.; Qin, X.; Wang, J.; Wang, F.; Deng, R.; Liu, X., Rare-earth doping in nanostructuredinorganic materials. *Chem. Rev.* **2022,** *122*, 5519.
12. Beaudry B. J.; Gschneidner Jr. K. A., *Preparation and basic properties of the rare earth metals*. Handbook on the Physics and Chemistry of Rare Earths, Elsevier, **1978**.
13. Atwood, D. A., *The rare earth elements: fundamentals and applications*. John Wiley & Sons, **2013**.
14. Laporte, O.; Meggers,W. F., Some rules of spectral structure. *J. Opt. Soc. Am.* **1925,** *11*, 464.
15. Judd, B. R., Optical absorption intensities of rare-earth ions. *Phys. Rev.* **1962,** *127*, 750.
16. Marin, R.; Jaque, D.; Benayas, A., Switching to the brighter lane: pathways to boost the absorption of lanthanide-doped nanoparticles. *Nanoscale Horiz.* **2021,** *6*, 209.
17. Algar, W. R.; Massey, M.; Rees, K.; Higgins, R.; Krause, K. D.; Darwish, G. H.; Peveler, W. J.; Xiao, Z.; Tsai, H. Y.; Gupta, R.; Lix, K.; Tran, M. V.; Kim, H., Photoluminescent nanoparticles for chemical and biological analysis and imaging. *Chem. Rev.* **2021,** *121*, 9243.
18. G. Chen, C. Y., and P. N. Prasad, Nanophotonics and nanochemistry: controlling the excitation dynamics for frequency up- and down-conversion inlanthanide-doped nanoparticles. *Acc. Chem. Res.* **2012,** *46*, 1474.
19. Haase, M.; Schafer, H., Upconverting nanoparticles. *Angew. Chem. Int. Ed.* **2011,** *50*, 5808.

20. Zheng, W.; Huang, P.; Tu, D.; Ma, E.; Zhu, H.; Chen, X., Lanthanide-doped upconversion nano-bioprobes: electronic structures, optical properties, and biodetection. *Chem. Soc. Rev.* **2015,** *44*, 1379.
21. Chen, G.; Qiu, H.; Prasad, P. N.; Chen, X., Upconversion nanoparticles: design, nanochemistry, and applications in theranostics. *Chem. Rev.* **2014,** *114*, 5161.
22. Naccache, R.; Yu, Q.; Capobianco, J. A., The fluoride host: nucleation, growth, and upconversion of lanthanide-doped nanoparticles. *Adv. Opt. Mater.* **2015,** *3*, 482.
23. Hemmer, E.; Benayas, A.; Legare, F.; Vetrone, F., Exploiting the biological windows: current perspectives on fluorescent bioprobes emitting above 1000 nm. *Nanoscale Horiz.* **2016,** *1*, 168.
24. Johnson, N. J.; He, S.; Diao, S.; Chan, E. M.; Dai, H.; Almutairi, A., Direct evidence for coupled surface and concentration quenching dynamics in lanthanide-doped nanocrystals. *J. Am. Chem. Soc.* **2017,** *139*, 3275.
25. Chen, B.; Wang, F., Combating concentration quenching in upconversion nanoparticles. *Acc. Chem. Res.* **2020,** *53*, 358.
26. Chen, G.; Liu, H.; Somesfalean, G.; Liang, H.; Zhang, Z., Upconversion emission tuning from green to red in Yb^{3+}/Ho^{3+}-codoped $NaYF_4$ nanocrystals by tridoping with Ce^{3+} ions. *Nanotechnology* **2009,** *20*, 385704.
27. Zheng, X.; Kankala, R. K.; Liu, C.-G.; Wang, S.-B.; Chen, A.-Z.; Zhang, Y., Lanthanides-doped near-infrared active upconversion nanocrystals: upconversion mechanisms and synthesis. *Coord. Chem. Rev.* **2021,** *438*, 213870.
28. Yan, C.; Zhao, H.; Perepichka, D. F.; Rosei, F., Lanthanide ion doped upconverting nanoparticles: synthesis, structure and properties. *Small* **2016,** *12*, 3888.
29. Yan, C. H.; Yan, Z. G.; Du, Y.-P.; Shen, J.; Zhang, C.; Feng, W., *Controlled synthesis and properties of rare earth nanomaterials*. Handbook on the Physics and Chemistry of Rare Earths, Elsevier, **2011**.
30. You, W.; Tu, D.; Zheng, W.; Huang, P.; Chen, X., Lanthanide-doped disordered crystals: Site symmetry and optical properties. *J. Lumin.* **2018,** *201*, 255.
31. Wang, F.; Han, Y.; Lim, C. S.; Lu, Y.; Wang, J.; Xu, J.; Chen, H.; Zhang, C.; Hong, M.; Liu, X., Simultaneous phase and size control of upconversion nanocrystals through lanthanide doping. *Nature* **2010,** *463*, 1061.
32. Ćirić, A.; Stojadinović, S.; Brik, M. G.; Dramićanin, M. D., Judd-Ofelt parametrization from emission spectra: The case study of the Eu^{3+} $^5D_1$ emitting level. *Chem. Phys.* **2020,** *528*.
33. Shi, R.; Brites, C. D. S.; Carlos, L. D., Hexagonal-phase $NaREF_4$ upconversion nanocrystals: the matter of crystal structure. *Nanoscale* **2021,** *13*, 19771.
34. Quintanilla, M.; Hemmer, E.; Marques-Hueso, J.; Rohani, S.; Lucchini, G.; Wang, M.; Zamani, R. R.; Roddatis, V.; Speghini, A.; Richards, B. S.; Vetrone, F., Cubic versus hexagonal - phase, size and morphology effects on the photoluminescence quantum yield of $NaGdF_4$:Er^{3+}/Yb^{3+} upconverting nanoparticles. *Nanoscale* **2022,** *14*, 1492.
35. Fan, Y.; Liu, L.; Zhang, F., Exploiting lanthanide-doped upconversion nanoparticles with core/shell structures. *Nano Today* **2019,** *25*, 68.
36. Xu, S.; Fang, D.; Zhang, Z.; Jiang, Z., Effect of OH− on upconversion luminescence of Er^{3+}-doped oxyhalide tellurite glasses. *J. Solid State Chem.* **2005,** *178*, 2159.

37. Boyer, J. C.; Gagnon, J.; Cuccia, L. A.; Capobianco, J. A., Synthesis characterization and spectroscopy of $NaGdF_4:Ce^{3+},Tb^{3+}/NaYF_4$ core/shell nanoparticles. *Chem. Mater.* **2007,** *19*, 3358.
38. Vetrone, F.; Naccache, R.; Mahalingam, V.; Morgan, C. G.; Capobianco, J. A., The active-core/active-shell approach: a strategy to enhance the upconversion luminescence in lanthanide-doped nanoparticles. *Adv. Funct. Mater.* **2009,** *19*, 2924.
39. Quintanilla, M.; Ren, F.; Ma, D.; Vetrone, F., Light management in upconverting nanoparticles: ultrasmall core/shell architectures to tune the emission color. *ACS Photonics* **2014,** *1*, 662.
40. He, S.; Johnson, N. J. J.; Nguyen Huu, V. A.; Cory, E.; Huang, Y.; Sah, R. L.; Jokerst, J. V.; Almutairi, A., Simultaneous enhancement of photoluminescence, MRI relaxivity, and CT contrast by tuning the interfacial layer of lanthanide heteroepitaxial nanoparticles. *Nano Lett.* **2017,** *17*, 4873.
41. Shi, R.; Brites, C. D. S.; Carlos, L. D., Understanding the shell passivation in Ln^{3+}-doped luminescent nanocrystals. *Small Structures* **2022,** *3*, 25.
42. Dühnen, S.; Haase, M., Study on the intermixing of core and shell in $NaEuF_4/NaGdF_4$ core/shell nanocrystals. *Chem. Mater,* **2015,** *27*, 8375.
43. Zhou, J.; Del Rosal, B.; Jaque, D.; Uchiyama, S.; Jin, D., Advances and challenges for fluorescence nanothermometry. *Nat. Methods* **2020,** *17*, 967.
44. Bradac, C.; Lim, S. F.; Chang, H. C.; Aharonovich, I., Optical nanoscale thermometry: from fundamental mechanisms to emerging practical applications. *Adv. Opt. Mater.* **2020,** *8*, 202000183.
45. del Rosal, B.; Ximendes, E.; Rocha, U.; Jaque, D., In vivo luminescence nanothermometry: from materials to applications. *Adv. Opt. Mater.* **2017,** *5*, 1600508.
46. Brites, C. D. S.; Millán, A.; Carlos, L. D., Lanthanides in luminescent thermometry. In *Handbook on the Physics and Chemistry of Rare Earths*, Elsevier, **2016**.
47. Jaque, D.; Vetrone, F., Luminescence nanothermometry. *Nanoscale* **2012,** *4*, 4301.
48. Quintanilla, M.; Liz-Marzán, L. M., Guiding rules for selecting a nanothermometer. *Nano Today* **2018,** *19*, 126.
49. Brites, C. D.; Lima, P. P.; Silva, N. J.; Millan, A.; Amaral, V. S.; Palacio, F.; Carlos, L. D., Thermometry at the nanoscale. *Nanoscale* **2012,** *4*, 4799.
50. Brites, C. D. S.; Marin, R.; Suta, M.; Carneiro Neto, A. N.; Ximendes, E.; Jaque, D.; Carlos, L. D., Spotlight on luminescence thermometry: basics, challenges, and cutting-edge applications. *Adv. Mater.* **2023,** *35*, 2302749.
51. Wang, X. D.; Wolfbeis, O. S.; Meier, R. J., Luminescent probes and sensors for temperature. *Chem. Soc. Rev.* **2013,** *42*, 7834.
52. Vetrone, F.; Naccache, R.; Zamarron,A.; Fuente, A. J.; Sanz-Rodrí guez, F.; Maestro, L. M.; Rodriguez, E. M.; Jaque, D.; Sole, J. G.; Capobianco, J. A.; Temperature sensing using fluorescent nanothermometers. *ACS Nano* **2010,** *4*, 5.
53. Puccini, A.; Liu, N.; Hemmer, E., Lanthanide-based nanomaterials for temperature sensing in the near-infrared spectral region: illuminating progress and challenges. *Nanoscale* **2024,** *16*, 10975.
54. Wang, B.; Jiang, S.; Wang, X.; Gao, S., Magnetic molecular materials with paramagnetic lanthanide ions. *Sci. China, Ser. B: Chem.* **2009,** *52*, 1739.

55. Norek, M.; Peters, J. A., MRI contrast agents based on dysprosium or holmium. *Prog. Nucl. Magn. Reson. Spectrosc.* **2011,** *59*, 64.
56. Lauffer, R. B., paramagnetic metal complexes as water proton relaxation agents for NMR maging theory and design. *Chem. Rev.* **1987,** *87*, 901−927.
57. Louie, A., Multimodality imaging probes design and challenges. *Chem. Rev.* **2010,** *110*, 3146.
58. Li, Z.; Zhang, Y.; La, H.; Zhu, R.; El-Banna, G.; Wei, Y.; Han, G., Upconverting NIR photons for bioimaging. *Nanomaterials* **2015,** *5*, 2148.
59. Li, W.; Schierle, G. S. K.; Lei, B.; Liu, Y.; Kaminski, C. F., Fluorescent nanoparticles for super-resolution imaging. *Chem. Rev.* **2022,** *122*, 12495.
60. Prodi, L.; Rampazzo, E.; Rastrelli, F.; Speghini, A.; Zaccheroni, N., Imaging agents based on lanthanide doped nanoparticles. *Chem. Soc. Rev.* **2015,** *44*, 4922.
61. Burke, B. P.; Cawthorne, C.; Archibald, S. J., Multimodal nanoparticle imaging agents: design and applications. *Philos. Trans. A Math. Phys. Eng. Sci.* **2017,** *375*.
62. Yi, Z.; Luo, Z.; Qin, X.; Chen, Q.; Liu, X., Lanthanide activated nanoparticles: a toolbox for bioimaging, therapeutics, and neuromodulation. *Acc. Chem. Res.* **2020,** *53*, 2692.
63. Zhou, J.; Liu, Q.; Feng, W.; Sun, Y.; Li, F., Upconversion luminescent materials: advances and applications. *Chem. Rev.* **2015,** *115*, 395.
64. Lim, S. F.; Riehn, R.; Ryu, W. S.; Khanarian, N.; Tung, C.; Tank, D.; Austin, R. H., In vivo and scanning electron microscopy imaging of upconverting nanophosphors in caenorhabditis elegans. *Nano Lett.* **2006,** *2*, 169.
65. Abdul Jalil, R.; Zhang, Y., Biocompatibility of silica coated $NaYF_4$ upconversion fluorescent nanocrystals. *Biomaterials* **2008,** *29*, 4122.
66. Ong, L. C.; Ang, L. Y.; Alonso, S.; Zhang, Y., Bacterial imaging with photostable upconversion fluorescent nanoparticles. *Biomaterials* **2014,** *35*, 2987.
67. Chatterjee, D. K.; Rufaihah, A. J.; Zhang, Y., Upconversion fluorescence imaging of cells and small animals using lanthanide doped nanocrystals. *Biomaterials* **2008,** *29*, 937.
68. Yang, T.; Sun, Y.; Liu, Q.; Feng, W.; Yang, P.; Li, F., Cubic sub-20 nm $NaLuF_4$-based upconversion nanophosphors for high-contrast bioimaging in different animal species. *Biomaterials* **2012,** *33*, 3733.
69. Dong, R.; Li, Y.; Li, W.; Zhang, H.; Liu, Y.; Ma, L.; Wang, X.; Lei, B., Recent developments in luminescent nanoparticles for plant imaging and photosynthesis. *J. Rare Earths* **2019,** *37*, 903.
70. Skripka, A.; Mendez-Gonzalez, D.; Marin, R.; Ximendes, E.; Del Rosal, B.; Jaque, D.; Rodriguez-Sevilla, P., Near infrared bioimaging and biosensing with semiconductor and rare-earth nanoparticles: recent developments in multifunctional nanomaterials. *Nanoscale Adv.* **2021,** *3*, 6310.
71. Zhu, X.; Zhang, H.; Zhang, F., Expanding NIR-II lanthanide toolboxes for improved biomedical imaging and detection. *Acc. Mater. Res.* **2023,** *4*, 536.
72. Labrador-Paez, L.; Pedroni, M.; Speghini, A.; Garcia-Sole, J.; Haro-Gonzalez, P.; Jaque, D., Reliability of rare-earth-doped infrared luminescent nanothermometers. *Nanoscale* **2018,** *10*, 22319.

73. Naczynski, D. J.; Tan, M. C.; Zevon, M.; Wall, B.; Kohl, J.; Kulesa, A.; Chen, S.; Roth, C. M.; Riman, R. E.; Moghe, P. V., Rare-earth-doped biological composites as in vivo shortwave infrared reporters. *Nat. Commun.* **2013,** *4*, 2199.
74. Heffern, M. C.; Matosziuk, L. M.; Meade, T. J., Lanthanide probes for bioresponsive imaging. *Chem. Rev.* **2014,** *114*, 4496.
75. Chen, Z. H.; Wang, X.; Yang, M.; Ming, J.; Yun, B.; Zhang, L.; Wang, X.; Yu, P.; Xu, J.; Zhang, H.; Zhang, F., An extended NIR-II superior imaging window from 1500 to 1900 nm for high-resolution in vivo multiplexed imaging based on lanthanide nanocrystals. *Angew. Chem. Int. Ed.* **2023,** *62*, 202311883.
76. Degena, C. L.; Mamina, H. J.; Rettnera, C. T.; Rugar, D., Nanoscale magnetic resonance imaging. *PNAS* **2009,** *126*, 1313.
77. Brown M. A.; Semelka R., MRI: basic principles and applications. John Wiley & Sons, **2011**.
78. Na, H. B.; Song, I. C.; Hyeon, T., Inorganic nanoparticles for MRI contrast agents. *Adv. Mater.* **2009,** *21*, 2133.
79. Raymond, K. V.; Pierre, V. C., Next generation, high relaxivity gadolinium MRI agents. *Bioconjugate Chem.* **2005,** *16*, 3.
80. Wahsner, J.; Gale, E. M.; Rodriguez-Rodriguez, A.; Caravan, P., Chemistry of MRI contrast agents: current challenges and new frontiers. *Chem. Rev.* **2019,** *119*, 957.
81. Subha Viswanathan, Z. K., Kayla N. Green, S. James Ratnakar, and A. Dean Sherry, Alternatives to gadolinium based metal chelates for magnetic resonance imaging. *Chem. Rev.* **2010,** *110*, 2960.
82. Na, H. B.; Hyeon, T., Nanostructured T_1 MRI contrast agents. *J. Mater. Chem.* **2009,** *19*, 6267.
83. Park, Y. I.; Kim, J. H.; Lee, K. T.; Jeon, K.-S.; Na, H. B.; Yu, J. H.; Kim, H. M.; Lee, N.; Choi, S. H.; Baik, S.-I.; Kim, H.; Park, S. P.; Park, B.-J.; Kim, Y. W.; Lee, S. H.; Yoon, S.-Y.; Song, I. C.; Moon, W. K.; Suh, Y. D.; Hyeon, T., Nonblinking and nonbleaching upconverting nanoparticles as an optical imaging nanoprobe and T_1 magnetic resonance imaging contrast agent. *Adv. Mater.* **2009,** *21*, 4467.
84. Marckmann, P.; Skov, L.; Rossen, K.; Dupont, A.; Damholt, M. B.; Heaf, J. G.; Thomsen, H. S., Nephrogenic systemic fibrosis: suspected causative role of gadodiamide used for contrast-enhanced magnetic resonance imaging. *J. Am. Soc. Nephrol.* **2006,** *17*, 2359.
85. Johnson, N. J. J.; Oakden, W.; Stanisz, G. J.; Scott Prosser, R.; van Veggel, F. C. J. M., Size-tunable, ultrasmall $NaGdF_4$ nanoparticles: insights into their T_1MRI contrast enhancement. *Chem. Mater.* **2011,** *23*, 3714.
86. Gao, Z.; Ma, T.; Zhao, E.; Docter, D.; Yang, W.; Stauber, R. H.; Gao, M., Small is smarter: nano MRI contrast agents - advantages and recent achievements. *Small* **2016,** *12*, 556.
87. Ahren, M.; Selegard, L.; Klasson, A.; Soderlind, F.; Abrikossova, N.; Skoglund, C.; Bengtsson, T.; Engstrom, M.; Kall, P. O.; Uvdal, K., Synthesis and characterization of PEGylated Gd_2O_3 nanoparticles for MRI contrast enhancement. *Langmuir* **2010,** *26*, 5753.
88. Johnson, N. J.; He, S.; Nguyen Huu, V. A.; Almutairi, A., Compact micellization: a strategy for ultrahigh T_1 magnetic resonance contrast with gadolinium-based nanocrystals. *ACS Nano* **2016,** *10*, 8299.

89. Liu, N.; Marin, R.; Mazouzi, Y.; Cron, G. O.; Shuhendler, A.; Hemmer, E., Cubic versus hexagonal - effect of host crystallinity on the T_1 shortening behaviour of $NaGdF_4$ nanoparticles. *Nanoscale* **2019,** *11*, 6794.
90. Evanics, F.; Diamente, P. R.; van Veggel, F. C. J. M.; Stanisz, G. J.; Prosser,R. S., Water soluble GdF_3 and GdF_3/LaF_3-nanoparticle sphysical characterization and NMR relaxation properties. *Chem. Mater.* **2006,** *18*, 2499.
91. Bridot, J.; Faure, A. C.; Laurent, S.; Riviere, C.; Billotey, C.; Hiba, B.; Janier, M.; Josserand, V., Coll, J., Elst, L. V.; Muller, R.; Roux, S.; Perriat P.; Tillement, O., Hybrid gadolinium oxide nanoparticles multimodal contrast agents for in vivo imaging. *J. Am. Chem. Soc.* **2007,** *129*, 5076.
92. Hou, L., Qiao, R., Fang, F., Wang, X., Dong, C., Liu, K., Liu, C., Liu, Z., Lei, H., Wang, F. and Gao, M., $NaGdF_4$ nanoparticle based molecular probes for magnetic resonance imaging of intraperitoneal tumor. *ACS Nano* **2013,** *7*, 330.
93. Huang, J.; Hou, Y.; Liu, C.; Jing, L.; Ma, T.; Sun, X.; Gao, M., Chemical spacer design for engineering the relaxometric properties of core–shell structured rare earth nanoparticles. *Chem. Mater.* **2015,** *27*, 7918.
94. Hou, L., Qiao, R., Fang, F., Wang, X., Dong, C., Liu, K., Liu, C., Liu, Z., Lei, H., Wang, F. and Gao, M., $NaGdF_4$ nanoparticle based molecular probes for magnetic resonance imaging of intraperitoneal tumor. *ACS Nano* **2013,** *7*, 330.
95. Rodrigues, E. M.; Gálico, D. A.; Lemes, M. A.; Bettini, J.; T. Neto, E.; Mazali, I. O.; Murugesu, M.; Sigoli, F. A., One pot synthesis and systematic study of the photophysical and magnetic properties and thermal sensing of α and β-phase $NaLnF_4$ and β-phase core/shell nanoparticles. *New J. Chem.* **2018,** *42*, 13393.
96. Li, F.; Gu, W.; Wang, H.; Qi, Y.; Deng, Y.; Xiao, N.; Liu, Y.; Xu, Q.; Ye, L., Effect of surface functionalities on relaxometric properties of MR contrast agents based on $NaGdF_4$ nanoparticles. *RSC Adv.* **2013,** *3*, 5386.
97. Zhang, H.; Wu, Y.; Wang, J.; Tang, Z.; Ren, Y.; Ni, D.; Gao, H.; Song, R.; Jin, T.; Li, Q.; Bu, W.; Yao, Z., In vivo MR imaging of glioma recruitment of adoptive T-cells labeled with $NaGdF_4$ -TAT nanoprobes. *Small* **2018,** *14*.
98. Dash, A.; Blasiak, B.; Tomanek, B.; van Veggel, F. C. J. M., Validation of inner, second, and outer sphere contributions to T_1 and T_2 relaxation in Gd^{3+}-based nanoparticles using Eu^{3+} lifetime decay as a probe. *J. Phys. Chem. C* **2018,** *122*, 11557.
99. Kim, C. R.; Baeck, J. S.; Chang, Y.; Bae, J. E.; Chae, K. S.; Lee, G. H., Ligand-size dependent water proton relaxivities in ultrasmall gadolinium oxide nanoparticles and in vivo T_1 MR images in a 1.5 T MR field. *Phys. Chem. Chem. Phys.* **2014,** *16*, 19866.
100. Pan, D.; Caruthers, S. D.; Senpan, A.; Schmieder, A. H.; Wickline, S. A.; Lanza, G. M., Revisiting an old friend: manganese‐based MRI contrast agents. *WIREs Nanomed. Nanobiotechnol.* **2011,** *3*, 162.
101. Koretsky, A. P.; Silva, A. C., *Manganese‐enhanced magnetic resonance imaging (MEMRI)*. *NMR Biomed.* **2004**, *17*, 527.
102. Zheng, Y. J. a. W., Cardiovascular toxicities upon managanese exposure. *Cardiovasc. Toxicol.* **2005,** *05*, 345.
103. Terreno, E.; Castelli, D. D.; Viale, A.; Aime, S., Challenges for molecular magnetic resonance imaging. *Chem. Rev.* **2010,** *110*, 3019.

104. Silva, A. C.; Lee, J. H.; Aoki, I.; Koretsky, A. P., Manganese-enhanced magnetic resonance imaging (MEMRI): methodological and practical considerations. *NMR Biomed* **2004,** *17*, 532.
105. Na, H. B.; Lee, J. H.; An, K.; Park, Y. I.; Park, M.; Lee, I. S.; Nam, D. H.; Kim, S. T.; Kim, S. H.; Kim, S. W.; Lim, K. H.; Kim, K. S.; Kim, S. O.; Hyeon, T., Development of a T_1 contrast agent for magnetic resonance imaging using MnO nanoparticles. *Angew. Chem.* **2007,** *119*, 5493.
106. Xie, M.; Peng, X.; Fu, X.; Zhang, J.; Li, G.; Yu, X., Synthesis of Yb^{3+}/Er^{3+} co-doped MnF_2 nanocrystals with bright red up-converted fluorescence. *Scr. Mater.* **2009,** *60*, 190.
107. Banerjee, A.; Blasiak, B.; Dash, A.; Tomanek, B.; van Veggel, F. C. J. M.; Trudel, S., High-field magnetic resonance imaging: Challenges, advantages, and opportunities for novel contrast agents. *Chem. Phys. Rev.* **2022,** *3*, 011304.
108. Liu, S.; Brisset, J. C.; Hu, J.; Haacke, E. M.; Ge, Y., Susceptibility weighted imaging and quantitative susceptibility mapping of the cerebral vasculature using ferumoxytol. *J. Magn. Reson. Imaging* **2018,** *47*, 621.
109. Zhang, X.; Blasiak, B.; Marenco, A. J.; Trudel, S.; Tomanek, B.; van Veggel, F. C. J. M., Design and regulation of $NaHoF_4$ and $NaDyF_4$ nanoparticles for high-field magnetic resonance imaging. *Chem. Mater.* **2016,** *28*, 3060.
110. Subha Viswanathan, Z. K., Kayla N. Green, S. James Ratnakar, and A. Dean Sherry, Alternatives to gadolinium-based metal chelates for magnetic resonance imaging. *Chem. Rev.* **2010,** *110*, 2960.
111. Das, G. K.; Johnson, N. J.; Cramen, J.; Blasiak, B.; Latta, P.; Tomanek, B.; van Veggel, F. C., $NaDyF_4$ nanoparticles as T_2 contrast agents for ultrahigh field magnetic resonance imaging. *J. Phys. Chem. Lett.* **2012,** *3*, 524.
112. Key, J.; Leary, J. F., Nanoparticles for multimodal in vivo imaging in nanomedicine. *Int. J. Nanomedicine* **2014,** *9*, 711.
113. Ashton, J. R.; West, J. L.; Badea, C. T., In vivo small animal micro-CT using nanoparticle contrast agents. *Front. Pharmacol.* **2015,** *6*, 256.
114. Reeves, T. E.; Mah, P.; McDavid, W. D., Deriving hounsfield units using grey levels in cone beam CT: a clinical application. *Dentomaxillofac. Radiol.* **2012,** *41*, 500.
115. Lee, N.; Choi, S. H.; Hyeon, T., Nano-sized CT contrast agents. *Adv. Mater.* **2013,** *25*, 2641.
116. Lusic, H.; Grinstaff, M. W., X-ray-computed tomography contrast agents. *Chem. Rev.* **2013,** *113*, 1641.
117. Ginat, D. T.; Gupta, R., Advances in computed tomography imaging technology. *Annu. Rev. Biomed. Eng.* **2014,** *16*, 431.
118. Liu, Y.; Ai, K.; Lu, L., Nanoparticulate X-ray computed tomography contrast agents from design validation to in vivo applications. *Acc. Chem. Res.* **2012,** *45*, 1817.
119. Kim, B.; Park, S. H.; Hong, G. S.; Lee, J. H.; Lee, J. S.; Kim, H. J.; Kim, A. Y.; Ha, H. K., Iohexol versus diatrizoate for fecal/fluid tagging during CT colonography performed with cathartic preparation: comparison of examination quality. *Eur. Radiol.* **2015,** *25*, 1561.
120. Haller, C.; Hizoh, I., The cytotoxicity of iodinated radiocontrast agents on renal cells in vitro. *Invest. Radiol.* **2004,** *39*, 149.

121. McDonald, M. A.; Watkin, K. L., Small particulate gadolinium oxide and gadolinium oxide albumin microspheres as multimodal contrast and therapeutic agents. *Invest. Radiol.* **2003,** *38*, 305.
122. Eck, W.; Nicholson, A. I.; Zentgraf, H.; Semmler, W.; Bartling, S., Anti-CD4-targeted gold nanoparticles induce specific contrast enhancement of peripheral lymph nodes in X-ray computed tomography of live mice. *Nano Lett.* **2010,** *10*, 2318.
123. Chou, S. W.; Shau, Y. H.; Wu, P. C.; Yang, Y. S.; Shieh, D.; Chen,C. C., In vitro and in vivo studies of FePt nanoparticles for dual modal CT/MRI molecular imaging. *J. Am. Chem. Soc.* **2010,** *132*, 13270.
124. Ai, K.; Liu, Y.; Liu, J.; Yuan, Q.; He, Y.; Lu, L., Large-scale synthesis of Bi_2S_3 nanodots as a contrast agent for in vivo X-ray computed tomography imaging. *Adv. Mater.* **2011,** *23*, 4886.
125. Cheung, E. N. M.; Alvares, R. D. A.; Oakden, W.; Chaudhary, R.; Hill, M. L.; Pichaandi, J.; Mo, G. C. H.; Yip, C.; Macdonald, P. M.; Stanisz, G. J.; van Veggel, F. C. J. M.; Prosser, R. S., Polymer-stabilized lanthanide fluoride nanoparticle aggregates as contrast agents for magnetic resonance imaging and computed tomography. *Chem. Mater.* **2010,** *22*, 4728.
126. Zhou, L.; Zheng, X.; Gu, Z.; Yin, W.; Zhang, X.; Ruan, L.; Yang, Y.; Hu, Z.; Zhao, Y., Mesoporous $NaYbF_4/NaGdF_4$ core-shell up-conversion nanoparticles for targeted drug delivery and multimodal imaging. *Biomaterials* **2014,** *35*, 7666.
127. Hubbell, J. H.; Seltzer, S. M. X-ray mass attenuation coefficients, NIST standard reference database 126. https://dx.doi.org/10.18434/T4D01F (accessed 07. June 2023).
128. Xing, H.; Bu, W.; Zhang, S.; Zheng, X.; Li, M.; Chen, F.; He, Q.; Zhou, L.; Peng, W.; Hua, Y.; Shi, J., Multifunctional nanoprobes for upconversion fluorescence, MR and CT trimodal imaging. *Biomaterials* **2012,** *33*, 1079.
129. Ashokan, A.; Chandran, P.; Sadanandan, A. R.; Koduri, C. K.; Retnakumari, A. P.; Menon, D.; Nair, S.; Koyakutty, M., Development and haematotoxicological evaluation of doped hydroxyapatite based multimodal nanocontrast agent for near-infrared, magnetic resonance and X-ray contrast imaging. *Nanotoxicology* **2012,** *6*, 652.
130. Chen, F.; Huang, P.; Zhu, Y. J.; Wu, J.; Zhang, C. L.; Cui, D. X., The photoluminescence, drug delivery and imaging properties of multifunctional Eu^{3+}/Gd^{3+} dual-doped hydroxyapatite nanorods. *Biomaterials* **2011,** *32*, 9031.
131. Zhu, X.; Zhou, J.; Chen, M.; Shi, M.; Feng, W.; Li, F., Core-shell Fe_3O_4@$NaLuF_4$:Yb,Er/Tm nanostructure for MRI, CT and upconversion luminescence tri-modality imaging. *Biomaterials* **2012,** *33*, 4618.
132. Liu, Y.; Ai, K.; Liu, J.; Yuan, Q.; He, Y.; Lu, L., A high-performance ytterbium-based nanoparticulate contrast agent for in vivo X-ray computed tomography imaging. *Angew. Chem. Int. Ed.* **2012,** *51*, 1437.
133. Li, Y.; Gu, Y.; Yuan, W.; Cao, T.; Li, K.; Yang, S.; Zhou, Z.; Li, F., Core-shell-shell $NaYbF_4$:Tm@CaF_2@$NaDyF_4$ nanocomposites for upconversion/T_2-weighted MRI/computed tomography lymphatic imaging. *ACS Appl. Mater. Interfaces* **2016,** *8*, 19208.
134. Ferreira, F. S.; de Morais, A. J.; Santos Calado, C. M.; Iikawa, F.; Couto Junior, O. D. D.; Brunet, G.; Murugesu, M.; Mazali, I. O.; Sigoli, F. A., Dual magnetic field and temperature

optical probes of controlled crystalline phases in lanthanide-doped multi-shell nanoparticles. *Nanoscale* **2021,** *13*, 14723.

135. Cressoni, C.; Vurro, F.; Milan, E.; Muccilli, M.; Mazzer, F.; Gerosa, M.; Boschi, F.; Spinelli, A. E.; Badocco, D.; Pastore, P.; Delgado, N. F.; Collado, M. H.; Marzola, P.; Speghini, A., From nanothermometry to bioimaging: lanthanide-activated KY_3F_{10} nanostructures as biocompatible multifunctional tools for nanomedicine. *ACS Appl. Mater. Interfaces* **2023,** *15*, 12171.
136. Park, Y. I.; Lee, K. T.; Suh, Y. D.; Hyeon, T., Upconverting nanoparticles: a versatile platform for wide-field two-photon microscopy and multi-modal in vivo imaging. *Chem. Soc. Rev.* **2015,** *44*, 1302.
137. Chen, G.; Roy, I.; Yang, C.; Prasad, P. N., Nanochemistry and nanomedicine for nanoparticle-based diagnostics and therapy. *Chem. Rev.* **2016,** *116*, 2826.
138. Deng, Y.; Wang, H.; Gu, W.; Li, S.; Xiao, N.; Shao, C.; Xu, Q.; Ye, L., Ho^{3+} doped $NaGdF_4$ nanoparticles as MRI/optical probes for brain glioma imaging. *J. Mater. Chem. B* **2014,** *2*, 1521.
139. Fan, W.; Shen, B.; Bu, W.; Chen, F.; Zhao, K.; Zhang, S.; Zhou, L.; Peng, W.; Xiao, Q.; Xing, H.; Liu, J.; Ni, D.; He, Q.; Shi, J., Rattle-structured multifunctional nanotheranostics for synergetic chemo-/radiotherapy and simultaneous magnetic/luminescent dual-mode imaging. *J. Am. Chem. Soc.* **2013,** *135*, 6494.
140. Zhang, Y.; Das, G. K.; Vijayaragavan, V.; Xu, Q. C.; Padmanabhan, P.; Bhakoo, K. K.; Selvan, S. T.; Tan, T. T., "Smart" theranostic lanthanide nanoprobes with simultaneous up-conversion fluorescence and tunable T_1-T_2 magnetic resonance imaging contrast and near-infrared activated photodynamic therapy. *Nanoscale* **2014,** *6*, 12609.
141. Biju, S.; Harris, M.; Elst, L. V.; Wolberg, M.; Kirschhock, C.; Parac-Vogt, T. N., Multifunctional β-$NaGdF_4$:Ln^{3+} (Ln = Yb, Er, Dy) nanoparticles with NIR to visible upconversion and high transverse relaxivity: a potential bimodal contrast agent for high-field MRI and optical imaging. *RSC Adv.* **2016,** *6*, 61443.
142. Su, Y.; Hao, L.-N.; Liu, K.; Zhang, J.; Dong, L.; Xu, Y.; Lu, Y.; Qian, H.-S., Epitaxial growth of ultrathin layers on the surface of sub-10 nm nanoparticles: the case of β-$NaGdF_4$:Yb/Er@$NaDyF_4$ nanoparticles. *RSC Adv.* **2018,** *8*, 12944.
143. Mahalingam, V.; Naccache, R.; Vetrone, F.; Capobianco, J. A., Preferential suppression of high-energy upconverted emissions of Tm^{3+} by Dy^{3+} ions in Tm^{3+}/Dy^{3+}/Yb^{3+}-doped $LiYF_4$ colloidal nanocrystals. *Chem. Commun.* **2011,** *47*, 3481.
144. Yuan, W.; Yang, D.; Su, Q.; Zhu, X.; Cao, T.; Sun, Y.; Dai, Y.; Feng, W.; Li, F., Intraperitoneal administration of biointerface-camouflaged upconversion nanoparticles for contrast enhanced imaging of pancreatic cancer. *Adv. Funct. Mater.* **2016,** *26*, 8631.
145. Thanh, N. T.; Maclean, N.; Mahiddine, S., Mechanisms of nucleation and growth of nanoparticles in solution. *Chem. Rev.* **2014,** *114*, 7610.
146. Park, J.; Joo, J.; Kwon, S. G.; Jang, Y.; Hyeon, T., Synthesis of monodisperse spherical nanocrystals. *Angew. Chem. Int. Ed.* **2007,** *46*, 4630.
147. Dinegar, V. K. L. a. R. H., Theory, production and mechanism of formation of monodispersed hydrosols. *J. Am. Chem. Soc.* **1950,** *72*, 4847.
148. Goesmann, H.; Feldmann, C., Nanoparticulate functional materials. *Angew. Chem. Int. Ed.* **2010,** *49*, 1362.

149. Sugimoto, T., The theory of the nucleation of monodisperse particles. *J. Colloid Interface Sci.* **1991,** *150*, 208.
150. John, S. S.; Nan, Z.; Hu, N.; Schaefer, D. W.; Angelopoulos, A. P., A nanoscale-modified LaMer model for particle synthesis from inorganic tin–platinum complexes. *J. Mater. Chem. A* **2013,** *1*, 8903.
151. Mai, H.-X.; Zhang, Y.-W.; Si, R.; Yan, Z.-G.; Sun, L.-d.; You, L.-P.; Yan, C.-H., High-quality sodium rare-earth fluoride nanocrystals: controlled synthesis and optical properties. *J. Am. Chem. Soc.* **2006,** *128*, 6426
152. Murray, C. B.; Norris, D. J.; Bawendi, M. G., Synthesis and characterization of nearly monodisperse CdE-(E = S, Se, Te) semiconductor nanocrystallites. *J. Am. Chem. Soc.* **1993,** *115*, 8706.
153. Gai, S.; Li, C.; Yang, P.; Lin, J., Recent progress in rare earth micro/nanocrystals: soft chemical synthesis, luminescent properties, and biomedical applications. *Chem. Rev.* **2014,** *114*, 2343.
154. Dühnen, S.; Rinkel, T.; Haase, M., Size Control of Nearly Monodisperse β-$NaGdF_4$ Particles Prepared from Small α-$NaGdF_4$ Nanocrystals. *Chem. Mater.* **2015,** *27*, 4033.
155. Nüchter, M.; Ondruschka, B.; Bonrath, W.; Gum, A., Microwave assisted synthesis – a critical technology overview. *Green Chem.* **2004,** *6*, 128.
156. Kumar, A. T. N.; Hou, S. S., Tomographic phosphorescence lifetime multiplexing. *Opt. Lett.* **2018,** *43*, 3104.
157. Lingeshwar Reddy, K.; Balaji, R.; Kumar, A.; Krishnan, V., Lanthanide doped near infrared active upconversion nanophosphors: fundamental concepts, synthesis strategies, and technological applications. *Small* **2018,** *14*, e1801304.
158. Baghbanzadeh, M.; Carbone, L.; Cozzoli, P. D.; Kappe, C. O., Microwave-assisted synthesis of colloidal inorganic nanocrystals. *Angew. Chem. Int. Ed.* **2011,** *50*, 11312.
159. Halimi, I.; Rodrigues, E. M.; Maurizio, S. L.; Sun, H.-Q. T.; Grewal, M.; Boase, E. M.; Liu, N.; Marin, R.; Hemmer, E., Pick your precursor! Tailoring the size and crystal phase of microwave-synthesized sub-10 nm upconverting nanoparticles. *J. Mater. Chem. C* **2019,** *7*, 15364.
160. Bilecka, I.; Niederberger, M., Microwave chemistry for inorganic nanomaterials synthesis. *Nanoscale* **2010,** *2*, 1358.
161. Obermayer, D.; Gutmann, B.; Kappe, C. O., Microwave chemistry in silicon carbide reaction vials: separating thermal from nonthermal effects. *Angew. Chem. Int. Ed.* **2009,** *48*, 8321.
162. Panov, N.; Marin, R.; Hemmer, E., Microwave-assisted solvothermal synthesis of upconverting and downshifting rare-earth-doped $LiYF_4$ microparticles. *Inorg. Chem.* **2018,** *57*, 14920.
163. Nann, H.-Q. W. a. T., Monodisperse upconverting nanocrystals by microwave-assisted synthesis. *ACS Nano* **2009,** *3*, 5.
164. Ullah, S.; Hazra, C.; Ferreira-Neto, E. P.; Silva, T. C.; Rodrigues-Filho, U. P. R., Sidney J. L., Microwave-assisted synthesis of $NaYF_4$:Yb^{3+}/Tm^{3+} upconversion particles with tailored morphology and phase for the design of UV/NIR-active $NaYF_4$:Yb^{3+}/Tm^{3+}@TiO_2 core/shell photocatalysts. *Cryst. Eng. Comm.* **2017,** *19*, 3465.

165. Tong, L.; Li, X.; Zhang, J.; Xu, S.; Sun, J.; Cheng, L.; Zheng, H.; Zhang, Y.; Zhang, X.; Hua, R.; Xia, H.; Chen, B., Microwave-assisted hydrothermal synthesis, temperature quenching and laser-induced heating effect of hexagonal microplate β-$NaYF_4$: Er^{3+}/Yb^{3+} microcrystals under 1550 nm laser irradiation. *Sens. Actuators B Chem.* **2017,** *246*, 175.
166. Wawrzynczyk, D.; Piatkowski, D.; Mackowski, S.; Samoc, M.; Nyk, M., Microwave-assisted synthesis and single particle spectroscopy of infrared down- and visible up-conversion in Er^{3+} and Yb^{3+} co-doped fluoride nanowires. *J. Mater. Chem. C* **2015,** *3*, 5332.
167. Wang, H.-Q.; Tilley, R. D.; Nann, T., Size and shape evolution of upconverting nanoparticles using microwave assisted synthesis. *Cryst. Eng Comm.* **2010,** *12*.
168. Tong, L.; Li, X.; Hua, R.; Li, X.; Zheng, H.; Sun, J.; Zhang, J.; Cheng, L.; Chen, B., Comparative study on upconversion luminescence and temperature sensing of α- and β-$NaYF_4$:Yb^{3+}/Er^{3+} nano-/micro-crystals derived from a microwave-assisted hydrothermal route. *J. Lumin.* **2015,** *167*, 386.
169. Xu, L.; Zheng, H.; Pang, T.; Mao, J., Multicolor luminescence of hexagonal $NaYF_4$:Yb^{3+}/Ho^{3+}/Ce^{3+} microcrystals with tunable morphology under 940 nm excitation for temperature-responsive anti-counterfeiting. *J. Rare Earths* **2022,** *40*, 406.
170. Wu, T.; Hong, Y.; Song, L.; Zhu, Y.; Wang, J.; Zhu, Y.; Fang, J.; Chen, G., Synthesis of highly luminescent β-$NaYF_4$:Yb^{3+}, Er^{3+} upconversion nanoparticles regulated by sodium hexametaphosphate: For customs supervision. *Opt. Mater.* **2022,** *124*.
171. Amouroux, B.; Roux, C.; Marty, J. D.; Pasturel, M.; Bouchet, A.; Sliwa, M.; Leroux, O.; Gauffre, F.; Coudret, C., Importance of the Mixing and High-Temperature Heating Steps in the Controlled Thermal Coprecipitation Synthesis of Sub-5-nm Na(Gd-Yb)F_4:Tm. *Inorg. Chem.* **2019,** *58*, 5082.
172. Duan, C.; Liang, L.; Li, L.; Zhang, R.; Xu, Z. P., Recent progress in upconversion luminescence nanomaterials for biomedical applications. *J. Mater. Chem. B* **2018,** *6*, 192.
173. Liu, Y.; Tu, D.; Zhu, H.; Chen, X., Lanthanide-doped luminescent nanoprobes: controlled synthesis, optical spectroscopy, and bioapplications. *Chem. Soc. Rev.* **2013,** *42*, 6924.
174. Sedlmeier, A.; Gorris, H. H., Surface modification and characterization of photon-upconverting nanoparticles for bioanalytical applications. *Chem. Soc. Rev.* **2015,** *44*, 1526.
175. Zhu, X.; Wang, X.; Zhang, H.; Zhang, F., Luminescence lifetime imaging based on lanthanide nanoparticles. *Angew. Chem. Int. Ed.* **2022,** *61*, e202209378.
176. Liu, Y.; Tu, D.; Zhu, H.; Ma, E.; Chen, X., Lanthanide-doped luminescent nano-bioprobes: from fundamentals to biodetection. *Nanoscale* **2013,** *5*, 1369.
177. Bogdan, N.; Vetrone, F.; Ozin, G. A.; Capobianco, J. A., Synthesis of ligand-free colloidally stable water dispersible brightly luminescent lanthanide-doped upconverting nanoparticles. *Nano Lett.* **2011,** *11*, 835.
178. Lay, A.; Sheppard, O. H.; Siefe, C.; McLellan, C. A.; Mehlenbacher, R. D.; Fischer, S.; Goodman, M. B.; Dionne, J. A., Optically robust and biocompatible mechanosensitive upconverting nanoparticles. *ACS Cent. Sci.* **2019,** *5*, 1211.
179. Hemmer, E.; Quintanilla, M.; Légaré, F.; Vetrone, F., Temperature induced energy transfer in dye-conjugated upconverting nanoparticles: a new candidate for nanothermometry. *Chem. Mater.* **2014,** *27*, 235.

180. Wu, B.; Cao, Z.; Zhang, Q.; Wang, G., NIR-responsive DNA hybridization detection by high efficient FRET from 10-nm upconversion nanoparticles to SYBR green I. *Sens. Actuators B Chem.* **2018,** *255*, 2853.
181. Liu, Y.; Tu, D.; Zheng, W.; Lu, L.; You, W.; Zhou, S.; Huang, P.; Li, R.; Chen, X., A strategy for accurate detection of glucose in human serum and whole blood based on an upconversion nanoparticles-polydopamine nanosystem. *Nano Research* **2018,** *11*, 3164.
182. Ren, N.; Liang, N.; Yu, X.; Wang, A.; Xie, J.; Sun, C., Ligand-free upconversion nanoparticles for cell labeling and their effects on stem cell differentiation. *Nanotechnology* **2020,** *31*, 145101.
183. Wu, B.; Cao, Z.; Zhang, Q.; Wang, G., NIR-responsive DNA hybridization detection by high efficient FRET from 10-nm upconversion nanoparticles to SYBR green I. *Sensors Actuat. B-Chem.* **2018,** *255*, 2853.
184. Cai, L.; Huang, Y.; Sun, P.; Zheng, W.; Zhou, S.; Huang, P.; Wei, J.; Tu, D.; Chen, X.; Liang, Z., Accurate detection of β-hCG in women serum and cervical secretions for predicting early pregnancy viability based on time-resolved luminescent lanthanide nanoprobes. *Nanoscale* **2020**.
185. Zhu, X.; Zhang, H.; Zhang, F., Ligand-based surface engineering of lanthanide nanoparticles for bioapplications. *ACS Mater. Lett.* **2022,** *4*, 1815.
186. Gee, A.; Xu, X., Surface functionalisation of upconversion nanoparticles with different moieties for biomedical applications. *Surfaces* **2018,** *1*, 96.
187. Duong, H. T. T.; Chen, Y.; Tawfik, S. A.; Wen, S.; Parviz, M.; Shimoni, O.; Jin, D., Systematic investigation of functional ligands for colloidal stable upconversion nanoparticles. *RSC Adv.* **2018,** *8*, 4842.
188. Rafik Naccache, F. V., Venkataramanan Mahalingam, Louis A. Cuccia, and John A. Capobianco, Controlled synthesis and water dispersibility of hexagonal phase $NaGdF_4$:Ho^{3+}/Yb^{3+} nanoparticles. *Chem. Mater.* **2009,** *21*, 717.
189. Schwartz, C. A. T. a. J., Surface modification of Y_2O_3 nanoparticles. *Langmuir* **2007,** *23* 9158.
190. Yoshimura, Y.; Ohara, K., Thermochemical studies on the lanthanoid complexes of trifluoroacetic acid. *J. Alloys Compd.* **2006,** *408-412*, 573.
191. Johnson, N. J. J.; van Veggel, F. C. J. M., Sodium lanthanide fluoride core-shell nanocrystals: A general perspective on epitaxial shell growth. *Nano Research* **2013,** *6*, 547.
192. Naccache, R.; Chevallier, P.; Lagueux, J.; Gossuin, Y.; Laurent, S.; Vander Elst, L.; Chilian, C.; Capobianco, J. A.; Fortin, M. A., High relaxivities and strong vascular signal enhancement for $NaGdF_4$ nanoparticles designed for dual MR/optical imaging. *Adv. Healthc. Mater.* **2013,** *2*, 1478.
193. Zhang, H.; Li, Y.; Ivanov, I. A.; Qu, Y.; Huang, Y.; Duan, X., Plasmonic modulation of the upconversion fluorescence in $NaYF_4$:Yb/Tm hexaplate nanocrystals using gold nanoparticles or nanoshells. *Angew. Chem. Int. Ed.* **2010,** *49*, 2865.
194. Hemmer, E.; Quintanilla, M.; Légaré, F.; Vetrone, F., Temperature-Induced Energy Transfer in Dye-Conjugated Upconverting Nanoparticles: A New Candidate for Nanothermometry. *Chem. Mater.* **2014,** *27*, 235.
195. Gu, Y.; Qiao, X.; Zhang, J.; Sun, Y.; Tao, Y.; Qiao, S., Effects of surface modification of upconversion nanoparticles on cellular uptake and cytotoxicity. *Chem. Res. Chin. Univ.* **2016,** *32*, 474.

196. Sharmaa, R. K.; Mudringb, A.-V.; Pushpal Ghosha, Recent trends in binary and ternary rare-earth fluoride nanophosphors: How structural and physical properties influence optical behaviour. *J. Lumin.* **2017,** *189*, 44
197. Naccache, R.; Yu, Q.; Capobianco, J. A., The fluoride host: nucleation, growth, and upconversion of lanthanide-doped nanoparticles. *Adv. Optical Mater.* **2015,** *3*, 482.
198. Lahtinen, S.; Lyytikäinen, A.; Päkkilä, H.; Hömppi, E.; Perälä, N.; Lastusaari, M.; Soukka, T., Disintegration of hexagonal $NaYF_4$:Yb^{3+},Er^{3+} upconverting nanoparticles in aqueous media: the role of fluoride in solubility equilibrium. *J. Phys. Chem. C* **2016,** *121*, 656.
199. Lisjak, D.; Plohl, O.; Ponikvar-Svet, M.; Majaron, B., Dissolution of upconverting fluoride nanoparticles in aqueous suspensions. *RSC Adv.* **2015,** *5*, 27393.
200. Lisjak, D.; Plohl, O.; Vidmar, J.; Majaron, B.; Ponikvar-Svet, M., Dissolution mechanism of upconverting AYF_4:Yb,Tm (A = Na or K) nanoparticles in aqueous media. *Langmuir* **2016,** *32*, 8222.
201. Zhang, X.; Hayakawa, T.; Nogami, M.; Ishikawa, Y., Selective synthesis and luminescence properties of nanocrystalline GdF_3:$Eu^{3+}$with hexagonal and orthorhombic structures. *J. Nanomater.* **2010,** *2010*, 1.
202. Wang, X.; Zhuang, J.; Peng, Q.; Li, Y., Hydrothermal synthesis of rare-earth fluoride nanocrystals. *Inorg. Chem.* **2006,** *45*, 6661
203. Chunxia Li, J. Y., Piaoping Yang, Hongzhou Lian, and Jun Lin, Hydrothermal synthesis of lanthanide fluorides LnF_3 (Ln = La to Lu) nano/microcrystals with multiform structure and morphologies. *Chem. Mater.* **2008,** *20*, 4317.
204. Thoma, R. E.; Insley, H.; Hebert, G. M., The sodium fluoride-lanthanide trifluoride systems. *Inorg. Chem.* **1966,** *5*, 1222
205. Bulavin, L.; Sokol'skii, V.; Roik, O.; Kazimirov, V.; Plevachuk, Y.; Sklyarchuk, V.; Faidiuk, N., Structure and physical properties of ternary NaF–LiF–LnF_3(Ln = La, Nd) systems of eutectic compositions. *Phys. Chem. of Liq.* **2016,** *54*, 717.
206. Tian, Y.; Hua, R.; Yu, N.; Zhang, W.; Na, L.; Chen, B., Morphology and phase evolvement of Yb^{3+}/Er^{3+} co-doped $NaYF_4$ microtubes prepared with YF_3 submicrospindles as precursor. *J. Alloy. Compd.* **2011,** *509*, 9924.
207. Yu, X.; Bian, W.; Wang, T.; Zhou, D.; Qiu, J.; Xu, X., Up-conversion luminescence properties of lanthanide-doped LuF_3 with different morphologies synthesized via a facile ionothermal process. *Cryst. Eng. Comm.* **2015,** *17*, 2147.
208. Becerro, A. I.; Gonzalez-Mancebo, D.; Ocaña, M., Uniform, luminescent Eu:LuF_3 nanoparticles. *J. Nanopart. Res.* **2015,** *17*, 58.
209. Tao, F.; Chen, J.; Liu, Q.; Zhang, Q.; Wang, G.; Sun, Y.; Wang, Z., Formation mechanism and morphology-dependent luminescence of NdF_3 nanoplates with cavities. *Cryst. Eng. Comm.* **2017,** *19*, 2487.
210. Tian, Y.; Hua, R.; Chen, B.; Yu, N.; Zhang, W.; Na, L., Lanthanide dopant-induced phase transition and luminescent enhancement of EuF_3 nanocrystals. *Cryst. Eng. Comm.* **2012,** *14*.
211. Xiang, G.; Zhang, J.; Hao, Z.; Zhang, X.; Pan, G. H.; Chen, L.; Luo, Y.; Lu, S.; Zhao, H., Solvothermal synthesis and upconversion properties of about 10 nm orthorhombic LuF_3: Yb^{3+}, Er^{3+} rectangular nanocrystals. *J. Colloid. Interface Sci.* **2015,** *459*, 224.

212. Li, Y.; Wang, Y.; Song, Y.; Zhou, X.; Zheng, K.; Sheng, Y.; Zou, H., Controlled synthesis and luminescence properties of $GdF_3$with different crystalline phases and morphologies. *Cryst. Eng. Comm.* **2017,** *19*, 1517.
213. Wang, H.; Wang, Y.; Zhang, J.; Gaponik, N.; Rogach, A. L., Europium fluoride based luminescent materials: From hydrogels to porous cryogels, and crystalline $NaEuF_4$ and EuF_3 micro/nanostructures. *Mat. Sci. Eng. B* **2014,** *179*, 48.
214. Zhang, X.; Hayakawa, T.; Nogami, M.; Ishikawa, Y., Variation in Eu^{3+} luminescence properties of GdF_3:Eu^{3+} nanophosphors depending on matrix GdF_3 polytype. *J. Alloy. Compd.* **2011,** *509*, 2076.
215. Wang, M.; Huang, Q.-L.; Hong, J.-M.; Chen, X.-T.; Xue, Z.-L., Controlled synthesis and characterization of nanostructured EuF_3 with different crystalline phases and morphologies. *Cryst. Growth Des.* **2006,** *6*, 2169
216. Zhao, Q.; Shao, B.; Lu, W.; Jia, Y.; Lv, W.; Jiao, M.; You, H., Doping alkaline-earth: a strategy of stabilizing hexagonal GdF_3 at room temperature. *Dalton Trans.* **2013,** *42*, 15482.
217. Rodriguez-Liviano, S.; Nunez, N. O.; Rivera-Fernandez, S.; de la Fuente, J. M.; Ocana, M., Ionic liquid mediated synthesis and surface modification of multifunctional mesoporous Eu:GdF_3 nanoparticles for biomedical applications. *Langmuir* **2013,** *29*, 3411.
218. Du, P.; Liu, Y.; Kim, Y.-J.; Yu, J. S., One-Pot Synthesis of Homogeneous EuF_3 Nanoplates: A Near-Ultraviolet Light-Induced Red-Emitting Bifunctional Platform for in vitro Cell Imaging and Solid-State Lighting. *ChemistrySelect* **2019,** *4*, 2275.
219. Passuello, T.; Pedroni, M.; Piccinelli, F.; Polizzi, S.; Marzola, P.; Tambalo, S.; Conti, G.; Benati, D.; Vetrone, F.; Bettinelli, M.; Speghini, A., PEG-capped, lanthanide doped GdF_3 nanoparticles: luminescent and T_2 contrast agents for optical and MRI multimodal imaging. *Nanoscale* **2012,** *4*, 7682.
220. Pudovkin, M. S.; Korableva, S. L.; Krasheninnicova, A. O.; Nizamutdinov, A. S.; Semashko, V. V.; Zelenihin, P. V.; Alakshin, E. M.; Nevzorova, T. A., Toxicity of laser irradiated photoactive fluoride PrF_3 nanoparticles toward bacteria. *J. Phys. Conf. Ser.* **2014,** *560*.
221. Zhang, L.; Lin, H.; Xiang, X.; Cheng, Y.; Hua, C.; Wang, C.; Lin, S.; Xu, J.; Wang, Y., Nanostructured NdF3 glass ceramic: An efficient bandpass color filter for wide-color-gamut white LED. *J. Eur. Cer.* **2019,** *39*, 2155.
222. Lu, C.; Wu, H.; Chen, B.; Liu, H.; Zhang, Y., Improving the electrochemical properties of $Li_{1.2}Mn_{0.52}Co_{0.08}Ni_{0.2}O_2$ cathode material by uniform surface nanocoating with samarium fluoride through depositional-hydrothermal route. *J. Alloy Compd.* **2015,** *634*, 75.
223. Pratomo, S. B.; Oktadinata, H.; Pawawoi, Effect of DyF_3 and TbF_3 additions on the coercivity enhancement in grain boundary diffusion processed Nd-Fe-B permanent magnets. *AIP Conf. Proc.* **2018**, *1964*, 020019.
224. Li, J.; Jia, Y.; Xu, Y.; Yang, H.; Sun, L.; Yan, C.; Bie, L.; Ju, J., In situepitaxial growth of GdF_3 on $NaGdF_4$:Yb,Er nanoparticles. *Inorg. Chem. Front.* **2017,** *4*, 2119.
225. Yon, M.; Billotey, C.; Marty, J. D., Gadolinium-based contrast agents: From gadolinium complexes to colloidal systems. *Int. J. Pharm.* **2019,** *569*, 118577.
226. Johnson, N. J. J.; Oakden, W.; Stanisz, G. J.; Scott Prosser, R.; van Veggel, F. C. J. M., Size-tunable, ultrasmall $NaGdF_4$ nanoparticles: insights into their T_1 MRI contrast enhancement. *Chem. Mater.* **2011,** *23*, 3714.

227. Naccache, R.; Chevallier, P.; Lagueux, J.; Gossuin, Y.; Laurent, S.; Vander Elst, L.; Chilian, C.; Capobianco, J. A.; Fortin, M. A., High relaxivities and strong vascular signal enhancement for NaGdF4 nanoparticles designed for dual MR/optical imaging. *Adv. Healthcare Mater.* **2013,** *2*, 1478.
228. Qiao, X. F.; Zhou, J. C.; Xiao, J. W.; Wang, Y. F.; Sun, L. D.; Yan, C. H., Triple-functional core-shell structured upconversion luminescent nanoparticles covalently grafted with photosensitizer for luminescent, magnetic resonance imaging and photodynamic therapy in vitro. *Nanoscale* **2012,** *4*, 4611.
229. Wu, D.; Wu, X.; Lv, Y.; Wang, H., Influence of solubility on the particle size of fluorides crystalline precipitated from aqueous solutions. *Mater. Let.* **2008,** *62*, 3003.
230. Zhang, L.; He, R.; Gu, H.-C., Oleic acid coating on the monodisperse magnetite nanoparticles. *Appl. Surf. Sci.* **2006,** *253*, 2611.
231. Menyuk, N.; Dwight, K.; Pierce, J. W., NaYF4: Yb,Er—an efficient upconversion phosphor. *Appl. Phys. Lett.* **1972,** *21*, 159.
232. Zheng, K.; Loh, K. Y.; Wang, Y.; Chen, Q.; Fan, J.; Jung, T.; Nam, S. H.; Suh, Y. D.; Liu, X., Recent advances in upconversion nanocrystals: Expanding the kaleidoscopic toolbox for emerging applications. *Nano Today* **2019,** *29*, 100797.
233. Xu, L.; Li, J.; Lu, K.; Wen, S.; Chen, H.; Shahzad, M. K.; Zhao, E.; Li, H.; Ren, J.; Zhang, J.; Liu, L., Sub-10 nm $NaNdF_4$ nanoparticles as near-infrared photothermal probes with self-temperature feedback. *ACS Appl. Nano Mat.* **2020**.
234. Du, P.; Ran, W.; Li, W.; Luo, L.; Huang, X., Morphology evolution of Eu^{3+}-activated $NaTbF_4$ nanorods: a highly efficient near ultraviolet light-triggered red-emitting platform towards application in white light-emitting diodes. *J. Mater. Chem. C* **2019,** *7*, 10802.
235. Li, Q.; Li, X.; Zhang, L.; Zuo, J.; Zhang, Y.; Liu, X.; Tu, L.; Xue, B.; Chang, Y.; Kong, X., An 800 nm driven $NaErF_4$@$NaLuF_4$ upconversion platform for multimodality imaging and photodynamic therapy. *Nanoscale* **2018,** *10*, 12356.
236. Zhang, J. Y.; Chen, S.; Wang, P.; Jiang, D. J.; Ban, D. X.; Zhong, N. Z.; Jiang, G. C.; Li, H.; Hu, Z.; Xiao, J. R.; Zhang, Z. G.; Cao, W. W., $NaYbF_4$ nanoparticles as near infrared light excited inorganic photosensitizers for deep penetration in photodynamic therapy. *Nanoscale* **2017,** *9*, 2706.
237. Herden, B.; Meijerink, A.; Rabouw, F. T.; Haase, M.; Jüstel, T., On the efficient luminescence of β-$Na(La_1{-}Pr)F_4$. *J. Lumin.* **2014,** *146*, 302.
238. Martinez-Esain, J.; Ros, J.; Faraudo, J.; Ricart, S.; Yanez, R., Tailoring the synthesis of LnF_3 (Ln = La-Lu and Y) nanocrystals via mechanistic study of the coprecipitation method. *Langmuir* **2018,** *34*, 6443.
239. Xu, J.; Gulzar, A.; Yang, P.; Bi, H.; Yang, D.; Gai, S.; He, F.; Lin, J.; Xing, B.; Jin, D., Recent advances in near-infrared emitting lanthanide-doped nanoconstructs: Mechanism, design and application for bioimaging. *Coord. Chem. Rev.* **2019,** *381*, 104.
240. Rocha, U.; Kumar, K. U.; Jacinto, C.; Villa, I.; Sanz-Rodriguez, F.; Iglesias de la Cruz M del, C.; Juarranz, A.; Carrasco, E.; van Veggel, F. C.; Bovero, E.; Sole, J. G.; Jaque, D., Neodymium-doped LaF_3 nanoparticles for fluorescence bioimaging in the second biological window. *Small* **2014,** *10*, 1141.

241. Rocha, U.; Silva, C. J. d.; Silva, W. F.; Guedes, I.; Benayas, A.; Maestro, L. M.; Elias, M. A.; Enrico Bovero; Frank C. J. M. van Veggel; Solé, J. A. G.; Jaque, D., Subtissue Thermal Sensing Based on Neodymium-Doped LaF3 Nanoparticles. *ACS Nano* **2013,** *7*, 1188
242. Liu, Y.; Zhou, S.; Zhuo, Z.; Li, R.; Chen, Z.; Hong, M.; Chen, X., In vitro upconverting/downshifting luminescent detection of tumor markers based on Eu^{3+}-activated core-shell-shell lanthanide nanoprobes. *Chem. Sci.* **2016,** *7*, 5013.
243. Ou, X.; Chen, Y.; Xie, L.; Chen, J.; Zan, J.; Chen, X.; Hong, Z.; He, Y.; Li, J.; Yang, H., X-ray nanocrystal scintillator-based aptasensor for autofluorescence-free detection. *Anal. Chem.* **2019,** *91*, 10149.
244. Carnall, W. T.; Goodman, G. L.; Rajnak, K.; Rana, R. S., A systematic analysis of the spectra of the lanthanides doped into single crystal LaF_3. *J. Chem. Phys.* **1989,** *90*, 3443.
245. Rodrigues, E. M.; Gaspar, R. D. L.; Mazali, I. O.; Sigoli, F. A., Polydimethylsiloxane composites containing core-only lanthanide-doped oleylamine-stabilized LaF_3 nanoparticles with high emission lifetimes. *J. Mater. Chem. C* **2015,** *3*, 6376.
246. Binnemans, K., Interpretation of europium(III) spectra. *Coord. Chem. Rev.* **2015,** *295*, 1.
247. Wurth, C.; Fischer, S.; Grauel, B.; Alivisatos, A. P.; Resch-Genger, U., Quantum yields, yurface yuenching, and yassivation efficiency for ultrasmall core/shell upconverting nanoparticles. *J. Am. Chem. Soc.* **2018,** *140*, 4922.
248. Sun, X.; Wang, X.; Chen, B.; Zhao, F.; Xu, X.; Ren, K.; Lu, Y.; Qiao, X.; Qian, G.; Fan, X., Phase and morphology evolution of luminescent $NaLnF_4$ (Ln = La to Yb) micro-crystals: understanding the ionic radii and surface energy-dependent solution growth mechanism. *Cryst. Eng. Comm.* **2019,** *21*, 6652.
249. Wang, H.; Nann, T., Monodisperse upconversion GdF3:Yb, Er rhombi by microwave-assisted synthesis. *Nanoscale Res. Let.* **2011,** *6*, 1
250. Bergstrand, J.; Liu, Q.; Huang, B.; Peng, X.; Wurth, C.; Resch-Genger, U.; Zhan, Q.; Widengren, J.; Agren, H.; Liu, H., On the decay time of upconversion luminescence. *Nanoscale* **2019,** *11*, 4959.
251. Chen, Y.; D'Amario, C.; Gee, A.; Duong, H. T. T.; Shimoni, O.; Valenzuela, S. M., Dispersion stability and biocompatibility of four ligand-exchanged $NaYF_4$: Yb, Er upconversion nanoparticles. *Acta Biomater.* **2020,** *102*, 384.
252. Wilhelm, S.; Kaiser, M.; Wurth, C.; Heiland, J.; Carrillo-Carrion, C.; Muhr, V.; Wolfbeis, O. S.; Parak, W. J.; Resch-Genger, U.; Hirsch, T., Water dispersible upconverting nanoparticles: effects of surface modification on their luminescence and colloidal stability. *Nanoscale* **2015,** *7*, 1403.
253. Liu, N.; Gobeil, N.; Evers, P.; Gessner, I.; Rodrigues, E. M.; Hemmer, E., Water dispersible ligand-free rare earth fluoride nanoparticles: water transfer versus $NaREF_4$-to-REF_3 phase transformation. *Dalton Trans.* **2020,** *49*, 16204.
254. Kaczmarek, S. M.; Tsuboi, T.; Ito, M.; Boulon, G.; Leniec, G., Optical study of Yb^{3+}/Yb^{2+} conversion in CaF_2 crystals. *J. Phys. Condens. Matter.* **2005,** *17*, 3771.
255. Jin, Q.; Gao, S.; Xu, Y.; Caggiano, A., A Feasible and Facile Method for the Anticounterfeiting of Down Fiber. *Adv. Mater. Sci. Eng.* **2021,** *2021*, 1.
256. Schroter, A.; Märkl, S.; Weitzel, N.; Hirsch, T., Upconversion nanocrystals with high lanthanide content: luminescence loss by energy migration versus luminescence enhancement by lncreased NIR absorption. *Adv.Funct. Mater.* **2022,** *32*.

257. Homann, C.; Krukewitt, L.; Frenzel, F.; Grauel, B.; Wurth, C.; Resch-Genger, U.; Haase, M., $NaYF_4$:Yb,Er/$NaYF_4$ core/shell nanocrystals with high upconversion luminescence quantum yield. *Angew. Chem. Int. Ed.* **2018,** *57*, 8765.
258. Gnach, A.; Lipinski, T.; Bednarkiewicz, A.; Rybka, J.; Capobianco, J. A., Upconverting nanoparticles: assessing the toxicity. *Chem. Soc. Rev.* **2015,** *44*, 1561.
259. Bednarkiewicz, A.; Marciniak, L.; Carlos, L. D.; Jaque, D., Standardizing luminescence nanothermometry for biomedical applications. *Nanoscale* **2020,** *12*, 14405.
260. Wang, Y. X., Superparamagnetic iron oxide based MRI contrast agents: current status of clinical application. *Quant. Imaging Med. Surg.* **2011,** *1*, 35.
261. Martin Rohrer, H. B., Jan Mintorovitch, P Martin Requardt, and Hanns-Joachim Weinmann, , Comparison of magneticproperties of MRI contrast media solutions at different magnetic field strengths. *Invest. Radiol.* **2005,** *40*, 10.
262. Harris, M.; Vander Elst, L.; Laurent, S.; Parac-Vogt, T. N., Magnetofluorescent micelles incorporating Dy(III)-DOTA as potential bimodal agents for optical and high field magnetic resonance imaging. *Dalton Trans.* **2016,** *45*, 4791.
263. Caravan, P.; Greenfield, M. T.; Bulte, J. W., Molecular factors that determine curie spin relaxation in dysprosium complexes. *Magn. Reson. Med.* **2001,** *46*, 917.
264. Zhang, Y.; Lin, J. D.; Vijayaragavan, V.; Bhakoo, K. K.; Tan, T. T., Tuning sub-10 nm single-phase $NaMnF_3$ nanocrystals as ultrasensitive hosts for pure intense fluorescence and excellent T_1 magnetic resonance imaging. *Chem. Commun.* **2012,** *48*, 10322.
265. Jin, X.; Fang, F.; Liu, J.; Jiang, C.; Han, X.; Song, Z.; Chen, J.; Sun, G.; Lei, H.; Lu, L., An ultrasmall and metabolizable PEGylated $NaGdF_4$:Dy nanoprobe for high-performance T_1/T_2-weighted MR and CT multimodal imaging. *Nanoscale* **2015,** *7*, 15680.
266. Biju, S.; Gallo, J.; Banobre-Lopez, M.; Manshian, B. B.; Soenen, S. J.; Himmelreich, U.; Vander Elst, L.; Parac-Vogt, T. N., A magnetic chameleon: biocompatible lanthanide fluoride nanoparticles with magnetic field dependent tunable contrast properties as a versatile contrast agent for low to ultrahigh field MRI and optical imaging in biological window. *Chem. Eur. J.* **2018,** *24*, 7388.
267. Zhao, J.; Hu, H.; Liu, W.; Wang, X., Multifunctional $NaYF_4$:Nd/$NaDyF_4$ nanocrystals as a multimodal platform for NIR-II fluorescence and magnetic resonance imaging. *Nanoscale Adv.* **2021,** *3*, 463.
268. Małgorzata Norek, E. K., Uli Zeitler, and Joop A. Peters, Tuning of the size of Dy_2O_3 nanoparticles for optimal performance as an MRI contrast agent. *J. Am. Chem. Soc.* **2008,** *130*, 6.
269. Yin, J.; Xu, F.; Qu, H.; Li, C.; Liu, S.; Liu, L.; Shao, Y., Dysprosium-doped iron oxide nanoparticles boosting spin-spin relaxation: a computational and experimental study. *Phys. Chem. Chem. Phys.* **2019,** *21*, 11883.
270. Gianolio, E.; Gregorio, E. D.; Aime, S., Chemical insights into the issues of Gd retention in the brain and other tissues upon the administration of Gd-containing MRI contrast agents. *Eur. J. Inorg. Chem.* **2019,** *2019*, 137.
271. McCormack, P. L., Iobitridol: a review of its use as a contrast medium in diagnostic imaging. *Clin. Drug Investig.* **2013,** *33*, 155.

272. Johnson, B.; Hinshaw, J. L.; Robbins, J. B.; Pickhardt, P. J., Objective and subjective intrapatient comparison of iohexol versus diatrizoate for bowel preparation quality at CT colonography. *AJR Am. J. Roentgenol.* **2016,** *206*, 1202.
273. Zhang, Y.; Vijayaragavan, V.; Das, G. K.; Bhakoo, K. K.; Tan, T. T. Y., Single-Phase $NaDyF_4$:Tb^{3+} Nanocrystals as Multifunctional Contrast Agents in High-Field Magnetic Resonance and Optical Imaging. *Eur. J. Inorg. Chem.* **2012,** *2012*, 2044.
274. Song, E.; Ye, S.; Liu, T.; Du, P.; Si, R.; Jing, X.; Ding, S.; Peng, M.; Zhang, Q.; Wondraczek, L., Tailored near-infrared photoemission in fluoride perovskites through activator aggregation and super-exchange between divalent manganese Ions. *Adv. Sci.* **2015,** *2*, 1500089.
275. Zhao, J.; Zhang, Z.; Wang, X., Fabrication of pH-responsive PAA-$NaMnF_3$@DOX hybrid nanostructures for magnetic resonance imaging and drug delivery. *J. Alloys Compd.* **2020,** *820*.
276. Nava-Avendaño, J.; Arroyo-de Dompablo, M. E.; Frontera, C.; Ayllón, J. A.; Palacín, M. R., Study of sodium manganese fluorides as positive electrodes for Na-ion batteries. *Solid State Ion.* **2015,** *278*, 106.
277. Yang, M.; Kc, A.; Garcia-Castro, A. C.; Borisov, P.; Bousquet, E.; Lederman, D.; Romero, A. H.; Cen, C., Room temperature ferroelectricity in fluoroperovskite thin films. *Sci. Rep.* **2017,** *7*, 7182.
278. Ye, S.; Zhao, M.; Song, J.; Qu, J., Core-shell structured $NaMnF_3$: Yb, Er nanoparticles for bioimaging applications. *RSC Adv.* **2017,** *7*, 52588.
279. Gocheva, I. D.; Nishijima, M.; Doi, T.; Okada, S.; Yamaki, J.-i.; Nishida, T., Mechanochemical synthesis of $NaMF_3$ (M=Fe, Mn, Ni) and their electrochemical properties as positive electrode materials for sodium batteries. *J. Power Sources* **2009,** *187*, 247.
280. Kc, A.; Borisov, P.; Shvartsman, V. V.; Lederman, D., Weak ferromagnetism and short range polar order in NaMnF3 thin films. *Appl. Phys. Lett.* **2017,** *110*.
281. Agnoli, F.; Zhou, W. L.; O'Connor, C. J., Synthesis of cubic antiferromagnetic $KMnF_3$ nanoparticles using reverse micelles and their self-assembly. *Adv. Mater.* **2001,** *13*, 3.
282. Du, Y. P.; Zhang, Y. W.; Yan, Z. G.; Sun, L. D.; Gao, S.; Yan, C. H., Single-crystalline and near-monodispersed $NaMF_3$ (M = Mn, Co, Ni, Mg) and $LiMAlF_6$ (M = Ca, Sr) nanocrystals from cothermolysis of multiple trifluoroacetates in solution. *Chem. Asian J.* **2007,** *2*, 965.
283. Hao, L.-N.; Liu, K.; Cheng, S.; Wang, Y.; Xu, Y.-J.; Qian, H.-S., $KMnF_3$ nanowires and nanoparticles: selected synthesis, characterization and magnetic properties. *Mater. Lett.* **2017,** *196*, 145.
284. Tang, Q.; Shen, J.; Zhou, W.; Liu, J.; Liu, Z.; Qian, Y., Fabrication, structure and magnetic properties of fluoroperovskite $KMnF_3$ nanostructures. *Inorg. Chem. Commun.* **2004,** *7*, 283.
285. Hwang, J.; Chun, J., Microwave‐assisted solvothermal synthesis of sodium metal fluoride (Na_xMF_y) nanopowders. *J. Am. Ceram. Soc.* **2019,** *102*, 6475.
286. Mai, H. X.; Zhang, Y. W.; Si, R.; Yan, Z. G.; Sun, L.; You, L. P.; Yan, C. H., High quality sodium rare-earth fluoride nanocrystals: controlled synthesis and optical properties. *J. Am. Chem. Soc.* **2006,** *128*, 11.
287. Peng, X.; Yang, W.; Wickham, J.; Scher E.; Kadavanich A.; Alivisatos,A. P., Shape control of CdSe nanocrystals. *Nature* **2000,** *404*, 59.

288. Wang, M.; Zhang, Y.; Yao, Q.; Ng, M.; Lin, M.; Li, X.; Bhakoo, K. K.; Chang, A. Y.; Rosei, F.; Vetrone, F., Morphology control of lanthanide doped $NaGdF_4$ nanocrystals via one-step thermolysis. *Chem. Mater.* **2019,** *31*, 5160.
289. Bai, Z.; Lin, H.; Imakita, K.; Montazami, R.; Fujii, M.; Hashemi, N., Synthesis of Er^{3+}/Yb^{3+}codoped $NaMnF_3$ nanocubes with single-band red upconversion luminescence. *RSC Adv.* **2014,** *4*, 61891.
290. Martín-Rodríguez, R.; Fischer, S.; Ivaturi, A.; Froehlich, B.; Krämer, K. W.; Goldschmidt, J. C.; Richards, B. S.; Meijerink, A., Highly efficient IR to NIR upconversion in Gd_2O_2S: Er^{3+} for photovoltaic applications. *Chem. Mater.* **2013,** *25*, 1912.
291. Huang, J.; Song, Y.; Sheng, Y.; Zheng, K.; Li, H.; Zhang, H.; Huo, Q.; Xu, X.; Zou, H., Gd_2O_2S:Eu^{3+} and Gd_2O_2S:Eu^{3+}/Gd_2O_2S hollow microspheres: solvothermal preparation and luminescence properties. *J. Alloys Compd.* **2012,** *532*, 34.
292. Nexha, A.; Carvajal, J. J.; Pujol, M. C.; Diaz, F.; Aguilo, M., Lanthanide doped luminescence nanothermometers in the biological windows: strategies and applications. *Nanoscale* **2021,** *13*, 7913.
293. Puccini, A.; Liu, N.; Hemmer, E., Praseodymium-doped nanoparticles: candidates for near-infrared-II double- and single-band nanothermometry. *ACS Mater. Lett.* **2024**, *6*, 1327.
294. Chang, Y.; Chen, H.; Xie, X.; Wan, Y.; Li, Q.; Wu, F.; Yang, R.; Wang, W.; Kong, X., Bright Tm^{3+}-based downshifting luminescence nanoprobe operating around 1800 nm for NIR-IIb and c bioimaging. *Nat. Commun.* **2023,** *14*, 1079.
295. Hazra, C.; Skripka, A.; Ribeiro, S. J. L.; Vetrone, F., Erbium Single‐Band Nanothermometry in the Third Biological Imaging Window: Potential and Limitations. *Adv. Opt. Mater.* **2020,** *8*, 2001178.
296. Nexha, A.; Carvajal, J. J.; Pujol, M. C.; Díaz, F.; Aguiló, M., Short-wavelength infrared self-assessed photothermal agents based on Ho,Tm:$KLu(WO_4)_2$ nanocrystals operating in the third biological window (1.45–1.96 μm wavelength range). *J. Mater. Chem. C* **2020,** *8*, 180.
297. Wang, Z.; Christiansen, J.; Wezendonk, D.; Xie, X.; Van Huis, M. A.; Meijerink, A., Thermal enhancement and quenching of upconversion emission in nanocrystals. *Nanoscale* **2019,** *11*, 12188.
298. Muñoz‐Ortiz, T.; Abiven, L.; Marin, R.; Hu, J.; Ortgies, D. H.; Benayas, A.; Gazeau, F.; Castaing, V.; Viana, B.; Chanéac, C.; Jaque, D.; Maturi, F. E.; Carlos, L. D.; Martín Rodrí guez, E.; García Solé, J., Temperature dependence of water absorption in the biological windows and its impact on the performance of Ag_2S luminescent nanothermometers. *Part. Part. Syst. Charact.* **2022,** *39*, 2200100.
299. Shen, Y.; Lifante, J.; Fernandez, N.; Jaque, D.; Ximendes, E., In vivo spectral distortions of infrared luminescent nanothermometers compromise their reliability. *ACS Nano* **2020,** *14*, 4122.
300. Jones, C. M. S.; Gakamsky, A.; Marques-Hueso, J., The upconversion quantum yield (UCQY): a review to standardize the measurement methodology, improve comparability, and define efficiency standards. *Sci. Technol. Adv. Mater.* **2021,** *22*, 810.
301. Zhang, C.; Yan, L.; Wang, X.; Zhu, S.; Chen, C.; Gu, Z.; Zhao, Y., Progress, challenges, and future of nanomedicine. *Nano Today* **2020,** *35*, 101008.